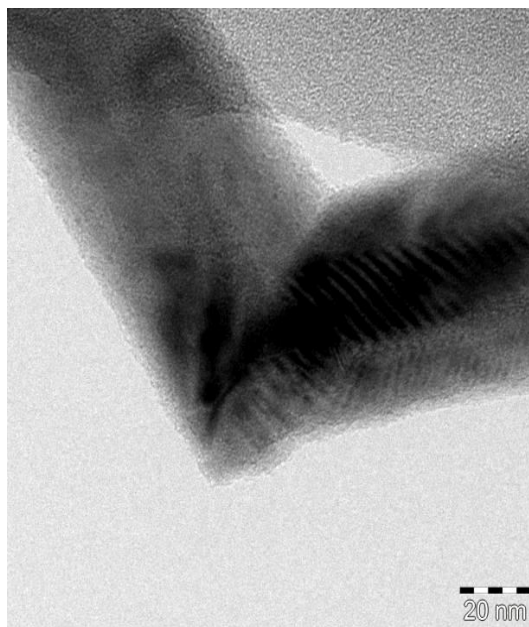


Synthesis, Characterization and Surface Modification of Titanium and Zinc Oxide Nanostructures for Nanotoxicity, Visible Light Emission and Photocatalytic Studies



Inaugural-Dissertation
zur Erlangung des Doktorgrades
der Mathematisch Naturwissenschaftlichen Fakultät
der Universität zu Köln

vorgelegt von
Osman Arslan
aus
Saruhanli,Manisa/Türkei



Köln, 2013

Bibliografische Information der Deutschen Bibliothek

Die Deutsche Bibliothek verzeichnet diese Publikation in der Deutschen Nationalbibliografie; detaillierte bibliografische Daten sind im Internet über <http://dnb.ddb.de> abrufbar.

Arslan, Osman:

Synthesis, Characterization and Surface Modification of Titanium and Zinc Oxide Nanostructures for Nanotoxicity, Visible Light Emission and Photocatalytic Studies
ISBN 978-3-86376-132-5

Angefertigt mit Genehmigung der
Mathematisch-Naturwissenschaftlichen Fakultät der
Universität zu Köln

Berichterstatter Prof. Dr. Sanjay Mathur
Prof. Dr. Axel G. Griesbeck
Prof. Dr. Gerd Meyer

Tag der mündlichen Prüfung 12 Dezember 2013

Alle Rechte vorbehalten

1. Auflage 2014

© Optimus Verlag, Göttingen

© Coverfoto:

URL: www.optimus-verlag.de

Printed in Germany

Papier ist FSC zertifiziert (holzfrei, chlorfrei und säurefrei,
sowie alterungsbeständig nach ANSI 3948 und ISO 9706)

Das Werk, einschließlich aller seiner Teile, ist urheberrechtlich geschützt. Jede Verwertung außerhalb der engen Grenzen des Urheberrechtsgesetzes in Deutschland ist ohne Zustimmung des Verlages unzulässig und strafbar. Dies gilt insbesondere für Vervielfältigungen, Übersetzungen, Mikroverfilmungen und die Einspeicherung und Verarbeitung in elektronischen Systemen.

Acknowledgements

I want to first thank to my Glorious Allah for giving me patience, perseverance and success and his latest Prophet and Messenger Muhammed Mustafa – Sallallahu Aleyhi ve Sellem- for teaching me how to be a Muslim and Mumin. All comes from Allah – Azze ve Celle- and everyone finds the true salvation in this world and hereafter who understands the Latest Holy Book Qur'an, follows it and the latest Messenger Muhammed Mustafa –Sallallahu Aleyhi ve Sellem- properly. I am extremely thankful to my Ustadh Osman Nuri Topbas (k.s.), his dear friends Ahmed Hamdi Topbas, Abdullah Sert, Dogan Gokmen and proud of being member of such a beautiful Muslim society. Kalbimin Antalya parcasi olan hocalarim Sadik Uzer, Osman Musara, Ramazan Yildiz ve orayi unutulmaz yapan tum agabey ve kardeslerim, Köln'de Lütfi Agabey ve ailesi, Adnan Kurt Agabey ve ailesi, Ibrahim Altun Agabey ve ailesi, Ali Kurt agabey ve ailesi, Atilla Abi ve ailesi, Mustafa Cinar Agabey ve ailesi, Veyis Celik Agabey ve ailesi, Yusuf Agabey (Allah cennetinde bulustursun, amin) ve ailesi, Adnan Sarp Agabey ve ailesi, Gazi Agabey, Muharrem Agabey, Fatih Camurlu Agabey, Timur agabey, Ömer&Ali Agabey, M.Moral agabey, Kenan agabey, M.Taha agabey, Yusuf agabey, Hak Genclik grubumuzun uyeleri, Caglayan Agabey, Murat agabey ve Cuma gününün aksamcileri! ve hepsinin aileleri ve isimlerini sayamadigim daha nice saygideger abilerime tesekkur ederim. Siz olmadan bu tez gercekten bir mana ifade etmezdi. Köln sehrini bana cennetten bir bahce yaptiniz!

I am indebted to my friend and advisor Prof. Dr. Sanjay Mathur for inviting me to Germany for this amazing journey into the nanoworld, for our first conversation at March 2009 , giving me the opportunity, encourage, responsibility, amazing guidance, positive criticism, focused commentary, mentorship and freedom to work in this area. I know I am hard to handle but will never forget your inexpressible contribution to my life Professor, thank you so much!

I am grateful to my committee members who helped for the formation of this thesis with their guidance and analysis.

Completion and positive results of this thesis would not have been possible without deep support and help of the members of the Institute of Inorganic and Material Chemistry, and my special thanks go to Dr. Yee Hwa Sehlleier, Dr. Stefan Stucky, Dr. Hao Shen, Dr. Lisong Xiao, Dr. Thomas Rügamer, Linus

Appel, Melanie Hassold, Lisa Czympiel, Mehtap Büyükyazi, Laura Wortmann, Konstantin Konstantynovski, Cristopher Waldman, Gregor Fornalczyk, Tessa Leuning, Dr. Mahboube Maleki, Bianka Müller, Thomas Ackermann, Johannes Pfrommer, Ralf Müller, Sebastian Sahler, Dr. Jun Pan, Dr. Aadesh Prataph Singh, Dr. Karthik Raveendran, Dr. Robin von Hagen, Dr. David Zopes, Dr. Irina Giebelhaus, Thomas Fischer, Daniela Hermann, Thomas Lehn, Michael Kessler, Manuel Langemann, Benjamin Stein, Silke Kremer, Karim Arroub, Anna Jurewicz, Dr. Yakup Gönüllü, Dr. Bilge Saruhan, Martin Hoffman, Rouhini Athavale, Peter Golus, Salma Tammam, Andreas Mettenböcker, Nurgül Tosun, Dr. Lhoussaine Belkoura, Dr. X Song, Dr. Ingo Pantenburg, Corinna Hegemann, Dr. Raquel Fiz, Dr. Wieland Tyrra, Shifa Siribbal, Dr. Frank Heinrich, Frau A. Roth, Frau A. Uhlemann, Frau C. Schaefer for their great help and Dr. Abdusalam Uheida, Terrance Burks, Dr. Jingwen Shi, Prof. Dr. Valerian Kagan, Prof. Dr. Harald Krug, Dr. Tina Thurnberr, Prof. Dr. Andrea Kuzmann, Dr. Soile Tuomela, Prof. Dr. Bengt Fadeel and all the other members of NANOMMUNE Project for forming such a great scientific atmosphere. I also express my sincere gratitude to Prof. Dr. Suprakas S. Ray, Dr. Manfred Scriba and other friendly members of CSIR. Thomas, Bonex, Charity, Ella, Sharon, Malcolm, Dr. James, Vuyiswa, Kelso, Simphiwe, Dr. Sreejarani, Dr. Jayita, Dr. David, Dr. Gugu and other unmentioned members of CSIR, thank you that you have provided an amazing environment for me during my stay. Nagi my brother, thank you man but I mean really thank you! I want to thank to Dr. Muhammed Sajid Hussain for Confocal Microscopy measurements, Dr. Dirk Hertel for fluorescence spectroscopy measurements, Ashish Lepcha for being so friendly, Shaista Ilyas for her great help, corrections and support, Prof. Ruschewitz, Klein and Meyer group members for their kind help, Kathrin Stirnat for EPR measurements, Johannes Schlafer for HR-TEM measurements, Dr. Trilok for his extra help and guidance, Dr. Alaeddin Gad for his friendship and humour, Dr J. Li for sharing my laboratory. Thank you Mesude, Yusuf, Okan, Dino and Annika for teaching me!

Thanks to other forgotten friends who helped during this thesis. You were all great!

Babam Abdullah Mesut Arslan
Annem Serife Arslan
Kardeslerim Fatma Betül Arslan,
Meryem Sümeyye Arslan
ve
Yusuf Sami Arslan için



Abstract

Size dependent quantum confinement and differential characteristics of the anisotropic ZnO and TiO₂ nanomaterials have attracted huge interest in the quest of new functional materials. In order to synthesize ZnO QD's for visible light emission applications, surface modulation for stability in dispersions and defect control at the surface is vitally important. Therefore long alkyl chain group (e.g. oleate) and biological molecule cysteine were used as vectors to regulate reactivity of the ZnO QD's and their visible light emission. Sol-gel chemistry serves as a versatile tool for the fabrication of controlled synthesis of quantum dots and to modify their properties for emission applications such as cell labeling, cell toxicity, solid-state light emission and to understand size/property correlation. High temperature liquid phase synthesis methods, namely heating up and hot injection method were applied toward the synthesis of anisotropic ZnO and TiO₂ nanoparticles. Using different ligand concentrations and reaction conditions, semiconductor nanostructures of unusual geometrical shapes were synthesized and characterized. Hexagonal crystal growing habit of ZnO provided unusual geometrically distorted examples of the hexagonal geometry that have not been reported so far in the literature. Furthermore, TiO₂ nanostructures with significant absorption in visible range of the solar spectrum were obtained by hot injection method and nitrogen doping. The rapid injection and decomposition of Ti-precursor and amine enabled to produce self assembled ball like and multibranched structures with remarkable visible range absorption. Utilization of different concentrations for the precursors provided the possibility of band gap engineering for the anisotropic TiO₂ nanostructures.

Zusammenfassung

Größenabhängige ZnO und TiO₂ anisotroper Nanomaterialien haben ein enormes Interesse bei der Suche nach neuen Funktionalisierten hervorgerufen. Für die Herstellung von ZnO Nanoteilchen „Quantum Dots“ für die Emission sichtbaren Lichts sind Veränderungen der Oberfläche - für die Stabilität in Dispersionen - sowie eine Kontrolle an der Oberflächen vorhandenen Defekte von wesentlicher Bedeutung. Zu diesem Zwecke wurden ZnO Nanopartikeln durch Einbringung von langkettige Alkyl-Gruppen (z. B. Oleate) sowie biologisch relevante Molekülen wie Cystein modifizierte, um die Reaktivität der ZnO „Quantum Dots“ und deren Emission seigen von sichtbarem Licht zu regulieren. Sol-Gel Prozesse dienen dabei als vielseitige Werkzeuge zur gezielten Synthese von Nanoskaligen Materialien und zum Modifizieren der Eigenschaften für die jeweiligen Anwendungen wie zum Beispiel für die Emission wie die Markierung von Zellen, Photokatalysator und UV- Absorber. Hochtemperaturmethoden in flüssiger Phase wie gezieltes Aufheizen und „Hot Injection“ wurden in dieser Arbeit, zur Synthese Kristallbau ZnO und TiO₂ Nanopartikel angewendet. Durch Verwendung unterschiedlicher Ligandenkonzentrationen und Reaktionsbedingungen konnten Halbleiter-Nanostrukturen in ungewöhnlichen geometrischen Formen erzeugt und charakterisiert werden. Die Kontrolle der Kristallwachstumprozesse von ZnO Nanostrukturen ermöglichte es, ungewöhnliche Morphologien zu erzeugen, die bisher in der Literatur noch nicht beschrieben wurden. Des Weiteren wurden TiO₂-Nanostrukturen durch die „Hot injection“-Methode erhalten, die eine signifikante Absorption auf Grund einer N-dotierung in sichbaren Bereich aufweisen. Die äußerst schnelle Injektion und spontane Zersetzung des Ti-haltigen Präkursors in Gegenwart eines Amins erlaubte die Darstellung selbstangeordneter Kugelartiger und verzweigter Standformiger Sternförmiger Strukturen mit bemerkenswerten Absorptionen im Bereich des sichtbaren Lichtes. Das Nutzen unterschiedlicher Präkursor-Konzentrationen ermöglicht den gezielten Aufbau anisotroper TiO₂-Nanostrukturen mit variabler Bandlücken.

Table of Contents

List of Figures	VII
List of Tables	XVII
Abbreviations and Symbols	XIX
1 Introduction	1
1.1 Nanomaterials: Opportunities and Challenges.....	1
1.2 Scope	1
2 State-of-the-Art: Nanostructure Synthesis	5
2.1 General Concepts of Nanostructure Fabrication.....	5
2.1.1 Bottom-up and Top-down Method	5
2.2 La-Mer Theory for the Nanoparticle Formation: Nucleation and Growth.....	6
2.2.1 Growth of the Nanoparticles	9
2.2.2 Ostwald Ripening.....	10
2.3 Kinetic versus Thermodynamic Control of Anisotropic Particles.....	11
2.3.1 Seed-Mediated Solution–Liquid–Solid (SLS) Growth.....	11
2.3.2 Oriented Attachment	12
2.3.3 Kinetically Induced Anisotropic Growth.....	13
2.3.3.1 Surface Energy and Selective Adhesion	13
2.3.3.2 Influence of the Phase of the Crystalline Seed.....	17
2.3.3.3 Thermodynamic or Kinetic Control of the Growth Regime.....	18
2.4 Nano-Synthetic Methods.....	21
2.4.1 Hot Injection Synthesis	21
2.4.2 Heating Up Method for Nanostructures.....	22
2.4.3 Sol Gel Method for Synthesis	23
2.4.3.1 Organically Modified Nanostructures by Sol Gel Method	24
2.4.4 Hydro-Solvo Thermal Method for Nanostructures.....	24

Table of Contents

2.5 MOx/Polymer Nanocomposites.....	25
2.5.1 Hybrid Inorganic Organic Polymer/MOx Nanocomposite.....	25
2.5.2 MOx@Clay Nanocomposite Structures	27
3 Experimental Part	29
3.1 Experimental Procedures	29
3.1.1 Synthesis of ZnO Nanostructures	29
3.1.1.1 Salt Elimination Method for Zn(Oleate) ₂	30
3.1.1.2 Amide Method for Zn(Oleate) ₂ Precursor.....	30
3.1.2 Ligand Controlled ZnO Quantum Dot Synthesis	31
3.1.2.1 Acetate Controlled ZnO QD Synthesis	31
3.1.2.2 Cysteine Capped Zwitterionic ZnO QD Synthesis	32
3.1.2.3 Oleate Capped ZnO QD Synthesis.....	32
3.1.2.4 Phase Transfer Synthesis of ZnO QD's	32
3.1.3 Heating Up Synthesis of Anisotropic ZnO Nanoparticles.....	33
3.1.3.1 Salt Assisted Surface Modification of ZnO Nanostructures.....	34
3.1.3.2 SiO ₂ @ZnO Core/Shell (Encapsulated) Nanostructures with Different Surface Modifications	35
3.1.4 Synthesis of TiO ₂ Nanostructures.....	36
3.1.4.1 Synthesis of one-dimensional TiO ₂ Nanofibers by Hydrothermal Method	37
3.1.4.2 Synthesis of Spherical TiO ₂ Nanoparticles by Heating Up Method.....	38
3.1.4.3 Synthesis of Multibranched, Elongated TiO ₂ Nanostructures by Hot Injection Method	38
3.1.5 Inorganic Organic Hybrid Polymer/ZnO Nanocomposite Synthesis	39
3.1.5.1 PLA/Hybrid Polymer/NP Nanocomposite Synthesis	41
3.1.5.2 ZnO@Clay Nanocomposite Preparation.....	42
3.2 Characterization Techniques.....	42

3.2.1	Transmission and High Resolution Transmission electron Microscopy.....	42
3.2.2	Scanning Electron Microscopy (SEM) and Electron Diffraction X-Ray (EDX)	43
3.2.3	X-Ray Diffraction Spectroscopy.....	43
3.2.4	Thermogravimetric Analysis	44
3.2.5	Atomic Force Microscopy (AFM)	44
3.2.6	Photoluminescence Spectroscopy	44
3.2.7	UV-Visible Spectroscopy	44
3.2.8	Surface Contact Angle	45
3.2.9	Dynamic Light Scattering (DLS).....	45
3.2.10	Zeta Potential Measurements	45
3.2.11	FT-Infrared Spectroscopy	45
3.2.12	NMR Spectroscopy	46
3.2.13	Confocal Microscopy	46
3.3	Material Properties Testing	46
3.3.1	Cell Cytotoxicity Tests.....	46
3.3.2	Cell Labeling by Visible Light Emitting QD's.....	47
3.3.3	Photocatalytic Activity Tests	47
4	Results and Discussion	51
4.1	Ligand Modulated Visible Light Emitting ZnO QD's.....	51
4.1.1	Fundamental Properties of ZnO QD's and Their Visible Light Emission	51
4.1.2	Acetate as Controlling Ligand for ZnO QD' s	52
4.1.2.1	UV-Visible Investigation and Particle Size Calculation.....	53
4.1.2.2	Photoluminescence Properties and Visible Light Emission	54
4.1.3	Cysteine Molecule as Surface Controlling Ligand for ZnO QD's	56
4.1.3.1	Optical Evolution and Band Gap Modulation of ZnO QD Formation under Cysteine Control	57

Table of Contents

4.1.3.2	Real Crystal Size, Morphology and Surface Properties of Cystein@ZnO QD's	60
4.1.3.3	PL Features and Stability of Cysteine Modified ZnO QD's	63
4.1.3.4	Cysteine Triggered Self Assembly in the ZnO QD's	68
4.1.4	Ultrastable Oleate@ZnO QD's for Phase Transfer and Storage	70
4.1.4.1	General and Swift Synthesis of Blue to Yellow Visible Light Emitting Oleate@ZnO QD's	71
4.1.4.2	NMR Measurements for Identification of Oleate Ligand	79
4.1.4.3	Ultrastability and Agglomeration Free Feature of Oleate@ZnO QD's	81
4.1.4.4	Phase Transfer Synthesis for Water Soluble ZnO QD's and Other Techniques for Visible Light Emission Manipulation	87
4.1.5	Nanomaterials and Discussion of Ligand@ZnO QD's	92
4.1.5.1	Cytotoxicity and Cell Labeling by Ligand@ZnO QD's	92
4.1.5.2	Selective UV-A (400-315 nm) and UV-B (315-280) Region Protection by ZnO QD's and Antibacterial, Transparent, Hybrid Nanocomposites	94
4.2	Anisotropic ZnO Nanoparticles by Heating Up Method	95
4.2.1	Basics of ZnO Heating Up Method	95
4.2.2	Plate like and and Pyramidal ZnO Nanoparticles by Heating Up	96
4.2.3	Distorted Examples of Anisotropic ZnO Nanoparticles by Heating Up Method	98
4.2.4	Crystallinity and Surface Modification of the Anisotropic ZnO Nanostructure	106
4.2.5	Optical, Thermal and Aqueous Properties of the Surface Modified ZnO Nanocrystals	108
4.2.6	Ligand@ZnO Nanostructures as Nanobiotechnology Nanomaterials	113
4.2.6.1	Ligand Effect for the Nanotoxicity and Gene Regulation	113

4.2.6.2	Cell Labeling by Fluorescein Modified ZnO Nanoplates.....	115
4.2.6.3	Photocatalytic activity of the Nanostructures for the Decomposition of Methylene Blue	116
4.3	Synthesis of Visible Light Active, Multibrached TiO ₂ Nanostructures by Hot Injection Method.....	118
4.3.1	Thermogravimetric Analysis of TiO ₂ Precursor for Hot Injection Method	119
4.3.2	Visible Light Active Spherical TiO ₂ by Hot Injection Method.....	121
4.3.2.1	Synthesis and Morphology Investigation of Visible Light Active Spherical TiO ₂	122
4.3.2.2	Band Gap Calculation of Spherical TiO ₂ Nanostructures.....	124
4.3.3	Crystallinity, Surface and Thermal Properties.....	124
4.3.4	Visible Light Active, Multibrached TiO ₂ NR by Hot Injection Method	126
4.3.4.1	Synthesis and Crystallinity of Visible Light Active Multibrached TiO ₂ Nanostructures	127
4.3.4.2	TEM Investigation of the Multibrached, Visible Light Active TiO ₂	128
4.3.4.3	Fundamental Nanorod Morphology for the TiO ₂ Nanostructures	129
4.3.4.4	Angle Between the Attaching Nanorods.....	133
4.3.4.5	Possible Formation Mechanism for the TiO ₂ Multibrached Nanostructures	135
4.3.4.6	Nanomaterial Applications of Spherical and Multibrached Visible Light Active TiO ₂ Nanostructures	138
4.3.5	Solar Light Driven Photocatalysis of Visible Light Active TiO ₂	138
4.4	Metal Oxide / Polymer Nanocomposites	140
4.4.1	Hybrid Inorganic Organic Polymer/MOx Nanocomposites	140
4.4.1.1	TiO ₂ Nanowire/Epoxy-amine Superhydrophilic Nanocomposite.....	141
4.4.2	Polymer and ZnO QD Nanocomposites	142

Table of Contents

4.4.2.1 Selective UV Protective Transparent ZnO/Hybrid Nanocomposites	143
4.4.3 Biodegradable PLA/Metal Oxide Nanocomposites.....	144
4.4.3.1 PLA/MEMO/ZnO QD Nanocomposites.....	144
4.4.4 ZnO QD@Clay Nanocomposites For Light Emitting Clays	151
5 Conclusions and Outlook	153
5.1 Conclusions	153
5.2 Outlook and Future Prospects	155
References	157
Ehrenwörtliche Erklärung	169
Curriculum Vitae	170

List of Figures

Figure 1	General ZnO and TiO ₂ nanostructure synthesis	2
Figure 2	Ligand library for the surface modification and core/shell protection of the nanoparticles.....	3
Figure 3	Several applications of ZnO and TiO ₂ nanostructures.	4
Figure 4	Scheme of complementary “top-down” and “bottom-up” approaches for fabrication of micro- and nano-structures ^[19]	5
Figure 5	Schematic diagram illustrating La Mer’s condition for stable nucleation ^[39]	6
Figure 6	Free energy diagramme explaining the critical nucleus ^[40]	8
Figure 7	Schematic of nucleation and growth of the nanocrystals in La Mer theory ^[41]	9
Figure 8	Sketch of Ostwald ripening process ^[43]	10
Figure 9	Alloy formation of the solution grown nanowires ^[45]	12
Figure 10	Schematic representation of oriented attachment processes ^[45]	13
Figure 11	Surface energy of wurtzite ZnS nanocrystals.	14
Figure 12	Surface modulation effects induced by surface-selective surfactants on either a) anisotropic rod or b) disc growth.	15
Figure 13	Shape evolution of TiO ₂ nanocrystals through the surface energy modulation effect by using surface selective lauric acid (LA) surfactants.	16
Figure 14	Temperature-mediated crystalline-phase control of a,b) MnS and c,d) CdS nanocrystals.....	18
Figure 15	a,b) Heterostructured rods formed by adding CdSe extensions to each end of CdS nanorods. c,d) Branched rods result from the nucleation of zinc blende CdTe on either end of the CdSe nanorods(continues).....	19
Figure 16	Comparison of a) thermodynamic and b) kinetic growth of PbS nanocrystals.....	20
Figure 17	Experimental set-up and reaction scheme for the hot-injection method ^[49]	22

Figure 18	Basic reactions of sol gel method from a metal alkoxide.....	23
Figure 19	Morphological variation schema for sol-gel method ^[52]	23
Figure 20	Solvo/hydrothermal synthesis installation ^[54]	25
Figure 21	Example of a hybrid formulation consisting of acrylic alkoxysilane, biodegradable PLA and ZnO QD's.	26
Figure 22	Idealized structure montmorillonite clay (without organic modification) showing two tetrahedral-site sheets fused to an octahedral-site sheet.....	27
Figure 23	Exfoliated (left) and intercalated (right) clay structures by polymeric architectures.....	28
Figure 24	Würtzite crystal structure of ZnO.	29
Figure 25	Amide procedure of ZnO QD synthesis from an organometallic precursor.	31
Figure 26	Non hydrolytic high temperature formation mechanism of ZnO nanoparticles from oleate precursor.....	33
Figure 27	Experimental set-up for the heating up method for ZnO nanocrystal synthesis.	34
Figure 28	General carboxylic acid modification of ZnO nanoparticles.....	35
Figure 29	Crystal structures of TiO ₂ phases and atomic orientation in the TiO ₂ crystal structures.....	37
Figure 30	Spherical TiO ₂ formation by Hot Injection method.	38
Figure 31	Hot Injection Synthesis of Multibranched TiO ₂	39
Figure 32	Partial hydrolysis of epoxy modified trialkoxysilane.....	40
Figure 33	Epoxy ring opening reactions in hybrid nanocomposites.	41
Figure 34	Schema for the nanoparticle surface modification.	41
Figure 35	MTT test for the cell viability.....	46
Figure 36	Photocatalytic process for the formation of charge carriers of TiO ₂ ^[86]	48
Figure 37	Photoluminescent processes suggested for ZnO nanoparticles ^[97]	52
Figure 38	UV Visible evolution of Acetate@ZnO QD's.....	53

Figure 39	a) TEM investigation of Acetate@ZnO QD's b) QD size distribution.	54
Figure 40	Visible green emission from the Acetate@ZnO QD's (aliquot times have been written in minutes below the solution).....	54
Figure 41	PL spectra for the QD's before and after storage.	55
Figure 42	Green to orange light shift for Acetate@ZnO QD's.....	55
Figure 43	Acetate@ZnO QD agglomeration and monolayer formation.	56
Figure 44	Cysteine-functionalized ZnO QDs and intermolecular interaction among surface-bound and free cysteine ligands.....	57
Figure 45	UV visible Evolution of the Cysteine @ ZnO QD's.	57
Figure 46	Band gap calculation of the ZnO quantum dot.	58
Figure 47	Band gap variation of Cysteine@ZnO QD's.	59
Figure 48	Particle size evolution for the formation of Cysteine@ZnO QD's.	60
Figure 49	TEM images and calculated particle size distribution of Cysteine@ZnO QD's.	61
Figure 50	XRD patterns of C1,C2,C3 and Acetate@ZnO QD's.	61
Figure 51	FTIR spectra of (a) free cysteine, (b) C0, (c) C3, (d) C2, and (e) C1 samples.....	62
Figure 52	Cysteine (C1) modified ZnO QD's visible light emission.	63
Figure 53	Photoluminescence feature of C2 QD's.....	63
Figure 54	Photoluminescence stability of Cysteine@ZnO QD's, before (left solution) and after (right solution) 1 week (C3).	64
Figure 55	Fluorescence lifetime and automatic correction of cysteine capped ZnO QD's (C3).....	65
Figure 56	EDX analysis and SEM images of the C1, C2 and C3.....	66
Figure 57	TGA investigation of Acetate@ZnO and C3.	66
Figure 58	TG-DTA analysis of pure cysteine, C1 and C2.....	67
Figure 59	Zeta potential measurements for Acetate@ZnO and Cysteine@ZnO.....	68

Figure 60	Assembly of ZnO QDs to form supra-structures and their hydrodynamical property observation with time.	69
Figure 61	Hydrodynamic size variation before and after self assembly.	70
Figure 62	Synthesis of Oleate@ZnO QD's by modified sol-gel method.	72
Figure 63	Evolution of the optical properties of Oleate@ ZnO QD's (ZnO-1).	73
Figure 64	TEM, HR-TEM and SAED patterns of ZnO-1.....	75
Figure 65	Size distributions in Oleate@ZnO nanoparticles.....	75
Figure 66	Visible light emission characteristics of ZnO-1.	76
Figure 67	Visible emissions of a)ZnO-2, b)ZnO-3 and c)Acetate@ZnO.....	77
Figure 68	Optical properties of ZnO-2, ZnO-3 ve ZnO-4, Inset images represent visible emission colour of the quantum dots.....	78
Figure 69	¹ H NMR for the Zn(Oleate) ₂ precursor.....	79
Figure 70	NMR investigation of ZnO quantum dot precursor Zn(Oleate) ₂	79
Figure 71	FT-IR observation of transformation of molecular precursor in the Oleate@ZnO QD.	80
Figure 72	NMR investigation of Oleate@ZnO QD's.	81
Figure 73	Core-shell structure of the Oleate@ZnO QD's for the synthesized Oleate@QD's.	82
Figure 74	TEM and HR TEM images of ZnO-2 (left) and ZnO-3 right.....	83
Figure 75	TEM investigation of oleate removal for ZnO-1.....	83
Figure 76	XRD patterns of ZnO-1 before and after heat treatment.	84
Figure 77	XRD patterns of the Acetate@ZnO and ZnO-2, ZnO-3.....	84
Figure 78	Comparison of the agglomeration behavior of a b)Acetate@ZnO and c-d) Oleate@ZnO QD's.	85
Figure 79	Stability observation of the Oleate@ZnO QD'in in EtOH (a-b-c) and CHCl ₃ (d-e-f) during 6 month with their TEM analysis after storage.....	86
Figure 80	TGA analysis of oleate loading for ZnO QD's.....	87

Figure 81 a)Oleate@ZnO QD's to Gluconic@ZnO QD b)Appearance before and phase transfer under UV illumination (λ_{\max} = 354 nm) c) TEM images before and after phase transfer with gluconic acid.	88
Figure 82 FT-IR confirmation of the phase transfer for gluconic acid	89
Figure 83 Salt like attachment of gluconate after phase transfer synthesis.	89
Figure 84 ZnO QD's solutions for different visible light emissions.....	90
Figure 85 Silica encapsulation causes quenching in visible light emission.	91
Figure 86 a) Confocal images of the HEK cells after 2h incubation b) MTT test for the cell viability during 4h with different dosing.....	93
Figure 87 Cysteine capped ZnO cell labeling and cytotoxicity.	94
Figure 88 Thermal decomposition profiles of precursor mixtures.....	96
Figure 89 Decomposition mechanism of ZnO precursor and FT-IR observation	97
Figure 90 FT-IR spectra for the comparison of beginning and final composition.....	98
Figure 91 Nanoplate morphology for the ZnO nanoparticles.	98
Figure 92 TEM investigation of the nanoplates diameter and length.	99
Figure 93 Hexagonal morphology of the ZnO nanocrystals.....	100
Figure 94 Distorted hexagonal nanocrystals of the ZnO.	101
Figure 95 Particle size distribution of the ZnO-distorted hexagonal nanoparticles.	102
Figure 96 Particle size distribution of the pyramid like ZnO NP's.....	102
Figure 97 TEM investigation of the pyramidal ZnO nanocrystals.	103
Figure 98 Heart shaped assembly from pyramidal ZnO nanoparticles.....	103
Figure 99 Nanoparticle twins of the pyramidal ZnO NP's.	104
Figure 100 TEM and particle size investigation of the ZnO nanorods.....	105
Figure 101 XRD pattern of the as-synthesized ZnO Nanorod.....	106
Figure 102 XRD pattern of the nanoplate like ZnO.....	106

Figure 103	XRD pattern of the pyramidal ZnO.	107
Figure 104	XRD pattern of the distorted hexagonal ZnO nanostructure.	107
Figure 105	FT-IR spectra for the bare ZnO nanocrystals.	108
Figure 106	FT-IR and UV Vis- absorption spectra of the folic acid modified ZnO Nanorods.	109
Figure 107	FT-IR and UV –Vis absorption spectra of the citric acid modified nanopyramids.	110
Figure 108	UV Vis spectrum for the Mandelate@ZnO nanoplate.	110
Figure 109	NMR spectra for mandelic acid modification of ZnO nanoplates.....	111
Figure 110	TEM investigation of the mandelic acid modified ZnO nanoplates.....	111
Figure 111	Thermal weight loss of the folic acid modified ZnO nanorods.	112
Figure 112	Thermal decomposition pattern of the citric acid modified ZnO nanopyramids.....	112
Figure 113	Schematic representation of some key events of ZnO toxicity in Jurkat cells ^[131]	114
Figure 114	Increasing amount of dissolution by the increasing amount of zinc species ^[131]	115
Figure 115	Fluorescein@ZnO nanoplate/nanopyramid cell labeling (bar=10 micrometer).	116
Figure 116	Photocatalytic activity of ligand modified ZnO nanoparticles	117
Figure 117	TiO ₂ precursor mixture evolution during the hot injection synthesis.	119
Figure 118	TGA decomposition profile of Ti-precursor mixtures.	120
Figure 119	FT-IR confirmation of the amide formation until 150 °C.	120
Figure 120	FT-IR confirmation of the amide formation for the Ti-precursor.....	121
Figure 121	Self assembly formation of the spherical TiO ₂ nanoparticles.	122
Figure 122	Self assembly spheres of TiO ₂ and their size distribution.	123

Figure 123	Band Gap calculation and SEM images of TiO ₂ nanoparticles and color comparison of spheres with P-25.....	124
Figure 124	XRD patterns of the spherical TiO ₂ nanoparticles.....	125
Figure 125	FT-IR investigation of the spherical TiO ₂ nanoparticles.....	125
Figure 126	Thermogravimetric analysis and EDX of the spherical TiO ₂ nanoparticles.	126
Figure 127	SEM images of the multibranched TiO ₂ nanocrystals and EDX investigation.....	127
Figure 128	XRD spectra and color difference of elongated TiO ₂	128
Figure 129	Schematic perspective of multibranching in the TiO ₂ Nanostructures.	129
Figure 130	Dipod like TiO ₂ nanostructures.	129
Figure 131	Tripod like nanostructures of TiO ₂	130
Figure 132	Examples of tetrapod like TiO ₂ nanostructures.	131
Figure 133	Obtained multipod TiO ₂ Nanostructures.	131
Figure 134	Fabricated alphabet nanogallery of TiO ₂ without size bars.....	132
Figure 135	Proximity of the different TiO ₂ nanostructures.	133
Figure 136	Angle distribution between the V shaped dipod structures.	133
Figure 137	HR-TEM image and SAED pattern of the TiO ₂ nanorods.	134
Figure 138	HR TEM investigation for the junction points.	135
Figure 139	Shape evolution of TiO ₂ nanocrystals through the surface energy modulation effect by using surface selective lauric acid (LA) surfactants ^[46]	136
Figure 140	Titanium alkoxide for the elongated nanostructures ^[83]	137
Figure 141	Distorted truncated and cube like truncated structures in the early stages of nanorod formation.	138
Figure 142	Solar light spectrum and solar driven visible light photocatalysis.....	138
Figure 143	Photocatalytic comparison activity of of P-25, TiO ₂ Rod and TiO ₂ Spheres by solar light.....	139

Figure 144 Hybrid nanocomposite preparation techniques left) UV curable right) epoxy amine.	140
Figure 145 TiO ₂ Nanowires by hydrothermal method by self dissolution of TiO ₂ nanoparticles.	141
Figure 146 Superhydrophilic nanocomposite coatings on glass (surface angle < 5°).	142
Figure 147 %5 (left) and %10 (right) percent ZnO QD containing nanocomposite coatings antibacterial testing.	142
Figure 148 Antibacterial test for 5% ZnO QD containing nanocomposite against to Pseudomonas Aeruginosa (left) and S. Aureus (right).	143
Figure 149 PLA/MEMO hybrid nanocomposite preparation.	144
Figure 150 ZnO QD addition into the PLA/MEMO nanocomposite structures for light emitting nanocomposites.	145
Figure 151 FT-IR investigation of UV curable PLA/MEMO nanocomposite mixtures.	145
Figure 152 Effect of UV curing for the PLA/MEMO nanocomposite structure.	146
Figure 153 Deformation by e-beam for the PLA/%10 MEMO nanocomposite	146
Figure 154 Change of roughness from PLA/%10 MEMO to PLA/%50 MEMO.	146
Figure 155 Cross sectional SEM analysis with increasing MEMO content (from %20 to %50 respectively).	147
Figure 156 Transparency of the %30 MEMO/PLA nanocomposite polymer.	148
Figure 157 Contact angle increase with increasing MEMO content.	148
Figure 158 PLA biodegradation with a commercial compost formulation.	149
Figure 159 Solid state light emitting nanocomposites.	149
Figure 160 FIB-Back scattering images of metal oxide/PLA for observing particle dispersion.	150

Figure 161 FIB image of liquid N₂ frozen MO_x/PLA nanocomposite structure..... 150

Figure 162 ZnO QD@Nanorod Clay Nanocomposites. 151

Figure 163 ZnO QD decoration for the plate like clays..... 152

Figure 164 Oleate@ZnO QD's and solid state light emitting nanocomposites..... 153

Figure 165 ZnO morphology gallery obtained by heating up method..... 154

Figure 166 TiO₂ morphology gallery and HR-TEM of TiO₂ by Hot Injection. 155

List of Tables

Table 1	Synthesis concentrations of Zn-Oleate complex.	30
Table 2	Band gap variation of growing Cysteine@ZnO QD's.....	59
Table 3	Time dependent particles size variation according to UV visible investigation	60
Table 4	Size, band gap and emission maxima list for ZnO a) Obtained from UV-Vis absorption b) Obtained from effective mass model ($m_e = 0.26 m_0$, $m_h = 0.59 m_0$, m_0 is the free electron mass, $\epsilon = 8.5$, and $E_g \text{ bulk} = 3.3 \text{ eV}$) c) From UV-Vis absorption.....	74
Table 5	Modification list for the ZnO nanocrystals.....	108

Abbreviations and Symbols

QD	Quantum Dot
SEM	Scanning Electron Microscopy
TEM	Transmission Electron Microscopy
HR-TEM	High Resolution Electron Microscopy
°C	Degree Celcius
EDX	Energy Dispersive X-Ray Spectroscopy
XRD	X-Ray Diffraction
FT-IR	Fourier Transformed Infra Red
UV –Vis	Ultraviolet- Visible
Raman	Raman Spectroscopy
EPR	Electron Paramagnetic Resonance Spectroscopy
NMR	Nuclear Magnetic Resonance Spectroscopy
DLS	Dynamic Light Scattering
FIB	Focused Ion Beam
PL	Photoluminescence Spectroscopy
μ	Prefix for Micro (1.10 ⁻⁶ m)
AFM	Atomic Force Microscopy
ppm	Parts per million
NP	Nanoparticle
NR	Nanorod
E _g	Band Gap Energy
eqv	equivalent
eV	electron volt
g	Gram
hν	Insident Photon Energy
Θ	Theta (diffraction angle)
h	hour-s
JCPDS	Joint Committee on Powder Diffraction Standards
v _{asym}	Asymmetric stretching mode
v _{sym}	Symmetric stretching mode
Mol	Mol amount
TGA	Thermogravimetric analysis
λ	Wavelength
nm	suffix for nanometer (1.10 ⁻⁹ m)

1 Introduction

1.1 Nanomaterials: Opportunities and Challenges

Among various metal oxide structures ZnO and TiO₂ have found wide spread applications due to their structural^[1-4], electronic^[5-7] and surface properties^[8-10]. Generally metal oxide nanomaterials have already begun to effect fundamental characteristics of future materials due to their unique, easy to manipulate and novel performances. Industrial applications of these metal oxides, require established synthesis strategies for scaled up production and detailed investigations of nanoparticles on possible toxicological effects on the living organisms. It is widely experienced that metal oxide nanomaterials, due to nanoparticle anisotropy, quantum confinement effects and surface reactivity need broad attention by an interdisciplinary (the chemical, physical, biological, material science) society. Detailed investigation of these properties, enable the synthesis of programmable nanomaterials which having specific material characteristics like particle size < 10 nm, or selectively elongated facets of nanoparticles for better catalytic efficiency^[11-12]. Since optical and morphological control leads to control of the light emission or defect oriented new properties, extremely sensitive synthesis methods are required to develop long term stable nanostructures. In addition to that catalytic or photocatalytic properties can be improved by fine control over shape and morphology during the selected synthetic methods. Higher yields for photovoltaic or water splitting features have been already observed for a variety of metal oxide nanostructures^[13-14]. On this basis, control of the synthetic methods for anisotropic nanomaterials, real time toxicologic observation of as-synthesized nanomaterial effects on the immune system of the living organisms which related to surface modification and their energy and clean environment applications such as photocatalysis applications have been aimed as main platform for the greener and cleaner energy solutions^[15-18].

1.2 Scope

In this thesis the scientific focus was on the liquid phase room and high temperature synthesis of anisotropic ZnO and TiO₂ nanostructures through Hydro-solvothermal (HS), Hot Injection (HI) and Heating Up (HU) methods. A control over nucleation process that can be tuned by controlling the processing conditions (precursor concentration, temperature) as well as by extrinsic factors (addition of surfactants, seeded growth) is expected to deliver reproducible

1 Introduction

synthetic materials for controlled synthesis of functional nanomaterials. In this context, the specific objective of this doctoral thesis research were;

i) Synthesis of ZnO, TiO₂ nanostructures by decomposition of different metal-organic precursors (Figure 1) followed by intrinsic encapsulation of as-formed nuclei by suitable ligands to control their shape, band gap and size

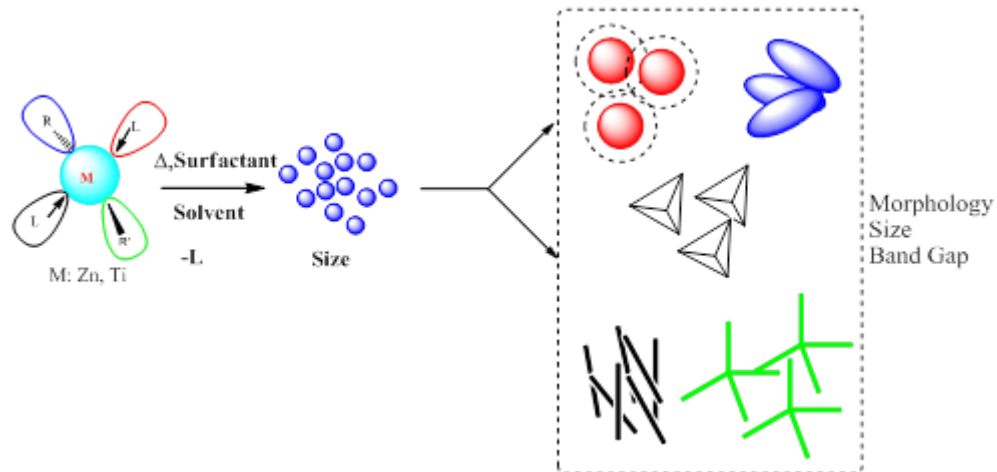


Figure 1 General ZnO and TiO₂ nanostructure synthesis

ii) Development of a library of inorganic-organic core-shell morphologies to produce Ligand@ZnO-TiO₂ nanostructures (Figure 2) with ligand shell and with different surface chemistry for the aim to obtain water dispersable ZnO-TiO₂ nanoparticles required to carry out cell tests and incorporate them into different polymer matrices

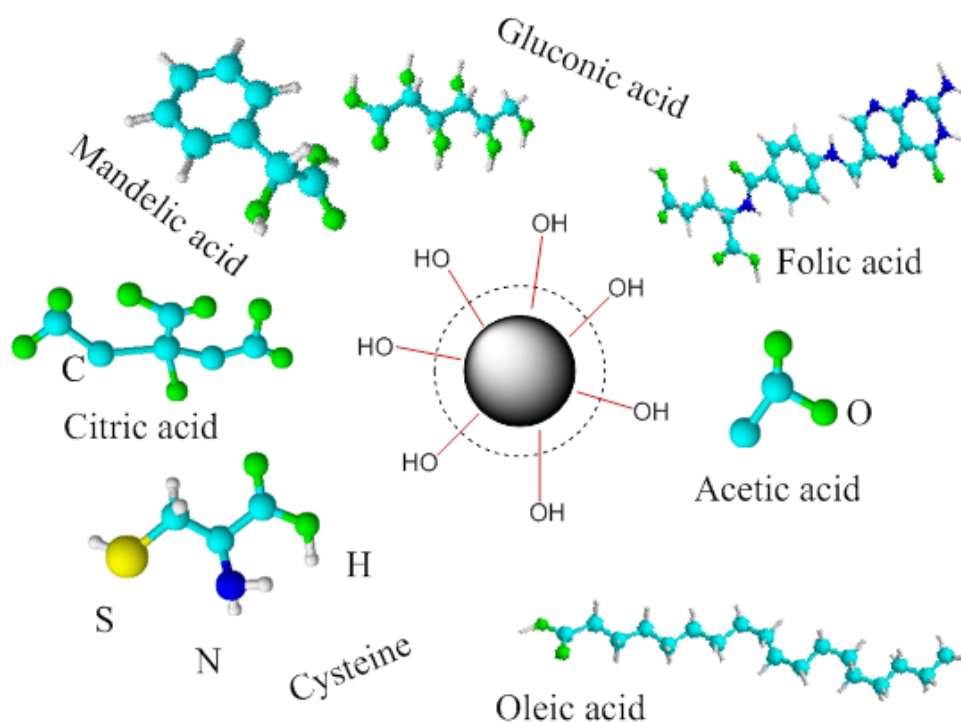


Figure 2 Ligand library for the surface modification and core/shell protection of the nanoparticles.

iii) Phase transfer studies as the ZnO nanoparticles synthesized in organic solvent need to be transferred to aqueous and protic (e.g. alcohol) reagents to undertake evaluation of their functional properties. Within this project it was necessary to investigate the optical (emission) properties, photocatalytic behaviours and cell toxicological influence of the substituted ligands

iv) Incorporation of the ZnO and TiO₂ to various polymer or hybrid structures to synthesize nanocomposites based on the chemical anchoring of metal oxide nanocrystals in polymer matrices by appropriate combination of coupling chemistry. By this anchoring it is aimed to obtain superhydrophilic, broadband antibacterial, selective UV absorptive, blue to red solid state visible light emitting, biodegradable or inorganic organic nanocomposites and modulation of the photocatalytic activity and cytotoxic control have been targeted (Figure 3).

1 Introduction

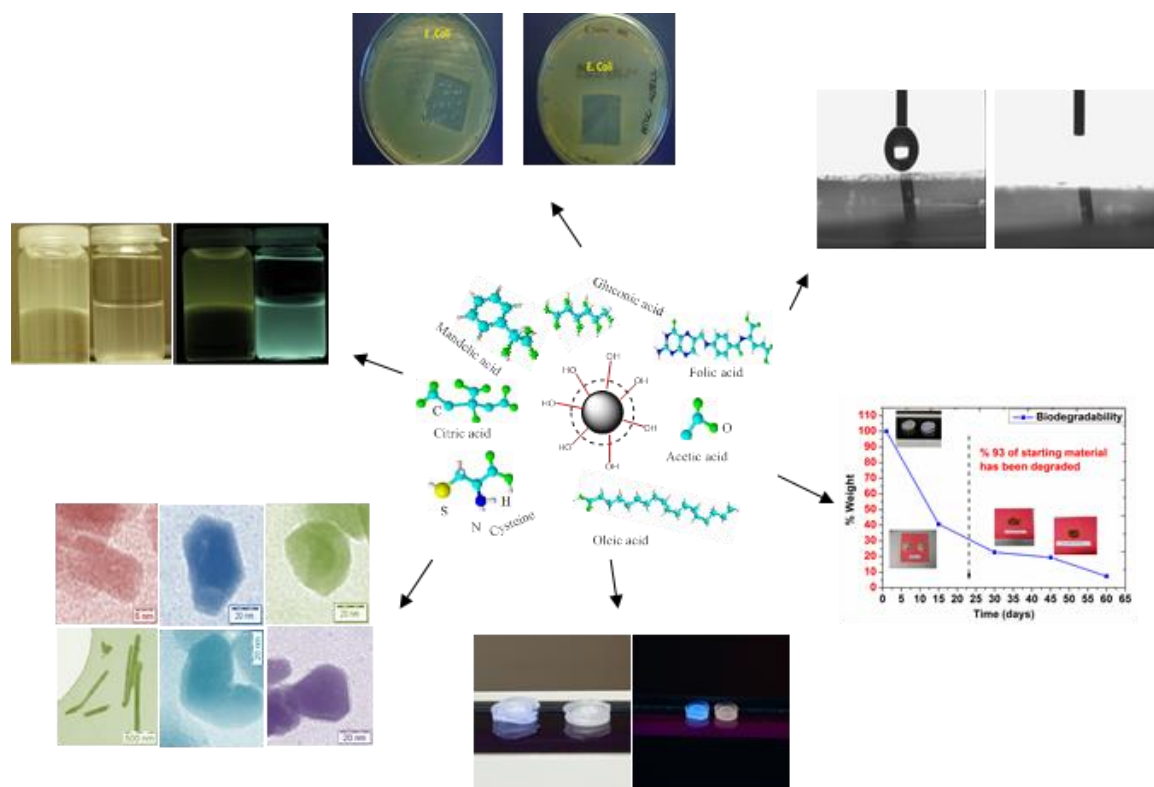


Figure 3 Several applications of ZnO and TiO₂ nanostructures.

v) Multi-morphological nanoparticles of ZnO and TiO₂ by controlling the nucleation and growth environment. Further, the influence of surface capping agents (surfactants) will be investigated to achieve a kinetic control over the evolution of particle databases. It is known that low metal ion concentration and low degree of supersaturation promotes the formation of acicular (needle like) structure that show unique properties due to their single crystalline nature and high aspect ratio.

2 State-of-the-Art: Nanostructure Synthesis

2.1 General Concepts of Nanostructure Fabrication

Controlled synthesis of nanomaterials is achieved basically by two methods which describe their starting point to reach the final form of the nanostructures. Bottom-up method starts from a well designed molecular complex and Top-down uses a miniaturization process to fabricate the nanostructures^[19].

2.1.1 Bottom-up and Top-down method

In Top-down approach, macroscopic structure can be miniaturized by applying appropriate etching and/or re-such as lithographic techniques^[20], UV light applications^[21], e-beam method^[22], nano imprinting lithography^[23], ball milling^[24] and mechanic attrition^[2-26]. This method found wide range applications in the commercial manufacturing processes for example electronics and daily life materials (Figure 4)^[27-30].

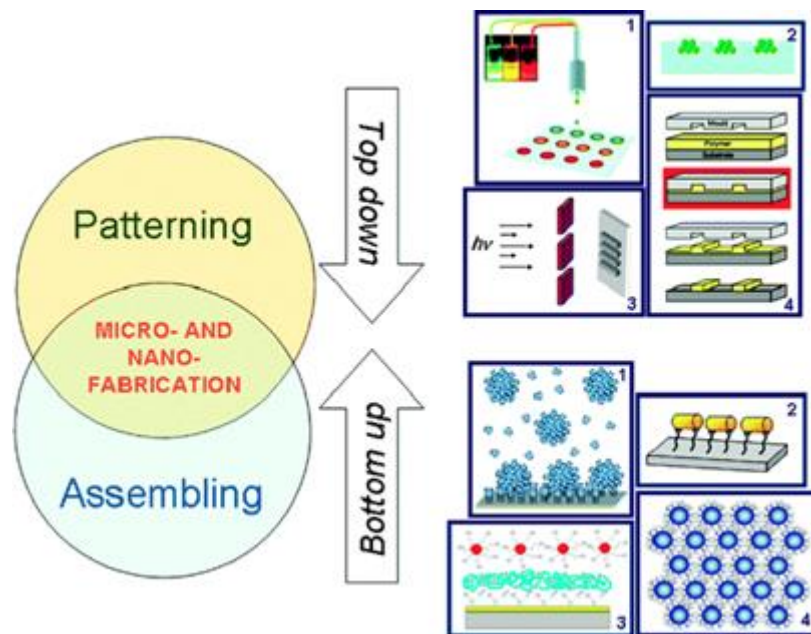


Figure 4 (taken from ref.19) Scheme of complementary “top-down” and “bottom-up” approaches for fabrication of micro- and nano-structures. For the bottom-up strategies: (1) host–guest chemistry, (2) covalent immobilization onto substrate, (3) electrostatic layer-by-layer deposition, (4) self-assembly . For the top-down strategies: (1) ink jet printing, (2) capillary assembly , (3) photolithography , (4) nanoimprinting lithography ^[1].

On the other hand, bottom-up approach is mostly used in the fabrication of nanostructures which requires atomic precision and well characterized beginning conditions and components such as designed molecular precursors. Several subclasses of this method are present such as supramolecular self-assembly^[31], surface directed ordering at interfaces (liquid crystals; LC)^[32], Langmuir–Blodgett (LB) synthesis method^[33], chemical vapour synthesis^[34], liquid phase methods^[35-36] (hot injection, microwave), combustion methods^[37-38].

2.2 La-Mer theory for the nanoparticle formation: Nucleation and Growth

Solution based production of nanocrystals follow two important steps; a) nucleation and b) growth of the nanocrystals. These processes are widely investigated and formulated.

La Mer and coworkers studied nucleation and growth of sulphur based structures and developed a theory which covers the formation of nanocrystals from homogeneous, supersaturated conditions. According to their mechanism synthesis of the colloid structure should be arranged in a way that the concentration of initial species increases rapidly and rising above the required saturation concentration for a short period of time so that the fast burst of nucleation occurs with the formation of a large number of nuclei in a short time. Particle growth is extremely fast and therefore lower the concentration below the nucleation level slowest step in the growth process.

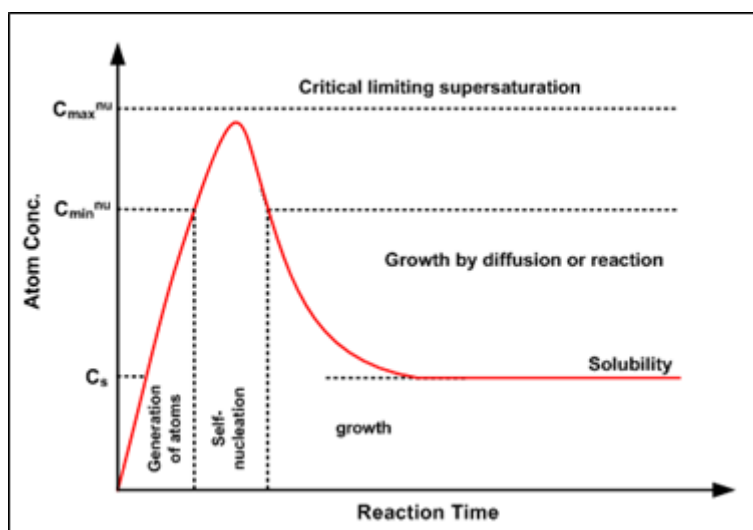


Figure 5 Schematic diagram illustrating La Mer's condition for stable nucleation^[39].

Therefore nucleation and growth become separated in time. Basic La Mer's mechanism is shown schematically in the Figure 5. It is easily seen that for monodispersed nanoparticles high rate of nucleation leading to the burst of nuclei formation in a short time is necessary. Thus an initial fast rate of growth of these formed nuclei to bring the concentration amount below the available nucleation concentration fastly is possible. By this, an eventual slow rate of growth causing elongated growth period if compared to the nucleation time is made. La Mer mechanism was later widely accepted and applied in preparation of various nearly-monodisperse particles from homogeneous solutions. In the early stages of nucleation available complexes collide to produce small clusters that are thermodynamically unstable and therefore can easily dissolve before they reach a critical radius (Figure 6) (r^*) or overcome a critical free energy barrier (ΔG^*) and become thermodynamically stable nuclei to grow further. These nuclei grow into nanoparticles at the constant consumption of free atoms in solution or unstable small clusters ($r < r^*$). In the classical nucleation theory, the nucleation process can be described according to Gibbs free energy. The excessive free energy (ΔG) basically contains two competing terms, *i.e.* the changes in surface and bulk free energies, reaches the self maximum when clusters grow to the critical size. The excess free energy can be described mathematically by the following equations.

$$\Delta G = \Delta G_s + \Delta G_v \text{ Eq 1}$$

$$= 4\pi r^2 \gamma + (-) 4/3 \pi r^3 \Delta G_v \text{ Eq 2}$$

here ΔG_v is the free energy change of the transformation per unit volume and γ is the interfacial tension *i.e.*, between the developing crystalline surface and the supersaturated solution^[39] in which it is located. Right side terms of the Eq 2 have opposite sign so their nucleus diameter dependency is completely different. According to these information we can easily understand that free energy ΔG , passes through a maxima called ΔG_{crit} corresponds to critical nucleus r_{crit} . For a spherical cluster we can derive the equation below by maximizing the Eq 2 and by setting;

$$d\Delta G/dr=0 ; d\Delta G / dr = 8 \pi r \gamma + 4\pi r^2 \Delta G_v = 0 \text{ Eq 3}$$

by rearranging the equation

$$r_{\text{crit}} = -2 \gamma / 4 \Delta G_v \text{ Eq 4}$$

where ΔG_v is a negative quantity. We can also find the

$$\Delta G_{crit} = 16\pi\gamma^3 / 3 (\Delta G_v) = 4\pi\gamma r_c^2 / 3 \text{ Eq 5}$$

Particles which are smaller than this critical size of the nucleus will dissolve or evaporate due to the thermodynamical conditions, because this is the only way for achieving reduction in the free energy. Oppositely if the nucleus size bigger than this critical size they will continue to grow. The rate of nucleation J, e.g. formed nuclei number per unit time per unit volume, can be expressed by widely known Arrhenius equation which is generally used for the thermally activated process;

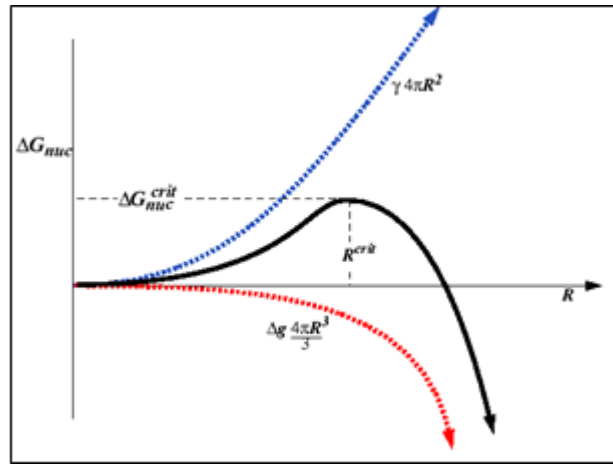


Figure 6 Free energy diagramme explaining the critical nucleus^[40].

$$J = A \exp (- \Delta G_v / t) \text{ Eq 6}$$

Where k is the Boltzmann constant, T temperature in K, A is a constant. Basic Gibbs/Thomson relationship for a non electrolyte solution can be written ;

$$\ln S = 2 \gamma v / kT r \text{ Eq 7}$$

where S is defined by another equation and v is the molecular volume :

$$- \Delta G_v = 2\gamma / r = kT \ln S / v \text{ Eq 8}$$

By using this equations from Equation 5;

$$\Delta G_{crit.} = 16 \gamma^3 v^2 / 3 (kT \ln S)^2 \text{ Eq 9}$$

and by rearranging with Eq 4;

$$J = A \exp (- 16 \gamma^3 v^2 / 3 k^3 T^3 (\ln S)^2) \text{ Eq 10}$$

can be obtained. This equation shows that three main variable govern the nucleation rate;

a) Temperature b) degree of supersaturation (S) and c) interfacial tension. It was later observed that La Mer's condition for nucleation is not completely necessary and sufficient for monodispersity and specific growth mechanisms also play an important role in deciding the size and the size distribution. Regardless of the rigorous validity of La Mer's prediction in the complex systems, the main idea of separating the nucleation stage and growth process in time is often used to obtain nearly monodisperse particles.

2.2.1 Growth of the Nanoparticles

Nucleation process takes place with constant monomer concentration and time. There will be a time which eventually surface growth of clusters seen to occur depleting the monomer supply. Thus if monomer concentration falls below the critical level for nucleation which is called critical supersaturation, then nucleation ends. Basically, the surface/volume ratio in smaller particles is quite high and therefore large surface area observed (Figure 7). In these particles surface excess energy becomes more and more important in lower sizes, forms a big percentage of total energy.

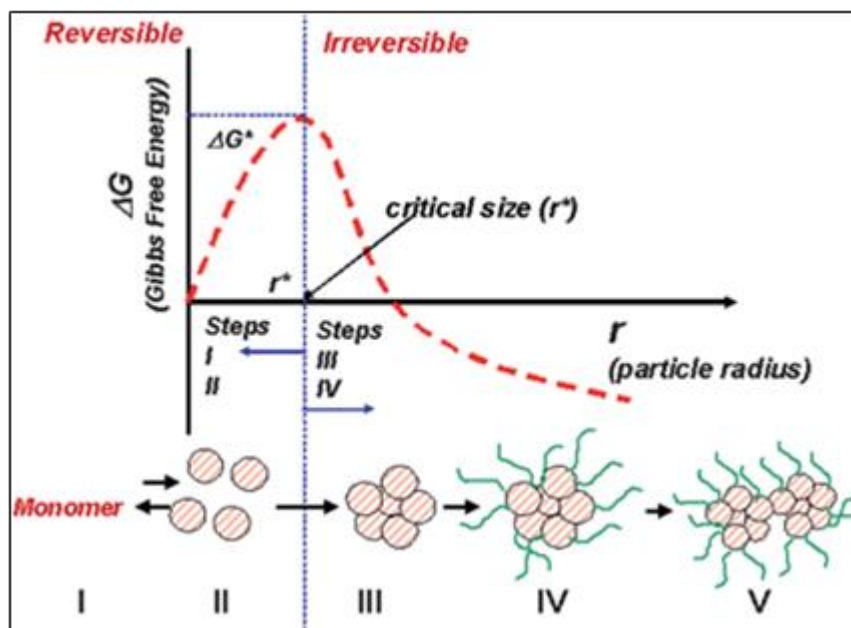


Figure 7 Schematic of nucleation and growth of the nanocrystals in La Mer theory^[41].

For the thermodynamic equilibrium, a mechanism which is allowing the formation of larger particles by consuming smaller particles reduces the surface energy and hence plays an important role in the nanocrystal formation. Basically colloidal crystals grow by available monomer diffusion onto the freshly obtained

nucleus surface followed by monomer reactions on the attached surface. These phenomena causing coarsening of the crystals is controlled either by mass transport or diffusion which generally known as Ostwald ripening process.

2.2.2 Ostwald ripening

Coarsening of the nanocrystals is a very important process which gives the latest shape of the nanoparticles. It was first time observed by Lifshitz and Slyozov then by addition of Wagner modern LSW theory has been formed^[42]. Since diffusion is dominated by the surface energy of the nanoparticle, interfacial energy gains enormous importance. This term is the energy associated with an interface due to various differences between the chemical potential of atoms in an interfacial area and atoms in neighboring bulk phases. So when the case is solid particle, chemical potential of this particle increases with decreasing particle size, the equilibrium solute concentration for a small particle is much higher than for a large particle (Figure 8).

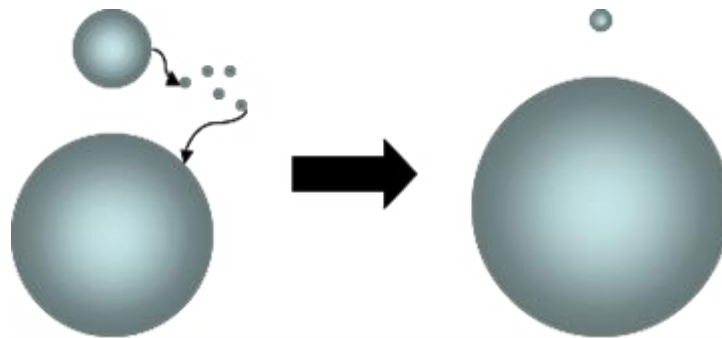


Figure 8 Sketch of Ostwald ripening process ^[43].

This phenomena is also described by the Gibbs–Thompson equation. Concentration gradients causes solid transportation from smaller to bigger particles. The equilibrium concentration of the nanocrystal's equilibrium concentration in the liquid phase is highly dependent on the local character of the solid phase. If there is differences in the local equilibrium concentrations, due to variations in local character, concentration gradients are rearranged and leads the growth of larger particles at the costs of smaller particles. Due to the surface, concentration and other effects there are 3 different coarsening mechanism;

- a) Diffusion Limited Growth: Lifshitz–Slyozov–Wagner (LSW) Theory and other Post-LSW theories
- b) Reaction-limited Growth

- c) Mixed Diffusion–Reaction Control
- d) Details of these three coarsening processes can be found in the literature very widely.

2.3 Kinetic versus Thermodynamic Control of Anisotropic Particles

Anisotropic nanocrystals do not show the same characteristics throughout the crystal^[44-45]. For example elongated nanocrystals can have different optical and band gap structures from its spherical one while chemical composition is the same. Basically three methods can be representative for the shape-controlling mechanisms in anisotropic nanocrystals^[45].

- 1) Seed-mediated solution–liquid–solid (SLS) growth
- 2) Shape transformation through oriented attachment
- 3) Kinetically induced anisotropic growth

It has been widely proposed and proved that, all of these growth mechanisms have a facile separation between the nucleation and growth stages, which is a prerequisite for the shape-controlled nanocrystal fabrication

2.3.1 Seed-Mediated Solution–Liquid–Solid (SLS) Growth

Use of proper nanocrystal seeds can facilitate highly anisotropic crystal growth. Under gas-phase like chemical vapor deposition (CVD), 1D silicon and germanium wires are obtained on a substrate through a vapor–liquid–solid (VLS) growth mechanism.

Using a similar approach for the anisotropic nanocrystals it is possible to obtain semiconductor nanowires by a solution–liquid–solid (SLS) process and this shows a simple example for the SLS fabrication.

Decomposition of the well characterized metal organic molecular precursor at defined high temperature produces different monomeric species in organic media which diffuse onto the seeds to form an alloy structure. If we increase the dissolution of monomers onto the seed, the supersaturated pure solid nanowire structures can grow out of the seed.

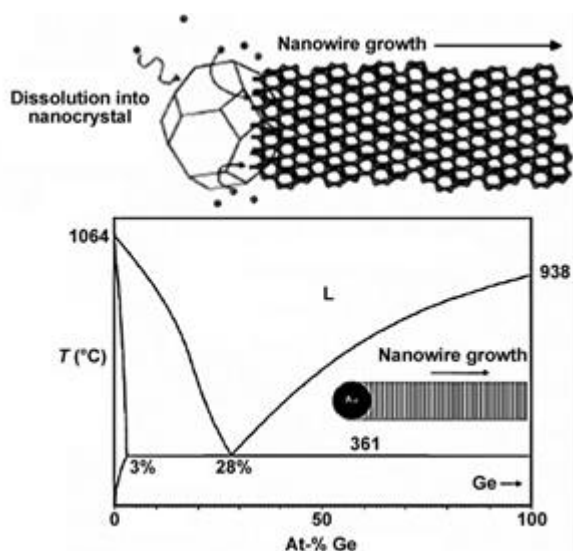


Figure 9 Alloy formation of the solution grown nanowires^[45].

Ge nanowires were obtained using gold nanocrystal seeds. As known above 360°C, Ge and Au would form an alloy first in equilibrium but when supersaturation occurs pure solid Ge expelled from medium (Figure 9)^[45].

2.3.2 Oriented attachment

Second anisotropic nanocrystal formation method is inorganic self-assembly through an oriented attachment process. Owing to the high surface to volume ratio of synthesized nanocrystals, the surface energy contributes to the total energy and as the surface area is reduced by aggregation processes, the total energy of the nanocrystal structures will decrease. The concept of “oriented attachment” was remarkably discussed by hydrolytic synthesis of TiO₂ nanocrystals (Figure 10). Truncated diamond-shaped anatase TiO₂ nanocrystals have three different facets: {001}, {121}, and {101}. Donnay–Harker rules predicts the surface energy of the available facet (001) is higher than other nanoparticle surfaces. Basically if sufficient thermal energy is available in the system then system would remove the high-energy surfaces which is thermodynamically favorable.

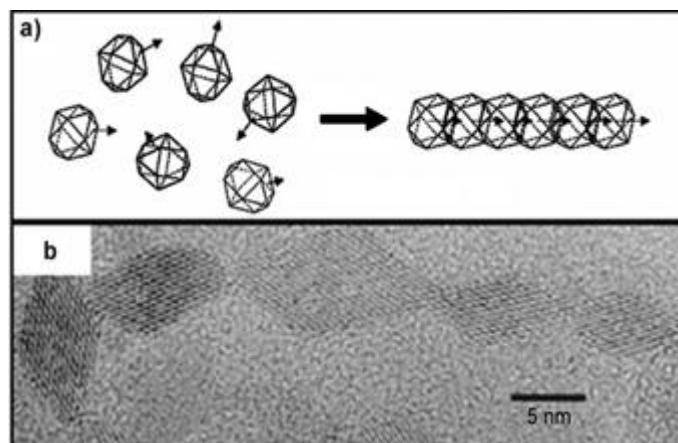


Figure 10 Schematic representation of oriented attachment processes^[45].

By this method diamond-shaped nanocrystals attached to each other along the [001] resulting necklace-shaped nanocrystal. The initial 0D nanocrystals align and come together along their dipole direction. After surface reconstruction to minimize the surface energy, 1D rod-based structures are obtained. Similar observations were made in the cases of both the hydrolytic growth of CdTe nanowires and the growth of ZnO and PbSe nanocrystals.

2.3.3 Kinetically Induced Anisotropic Growth

Anisotropical nanostructures are easily produced by kinetically labile molecular precursors. Due to the highly energetic facets and preferred surface ligand adsorption on initially formed nanocrystals, many different morphologies can be obtained. Three key factors determine the nanocrystal shape as presented below.

2.3.3.1 Surface energy and selective adhesion

Energetic character of the crystallographic faces of the nanocrystals has remarkable effect on the anisotropic growth patterns of the nanocrystals.

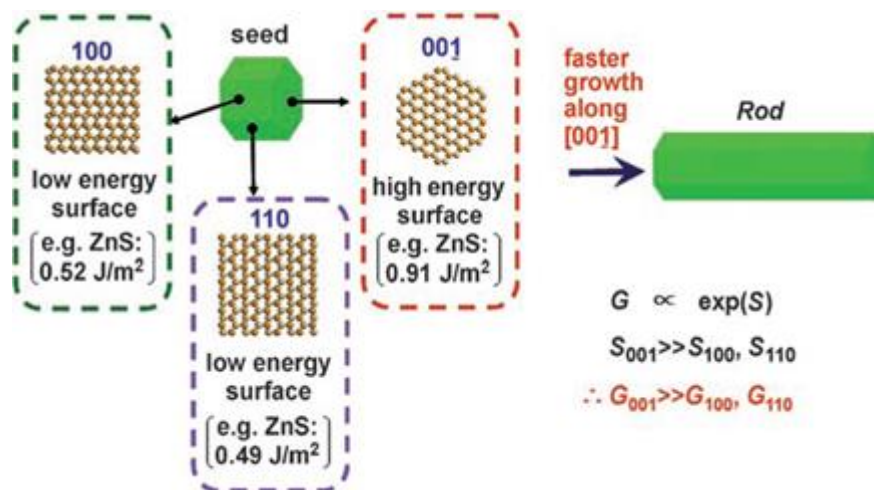


Figure 11 Surface energy of wurtzite ZnS nanocrystals. The (001) surface has the highest surface energy. Since the growth rate is exponentially proportional to the surface energy, the fastest growth occurs along the [001] direction in the kinetic growth regime; G =growth rate, S =surface energy^[45].

As an example, the surface energy of the (001) face (e.g. 0.9 Jm² for ZnS) is larger than other faces such as (100) and (110) (e.g. 0.5 J m²). Since the crystal growth rate is exponentially correlated to the surface-energy values induce much faster growth along the more active [001] direction of ZnS than the other directions, resulting in formation of ZnS nanorod elongated along the [001] direction (Figure 11).

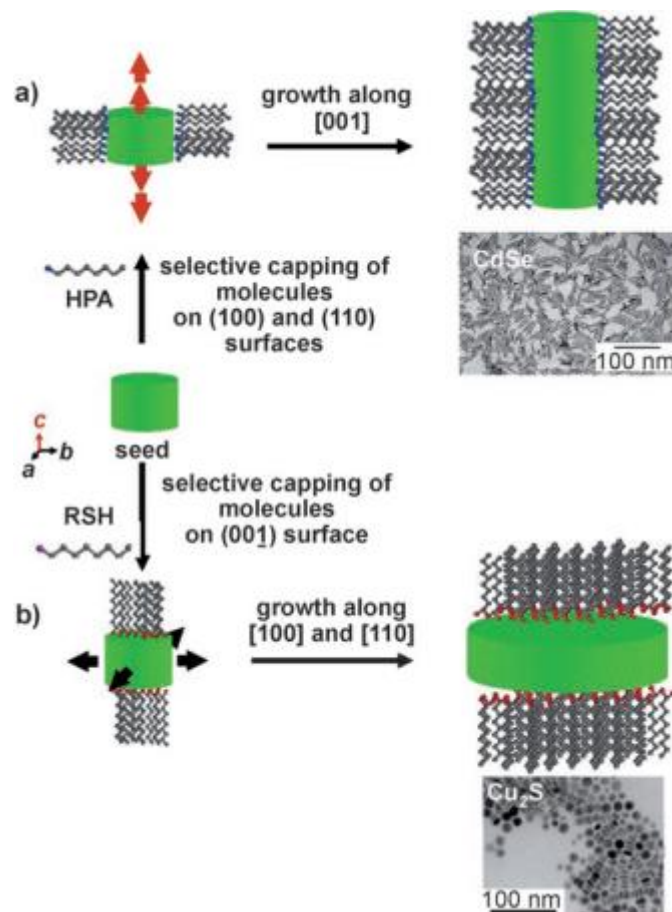


Figure 12 Surface modulation effects induced by surface-selective surfactants on either a) anisotropic rod or b) disc growth. When surfactant molecules specifically bind to the {100} and {110} surfaces of a hexagonal structure, preferential growth along the $h001i$ directions and therefore rod growth is facilitated (a). In contrast, when surfactant molecules bind to the {001} surfaces of a hexagonal structure, it prevents growth along the {001} direction and therefore disc shapes are obtained (b)^[45].

TiO₂ anatase structure normally has a tetragonal arrangement an anisotropic c-axis (Figure 13). When TiO₂ nucleus with a truncated octahedral, bipyramidal shape terminated by {001} and {101} faces nucleate, high-energy surface {001} induced complete elimination of the {001} of the surfaces which results in arrow- and diamond shaped nanocrystals seen. Lauric acid strongly binds to the {001} faces and reduces the growth rate along the {001} directions. Therefore growth of both direction is induced in {001} and {101} but the area of the {001} surface remains same, which finally produces nanorod. Excess lauric acid triggers growth along {101} which resulted in the formation of branched rods with a [101] branching direction.

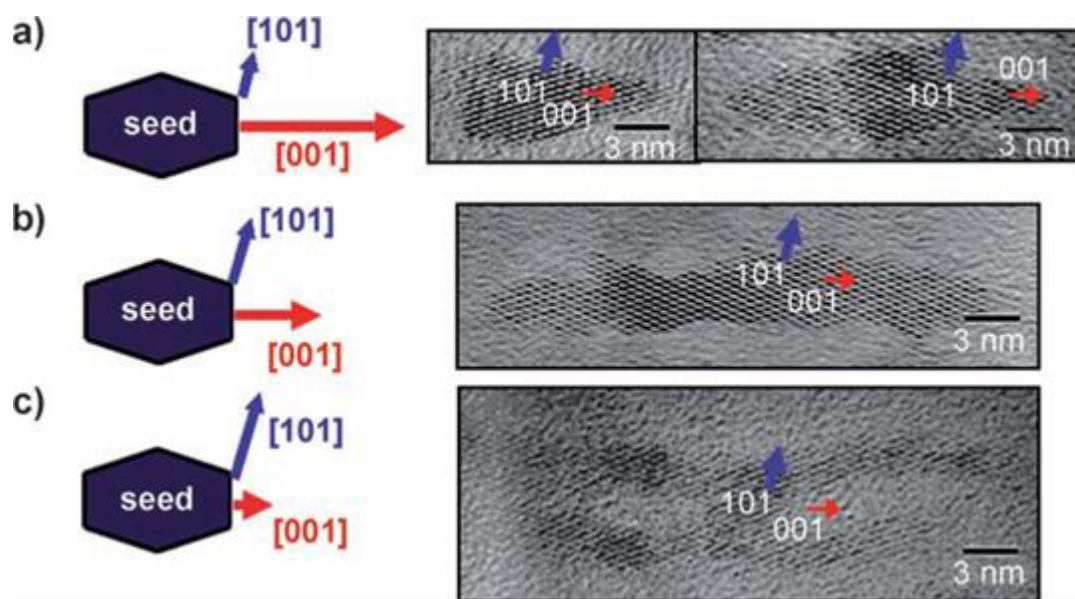


Figure 13 Shape evolution of TiO₂ nanocrystals through the surface energy modulation effect by using surface selective lauric acid (LA) surfactants. a) Bullet- and diamond-shaped nanocrystals are formed at low LA concentration. b,c) At higher LA concentrations rods (b) and branched rods (c) are formed^[45,46].

Similar examples of wurtzite structure have also been observed in various reports^[46]. The surface energy of the nanocrystals can be modulated by introducing surfactants which selectively adsorb onto surfaces of growing crystallites. After surfactants stabilize selective surfaces by “selective adhesion” then the growth rate difference between different crystallographic directions can be seen easier. Especially chalcogenide nanocrystals like CdSe shows remarkable differences in the nanorod synthesis. In hot injection synthesis if dimethylcadmium and TOPSe are injected into a hot mixture of TOPO and HPA, HPA amount that binds to the surfaces {100} and {110} of the growing crystallites modulates the growth pattern. At low HPA concentration or in the absence of HPA, only spherical nanocrystals are formed which shows exactly the role of surfactants. However, with higher HPA concentrations, nanorods are obtained since the surface-bound HPA molecules serve reduce the growth along {100} and {110} surfaces (Figure 12). Selective adhesion of surfactants can also induce compression along other axes. For example, in the formation of CuS nanodiscs if there is surface selective alkanethiol ligands attached to {001} faces by lowering the surface energy, 2D Cu₂S nanodiscs are formed. Beside other nanocrystal structures, anatase TiO₂ nanocrystals are another model system for

surfactant-assisted, surface-energy modulated anisotropic nanoparticle formation.

2.3.3.2 Influence of the phase of the crystalline seed

Crystallographic phase of the nucleated seeds is another important actor for the synthesis of anisotropic nanostructures. For example in a special case, if seed crystals are of the zinc blende phase, they tend to grow isotropically along the three crystallographic axes (a, b, and c directions), resulting in 0D shapes which means spheres and cubes. However, when seeds are formed in a wurtzite structure, crystals oppositely grow anisotropically and they yield in shapes such as rods and discs. Therefore crystalline phase control of the used seeds and further growth is of particular interest. Crystal seeds can potentially have a variety of different crystallographic phases and the stable phase is highly dependent on the environment and treated temperature. For example seed with a rocksalt phase is favourable at higher temperatures ($>200\text{ }^{\circ}\text{C}$) and due to this crystalline character isotropic cubes are easily formed. On the other hand, at lower temperature of around $120\text{ }^{\circ}\text{C}$, where the wurtzite phase is more stable, the growth of nanorods becomes favoured. Shapes of CdS nanocrystals can also be modified and adjusted by this temperature-mediated phase control of the initial seeds for obtaining desired morphology in nanocrystals. If we use high temperatures like ($300\text{ }^{\circ}\text{C}$) CdS seed are in the wurtzite phase and selectively 1D nanorod formation is observed whereas at lower temperatures zinc blende nuclei are preferred and tetrahedral seeds with four $\{111\}$ faces are seen.

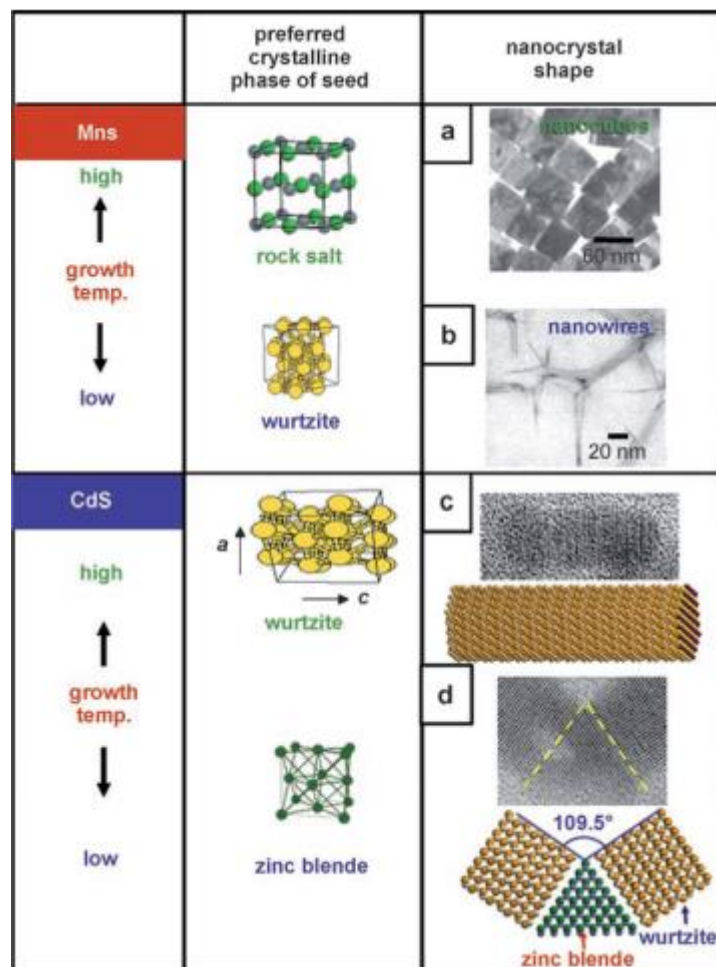


Figure 14 Temperature-mediated crystalline-phase control of a,b) MnS and c,d) CdS nanocrystals. At high temperature the formation of rock salt phase MnS nanocubes is preferred (a), while at low temperature branched MnS nanowires of wurtzite phases are obtained (b). Similarly, at high temperature CdS rods are grown from seeds in the wurtzite phase (c), while at low temperature CdS bipods are grown from zinc blende tetrahedral seeds (d) ^[45] are seen. The epitaxial growth of wurtzite pods along the [001] direction from the {111} faces occurs and as a result, CdS bipods are formed (Figure 14). For obtaining multibranch nanostructures such crystalline-phase effects should be analysed carefully.

2.3.3.3 Thermodynamic or kinetic control of the growth regime.

Morphology control of nanocrystals is a platform which is governed by thermodynamic and kinetic growth regimes effect differently. If there is thermodynamic growth regime it is easily understand as the final shape of the nanocrystal becomes isotropic. Thermodynamic control means;

- a) sufficient supply of thermal energy (kT)
- b) low flux of monomers

On the contrary, anisotropic control along a specific direction is favoured by kinetic regime and it is promoted by high flux of monomers. A growth model which was proposed by Peng and co-workers by the diffusion flux of monomers and according to this model, thermal reaction of CdO and alkylphosphonic acids (APAs) react and form Cd-APA complexes which are relatively stable and maintains a high monomer concentration in the diffusion layer of the growing crystallites.

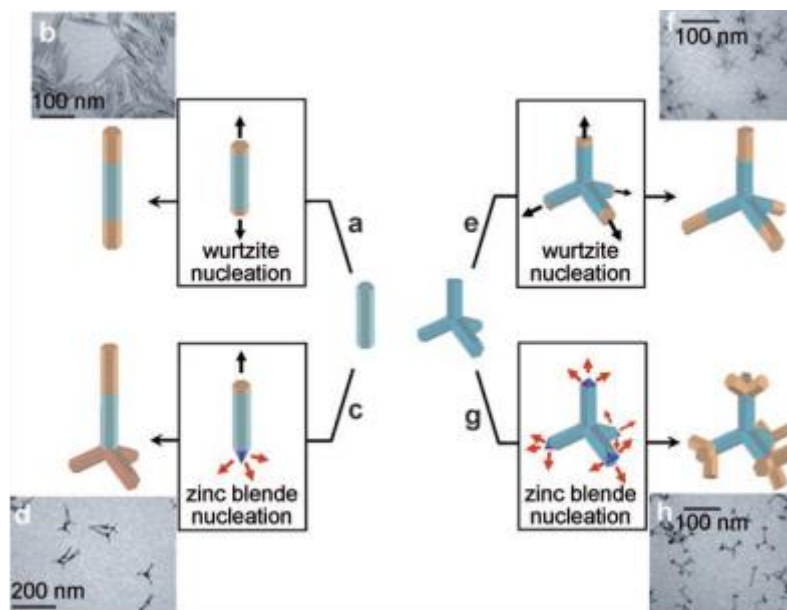


Figure 15 a,b) Heterostructured rods formed by adding CdSe extensions to each end of CdS nanorods. c,d) Branched rods result from the nucleation of zinc blende CdTe on either end of the CdSe nanorods. e,f) Extending each arm of a CdSe tetrapod linearly with wurtzite CdTe yields extended tetrapods. h,g) Branched tetrapods result from the nucleation of zinc blende CdTe branch points on the end of each arm of a CdS tetrapod^[45].

So if analysis is done for the crystal growth of CdSe nanocrystals (Figure 15) results show growth through four modes:

- 1) 1 D growth, 2) 3D growth, 3) 1D to 2D ripening, 4) Ostwald ripening

During a 1D favoured growth, a high diffusion flux of monomers into the diffusion layer promotes the preferential 1D growth of monomers on the highest energy (001) surface. If monomer concentration decreases diffusion flux also

decreases. If there is relatively low diffusion flux this favours an equi-directional growth of the nanocrystals (the 3D growth stage).

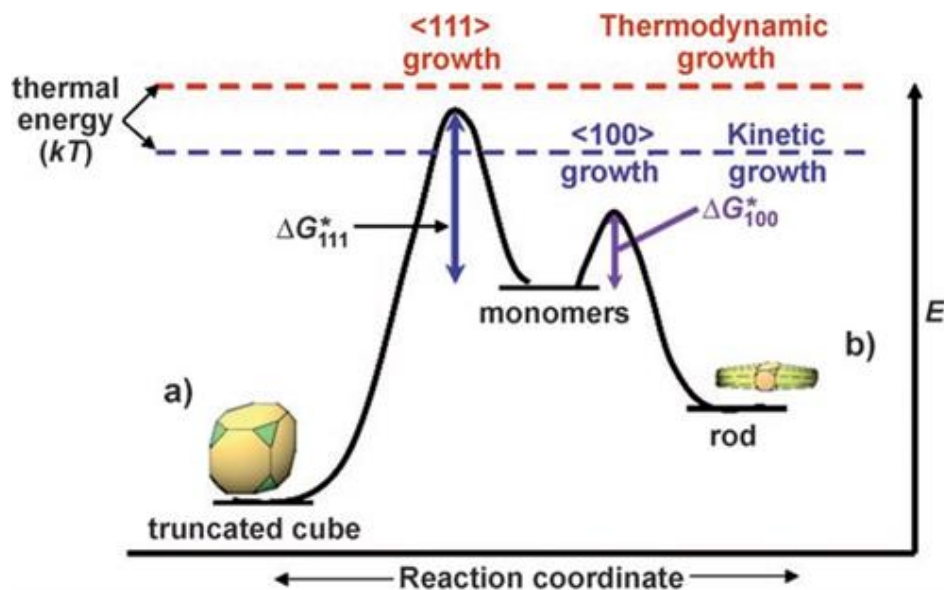


Figure 16 Comparison of a) thermodynamic and b) kinetic growth of PbS nanocrystals. At high temperature, the formation of thermodynamically stable structures (truncated cubes) is preferred. At low temperature, however, a shift of growth regime to the kinetic process results in rod growth^[45].

If the concentration of available monomers is low then system reaches equilibrium by dissolution and re-growth of the monomers from the (001) face onto the other growing faces (the 1D to 2D ripening stage). At last, if there is very low amount of concentration for the monomer, the nanocrystals grow by an interparticular Ostwald ripening process. PbS nanocrystals also show rock salt structure which have interesting shape variations and can be examined as a model for such growth regimes. In the method if we inject molecular precursor of PbS quickly, this promotes the formation of tetrahedral seeds that are terminated by {100} and {111} faces. These faces also competitively behave during the growth stage which determines the latest shape and morphology of the nanocrystals. (Figure 16) Interestingly at this stage if there is dodecanethiol surfactants, this causes that {100} surface has a higher surface energy than the {111} surface. When we provide excess thermal energy (i.e. high temperature), formation of thermodynamically stable 0D truncated-cube-shaped PbS nanocrystals observed. Interestingly again, in lower temperature conditions (120 °C), the growth process of the nanocrystals shifts into the kinetic regime which provides 1D rods and multipod structures.

2.4 Nano-Synthetic Methods

As mentioned earlier top down and bottom up methods generally covers the concept of nanomaterial synthesis. But in this thesis bottom-up methods have been used for the nanomaterial synthesis which can be explained shortly as follows.

2.4.1 Hot Injection Synthesis

Detailed understanding of hot injection synthesis started in 1993 when Murray published^[47-48] the controlled synthesis and characterization of the nearly mono-dispersed CdX (X=Se, Te, S) nanocrystals in trioctylphosphine oxide (TOPO) as solvent. This work was based on the decomposition of a room temperature (cold) precursor solution by injecting it into the hot solvent with another surfactants. Investigations showed that upon fast injection of this cold precursor was inducing a high degree of supersaturation quickly which leads a short burst of nucleation (Figure 17). During nucleation process precursor concentration in the mixture decreases abruptly^[47]. Cold injection of the precursor molecules causes a drop in the temperature and in addition to that low concentration of unreacted remaining precursor prevent another nucleation process. After that temperature of the reaction mixture is increased to the value that is allowing the controlled and slow growth of the nuclei to larger nanocrystals. Still the nucleation process is suppressed and under control. This is the method of separation for the nucleation and growth which provides monodispersed and narrow size distributed nanocrystals. Different surface ligands or surfactants consisting of a coordinating head group and a long alkyl chain are adsorbed onto the nanocrystal surfaces reversibly during the growth process. This adsorbed layer stabilizes the nanocrystal in the solution beside its help for growing. Especially the surfactants with different functional groups and binding affinities allow remarkable control over nanocrystal size and distribution. After nanocrystals have been separated by an organic solvent they can be re-dispersed in a suitable, usually polar and organic solvents. Since surface ligands provide protection and stability, it is possible to exchange the ligands by another proper surface agent to increase the dispersibility which is called phase transfer. Phase transfer synthesis enable the redispersion of these nanocrystals in another polar or apolar solvent. Preparation of II-VI, IV-VI and III-V semiconductor nanocrystals is easier and repeatable by hot injection method. Hot injection synthesis has been extended to the metal and metal oxide nanostructures. For example Trentler et al. applied hot injection synthesis method to the TiO₂

nanocrystals. Cold injection provided nearly spherical anatase titania nanocrystals with TOPO and heptadecane. One example of the particle surface control can be observed here which surface selective lauric acid and TOPO as non selective surfactant. Hot injection synthesis was also applied for MnO, ZnO, ZrO₂, CeO₂ or Fe₂O₃ nanocrystals.

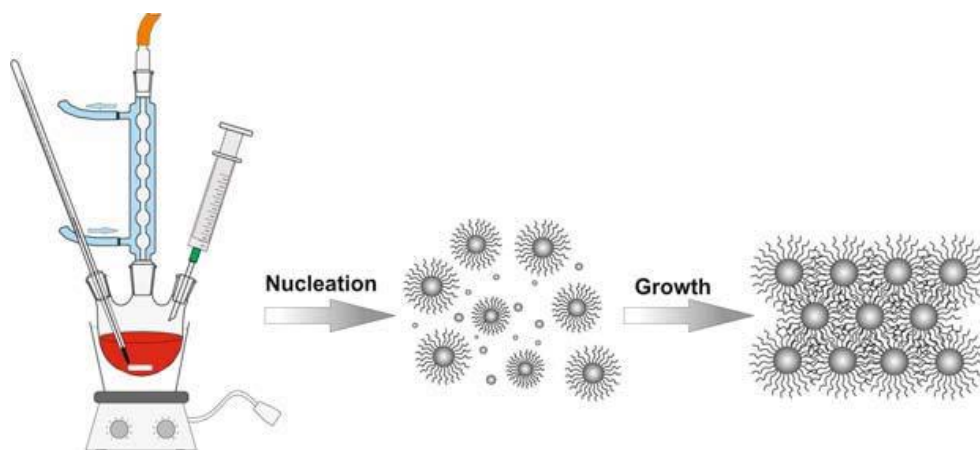


Figure 17 Experimental set-up and reaction scheme for the hot-injection method^[49].

2.4.2 Heating Up Method for Nanostructures

Heating Up method is slightly different from hot injection synthesis in terms of the temperature control. Reaction mixture is being prepared at low temperature and by controlled heating crystallization process begins. After crystallization process proper ligands are removed for obtaining nanostructure. Heating up method generally requires specific precursors for the desired nanostructure formation. Still heating up method has particular advantages when compared to hot injection method. For example it is possible to produce large scale nanostructures and size uniformity can be also achieved with high precision. First noticeable synthesis for the Heating Up method has been made by pioneer Hyeon et al. for obtaining large scale monodispersed iron oxide nanoparticles^[50]. Previous procedure by Bentzon et al. was published for the production of iron oxide by the decomposition of iron pentacarbonyl into a mixture of octyl ether and oleic acid at 100 °C. This method simply produces iron oleate intermediate complexes which then decomposed further at high temperatures like 300 °C into metallic iron and by oxidation Fe₂O₃ is obtained using mild oxidant trimethylamine oxide. Crystal size and morphology can be modified by carbonyl to oleic acid ratio as in the hot injection method. Heating up method became very important in the last decade for the synthesis and large scale production of metal oxide nanomaterials. Simply starting from acetylacetonate complexes of

iron and manganese 1,2 hexadecanediol, oleic acid and oleylamine in benzyl ether can be used for iron or manganese oxides. As previously mentioned heating up procedure is scalable which is contrast to other nanocrystal synthesis techniques. Many different nanostructure synthesis have been successfully conducted with desired conditions using heating up method.

2.4.3 Sol Gel Method for Synthesis

Sol gel chemistry based on the hydrolysis and condensation reactions of the proper precursors generally silicon and transition metal alkoxides. In addition to that carboxylates, chlorides, nitrates, sulphates and other salt type precursors of transition metals also known as sol-gel precursor. Materials are synthesized via the hydrolytic polycondensation of the precursors at room temperature from liquid precursors under controlled conditions^[51].,

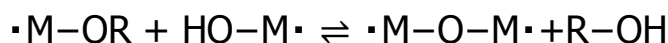
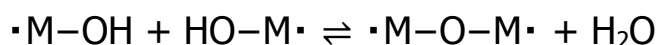
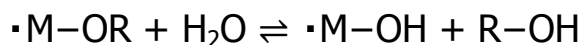


Figure 18 Basic reactions of sol gel method from metal alkoxide.

The synthesis is generally carried out in an organic solvent (alcohols generally, through simultaneous or sequential reactions of hydrolysis (Figure 18) and polycondensation releasing water and/or alcohols as shown above.

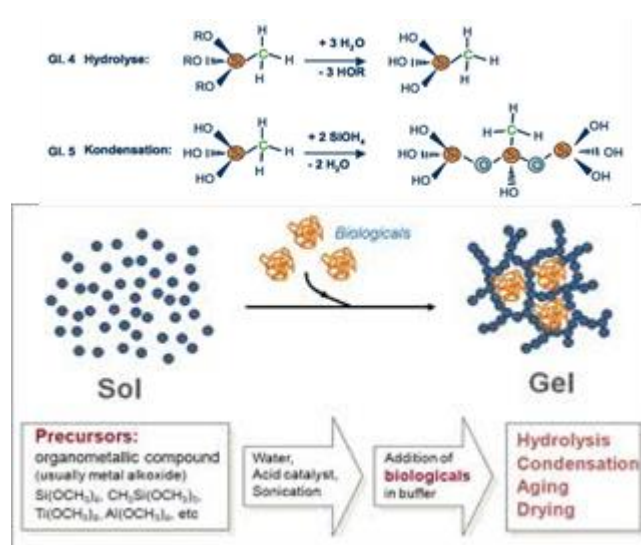


Figure 19 Morphological variation schema for sol-gel method^[52].

Hydrolysis and condensation reactions of the sol gel method do not proceed with the same speed when we compared silicon and other transition metal alkoxides. Due to the low polarity of the Si-O bonding ($\delta^+ = 0,32$) in silicon-oxygen containing polymers, acidic or basic catalysis is necessary for the silicon alkoxides. Acidic or basic catalyzed reactions (Figure 19) have a huge effect on the final materials since catalysts trigger and fasten specifically hydrolysis or condensation reactions.

2.4.3.1 Organically Modified Nanostructures by Sol Gel Method

Alkoxysilanes are the far most used sol gel precursors. They also used for the surface modification and inorganic organic hybrid nanostructure preparations. They have a general denotation of $R'Si(OR)_{4-R}$ which R' is a functional organic group^[53]. Theoretically all the organically modified alkoxysilanes do the same hydrolysis and condensation reaction of the tetraalkoxysilane (TEOS). Additionally because they have R' functional group (e.g. epoxy, amino, acrylic, thiol, isocyanate etc.) they can give extra functionality to the synthesized nanostructure. Organically modified alkoxysilanes are very widely used in the nanoparticle surface modifications for functionalization. When they are used on the functionalization process they follow the same hydrolysis and condensation reactions on the nanoparticle surface which is generally accepted as $-OH$. It is also possible to make finely arranged spherical silica particles by a method called Stöber Process. Stöber Process uses ammonia water, alcohol and tetraalkoxysilane to produce perfectly spherical nanoparticles. When a particle is used together with Stöber Process then we can easily obtain core/shell nanoparticles. After this step when we use another organically functional alkoxysilane we can functionalize the surface of core/shell structures for further applications.

2.4.4 Hydro-Solvo Thermal Method for Nanostructures

Hydro-Solvothermal method is a bottom-up way to produce nanomaterials. It can be used in the synthesis of metals, semiconductors, ceramics, and polymers. Generally when a proper solvent is used under moderate to high pressure (typically between 1 atm and 10,000 atm) and temperature (typically between 100 °C and 1000 °C) these conditions increases the precursor interaction and nanomaterial synthesis.

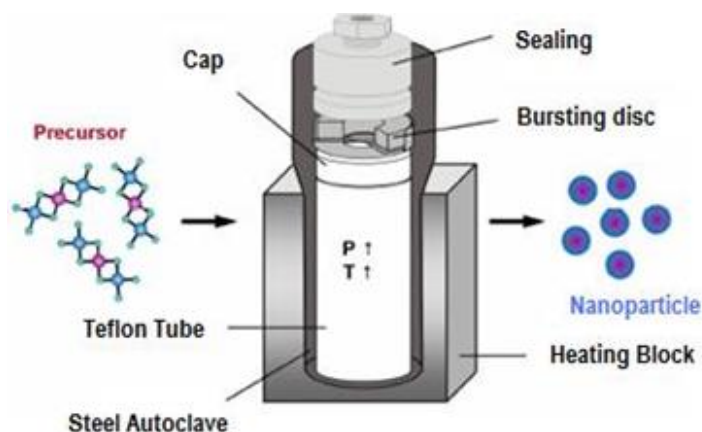


Figure 20 Solvo/hydrothermal synthesis installation^[54].

When we use water as solvent material, the method is called “hydrothermal synthesis.” The synthesis under hydrothermal conditions requires lower temperatures since water has a supercritical point as 374 °C. It is possible to obtain many anisotropic structures, single crystals, and nanocrystals. It is also possible to control the morphology of the solvent by manipulating the solvent supersaturation, chemical of interest concentration, and kinetic control (Figure 20). The method can be used to prepare thermodynamically stable and metastable states including novel materials that is hard to synthesize by other traditional methods^[55].

2.5 MOx/Polymer Nanocomposites

Nanocomposite structures are basically mixture of two different component in the nano regime which provides a sum of each properties arising from the each components. Interaction of the polymer/particle interface can be manipulated for obtaining better mixtures some other extra specific properties. Organic polymeric structures are generally suffer from the low thermal resistance, easy deformation and low durability. Incorporation of nano-micro particles into these organic polymers may lead enhancement of the thermal character, gas diffusion features, increase in the durability and stiffness.

2.5.1 Hybrid Inorganic Organic Polymer/MOx Nanocomposite

Hybrid inorganic organic nanostructures represents “a thing made by combining two different elements”. In the material science this concept can be written like “something that is obtained by mixing different types of materials” and we can obtain a new material that can be called hybrid material or nanocomposite^[56-58]. Shortly a hybrid of organic and inorganic is a combination of organic materials

2 State of the Art: Nanostructure Synthesis

(polymers) and inorganic materials (inorganic polymers, nanoparticles etc.). In order to distinguish them from the conventional composite structures which are simple mixtures, it is necessary to call the materials “hybrid materials” when the level of interaction for different types of materials is at the nanometer level, or sometimes at the molecular level. By synthesizing such hybrid materials, it is possible to observe very interesting features that are not found in the organic polymer or the inorganic material independently. As an example, polymer structures are flexible and not resistant to heat and inorganic structures are brittle and requires high temperature applications for preparation.

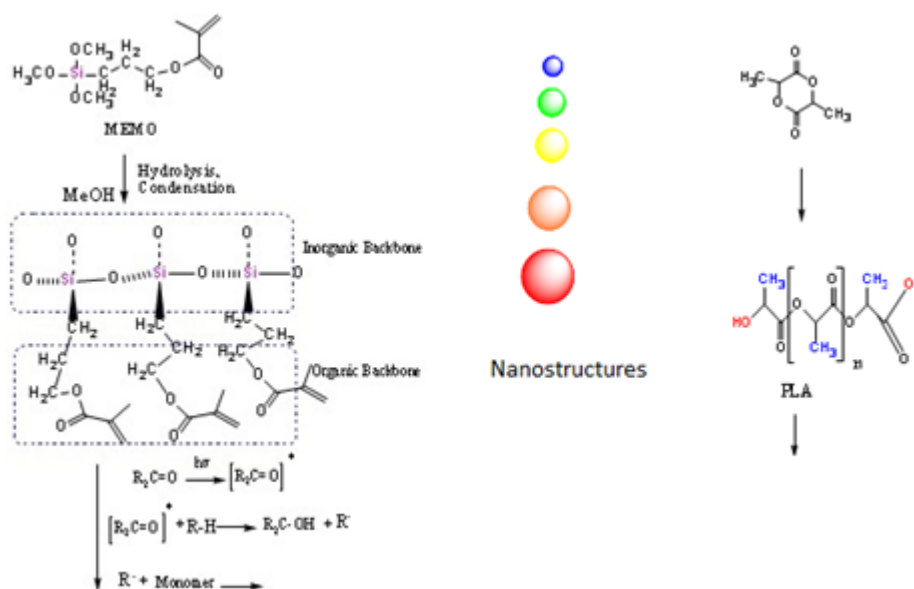


Figure 21 Example of a hybrid formulation consisting of acrylic alkoxy silane, biodegradable PLA and ZnO QD's.

But in hybrid nanomaterials we can observe a material which is like plastic but have excellent mechanical strength and thermal stability. Organically modified silanes or (ORMOSIL's) and Organically Modified Ceramics (ORMOCER's) are very broad examples of these hybrid materials. In addition to these examples we can also use conventional polymers like epoxy, polyurethane, acrylate or biodegradable structures like polylactide in the process of hybrid material preparation. Generally second and third part (if necessary) is introduced into conventional polymers for novel material applications. Synthesized final hybrid nanostructure therefore carries the properties of each component due to the fine interaction of these components. Hydrogen bonding, common polymeric chain interaction, chemical encapsulation or modification, soft-hard acid base interaction are the main interaction examples of these finely mixed nanocomposite items. Since composite term is used generally for the simple

mixed systems, nanocomposite is also used for these finely controlled and molecularly engineered inorganic organic hybrid nanostructures (Figure 21).

2.5.2 MO_x@Clay Nanocomposite Structures

Clays have layered structure and these layers are built from tetrahedral sheets in which a silicon atom is surrounded by four oxygen and additionally octahedral sheets in which a metal like aluminium or magnesium is surrounded by eight oxygen atoms.

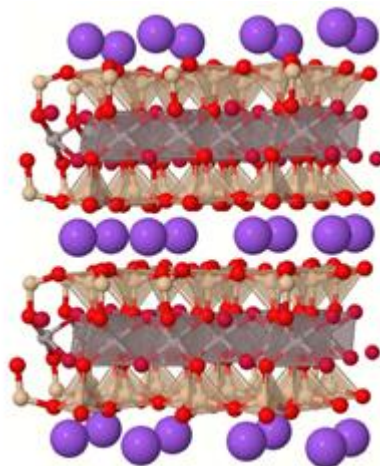


Figure 22 Idealized structure montmorillonite clay (without organic modification) showing two tetrahedral-site sheets fused to an octahedral-site sheet. Red Sphere= oxygen Grey spheres=Si, Al, or Mg atoms. Purple spheres =Na or K ions.

The tetrahedral (T) and octahedral (O) sheets are fused and connected properly by sharing the oxygen atoms. (Figure 22) When oxygen atoms are not bonded they transform into hydroxyl form. Two main arrangements of tetrahedral and octahedral sheets fused and connected for producing one layer structure of clay. If one T is fused with O (1:1) kaolin group is formed with the general formula of $\text{Al}_2\text{Si}_2\text{O}_5(\text{OH})_5$ and the layer thickness of ~ 0.7 nm. If structure consists of one octahedral sheet sandwiched between two tetrahedral sheets (2:1) with the total thickness of 0.94 nm is well known as phyllosilicates.

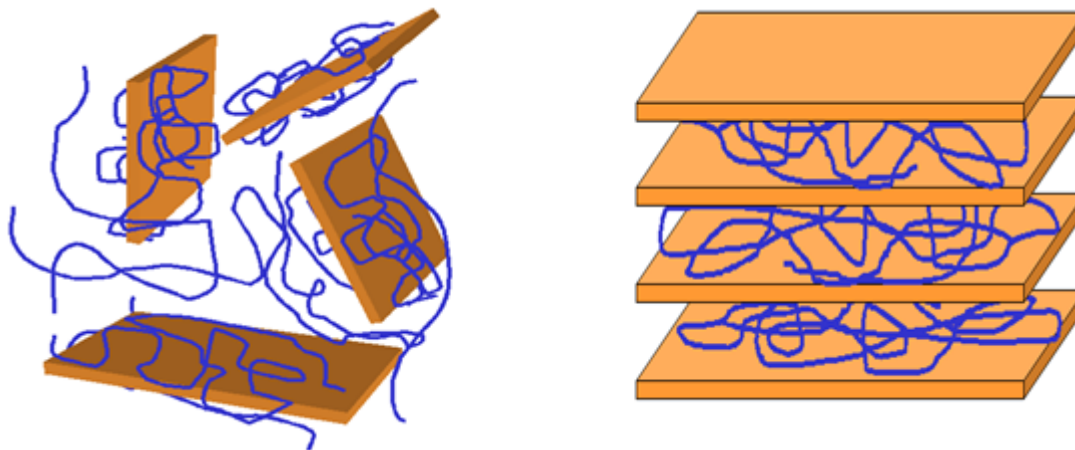


Figure 23 Exfoliated (left) and intercalated (right) clay structures by polymeric architectures.

The 2:1 phyllosilicate layers are generally electrostatically neutral with no inter layer ion (not K or Na) present known as pyrophyllite. Since there is no interlayer cations the layers do not expand in water. But when silicon in tetrahedral sheets is replaced by aluminium atoms, the 2:1 structure is formed which called mica. The layers of these structures stay almost together with a regular layer gap between two layer. This gap is generally called inter layer or gallery. The thickness of one to one layer is called d-spacing (d_{001}) or basal spacing which can be determined by small angle X-Ray. The inter layer distance is about 1 nm for montmorillonite. The unique intercalation/exfoliation (Figure 23) behavior of clay minerals which is responsible to the high aspect ratio of clay type makes these minerals an important component of the polymer nanocomposites technology. Since their reinforcing filler effects can enforce a polymer's gas barrier, thermal stability, stiffness, optical properties modification of these clays play an important role for the final materials obtained from polymers hybrid nanostructures^[59-60]. If we can properly modify the surface of the clays by selected special chemical precursors like organically modified alkoxy silanes or quantum dot nanoparticles, it is possible to extend the application areas of the nanocomposite structures; like visible (blue, green, orange, yellow light emitting) light emitting or selective UV protected nanocomposites.

3 Experimental Part

3.1 Experimental procedures

In this section the synthesis and analytical characterization methods for the nanostructures are presented.

3.1.1 Synthesis of ZnO Nanostructures

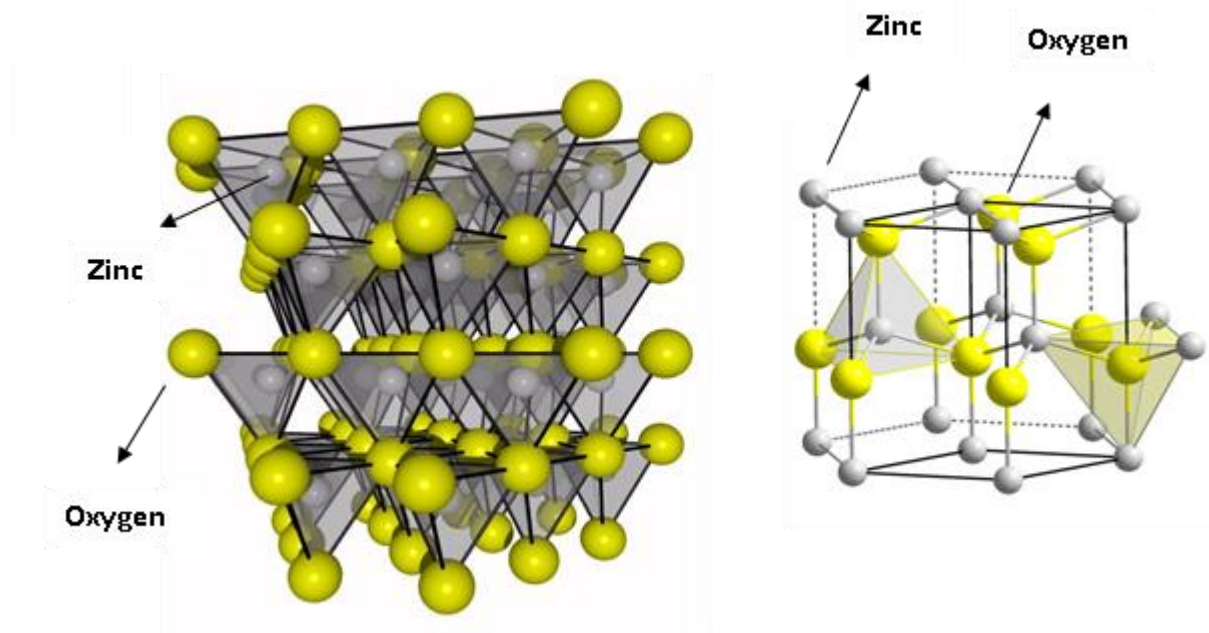


Figure 24 Wurtzite crystal structure of ZnO.

Zinc oxide is a direct, wide bandgap semiconductor and has promising properties for optoelectronics^[61], spintronic devices^[62] and sensor applications^[63]. It is generally used for sunscreens^[64], catalysts^[65], paint pigment^[66] and as transparent conducting electrodes^[67]. Its band gap is 3.37 eV makes it transparent in visible light and operates in the UV to blue wavelengths. The exciton binding energy is ~ 60 meV for ZnO and this higher exciton binding energy enhances the luminescence efficiency of light emission. ZnO has a hexagonal wurtzite crystal structure, with lattice parameters $a=3.25\text{\AA}$ and $c=5.12\text{\AA}$. The Zn atoms are tetrahedrally coordinated with four O atoms (Figure 24), where the Zn d-electrons hybridize with the O p-electrons. The bonding between the Zn atoms and O atoms is highly ionic, due to the large difference in their electronegative values (1.65 for Zn and 3.44 for O). Alternating Zn and O layers form the crystal structure. There is a separation between the nanoparticles and quantum dots in a way that the particle as a quantum dot is so small that its exciton levels are confined in all three spatial x,y and z dimensions. Therefore a

3 Experimental Part

quantum dot is another concept (subclass) of the nanoparticles. For investigations of quantum dot basics, ZnO is quite proper since its size regime 2-7 nm reveal quantum size effects, for example shift in the band gap, at the same time as they are big particle enough to be observed by X-ray diffraction. Even though ZnO is not a perfect material for light harvesting due to its narrow UV absorption it can be used as a proper model system for charge transport and UV absorption phenomena^[4].

3.1.1.1 Salt Elimination method for Zn(Oleate)₂

For the formation of zinc-oleate complex 1 eqv zinc chloride (ZnCl₂, 36,6 mmol, Acros, 98%) was reacted by 2 eqv. sodium oleate. In a typical synthesis, 5.0 g of zinc chloride and 24.35 g of sodium oleate (80 mmol, Sigma Aldrich, 99%) were dissolved together in a three neck flask in a mixture solvent composed of 80 mL ethanol, 60 mL distilled water, and 140 ml hexane. This mixture was heated to 70 °C and refluxed at that temperature for 4-5 h. When reflux ended, the upper organic layer containing the zinc – oleate complex was separated by separation funnel and washed with 15 mL distilled water.

Table 1 Synthesis concentrations of Zn-Oleate complex.

	$2\text{NaOleate} + \text{ZnCl}_2 \rightarrow \text{Zn(Oleate)}_2 + 2 \text{NaCl}$			
Mol.Weight	304.45	136.29	628.31	58.5
Equivalence	2 eqv	1 eqv	1 eqv	2 eqv
Mass	22.3 g	5.0 g	2299 g	4.288
Mol	0.0733	0.0366	0.0366	0.0733

The resulting waxy solid has become solid after hexane was evaporated by rotary evaporator. Resulted material is the zinc - oleate complex in its solid form and generally quite clear white. When colour is yellowish then it should be washed again with water and less amount of hexane.

3.1.1.2 Amide Method for Zn(Oleate)₂ Precursor

For the synthesis of ZnO QD's, Zinc-oleate complex has been prepared from a organometallic precursor was used that can be obtained in high purity. For a typical synthesis, 1 equivalent (H-DMS) HSi(NMe₃)₂ was reacted with 1 equivalent n-BuLi for the lithiated intermediate synthesis in a liquid nitrogen/EtOH bath at -78 °C. To this intermediate mixture, 0.5 equivalent

3 Experimental Part

ZnCl₂ in absolute THF was introduced at -78 °C and allowed to react for at least 30 h at this temperature. After the reaction was completed [Zn(SiMe₃)₂] (Figure 25) was collected by distillation under reduced pressure (p=1.10⁻² mbar).

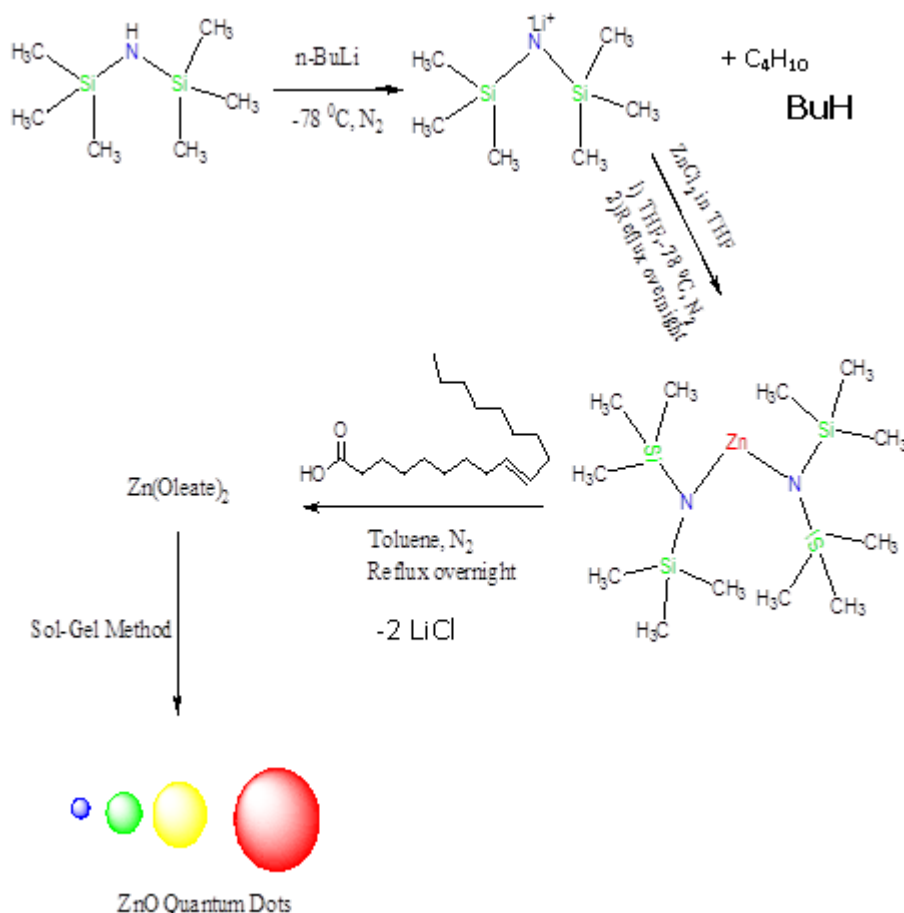


Figure 25 Amide procedure of ZnO QD synthesis from an organometallic precursor.

3.1.2 Ligand Controlled ZnO Quantum Dot Synthesis

In this part the synthesis methods of ZnO QD's with different ligand modifications is described.

3.1.2.1 Acetate Controlled ZnO QD Synthesis

For a general synthesis of acetate modified ZnO quantum dots, 5 mmol from of Zn(CH₃COO)₂·2H₂O (Acros, MW: 219,50 g/mol) was dissolved in the EtOH. 7 mmol LiOH·H₂O (Aldrich, MW: 41,96 g/mol) was dissolved in MeOH. Zn was quickly added to the clean solutions of precursor which was dissolved in EtOH. The resulting mixture was refluxed for 90 min at defined temperature (with or without nitrogen atmosphere), whereby aliquots were collected at different time intervals (10, 30, 60, and 90 min). This method is called "Swift Synthesis". As

3 Experimental Part

prepared quantum dots were precipitated out by hexane and washed with H₂O, ETOH and hexane when necessary. This method is a modification of the Meulenkamp^[68] method for ZnO QD synthesis which has been applied in all quantum dot synthesis cases.

3.1.2.2 Cysteine capped zwitterionic ZnO QD Synthesis

Cystein capped ZnO QDs were prepared by using 5 mmol of Zn (CH₃COO)₂·2H₂O dissolved in EtOH under vigorous stirring at 50 °C. The resulting clear solution was mixed with a mixture of different amount of cysteine and 7 mmol LiOH·H₂O in MeOH. The amount of cysteine was varied to obtain quantum dots of different sizes. The diluted reaction mixture was refluxed for 90 min at 55 °C under nitrogen atmosphere, whereby aliquots were collected at different time intervals (10, 30, 60, and 90 min) to record the particle size evolution by optical absorption spectra. The prepared ZnO QDs were precipitated out by adding hexane to the solutions and were washed with water, ethanol and hexane respectively and dried in vacuum for 6 h.

3.1.2.3 Oleate Capped ZnO QD Synthesis

Oleate controlled ZnO QD's have been prepared by using 5 mmol Zn(Oleate)₂ dissolved in EtOH at defined temperature and addition of this milky solution into 7 mmol LiOH·H₂O/MeOH mixture. Nitrogen atmosphere can be used for the protection. Aliquots have been collected at different time intervals for photoluminescence and particle size distribution investigation. By changing the temperature and reactant ratio, it was possible to obtain different visible light emission and particle size. For example 5:7 proportion of LiOH:Zn has been used for the long term investigation of the oleate modified ZnO QD's at 80°C (ZnO-1). Synthesis at 50-55 °C with the same proportion of reactants resulted with a very bright blue visible emission in swift synthesis (ZnO-2). When the LiOH:Zn proportion was 1:2 green emitting ZnO quantum dots were obtained (ZnO-3). Prepared ZnO QD's were precipitated out by adding hexane to mixture after completed the reflux time followed by repeated washing with H₂O, EtOH and acetone respectively.

3.1.2.4 Phase Transfer Synthesis of ZnO QD's

For the phase transfer synthesis of ZnO QD's, Oleate@ZnO quantum dots were dispersed in CHCl₃ and ultrasonicated for 5 minutes to obtain a clear solution. Concentration of the ZnO defines the milky character of the mixture probably due to the formation of large agglomerates. When the ZnO quantum dots from this organic phase were transferred to water phase, we dissolve the chosen

3 Experimental Part

organic acid (for example, gluconic acid, mandelic acid, citric acid etc.) in the water phase and mix it with the CHCl_3 which contains the ZnO QD's. Small ultrasonication period, 5 minutes was enough for the phase transfer synthesis. Still for a better coverage of the substituted ligand it is possible to reflux the quantum dots after phase transfer. Excess amount of the acidic ligands caused dissolution. After phase transfer quantum dots have been washed with acetone 2 times and dried in oven at 80°C .

3.1.3 Heating Up Synthesis of Anisotropic ZnO Nanoparticles

Heating up synthesis of the ZnO nanocrystals have been achieved by heating the ($290\text{-}300^\circ\text{C}$) mixture of $\text{Zn}(\text{Oleate})_2/\text{Oleylamine}$ (% 80-90 Riedel Haen)/Oleic acid (Riedel Haen) in the three necked flask. Using different precursor combinations it was possible to obtain plate like, nanorod, triangle-pyramid like ZnO nanocrystals[69-70] (Figure 26). For a common synthesis the required amount of precursor mixture was placed in a three necked flask. This flask has been heated with $5^\circ\text{C}/\text{min}$ heating range under the argon atmosphere until the

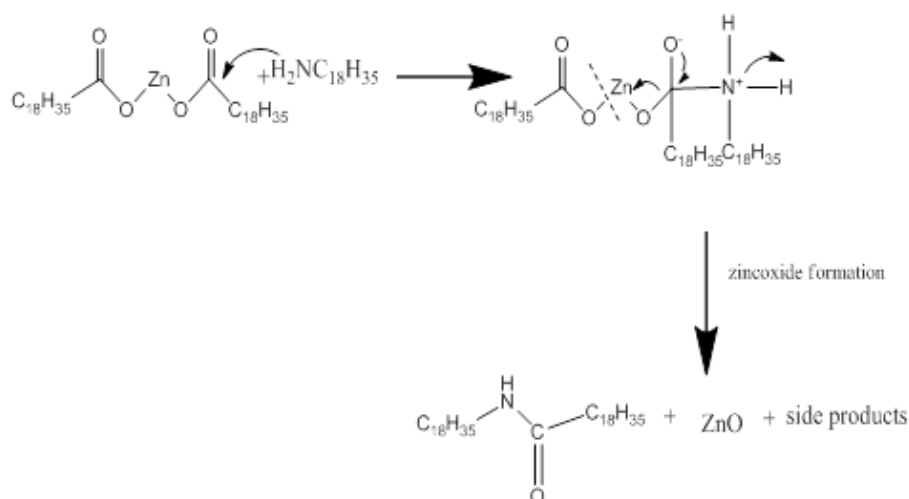


Figure 26 Non hydrolytic high temperature formation mechanism of ZnO nanoparticles from oleate precursor

$280\text{-}320^\circ\text{C}$ temperature. After reaching this temperature they have kept at this temperature 1 h. have been kept 1 hour (Figure 27). Cloudy, yellowish mixture of suspensions of nanoparticles have been observed during and after the reaction.

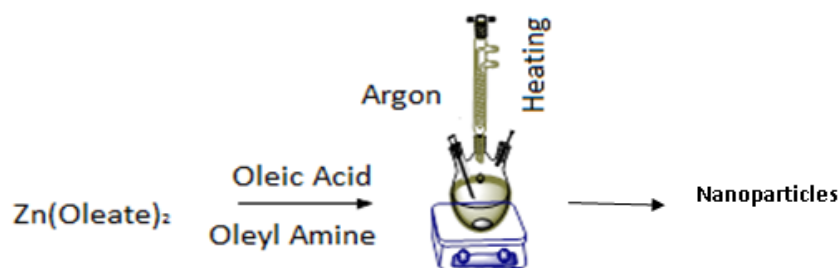


Figure 27 Experimental set-up for the heating up method for ZnO nanocrystal synthesis.

After reaction flask was cooled down the room temperature, large amount of EtOH was added for precipitation and nanoparticles have been centrifuged at 11 000 rpm by washed 4-5 times by this solvent and dried under vacuo. Reaction mechanism follows a non-hydrolytic decomposition (Figure 26) route for the formation of ZnO nanoparticles. It is possible to follow the nanoparticle formation by FT-IR spectroscopy.

3.1.3.1 Salt Assisted Surface Modification of ZnO Nanostructures

Obtained ZnO nanocrystals have been modified (Figure 28) by different type of surface agents for controlling the surface character and solubility. In a typical synthesis 250 mg nanoparticle have been dispersed in 50 ml toluene ultrasonicated 15 minutes. In another flask, modification agent (mandelic acid for example) has been dissolved in 10 ml of EtOH and ultrasonicated until a clear solution was obtained.

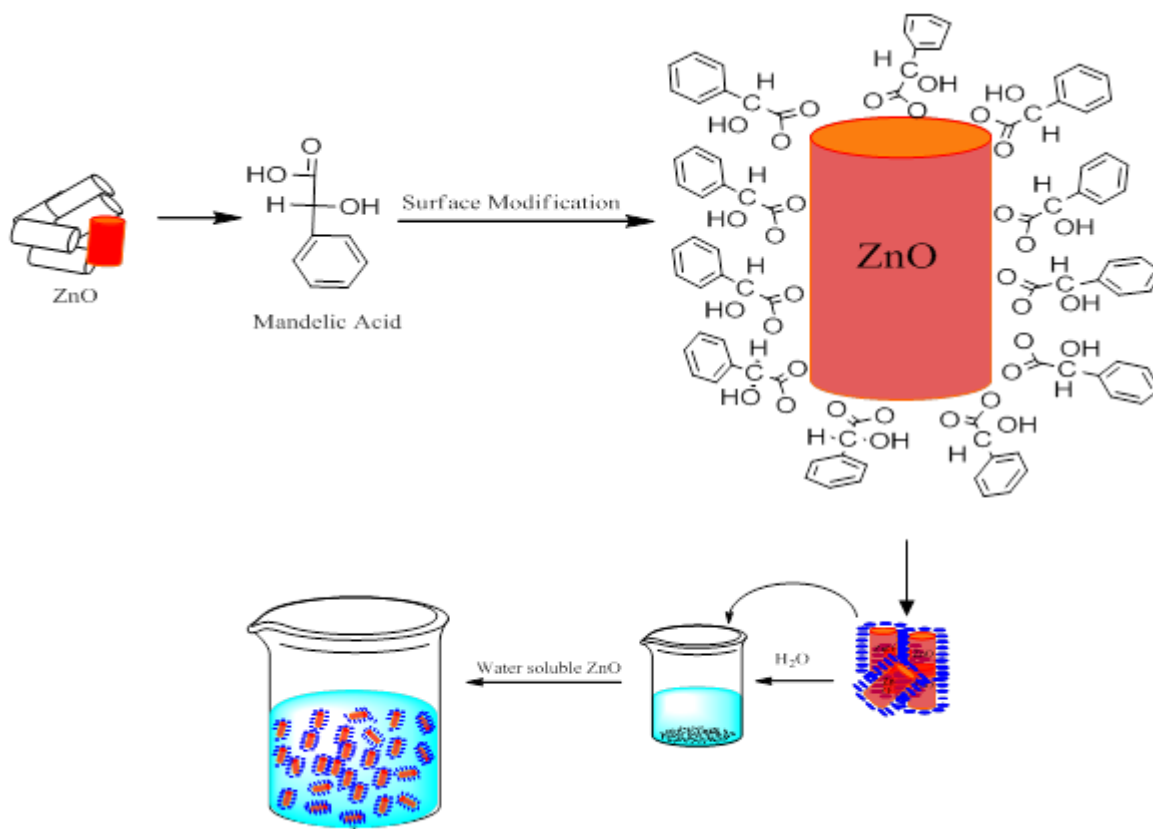


Figure 28 General carboxylic acid modification of ZnO nanoparticles.

Mixture was sonicated 10 more minutes and refluxed at 75° C for 2 hours. In order to remove the excess acidic agent, obtained nanoparticles have been washed with EtOH and acetone and modified particles have been dried under vacuo.

3.1.3.2 SiO₂@ZnO Core/Shell (Encapsulated) Nanostructures with Different Surface Modifications

In a flask 500 mg ZnO nanoparticles were dispersed and ultrasonicated as much as possible in 50 ml water. Then 30 ml water 100 ml EtOH mixture is added and mixture was stirred for 10 minutes. Concentrated ammonia (NH₃) was used for bringing the pH value up to around 10.0-10.5 which was measured by pH-meter. This mixture was stirred around 30 minutes more and then 2 ml TEOS (Tetraethoxysilane) was drop by drop added. Long chain organic molecules and long chain alcohols (like octanol) may enlarge the size of the silica. Whole addition must be completed in 30 minute-1 hour period. After completing the addition, mixture is stirred around 20 hours at room temperature. After centrifugation, particles are washed with EtOH, water and acetone. This method is a slightly modified Stöber method for the core shell nanoparticles. Particles

3 Experimental Part

are dried at 80°C for 24 hours under vacuuo. For increasing the solubility we can modify the surface of silica shell by different ligans. For example; 100 mg of SiO₂@ZnO particles have been dispersed in 30 ml EtOH and stirred 30 minutes. Then 20 mg mercaptopropyl trimethoxysilane, aminopropyl trimethoxysilane which was dissolved in 10 ml EtOH/2 ml water mixture added into the above solution. After stirring at 60°C around 10 hours, particles were centrifuged and washed with EtOH and acetone respectively.

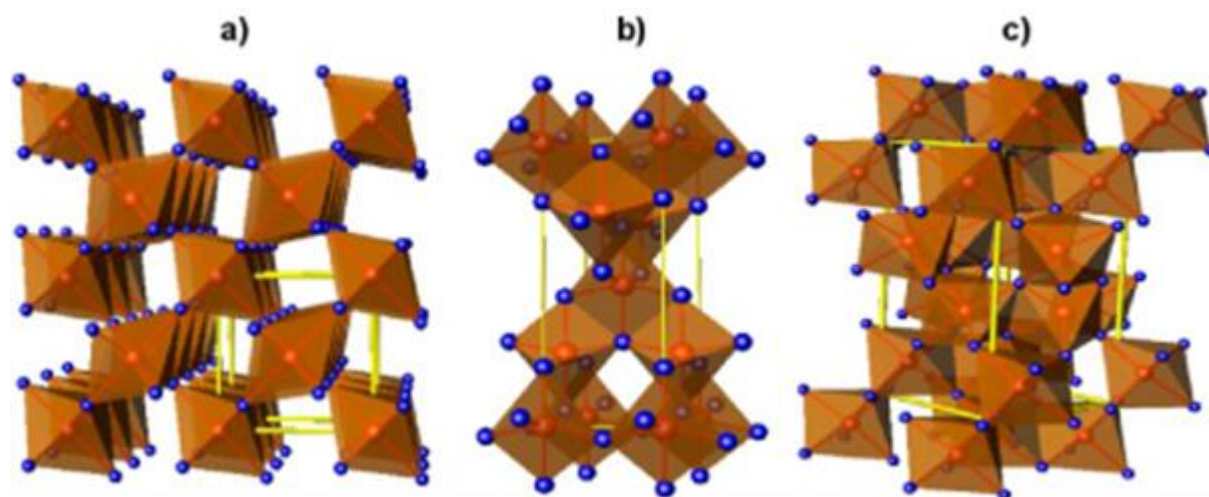
3.1.4 Synthesis of TiO₂ Nanostructures

Titanium dioxide (TiO₂) is a transition metal oxide and widely used semiconductor^[71] which mainly has three crystal structures: anatase, rutile, brookite. It is an n-type semiconductor which means electrons are the majority charge carriers. Additionally it has been reported that 3 synthetic (monoclinic, orthorhombic and triclinic) and 5 high temperature modification of TiO₂ have also been observed, three metastable phases can be produced synthetically (monoclinic[72], tetragonal[73] and orthorhombic[74]), and five high-pressure forms (α -PbO₂-like[75], baddeleyite-like[76], cotunnite-like[77], orthorhombic OI[78], and cubic[79] phases). Generally, anatase crystal structure and rutile crystal structure are most investigated forms of TiO₂ due to their wide solar , photocatalytic, nanoelectronics and water splitting applications[71]. Especially photocatalytic or light assisted oxidation properties make TiO₂ as an ideal photocatalytic nanomaterial. Still its application areas are limited to the Ultraviolet (UV) region of the light spectrum. Due to its high band gap energy, (Anatase= 3,2 eV) only 4% of the solar radiation can be harvested and used appropriately.

Lattice structure for anatase and rutile modifications (Figure 29) is generally described as distorted octahedra of TiO₆²⁻. This geometry simply means that Ti center atom (cation) (Ti⁴⁺) surrounded by 6 oxygen (O²⁻) atoms (anions). There is some small differences in the rutile and anatase structures but these small differences cause electronic differentiations. Each octahedron a) has an amount of distortion and b) different shape of these octahedral connections . For example, in anatase structure four octahedron share the edge oxygen pairs and also four octahedron share a corner oxygen pair. As a result each octahedron is in contact with eight neighboring octahedrons. As a contrast in rutile structure each octahedron is in contact with 10 neighboring octahedrons. Also two octahedrons share the edge oxygen pairs and in addition to that eight octahedrons share the corner oxygen atoms. These contact geometries show us

3 Experimental Part

that anatase has highly distorted structure if we compared to rutile. This distortion causes longer Ti-O-Ti bonds but shorter Ti-O bonds in rutile. Small orthorhombic distortion of the rutile structure is responsible for the energy band gap difference between the anatase (3,2 eV) and rutile (3,0 eV) crystal structure[71].



a)Rutile b) Anatase c) Brookite

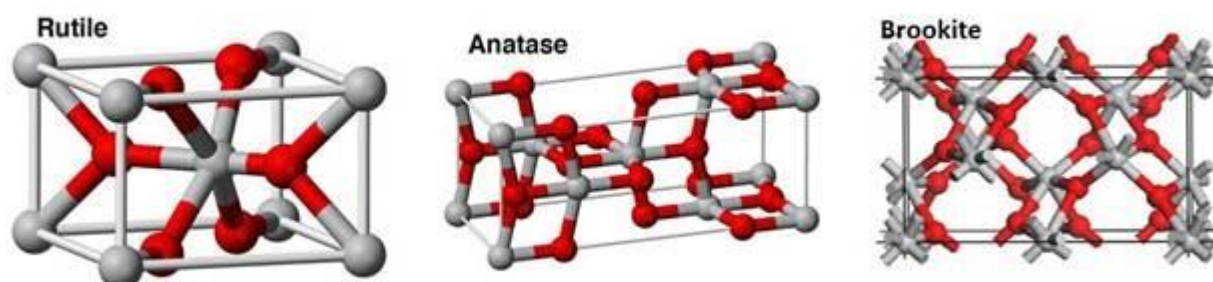


Figure 29 Crystal structures of TiO₂ phases and toxic orientation in the TiO₂ crystal structures.

Even though rutile has a smaller band gap energy it has been confirmed that anatase shows more reactivity in the exciton formation and photocatalytic activity. Irregularities in the crystal structure cause oxygen deficiencies and remarkable changes in the photocatalytic activity.

3.1.4.1 Synthesis of one-dimensional TiO₂ nanofibers by hydrothermal method

Elongated fiber like TiO₂ can be prepared from commercial TiO₂ nanoparticles^[80-81]. In order to obtain fibers, 30 ml, 10 M NaOH and 500 mg (Acros, TiO₂ Aeroxide P-25, MW: 79,88 g/mol) has been ultrasonicated 30

3 Experimental Part

minutes and then placed into hydrothermal tube and kept under the conditions of 200 °C, 24 h. After synthesis, elongated nanostructures have been centrifuged and washed with acetone 3 times.

3.1.4.2 Synthesis of Spherical TiO₂ nanoparticles by Heating Up Method

Synthesis of TiO₂ nanoparticles by heating up method has been employed by the same installation as in ZnO nanocrystal synthesis.

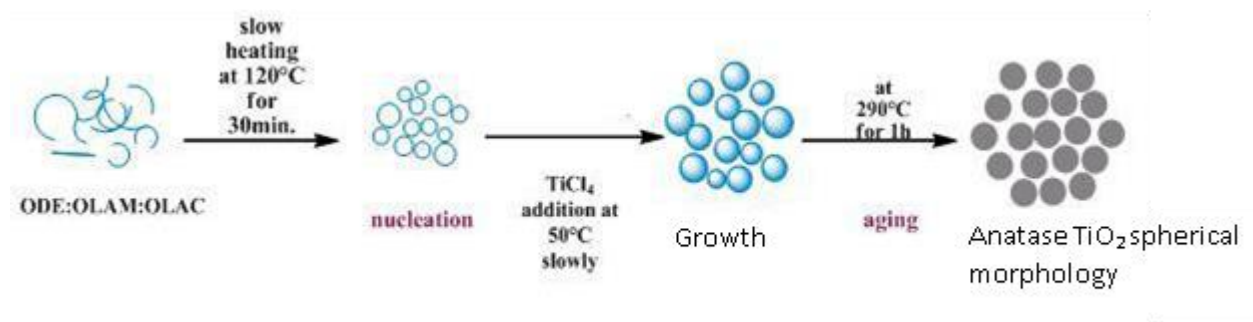


Figure 30 Spherical TiO₂ formation by Hot Injection method.

All syntheses (Figure 30) were carried out under air-free conditions using a standard Schlenk line setup. 2,5 ml Octadecene (2 g) 3,37 ml Oleic acid (1 eqv) and 28 ml Oleylamine (9 eqv %85) have been loaded into a three-neck flask and heated at 120°C for 30 min. After the half an hour mixture was cooled down to 50°C under N₂ flow and 0,88 ml TiCl₄ (Fluka, MW: 189.68, 1 eqv) was introduced into the flask and heated to 290°C. Reaction mixture has been kept for an hour at this temperature for the non-hydrolytic decomposition of Ti-precursor and nanocrystal formation. When kept at this temperature reaction mixtures color transforms to light blue from colourless then dark blue and to brown gradually. If temperature, reactant concentration and heating time are changed resulting particles are also show different characteristics. Final mixture was white milky which shows the nanoparticle formation. EtOH has been added to precipitate the nanoparticles and centrifugation has been done at 10 000 rpm, 5 min was applied. Nanocrystals have been washed with EtOH, water and acetone respectively (3 times) and particles have been dried under vacuo.

3.1.4.3 Synthesis of multibranched, elongated TiO₂ nanostructures by Hot Injection Method

Hot Injection synthesis of TiO₂ has been done with a small modification to heating up method. After formation of TiO₂ nanoparticles a defined amount of precursor mixture has been injected into the reaction flask (Figure 31).

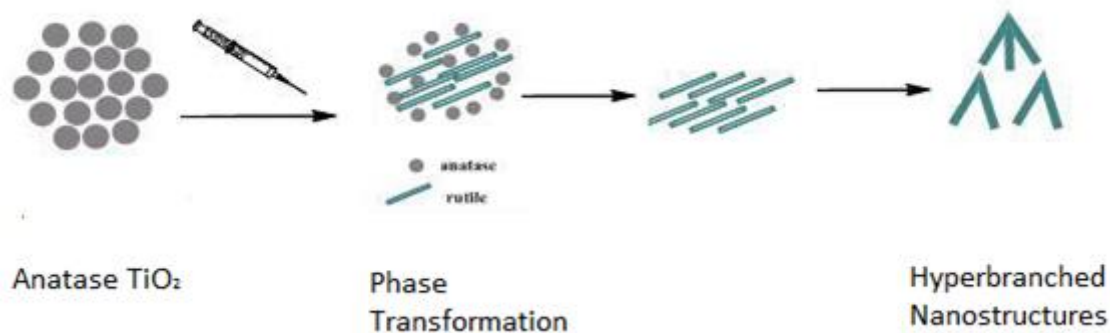


Figure 31 Hot Injection Synthesis of multibranching TiO_2 .

For a typical synthesis, which has been carried out under air-free conditions using a standard Schlenk line setup, 3.81 ml ODE (3 g), 0.42 ml OLAC (1 eqv 75%) and 20.20 ml OLAM (52 eqv, %85) have been transferred into a three-neck flask and heated at 120°C for 30 min. Mixture then cooled down to 50°C under N_2 flow and TiCl_4 (1 eqv) mmol has been introduced and the flask has heated up to 290°C . Temperature was kept at 290°C , 1 h. In another flask an injection mixture prepared as 1,17 ml OLAM, 1,27 ml ODE and 0,33 ml TiCl_4 . After 1h heating, injection mixture was injected slowly for arranging the monomer flux properly into the reaction mixture at 290°C . This injection mixture has been change for the synthesis of different TiO_2 nanoparticles. During the reaction aliquots have been collected for the observation of particle evolution. After a non-hydrolytic decomposition of Ti-precursor and kinetic control of the nanocrystal formation we have obtained hyperbranched, spherically assembled, spherical nanocrystals. During the injection flask was almost dark reddish brown and turn into yellowish gradually. After completing the heating, final mixture has been diluted with EtOH and centrifuged. Afterwards they have been washed with acetone and dried under vacuo^[82-84].

3.1.5 Inorganic Organic Hybrid Polymer/ZnO Nanocomposite Synthesis

Nanoparticle filled inorganic organic nanocomposites synthesis has been employed for the TiO_2 and ZnO nanoparticles. For a ZnO embedded nanocomposite material, organically modified trialkoxysilane precursor should be hydrolysed firstly for increasing the $-\text{OH}$ amount in the precursor polymer. For this reason 1 eqv amount of 0,1 M HCl is added into the organically modified trialkoxysilane for hydrolyzing the structure. Actually trialkoxysilane has 3 hydrolysable alkoxy groups. Therefore instead of full hydrolysis by 0,1 M HCl, partial hydrolysis is employed which should be 3 eqv 0,1 M HCl. After 6

3 Experimental Part

hours, due to the After 6 hours nanofiller (ZnO or TiO₂) is introduced for increasing the dispersion and hydrolysis and condensation reactions an oligomeric siloxane structure is formed carrying organic functional groups on a silicon skeleton^[85] (Figure 32). surface modification effect of the nanoparticles. Due to the unique propagation method of the sol-gel reaction, it is possible to disperse the particles and obtain an homogeneous nanocomposite structure. Afterwards highly dispersed nanoparticle containing structure is polymerized according to its polymerizable group (Figure 33) such as acrylate, epoxy, double bond etc.

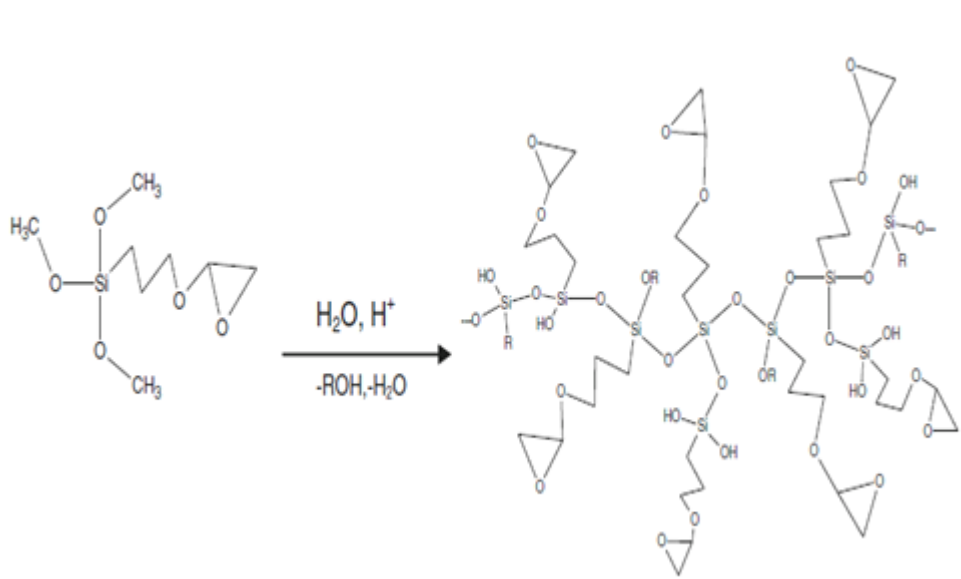


Figure 32 Partial hydrolysis of epoxy modified trialkoxysilane.

These interactions are vitally important since when nanoparticle is modified and introduced correctly, obtained nanocomposite becomes transparent. Application methods of these polymeric hybrid formulations are widely known such as spin coating, spray coating etc.

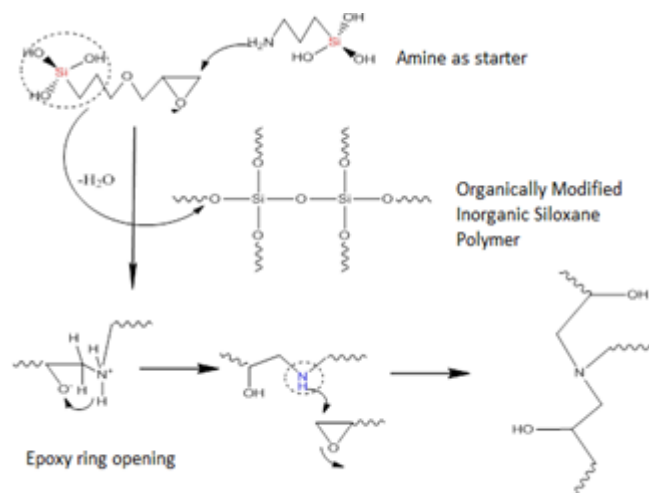


Figure 33 Epoxy ring opening reactions in hybrid nanocomposites.

Depending on the introduced nanoparticle and organically functional group type, these obtained nanocomposite structures can be cured by UV, IR or thermally and they show antibacterial, photocatalytic, superhydrophilic, UV protective, scratch and abrasion resistant properties due to the introduced nanoparticles formulations^[85]. Figure 34 shows an interaction between a particle and alkoxy silane backbone.

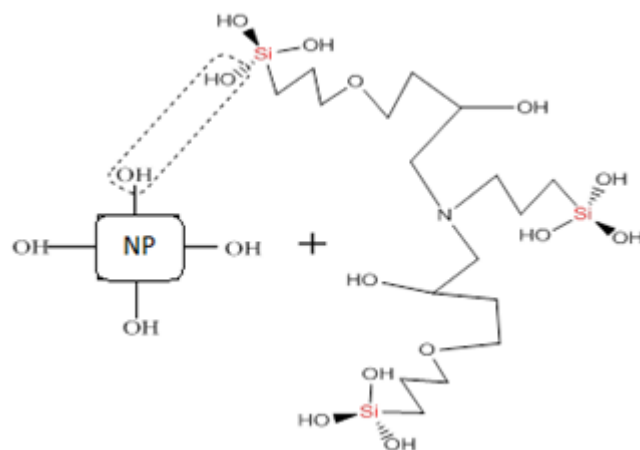


Figure 34 Schema for the nanoparticle surface modification.

3.1.5.1 PLA/Hybrid Polymer/NP Nanocomposite Synthesis

Hybrid polymer/ PLA (Dow Coring) nanocomposite structure was synthesized similarly to the previous description^[85]. Methacryloxypropyl trimethoxy silane (MEMO, Dynasilane) was incorporated into the PLA/THF mixtures varying from %10 to %50 (w/w). Before incorporation, MEMO/Benzophenone (Sigma Aldrich, MW: 182,22 g/mol) mixture was prepared and hydrolysis of the

3 Experimental Part

MEMO according to its hydrolyzable alkoxy groups was acquired during 6h. During water addition the solution was stirred vigorously. Nanoparticles have been introduced by dispersing them in the hydrolysed hybrid precursor. After addition of the nanoparticles, final formulation was stirred half an hour for homogeneity. Solvent was removed and UV light and thermal treatment were used for curing. Synthesized novel hybrid structures were coated onto the glass substrates by spin coating method with 2000 rpm, 10 second conditions. Biodegradability was tested in a commercial compost at 55 ± 2 °C.

3.1.5.2 ZnO@Clay Nanocomposite Preparation

ZnO QD@Clay structure synthesis has been conducted for rod like and plate like clays. During the preparation of the composite structure firstly 5 mmol $\text{Zn}(\text{CH}_3\text{COO})_2$ precursor was dissolved in EtOH at 85 °C and after obtaining a clear solution, 2 g of clay particles has been introduced in to the reaction mixture. After introducing clay, reaction mixture was stirred for more than an hour. This step is for the adsorption of zinc on the clay surface. After adsorption process 7 mmol $\text{LiOH}\cdot\text{H}_2\text{O}$ has been added into the solution which dissolved in MeOH prior to addition. Reflux has been conducted 24 hours at 85 °C and aliquots have been taken for the nanoparticle evolution analysis. Finally mixture has been centrifuged and washed with acetone and composite structure has been dried in oven at 90°C.

3.2 Characterization techniques

3.2.1 Transmission and High Resolution Transmission electron microscopy

In Transmission Electron Microscopy a beam of electrons is transmitted through a nanomaterial or thin structure interacting with the structure as it passes through. Due to the interaction of the electrons the image is magnified and focused and transmitted into a computer screen or it is detected by a sensor such as a CCD camera. Since small de Broglie wavelength of electrons it is possible to get remarkably higher resolutions for the observation of nanocrystals. TEM images of the nanostructures have been analyzed on the Cu grids dropped from its solution. Particle size and morphology have been investigated with TEM (LEO 912 Omega, Zeiss, Oberkochen, Germany) operated at 120kV with zero loss conditions. The energy-filtered electron micrographs were recorded with a high-speed scanning camera (sharp: eye, 2048 x 2048 pixels, TRS, Moorenweis, Germany) under remote control using the image acquisition system (iTEM, Olympus Soft Imaging Solutions GmbH, Münster, Germany).

3.2.2 Scanning electron microscopy (SEM) and Electron Diffraction X-Ray (EDX)

Scanning electron microscope (SEM) produces detailed images by scanning nanomaterials, small items, thin films with a high-energy beam of electrons in a raster scan pattern. When electrons interact with surface and scatter electrons, the detector of microscope collects this information and produce signals that contain information about the sample's surface topography, composition, and other properties such as electrical conductivity. The types of signals produced by an SEM include secondary electrons, back-scattered electrons (BSE), characteristic X-rays, light, specimen current and transmitted electrons. Basically X-rays are emitted by beam material interaction and if electron beam removes an inner shell electron from the sample, causing a higher energy electron to fill the shell and release energy. Therefore these X-rays are used to identify the composition and measure the abundance of elements in the sample which called as Energy Dispersive X-ray spectroscopy (EDX). Surface morphology of the QD layer and EDX analysis were acquired by Nova Nano SEM 430 on silicon substrates which ultrasonically cleaned in acetone bath before use.

3.2.3 X-Ray Diffraction spectroscopy

In X-ray scattering scattered intensity of an X-ray beam hitting a sample as a function of incident and scattered angle, polarization, and wavelength or energy is recorded. Especially X-ray powder diffraction method is mostly used for the identification of unknown crystalline materials and mixtures in some cases. This method makes also possible to define fine-grained minerals, identification of unit cell dimensions and sample purity. Additionally by XRD technique it is possible to determine crystal structures using Rietveld refinement and characterize thin films samples.

$$n \lambda = 2 d \sin (\theta) \text{ Eq 11}$$

Where d is interplane distance (d) of crystal was calculated by Bragg's Law, λ is the wavelength of the x-ray, θ is the angle of the diffracted wave and n is the integer known as the order of the diffracted beam. The powder X-ray diffraction (XRD) patterns of as-synthesized and thermally treated ZnO QD's were measured with a STOE-STADI MP vertical system in transmission mode using Cu K α ($\lambda=0.15406$ nm) radiation.

3.2.4 Thermogravimetric Analysis

Thermogravimetric analysis measures the changes of materials in weight in relation to change in temperature. Therefore analysis require high precision for the measurement of weight, temperature, and temperature change. Thermal analysis and surface modification properties of the prepared structures was carried out in the temperature range from 30 to 800°C with a heating rate of 10°C/min under nitrogen atmosphere (flow rate; 25 ml/min) using Mettler Toledo TGA/DSC 1 Stare systems.

3.2.5 Atomic force microscopy (AFM)

In the Atomic Force Microscopy, a sharp tipped cantilever is placed onto the substrate surface which scans it with different modes namely contact or non-contact mode. Information obtained is the substrate surface topography and chemical/physical character of the surfaces. Analysis of the AFM have been done with XE 100 Park Systems in non contact method.

3.2.6 Photoluminescence Spectroscopy

Photoluminescence (PL) spectroscopy is the investigation of spontaneous emission of light from a material under optical excitation. When material absorbs photons (electromagnetic radiation) it should re-emit photons which means an excitation to a higher energy state and then a return to a lower energy state accompanied by the emission of a photon possessing energy corresponding to the band gap. In this thesis Fluoromax 3 Yvon Horuiba has been used for the determination of PL structures of the nanomaterials. Nanomaterial first dispersed in EtOH and afterwards measurement showed the desired spectra.

3.2.7 UV-Visible Spectroscopy

Ultraviolet-visible spectrophotometry (UV-Vis or UV/Vis) refers to absorption spectroscopy or reflectance spectroscopy in the ultraviolet-visible spectral region of the electromagnetic spectrum. Due to its highly energetic nature, molecules can undergo electronic transitions. UV/Vis spectroscopy is widely used in analytical chemistry for the quantitative determination of different analytes and optical properties of the nanomaterials. Generally in the thesis, UV Vis measurements have been done with Perkin Elmer Lambda 950 in 200-800 nm range. Since photocatalytic investigations use also this same technique, it is possible to determine photocatalytic decomposition rates.

3.2.8 Surface contact angle

Contact angle is used for detecting water or some specific other liquid repellency or affinity of the surfaces. One drop is given onto the surface and with the help of a camera contact angle is measured. In this thesis Krüss systems have been used for the contact angle measurements.

3.2.9 Dynamic Light Scattering (DLS)

Dynamic light scattering method or photon correlation spectroscopy is a method which can be used to determine the hydrodynamic size distribution profile of small particles in suspension or polymers in solution. In this method photon correlation spectroscopy (PCS), measures source laser light that is scattered from dissolved items or suspended particles. Since there is a Brownian motion of the molecules and particles in solution fluctuations of the scattering intensity can be observed. In this thesis Malvern Nano ZS has been used for the determination of DLS values of the nanoparticles which generally dispersed in water. PMMA cuvettes have been used as solvent container.

3.2.10 Zeta Potential Measurements

Zeta potential is a term which is related to the particle surface in a liquid media. According to widely known theory small structures form a double electrical layer in the solutions and these electrical double layer defines the fate of the small structures. Zeta potential (ζ) is used to predict the stability of the dispersed formulations and potentially provides valuable information for long-term stability. The general dividing line between stable and unstable suspensions is accepted as +30 or -30 mV. If the particles have more positive than +30 mV or more negative than -30 mV, they are normally considered to be stable. These observations and results are affected by pH, conductivity of the medium and concentration. In this thesis Malvern Nano ZS has been used with a specifically designed cells for the zeta potential measurements.

3.2.11 FT-Infrared Spectroscopy

FT-IR stands for Fourier Transform InfraRed, the preferred method of infrared spectroscopy. In infrared spectroscopy, IR radiation is passed through a sample which some of the radiation is absorbed by the sample and some of it is transmitted. The resulting spectrum represents the molecular absorption and transmission characteristics, creating a molecular finger print of the sample. This makes infrared spectroscopy useful for several types of analysis. For the analysis by FT-IR we have used Perkin Elmer 400, 4000-400 cm^{-1} range and simply

3 Experimental Part

dropped a little material onto the measuring platform on ATR Universal Sampling Accessory.

3.2.12 NMR Spectroscopy

NMR spectra have been recorded with a Bruker AVANCE II 300 spectrometer at 298 K, with NMR spectroscopic frequencies (external standarts) ^1H : 300,1 MHz (TMS) for the detection of surface attachment and other applications.

3.2.13 Confocal Microscopy

It has been used for the detection of luminescent species under the microscope for cell labeling applications. Leica LSM TCS SP5, Germany system and necessary excitation wavelength have been used for the imaging studies.

3.3 Material Properties Testing

Synthesized nanoparticles have been used for the some specific applications in the nanocomposite form. This part described the specific tests of the obtained nanomaterials.

3.3.1 Cell Cytotoxicity Tests

The cell toxicity studies performed on the particles described in this thesis were performed in collaboration with internal and external partners. The procedures described here are based on the protocols developed by Mr. Karim Arroub (Ph.D. student, Research Group Prof. Dr. Sanjay Mathur).

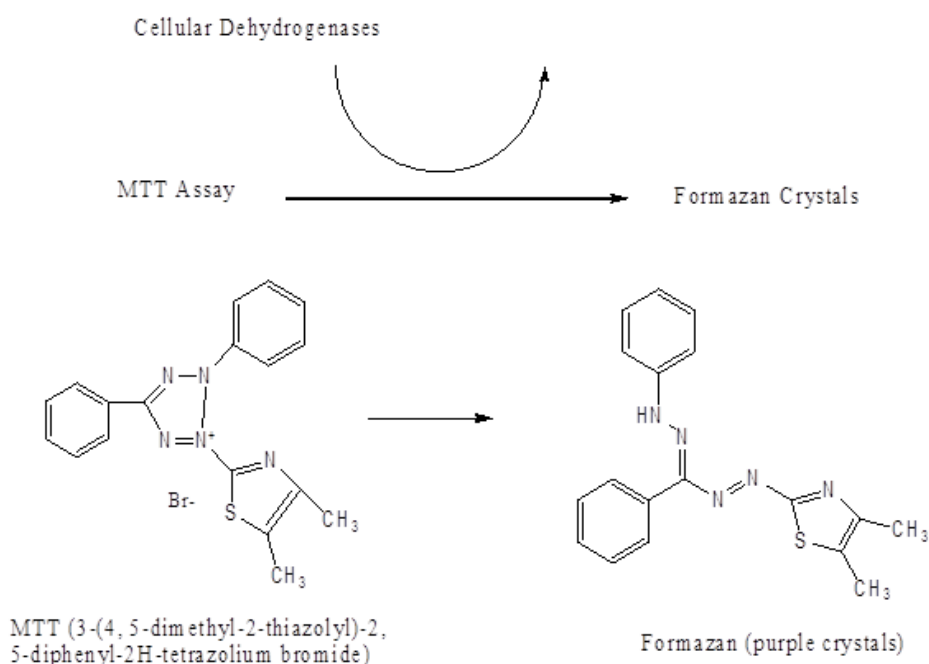


Figure 35 MTT test for the cell viability.

3 Experimental Part

Cytotoxicity of quantum dot or nanoparticles have been determined by the 3-(4,5-dimethylthiazol-2-yl)-2,5-diphenyltetrazolium bromide (MTT) assay (Carl Roth, Karlsruhe, Germany). Mitochondrial dehydrogenases of viable cells reduce the water soluble yellow MTT to water-insoluble formazan crystals (Figure 35) . These were solubilized with 4mM HCl in isopropanol containing 0,1% Tergitol solution (Sigma Aldrich, Steinheim, Germany). After exposure to the different amount of modified nanoparticles, 20 μ l MTT solution (5mg/ml stock solution) was added to each well and incubated at 37°C for different time periods. Medium was removed and 200 μ l MTT solvent was added to each well and mixed thoroughly. The absorbance was read at 620 nm by enzyme-linked immunosorbent assay (ELISA) (Elx800, Biotek). The results were computed in relation to an untreated control.

3.3.2 Cell Labeling by Visible Light Emitting QD's

Labeling studies have been done with Dr. Muhammed Sajid Hussein, Institute of Biochemistry and Genetics, University of Cologne. For the labeling applications used quantum dots have been introduced into necessary cell medium and incubated at 37 °C for different time periods. For the labeling applications, as an example HEK 293 human kidney cells were cultured on 12 mm coverslips, together with ZnO quantum dots. Then prepared cells were mounted on glass slides with gelvatol. Glass slides are placed onto the holder under microscope objective and images are taken by corresponding excitations by confocal microscope (Leica, Germany, LSM TCS SP5).

3.3.3 Photocatalytic Activity Tests

Photocatalytic activity in semiconductors is the term which is used for the process of recombination of charge carriers obtained by light irradiation. Since TiO₂ and ZnO are metal oxide semiconductors their HOMO is termed valence band and LUMO is termed conduction band. Light absorption by this metal oxides effectively results that electrons from oxygen are transferred to the vacant titanium d-orbitals.

3 Experimental Part

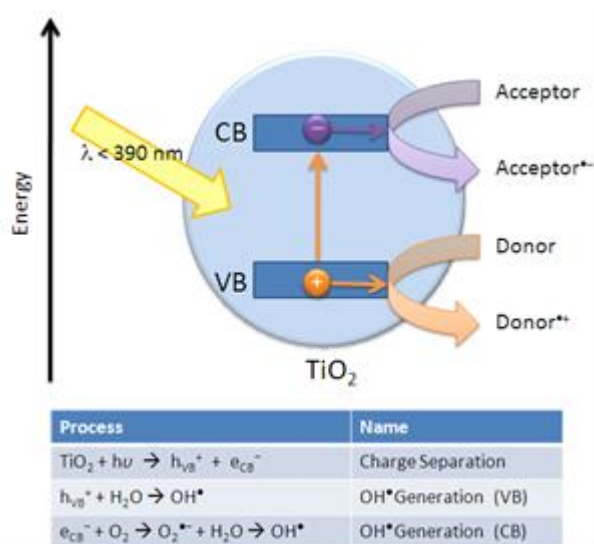


Figure 36 : Photocatalytic process for the formation of charge carriers of TiO_2 ^[86].

For anatase (3.2 eV) and rutile (3.0 eV) and (3.2 eV) for ZnO, this transition is in the UVA region, resulting in a sharp absorption band at 300-400 nm. Therefore promotion of an electron from valence to conduction band, on irradiation by UV (or visible) light, results in a ‘hole’ in the valence band that assigned a positive charge for showing its loss of negative electron (denotation is arbitrary) (Figure 36). The hole has the power of oxidation since valence band and (or oxygen orbital) requires to retrieve its own electron density after losing electron by irradiation. This process can be done by returning the electron from conduction band, recombining with the valence band called recombination is a sum of radiative (*i.e.* emission may be observed) and non-radiative processes. Many different pathways are possible which make the materials a photocatalysts. Obtained hole has the potential to oxidise water which maybe on the surface of the semiconductor resulting in the formation of hydroxyl radicals. Hydroxyl radicals are very powerful oxidating agents can easily oxidise any organic and inorganic molecules which are available in nearby untill carbon dioxide (CO_2) and water (H_2O). Conduction band at the same time is where the electron has no hole to recombine with, since it has oxidised surface bound water. It achieves an alternative to reduce and therefore reduces oxygen to form the superoxide anion. This anion subsequently react with water to form hydroxyl radical. This process provides a very useful photocatalytic self cleaning procedure^[71]. In the photocatalytic experiments, methylene blue has been used to evaluate the photocatalytic activity of the bare and modified nanoparticles. Before applications, absorption maxima has been found for the MB. Defined

3 Experimental Part

amount of MB was dissolved in water and nanoparticle were dispersed. To ensure the adsorption of the dye, solution were stirred at dark conditions during the 1 h. Subsequently solution was irradiated with mercury lamp (352 nm) or solar simulator and UV-Vis absorption measurements have been taken consecutively. Particles were centrifuged and separated before the UV-Vis measurements.

4 Results and Discussion

4.1 Ligand Modulated Visible Light Emitting ZnO QD's

In this chapter, synthesis and characterization of the ligand and surface controlled synthesis of ZnO QD's have been analysed thoroughly.

4.1.1 Fundamental Properties of ZnO QD's and Their Visible Light Emission

As an n-type semiconductor^[4] ZnO is a very important material for gas sensors^[87], optical waveguides^[88], and solar cells^[89-90]. Among many different morphological examples of ZnO QD's^[91-96] are gaining great interest due to their size dependent visible light emission characteristics^[95]. Generally ZnO photoluminescence has two basic components^[96]. One is the typical exciton emission or near-band-edge emission, i.e., photo-generated electron recombination with holes in the valence band or in traps near the valence band. For this process, generally 370 nm emission (UV light) is seen due to room temperature band gap (3.37 eV) character of ZnO^[1]. Beside that there is a visible light emission or deep-level emission related with oxygen vacancies, but the description of this emission mechanism is not perfectly clear so far^[97]. Two widely known mechanism are available for the visible light emission of ZnO QD's^[97] (Figure 37). a) recombination of a shallowly trapped electron with a hole in a deep trap and b) recombination of an electron in singly occupied oxygen vacancies with a photo-generated hole in the valence band. Since it is difficult to determine the exact location and the energy it is also difficult to determine the exact location and the energy level of the deep traps but there are some theories like, van Dijken and co-workers^[98-100] assigned ZnO visible emission (green–yellow) to the deep hole trap by comparing the PL shift of ZnO quantum dots of different diameters with a theoretical model based on the intensity ratio between two emission peaks.

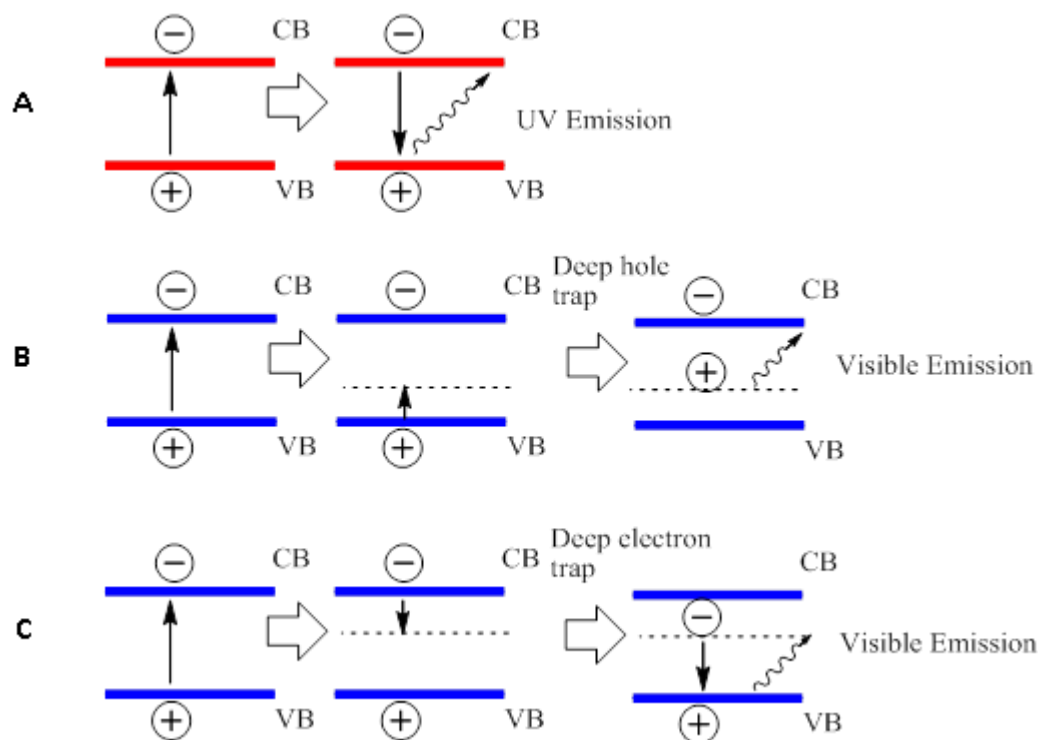


Figure 37^[97]: Photoluminescent processes suggested for ZnO nanoparticles. (A) Typical exciton emission, (B) recombination of a shallowly trapped electron with a deeply trapped hole, and (C) recombination of a shallowly trapped hole with a deeply trapped electron. In order to simplify the maps, the shallow traps near the valence band (VB) and the conductance band (CB) are not marked here.

No matter how many different theoretical explanation exists there is one clear thing that ZnO visible emission intensity depends on its different defect concentrations. So if we can increase the defect density we can increase the visible emission intensity. For the liquid systems sol–gel technique at room temperature is a very easy and common method to obtain ZnO with highly visible emission since obtained particles have a lot of defects. Visible luminescent ZnO nanoparticles colloids were invented and studied intensively which was obtained by hydrolyzing zinc acetate in ethanol, which appears as a very simple method.

4.1.2 Acetate as Controlling Ligand for ZnO QD' s

After the work by Spanhel and Anderson^[101], Meulenkamp^[68] at 1998 developed a synthesis and more importantly a particle size determination method for ZnO quantum dots from the UV Visible absorption spectrum. The preparation procedure described by Spanhel and Anderson, which has also been used by other groups, was used but it was modified slightly. According to the procedure

4 Results and Discussion

5 mmol sample of $\text{Zn}(\text{CH}_3\text{COO})_2 \cdot 2\text{H}_2\text{O}$ was dissolved in 50 mL of boiling ethanol at atmospheric pressure. Contrary to Spanhel and Anderson and other workers, solution was not refluxed but cooled down to 0 °C. 7 mmol sample of $\text{LiOH} \cdot \text{H}_2\text{O}$ was dissolved in 50 mL of ethanol at room temperature in an ultrasonic bath and cooled to 0 °C. The hydroxide-containing solution was added dropwise to the $\text{Zn}(\text{CH}_3\text{COO})_2 \cdot 2\text{H}_2\text{O}$ suspension under vigorous stirring at 0°C. The ZnO sol was stored at 4°C to prevent rapid particle growth. Since ZnO shows quantum size effects until >7-8 nm UV/vis absorbance spectra provide a convenient way to investigate particle growth. Therefore to equate E_g (band gap) with the wavelength at which the absorption is 50% of that at the excitonic peak (or shoulder), called $\lambda_{1/2}$. According to the investigations it has been found that curves are fitting to an equation like ;

$1240 / \lambda_{1/2} = a + b/D + c/D^2$ Eq 12 in nm, diameter D in Å). Generally it is taken as a= 3.301 b) 294.0 c) 1.09 Meulenkamp equation¹ provides a fundamental understanding on the particle size and its quantum confinement. Acetate modified ZnO QD's represent an easy way for the synthesis and investigations of the ZnO QD fabrication. Optical evolution of the as-synthesized QD's has also been detected by UV-Vis absorption spectroscopy.

4.1.2.1 UV-Visible Investigation and Particle Size Calculation

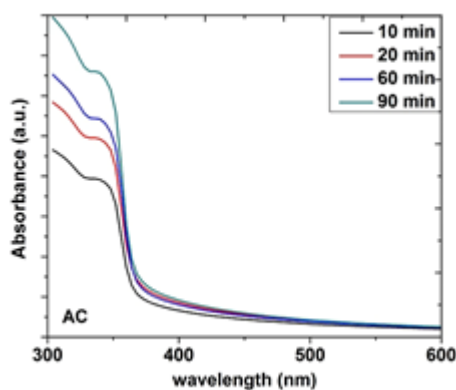


Figure 38 UV Visible evolution of Acetate@ZnO QD's.

Optical properties of the as-synthesized ZnO QD's have been presented in Figure 38. According to the Meulenkamp equation quantum dot size can be calculated from the UV visible absorption data (Table 2).

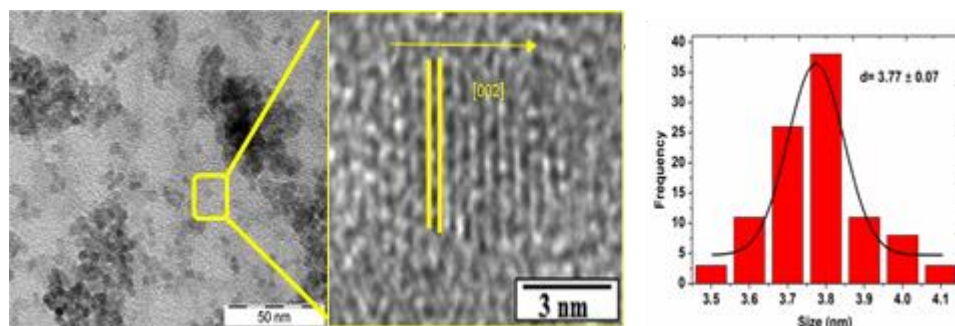


Figure 39 a) TEM investigation of Acetate@ZnO QD's b) QD size distribution.

Theoretical calculations showed that, since UV absorption maxima does not remarkably change during the reflux and UV absorption measurement QD's size has been listed between as 4,0 and 5,0 nm. But after TEM investigation of the Acetate@ZnO QD's, analysis has revealed that quantum dot size was actually varying from 3,0-4,0 nm and exactly 3,77 in this case.(Figure 39). HR-TEM investigation showed a clear wuertzite type crystal structure which elongates through [002] direction. By HR-TEM analysis we could reveal that the d–d spacing of Acetate@ZnO QD's is 0.26 nm.

4.1.2.2 Photoluminescence Properties and Visible Light Emission

Expectedly swift synthesis and visible light emission of Acetate@ZnO QD's exhibits conventional characteristics of mentioned quantum dot properties.

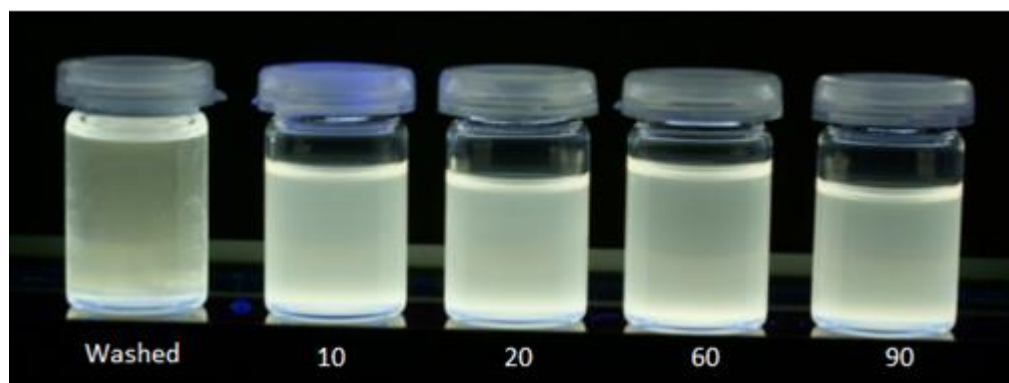


Figure 40 Visible green emission from the Acetate@ZnO QD's (aliquot times have been written in minutes below the solution).

If quantum dot solutions are prepared in alcoholic medium at room temperature conditions, they appear like slightly milky transparent solutions. However if they are illuminated with a commercial UV source ($\lambda = 354$ nm) effects of the quantum confinement can be seen easily (Figure 40). PL spectra of the as-synthesized quantum dots shows 2 main peaks (Figure 41). One which is placed on the $\lambda_{em} = 365-370$ nm arises from the band gap emission of the ZnO quantum

4 Results and Discussion

dots and lies within the UV region. Additionally its peak intensity is lower than the visible light emission peak. Second emission which appears first at $\lambda_{em}=546$ nm is the visible light emission which is due to the oxygen defects of the quantum dot surface structure.

In addition to the oxygen defects, there are many proposed sources for the visible light emission of the ZnO quantum dots but this feature generally attributed to the oxygen defects.

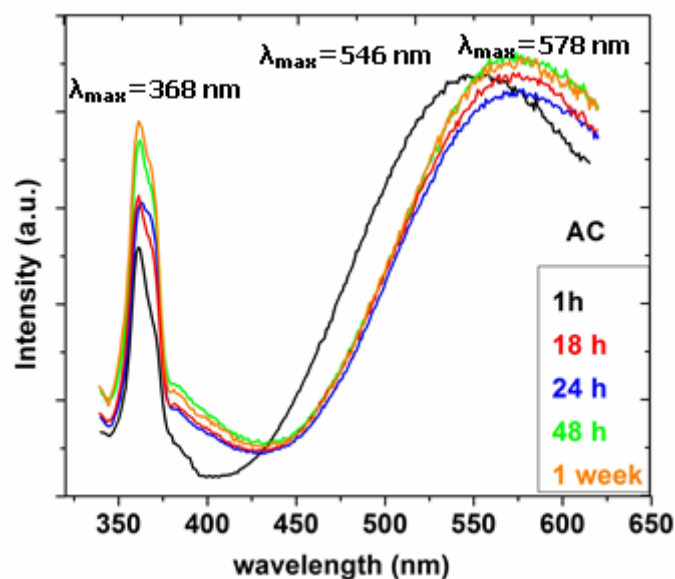


Figure 41 PL spectra for the QD's before and after storage.

As-synthesized and washed Acetate@ZnO QD's which are showing green emission are not effectively protected from the particle interaction and therefore quantum dots start to agglomerate.

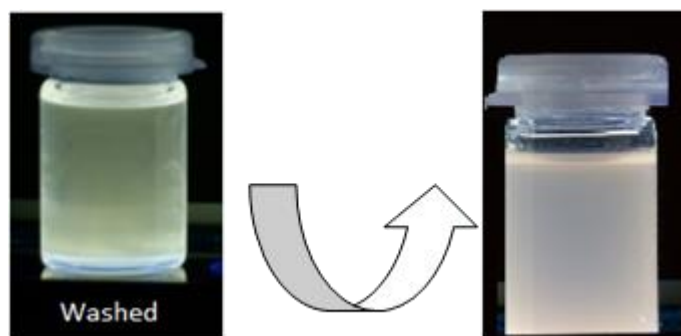


Figure 42 Green to orange light shift for Acetate@ZnO QD's.

Interestingly also quantum dots changed their visible light emission from green to orange ($\lambda_{em}=580-610$ nm) after storage as evidenced (Figure 42). Additionally TEM images after storage unveiled the morphological differences of the

Acetate@ZnO QD's since agglomerated quantum dots (Figure 43) are seen as monolayers which effects the visible light emission. Due to the Ostwald ripening, smaller quantum dots gets attached to the bigger ones and defect oriented visible light peak shifts toward red region.

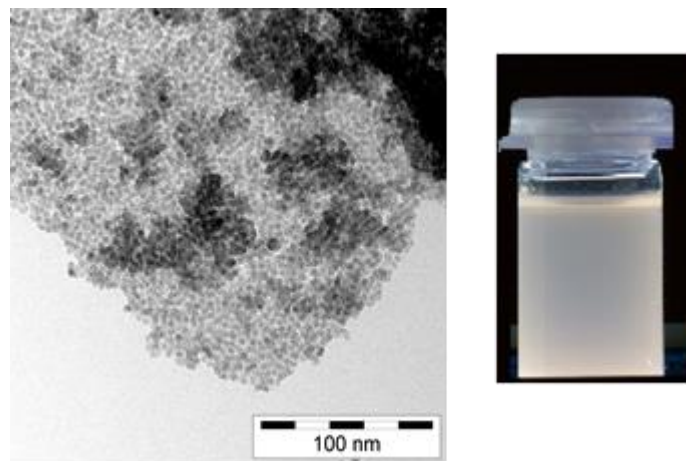


Figure 43 Acetate@ZnO QD agglomeration and monolayer formation.

Obtained characteristic properties provided a platform to obtain a deeper control on the surface defect modulation for the surface controlled growth of ZnO QD's.

4.1.3 Cysteine Molecule as Surface Controlling Ligand for ZnO QD's

Inadequate stability of the common Acetate@ZnO QD's requires surface modulation for controlling the defects on the QD surface. For this aim, appropriate solvents can be used as a quencher after the nucleation burst by using their strong adsorption properties onto the different formed structures. Additionally, micelle formation for the control of the particle/polymer interface or injection of suitable capping ligands, even wide range biomolecules like glutamic acid^[102] and histidine^[103] can be used to control the particle growth of the ZnO QD's. If we change the surface controlling agent we can also functionalize the quantum dots surface and add an additional chemical feature. Change in the capping ligand or polymer leads to anisotropic or hierarchical structures such as elongated prisms or flowerlike aggregates, respectively. By taking these coordinative effects altogether, the use of capping ligands possessing high chemical affinity toward ZnO due to the hard-soft acid base rule or interfacial chelation has proved to be effective method in exemplifying an arrested growth of nanoparticles as well as to control the hierarchy and orientation of the nanocrystals. For this aim we have used cysteine which is a biologically important molecule containing amino, thiol, and carboxylic functional groups and also capable of undergoing specific reactions with the

metal centers (Figure 44). Investigation of cysteine capping on the synthesis of ZnO QDs resulted many different concepts^[104].

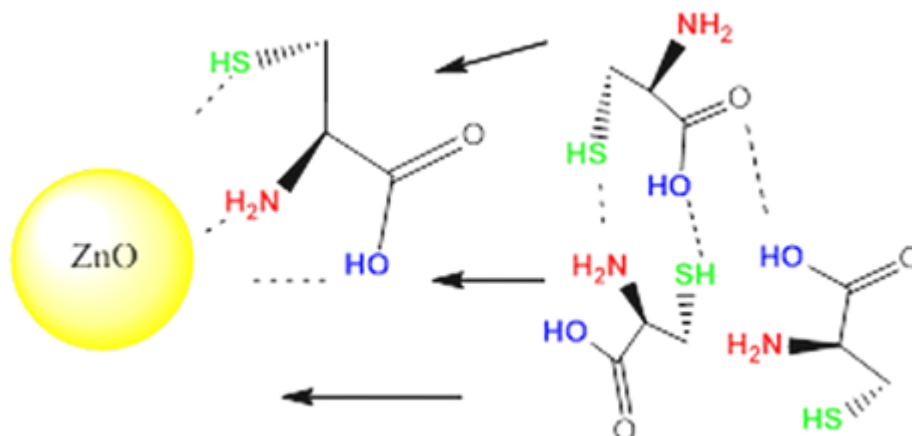


Figure 44 Cysteine-functionalized ZnO QDs and intermolecular interaction among surface-bound and free cysteine ligands.

In order to compare the differences with the common acetate modification we have varied the cysteine amount systematically for controlling the emission and size evolution. Therefore 2.5, 5.0, and 7.5 mmol cysteine introduced into the common acetate directed system and samples have been labeled as C1, C2, and C3, respectively. By keeping the Acetate@ZnO QD's as C0. The diluted reaction mixture was refluxed for 90 min at 55 °C under nitrogen atmosphere, whereby aliquots were collected at different time intervals (10, 30, 60, and 90 min) to record the particle size evolution by optical absorption spectra.

4.1.3.1 Optical Evolution and Band Gap Modulation of ZnO QD Formation under Cysteine Control

As mentioned before electronic transition from valence to conduction band determines the shape of the UV absorption and therefore the confinement effects observed in nanoscopic particles caused an enlargement of the band gap (E_g).

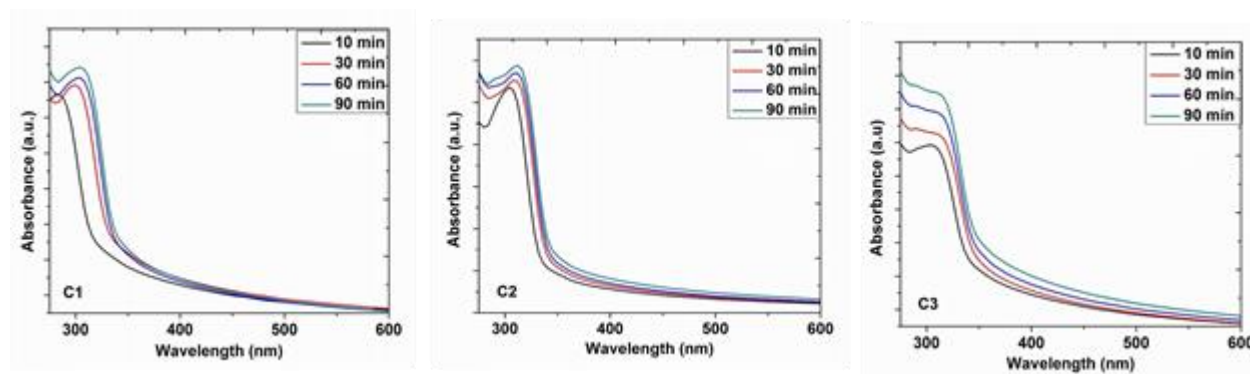


Figure 45 UV visible Evolution of the Cysteine @ ZnO QD's.

4 Results and Discussion

For theoretical size calculation, the half of the excitonic peak width from the absorption spectra of ZnO suspensions at various reaction times was also measured and substituted in the Meulenkamp equation to calculate the average E_g values. This calculation have been done for different amount of cysteine modified ZnO QD's and compared with Acetate@ZnO's. If we compare UV-visible absorbance spectra of Acetate@ZnO and Cysteine@ZnO (Figure 45) synthesized under different reaction conditions at various reflux time periods we can simply calculate the band gaps by the following equation:

$$\alpha hv = C (hv - E_g) \text{ Eq 13}$$

where where α is the absorption coefficient, C is a constant, $h\nu$ is the photon energy in eV, and E_g is the band gap energy of the semiconductor. The calculated band gap energies (Figure 46) showed that increasing amount of cysteine decreased the band gap energy of QDs.

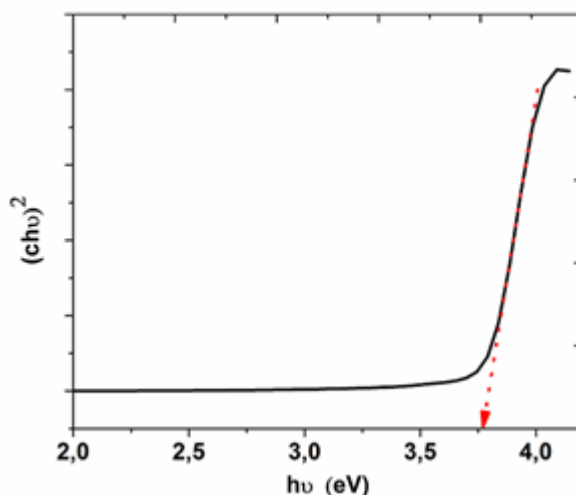


Figure 46 Band gap calculation of the ZnO quantum dot.

It is known that by using a suitable capping agent like cysteine, it is possible to control and manipulate coarsening effects in nanoparticles. It was observed that the particle size increased upon increasing the cysteine amount (Table 2). In solution, surface complexation or solution coordination takes place for chelation of zinc species in $Zn(OH)_4$. Under the basic conditions, cysteine plays a major role for the formation of ZnO QDs. Apparently, thiol groups cause the zinc release or acceleration of the release process to form zinc–cysteine complexes.

Table 2 Band gap variation of growing Cysteine@ZnO QD's

Time(min)	C 1(eV)	C 2(eV)	C 3(eV)	Ac(eV)
10	3.81	3.79	3.67	3.44
30/20	3.78	3.72	3.62	3.44
60	3.74	3.68	3.60	3.44
90	3.72	3.67	3.59	3.43

Therefore increasing the cysteine amount, the zinc concentration is relatively decreased in the medium due to the formation of soluble zinc–cysteine complexes.

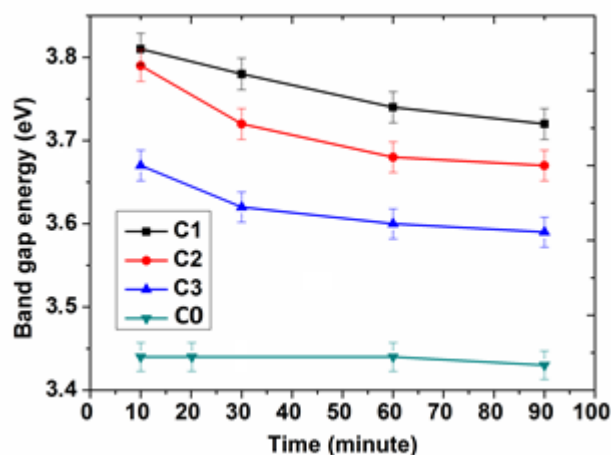
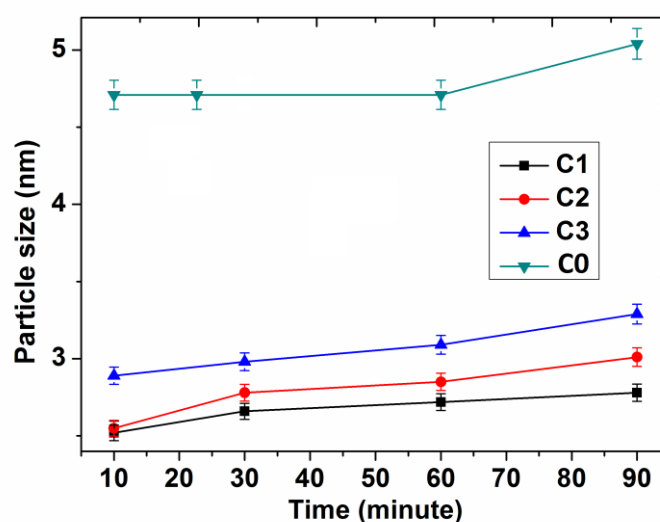


Figure 47 Band gap variation of Cysteine@ZnO QD's.

Calculated band gap and particle size values have been shown in Figure 47, Figure 48 Table 2. As for $Zn(OH)_2$, it has lower thermodynamic stability than ZnO and this intermediate transforms into ZnO spontaneously. When the concentration of the zinc hydroxide species in the medium exceeds a critical value, ZnO begins to self nucleate. However by systematic cysteine complexation, zinc concentration is decreased, which favors aggregation of ZnO nanocrystals to form larger particles.

Table 3 Time dependent particles size variation according to UV visible investigation

Time (min)	AC (nm)	C1 (nm)	C2 (nm)	C3 (nm)
10	4.71	2.52	2.55	2.89
20/30	4.71	2.66	2.78	2.98
60	4.71	2.72	2.85	3.09
90	5.04	2.78	3.01	3.29

**Figure 48** Particle size evolution for the formation of Cysteine@ZnO QD's.

4.1.3.2 Real Crystal Size, Morphology and Surface Properties of Cystein@ZnO QD's

TEM investigation of the Cystein@ZnO QD's provided a real time understanding on the cysteine capped quantum dots. Intermolecular interaction among surface-attached cysteine molecules evidently induced particle agglomeration with particle size gradually increasing upon increasing cysteine concentration (Figure 49) (C1: 2.5 nm, C2: 2.8 nm, and C3: 3.1 nm). However, the common Acetate@ZnO QD's prepared under similar conditions displayed an average size of 3.8 nm, which indicates that particle growth is suppressed due to the presence of cysteine as a surface chelating agent. XRD patterns of Acetate@ZnO and Cysteine@ZnO nO QDs at different cysteine concentrations showed wurtzite structure in both cases (JCPDS Card No.36-1451) (Figure 50). As in Acetate@ZnO no other crystalline impurities or residues were for

4 Results and Discussion

Cysteine@ZnO while the peak broadenings can again be attributed to the very small grain size (<5 nm). Conventional (C0) and cysteine-functionalized ZnO QDs (C1–C3). Sharpness of the diffraction patterns are slightly different and Acetate@ZnO shows better patterns.

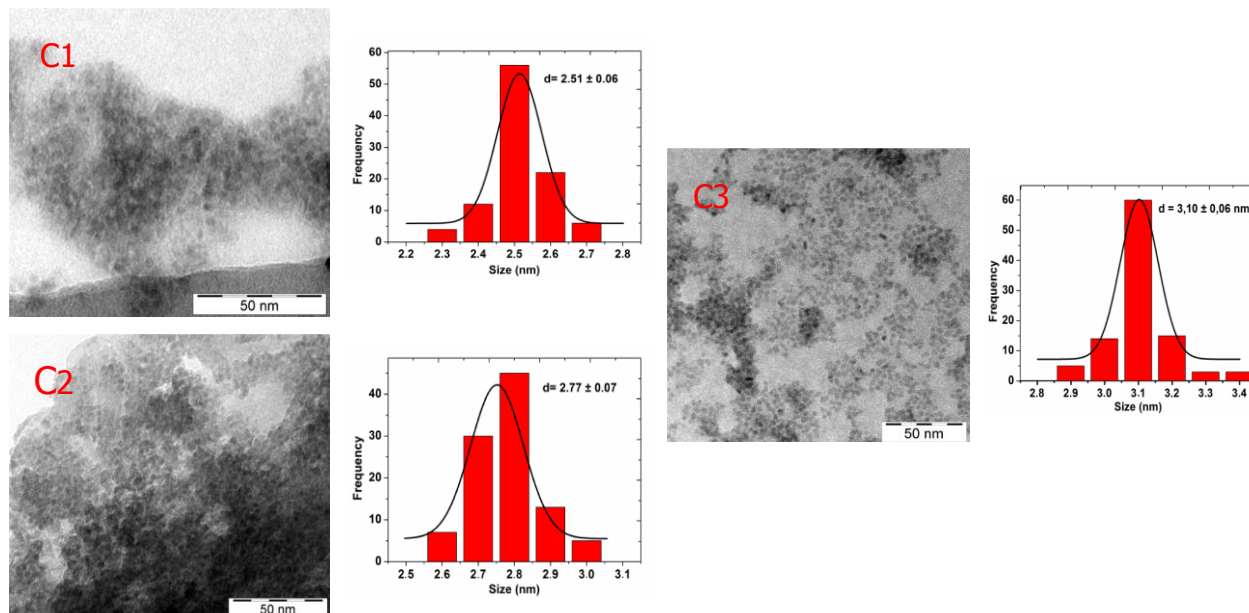


Figure 49 TEM images and calculated particle size distribution of Cysteine@ZnO QD's.

As presented above, Transmission electron microscopy (TEM) revealed spherical grains with a predominantly narrow size distribution HR-TEM analysis revealed that again ZnO QDs have the growth direction as [002] in with a d - d spacing of 0.26 nm that corresponds to ZnO.

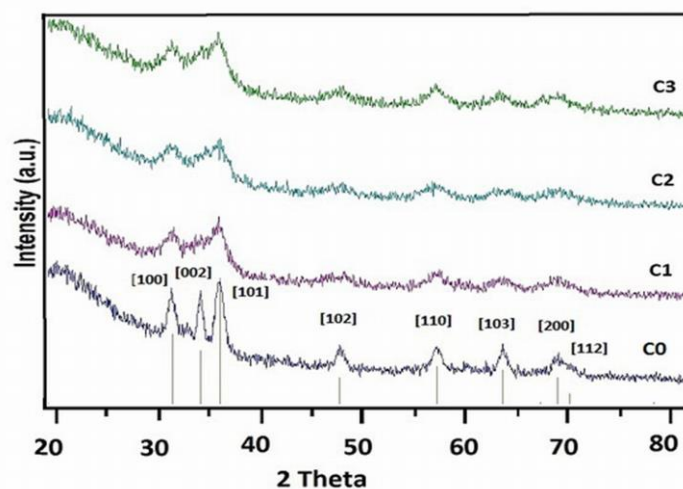


Figure 50 XRD patterns of C1,C2,C3 and Acetate@ZnO QD's.

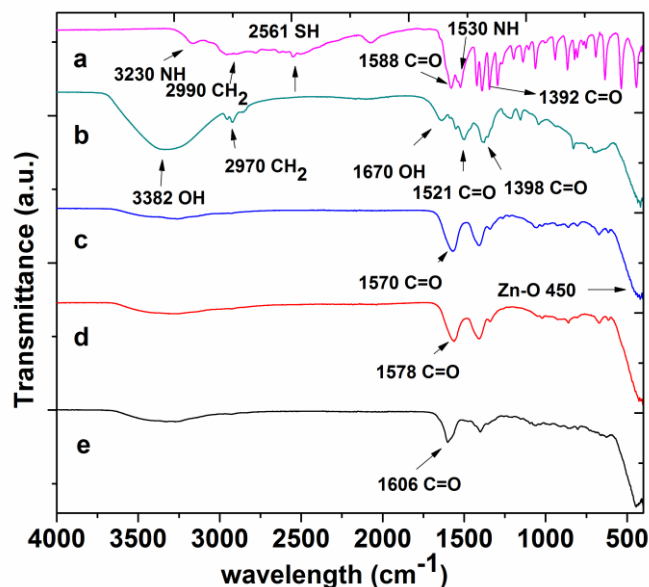


Figure 51 FTIR spectra of (a) free cysteine, (b) C0, (c) C3, (d) C2, and (e) C1 samples.

In order to analyse the surface characteristics of the Cysteine@ZnO QD's Fourier Transform Infrared (FTIR) spectra (Figure 51) has been used. Starting from pure cysteine, Acetate@ZnO QD's and Cystein@ZnO QD's have been analysed accordingly. Cysteine-capped QDs exhibited zwitterionic (internal salts) structure and showed the spectral characteristics of both carboxylic and primary amine groups (Fig. 51 FTIR). In the case of free cysteine, peaks at 1588 and 1392 cm^{-1} correspond to the asymmetric and symmetric carbonyl stretching. The peak at 1525 cm^{-1} is due to N–H bending, whereas a broad band of N–H stretching is observed in the range 3000–3500 cm^{-1} together with the acidic function. These results are in good agreement with the reported FTIR spectra of a general amino acid. A shift in the position of COO^- and N–H stretching is likely due to a change in their dipole moment when cysteine binds to metal or metal oxide surface with high electron density. Consequently, the large band from 2300 to 3300 cm^{-1} has shifted to higher wave numbers. Zn–O band at 450–460 cm^{-1} is evident in all ZnO QDs (C0, C1, C2, and C3), although the amount of the cysteine caused a systematic shift as seen in Fig. 7. The carbonyl stretching peak is at 1606 cm^{-1} (C1), 1578 cm^{-1} (C2), and 1570 cm^{-1} (C3) showing possible changes in the carbonyl asymmetric and symmetric stretching with different loading of cysteine amount.

4.1.3.3 PL Features and Stability of Cysteine Modified ZnO QD's

Photoluminescence measurements on Cystein@ZnO QD's dispersed in ethanol showed visible yellow luminescence. It has been found that there is no huge effect of cysteine concentration on the visible light emission peak position (Figure 52 and Figure 53). More important thing here is the stability of covered ZnO QD surface. As presented before, visible emission from conventional Acetate@ZnO QDs showed a shift toward longer wave lengths due to the Ostwald ripening and particle growth whereas the visible emission color of C3 remained unchanged upon storage for a week (Figure 54). As in Acetate@ZnO QD's emission spectra of the quantum dots have 2 different emission peaks.

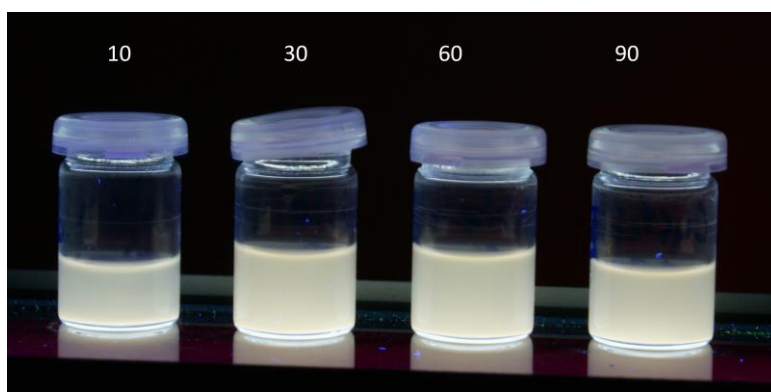


Figure 52 Cysteine (C1) modified ZnO QD's visible light emission.

First one represents the band gap emission and the second one represents the surface defect emission of the ZnO QD's. The observed visible luminescence in ZnO QDs evident as a broad band with maximum between 2.20 and 2.10 eV supported that it possibly originates from the native oxygen defects, which their synthesis and characterization have attracted a reasonable interest by scientists,

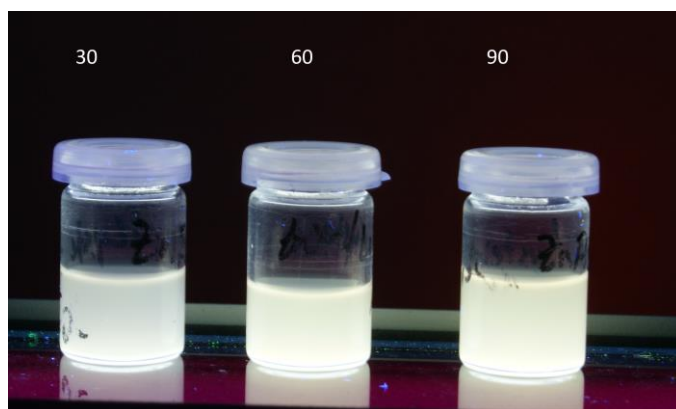


Figure 53 Photoluminescence feature of C2 QD's.

4 Results and Discussion

can be controlled by surface modification. The emission in the UV region for both cysteine-modified and conventional ZnO QDs was attributed to the recombination of trapped shallow charge carriers (exciton emission).

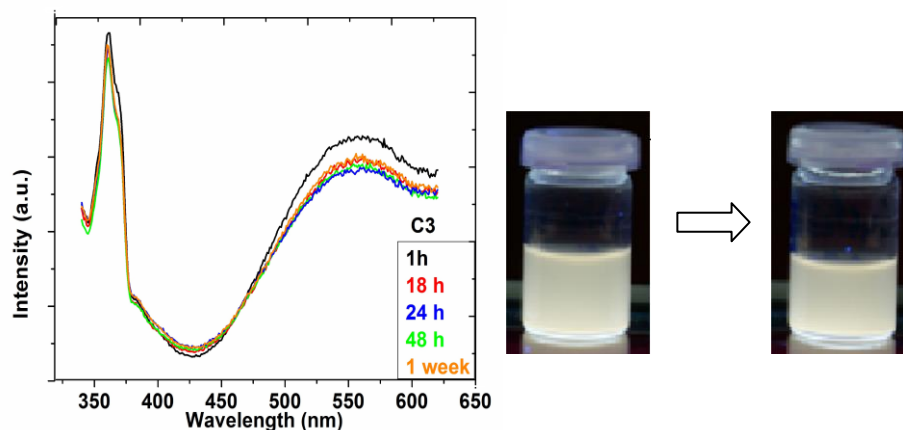


Figure 54 Photoluminescence stability of Cysteine@ZnO QD's, before (left solution) and after (right solution) 1 week (C3).

For cysteine-modified ZnO QDs, the intensity of UV and visible emission peaks decreased slightly over a period of 18 h, but the peak position remained unchanged for more than a week supporting their colloidal stability. Stability of the ZnO QD's provide us many positive feedbacks like long term use, unchanged peak position and known surface character for the further reactions. Due to the highly stable nature of the cysteine capped ZnO quantum dots it is possible to use them as a cell marker by introducing these quantum dots into the cell available medium. By observing the time resolved photoluminescence spectra of the C3 we have detected the efficiency of the radiative recombination. The photoluminescence decay spectra of the C3 with exponential fits were given in Figure 55. For the detection of lifetime sample was recorded at 375 nm excitation wavelength at room temperature and lifetime of the sample was calculated by using specific fit-software (Pico Quant Fit) and analysed.

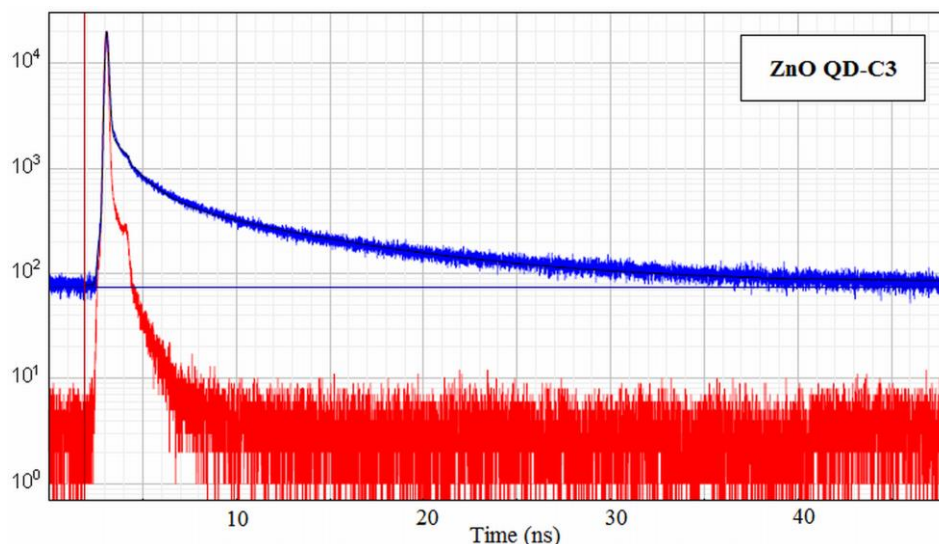


Figure 55 Fluorescence lifetime and automatic correction of cysteine capped ZnO QD's (C3)

Analysis has been done according to the equation below;

$$I(t) = \sum_{i=1}^n a_i e^{-t/\tau_i} \quad \text{Eq 14}$$

where i is the number of exponentials and τ_i and a_i are the lifetime and the preexponential factor for each component. Calculated average lifetime has been found as 6 nanoseconds. Automatic correction of the fluorescence lifetime has also been presented.

Another additional property of the synthesized quantum dots are their zwitterionic character. Cysteine-functionalized zwitterionic ZnO QDs exhibiting interesting optical absorption behavior in the visible range and extraordinary colloidal stability over a wide pH range due to the zwitterionic nature of the surface. The stability of the optical emission in cysteine@ZnO nanoparticles was attributed to the chemical coordination of the ligands to Zn centers that concomitantly reduce the numerical density of oxygen defects on or near the surface. In addition, the presence of a sterically compact hydrophilic (thiol) shell can be detected by EDX spectroscopy as presented (Figure 56). To the best of our knowledge, this is the first report on single amino acid coated ZnO QD's, which in view of their excellent solubility are suitable for investigating cell-nanoparticle interactions.

4 Results and Discussion

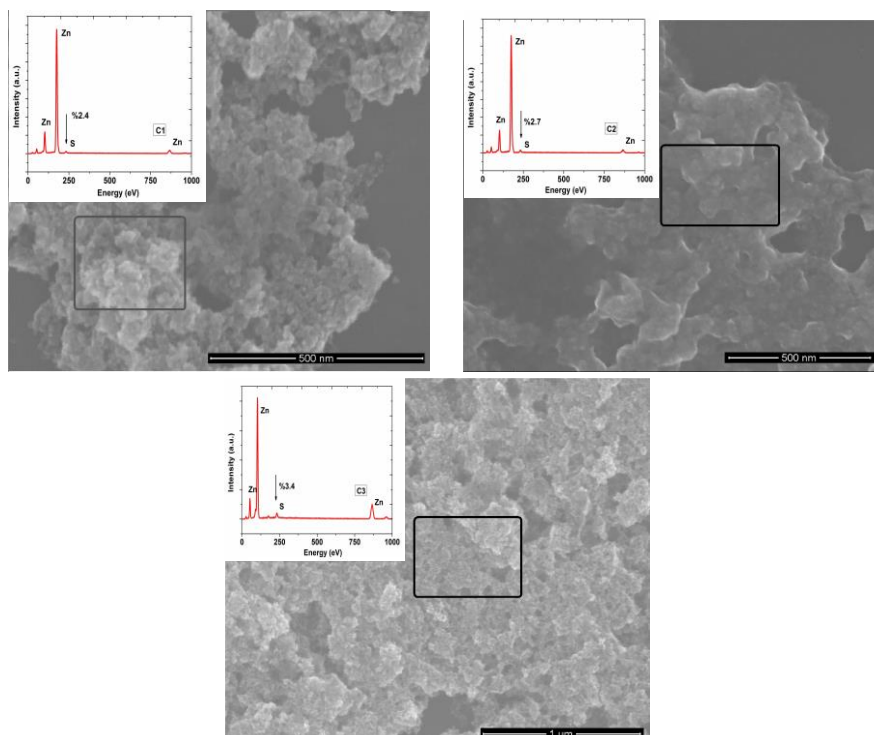


Figure 56 EDX analysis and SEM images of the C1, C2 and C3.

Elemental analysis measurement revealed an increasing amount of cysteine immobilization due to the multilayer adsorption on the ZnO QD's. Cystein adsorption on the surface of the ZnO QD's causes interparticle interaction and due to this interaction, multilayers of the cysteine molecules are seen. EDX analysis reveal this increasing amount of cysteine level with their morphological structure as shown in the SEM images.

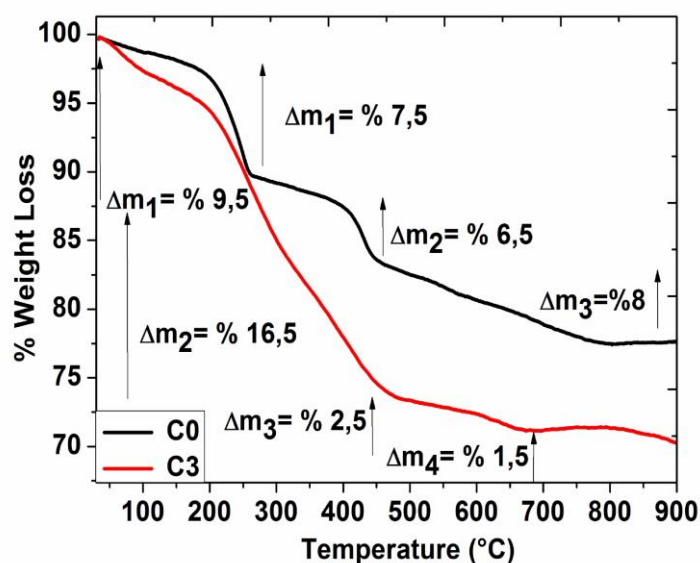


Figure 57 TGA investigation of Acetate@ZnO and C3.

4 Results and Discussion

Another additional information about the surface character of the Cystein@ZnO QD's is their thermal decomposition profiles. Since increasing amount of cysteine would increase the thermal weight loss this can be also another evidence for the cysteine protection. Figure 57 and Figure 58 show TG/DTA analysis of the Acetate@ZnO and Cystein@ZnO QD's. For the conventional Acetate@ZnO, in the first (until 250 °C) and second steps (250–432 °C), volatile components, adsorbed humidity, and organic groups were removed which is 73% of the total removed amount. After this, event decomposition was terminated at around 800 °C. By analyzing the pure cysteine decomposition profile (Figure 54), it was found that the decomposition of cysteine occurred in a single step.

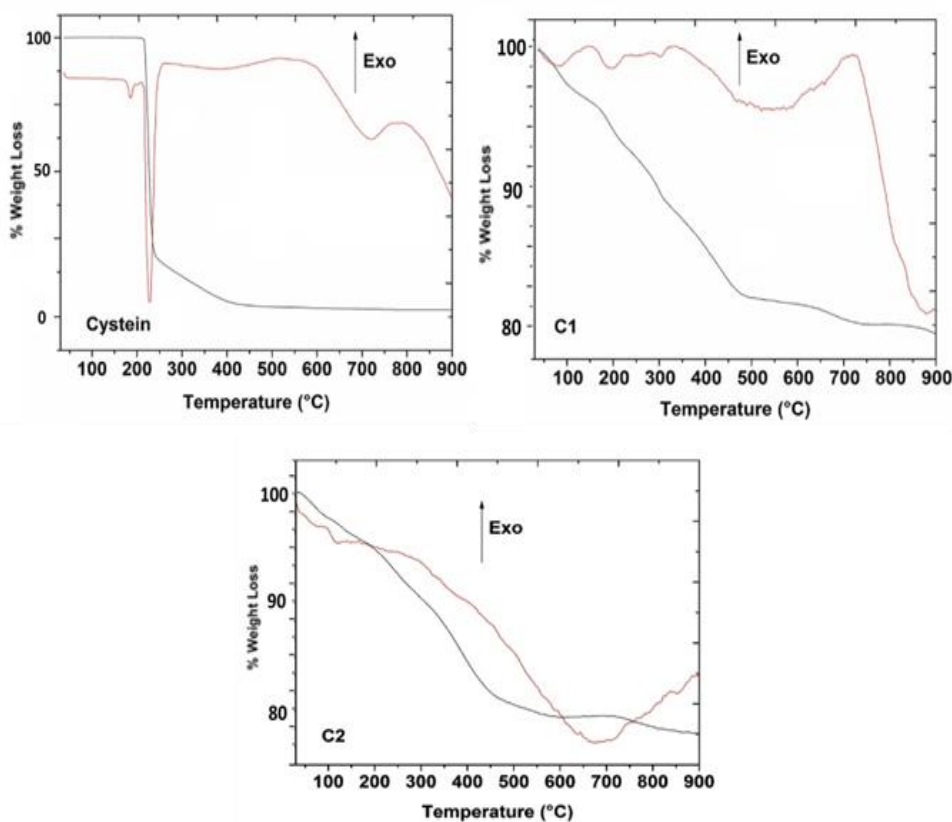


Figure 58 TG-DTA analysis of pure cysteine, C1 and C2.

Since it is an organic molecule, till 230 °C, organic groups and adsorbed humidity were removed, whereas the complete decomposition ended at 450 °C. Increased amount of surface-bound cysteine and its removal during the differential thermogravimetric analysis was observed in C1:10% , C2:12% , C3:16% in the given order. C1, C2, and C3 decomposed in four steps, whereby the first two steps can be attributed to the removal of adsorbed humidity and partial cysteine removal of the cysteine shell. With increasing cysteine,

decomposition accordingly increased (Fig. S3) (C1:10% C2:12% C3:16%). However, this process was accompanied with temperature shifts (290 °C for C1, 300 °C for C2, and 310 °C for C3) probably due to physisorbed layers of cysteine molecules. In the third step, chemisorbed cysteine molecules were removed until 450 °C and chemisorbed residual organic moieties were eliminated from the surface. Theoretically if a monolayer of the cysteine ligand is available on the smaller quantum dots surface, since its surface area is bigger, we would see a bigger weight loss. But analysis here shows that this concept is not completely valid here. Total weight loss increased from C1 to C3, which can be attributed to the higher concentration of immobilized cysteine molecules on the QDs and multilayered ligand adsorption.

4.1.3.4 Cysteine Triggered Self Assembly in the ZnO QD's

Owing to the zwitterionic character of immobilized cysteine molecules on the ZnO QD's, it is possible to modulate the surface charging by zeta potential (ζ) measurements which were conducted at different pH values (pH: 2–13) (Figure 59). The zeta potential of conventional ZnO QDs was found to decrease with increasing pH, however around pH . 6, an increase was observed that was attributed to the ion adsorption on ZnO QDs. Functional groups on the quantum dot surface causes a specific situation. Every kind of functional group like carboxy, thiol or amino groups and their distribution on the nanoparticle surface may contribute to the short range intermolecular interaction.

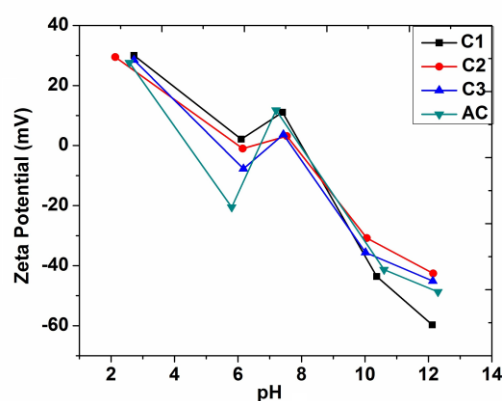


Figure 59 Zeta potential measurements for Acetate@ZnO and Cysteine@ZnO.

Among these interactions hydrogen bonding would be sufficient enough to bring nanoparticles together but not strong enough for a complete regular self assembly formation. Hence when the particles are close enough van der Waals interactions and dipole-dipole forces between them contribute to the final structure and form the spherical structures ranging from 150-200 nm. Cysteine

4 Results and Discussion

molecules on the QD surface therefore are bringing the nanoparticles together providing a self assembly in the ethanolic solutions. This self assembly formation (Figure 60) can also be defined by hydrodynamic measurements since hydrodynamic size (Figure 61) of the quantum dots have been increased into the values which are observable in SEM as presented above.

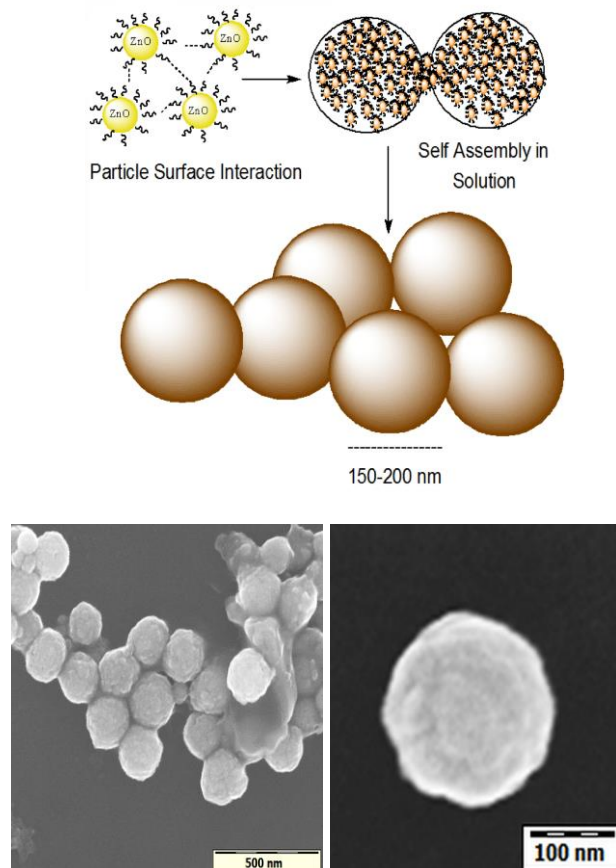


Figure 60 Assembly of ZnO QDs to form supra-structures and their hydrodynamical property observation with time.

As mentioned before, surface defect structure can be controlled by surface ligands and extra functional character of the ligands can favor different assembly nanostructures as presented above. Still the total control of the ZnO QD surface should be always accessible somehow that anytime when you need a quantum dot size, quantum dot functionality or quantum dot stability one only need to select the proper precursor conditions. For this reason oleate capped ZnO QD's and synthesis concept have been developed.

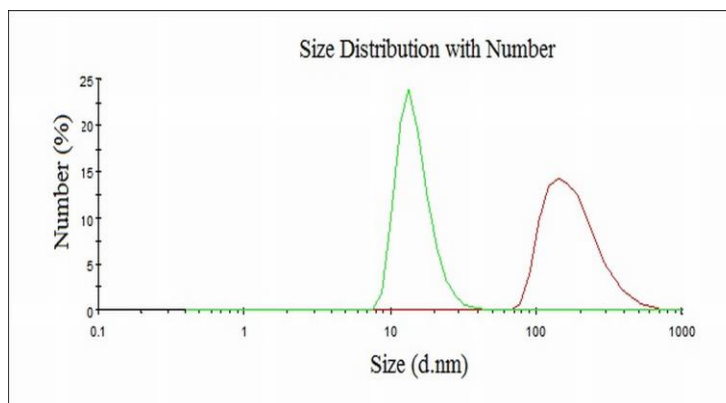


Figure 61 Hydrodynamic size variation before and after self assembly.

4.1.4 Ultrastable Oleate@ZnO QD's for Phase Transfer and Storage

In this section, ultrastable oleate capped, visible light emitting ZnO quantum dots (QD's) have been synthesized by a modified sol-gel method and their properties were examined for a fabrication of large amount ZnO QD synthesis. As explained before it is challenging to fabricate stable ZnO QD's due to the surface and agglomeration effects. We have modified sol-gel method to obtain Oleate@ZnO QD's and NMR investigation clearly revealed surface chelation with oleate ligand. Observed PL measurements with UV-Visible evolution curves showed fine control on the particle growth and profound steric effect of oleate groups. Since the behavior of oleate groups present on the surface of the synthesized quantum dots final properties have been changed. HR-TEM investigation with XRD results confirmed the crystalline and highly monodispersed ZnO QD's. Investigated ZnO QD's are easily controllable in the desired size range, visible light emission wavelength and extremely stable with bulky ligands providing surface defect control confirmed by NMR on the surface. This is a quite new method for large scale quantum dot synthesis. Synthesized ZnO QD's are suitable to be hydrophilic when oleate groups are substituted with desired hydrophilic ligand by phase transfer synthesis even after long time storage. Therefore, synthesized quantum dots can be stored long time and can be reactivated for the aqueous applications. This phase transfer method provides wide range applications for the visible light emitting ZnO QD's like ink-jet printing for nano-electronics, cell labelling or ZnO QD embedded light emitting hybrid nanocomposites for the required applications.

4.1.4.1 General and Swift Synthesis of Blue to Yellow Visible Light Emitting Oleate@ZnO QD's

Due to the size dependent photoluminescence properties of the ZnO nanomaterials, they attract significant interest in the last decade^[1]. As presented in previous section we have also attempted to develop a method for a general use and fabrication of ZnO QD's. Contrary to chalcogenide quantum dots, ZnO emission is less studied despite its easy to prepare conditions and low cost. By varying the surface character which indirectly means the oxygen vacancy control, it is possible to tune the emission properties of the ZnO nanoparticles. Generally for tuning the visible luminescence properties of ZnO in the conventional method, molar ratio of (LiOH/Zn) provides the most important parameter. Additionally many report have arised using different basic conditions but Li and OH method is more or less the essential. By changing the molar ratio we basically change the particle size of the ZnO QD's and visible luminescence properties as well. It is already known that radiative recombination of the conduction band electron/valence band hole and its direct association with the UV absorption points that ZnO UV emission is size dependent because of the nanoparticles quantum confinement which means a direct relationship with the emission. In this manner, oxygen vacancies (V_o), oxygen interstitials (O_i), zinc vacancies (V_{zn}) and zinc interstitials (Z_i) were assigned as responsible for the emission of the ZnO nanoparticles^[105-111]. In previous section, it has shown that cysteine provided a method for the control of these defects. Conventionally synthesized ZnO quantum dots by sol-gel method^[1] (e.g. acetate@ZnO) are tend to aggregate and gradually grow which leads to the red-shift in the fluorescence spectra. This has been already shown in the first part. It is known that room temperature conditions are suitable for Ostwald ripening and fluorescence shift. We therefore reporti a facile method for the synthesis, visible light emission tuning and ultrastable ZnO QD's.

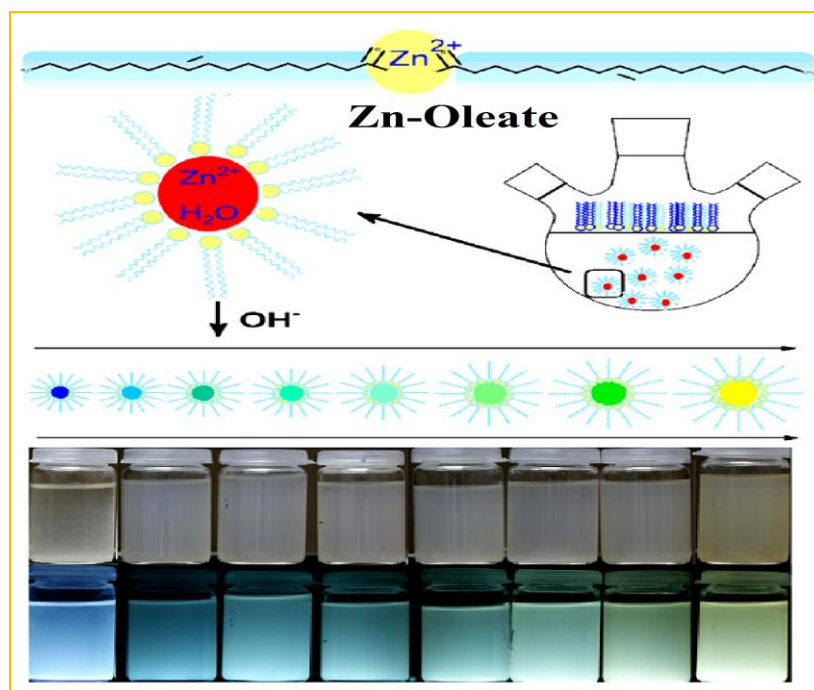


Figure 62 Synthesis of Oleate@ZnO QD's by modified sol-gel method.

Starting from well designed precursor Zn(oleate)_2 , ZnO QD's have been fabricated by modified sol-gel method. By increasing the reflux time and varying the (LiOH/Zn) ratio it is possible to modulate emission properties which means the direct defect control of the quantum dot surface. Fabrication of the ZnO QD's (Figure 62) produced oleate capped QD's which are capable of ultrastability for long time storing^[112]. For a general blue to yellow Oleate@ZnO QD's synthesis, prepared and analyzed molecular precursor Zn(Oleate)_2 has been dissolved in EtOH at 80 °C and calculated LiOH/MeOH mixture was added into this solution. This starts the formation of quantum dots immediately. Addition of the LiOH/MeOH mixture causes the fast formation of the oleate capped intermediate zinc precursors due to the higher concentration of the oleate molecules and a white milky colour was observed. At the early stages of the synthesis, oleate precursor in alcoholic mixture at 80 °C was completely transparent. For the complete control reactions have been done under the nitrogen atmosphere and solution mixture was refluxed for different time periods (10, 30, 60, 90 minutes and 7, 21, 30, 96 hours) at constant temperature. In this part we have rexlused 96 hours for observing the final effects and and this quantum dots etiquetted as ZnO-1 after cleaning and washing procedure.

Additionally here, we are presenting a new, so called "swift method" which composed of 90 minutes reflux of the precursor under the controlled temperature and (LiOH/Zn) ratio conditions for the fabrication. Additionally, conditions

4 Results and Discussion

provided by swift synthesis method eliminate the other competitive parameters which is bringing extra costs and parameters, like uncontrolled particle growth, inadequate stability which is leading to possible uncontrolled modulation in the visible light emission due to the aggregation have been overcome. In the swift synthesis, reflux time was limited until 90 minutes and temperature with Zn/LiOH ratio have been varied and for example at 55 °C, 5/7 Zn/LiOH ratio has been labeled ZnO-2, 1/2 Zn/LiOH ratio 55°C ZnO-3 and of course for comparison, common Acetate@ZnO QD's have been synthesized from $\text{Zn}(\text{CH}_3\text{COO})_2 \cdot \text{H}_2\text{O}$ in 5/7 Zn/LiOH ratio at 55 °C and etiquetted as ZnO-4.

UV Visible absorption spectra (Figure 63) for the ZnO-1 Oleate@ZnO QD's it is seen that, depending on the Zn/LiOH ratio, UV absorption shows an increasingly shifting peak position. This generally starts from 290 until 350 nm as presented. It is possible to calculate the band gap and particle size from the UV absorption plottings by a method as presented before. It is necessary to control the real size of the Oleate@ZnO

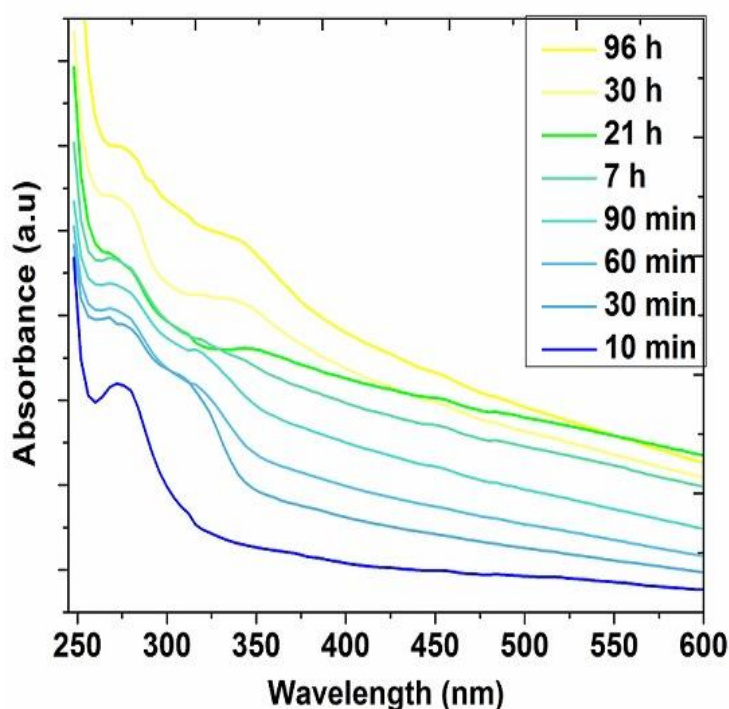


Figure 63 Evolution of the optical properties of Oleate@ ZnO QD's (ZnO-1).

QD's obtained from TEM investigation with theoretical calculations for comparison of results. According to these results we need to control the real size of the Oleate@ZnO QD's to control if these theoretical results are consistent with the results. Results showed that oleate groups provided an extra situation and

4 Results and Discussion

governed the surface defects. UV Visible and effective mass calculation results are slightly different and higher from real TEM and HR-TEM image measurements of the ZnO-1 QD's which were presented in Table 4. Selective area electron diffraction (SAED) pattern and QD's crystal structure (Figure 64) has been detected as wurtzite by measuring their d-spacing of [002] facets as 0,26 nm. Same observations have been confirmed in ZnO-2, ZnO-3 and ZnO-4 by measuring the same fringes.

Table 4 Size, band gap and emission maxima list for ZnO a) Obtained from UV-Vis absorption b) Obtained from effective mass model ($m_e = 0.26 m_0$, $m_h = 0.59 m_0$, m_0 is the free electron mass, $\epsilon = 8.5$, and $E_g \text{ bulk} = 3.3 \text{ eV}$) c) From UV-Vis absorption.

Synthesis Time	Size ^a (nm)	Size ^b (nm)	Band Gap ^c (eV)	Visible Maxima (eV)	UV Maxima (eV)
10 min	---	---		2.76	3.72
30 min	2.08	2.5	3.60	2.63	3.56
60 min	2.20	2.7	3.58	2.62	3.51
90 min	2.20	2.7	3.58	2.62	3.51
7 h	2.33	2.9	3.41	2.46	3.35
21 h	3.08	3.8	3.34	2.40	3.17
30 h	3.19	3.9	3.22	2.35	3.14
96 h	3.30	4.1	3.01	2.29	3.08

When we observe the emission characteristics of the quantum dots synthesized, there are some specific points which are recognized easily. First thing is that the visible emission intensity is always higher than UV intensity meaning that proximity of the surface defects are high which is not surprising due to the extremely small size of the ZnO quantum dots. Extremely small ZnO quantum dots provide big surface areas for the available oxygen defects which can be controlled by the surface ligands as shown with cystein here.

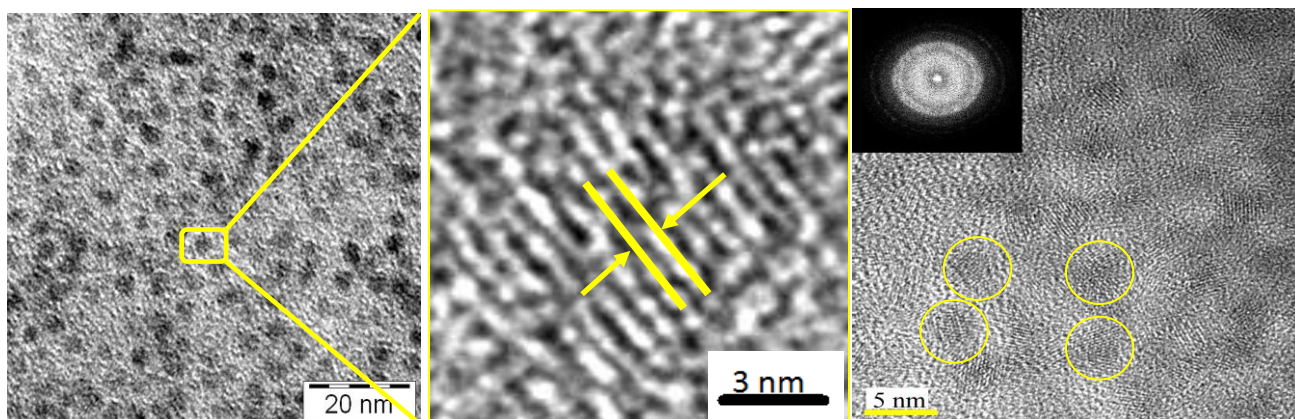


Figure 64 TEM, HR-TEM and SAED patterns of ZnO-1.

Secondly as the size of the quantum dots (Figure 65) gets bigger and bigger so that a shift is observed towards to higher wavelengths in the UV and visible light emission peak position.

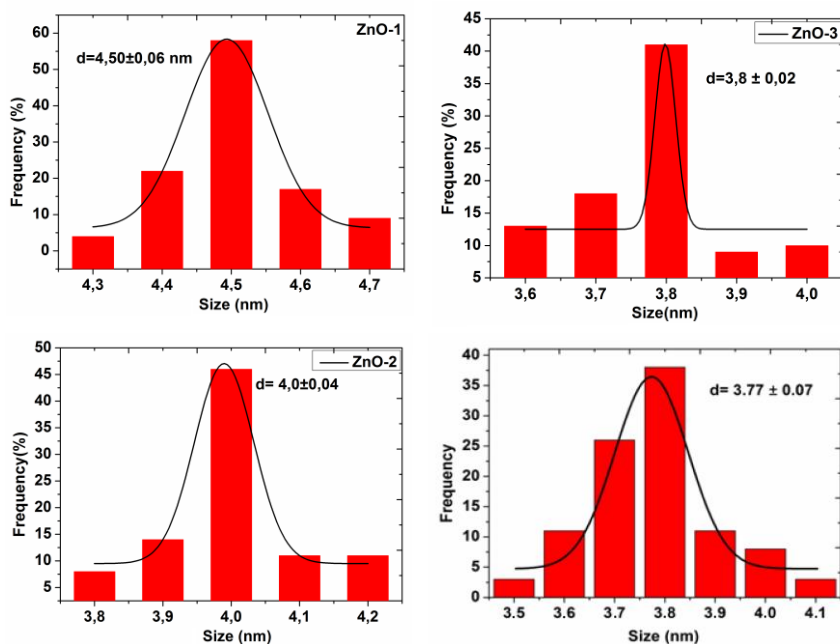


Figure 65 Size distributions in Oleate@ZnO nanoparticles.

This naturally arises from the quantum confinement of the Oleate@ZnO QD's. Therefore we can conclude that oleate groups serve an important performance of producing the ZnO QD's and inhibiting the grain growth. They control the emission properties, they control the agglomeration which will be showed and clarified later they control the morphology, they control the stability and

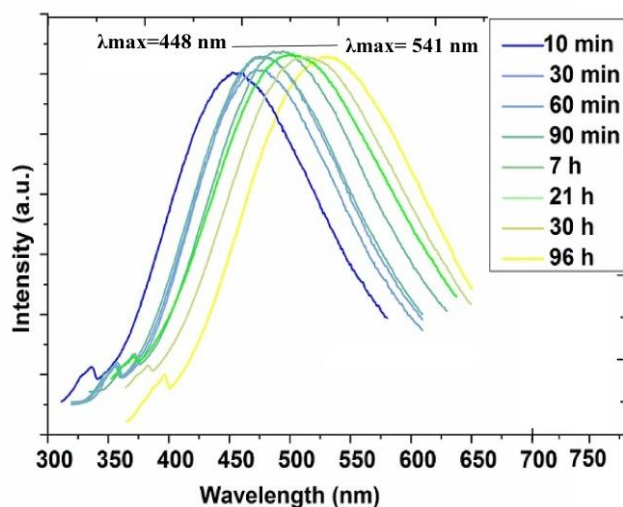


Figure 66 Visible light emission characteristics of ZnO-1.

particle size together shortly most fundamental characteristics of the ZnO quantum dots. Visible emission character of the Oleate@ZnO QD's are presented in Figure 66. According to these visible emission spectra it is obvious that ZnO-1 shows an amazing shift starting from about 440 nm until 545 nm. Ongoing reflux for the ZnO-1 provided that light shift will be more and more representing higher difference from the early stages of quantum dot growth. In addition to that if it is analyzed, other swift synthesis method results (Figure 67 and Figure 68) of the quantum dots which can see a clear blue emission at $\lambda_{\max}=442$ nm for the ZnO-2 which is apparently higher (almost 10 times) from the acetate capped ZnO QD's (emission $\lambda_{\max}=537$ nm) (ZnO-4) as observed by their UV-Visible and PL measurements. This revealed that visible emission intensity of acetate@ZnO is almost 2 times higher than its UV emission. It is widely known that UV emission arises from the band gap feature of the particle but visible emission has different sources[97]. Detailed TEM investigation shows that ZnO-4 is heavily agglomerated. It is widely known that high temperature show fast growth and therefore it was anticipated that decrease in temperature could provide a better control on the QD growth. Analysis results showed that, Zn(Oleate)₂ based quantum dots form

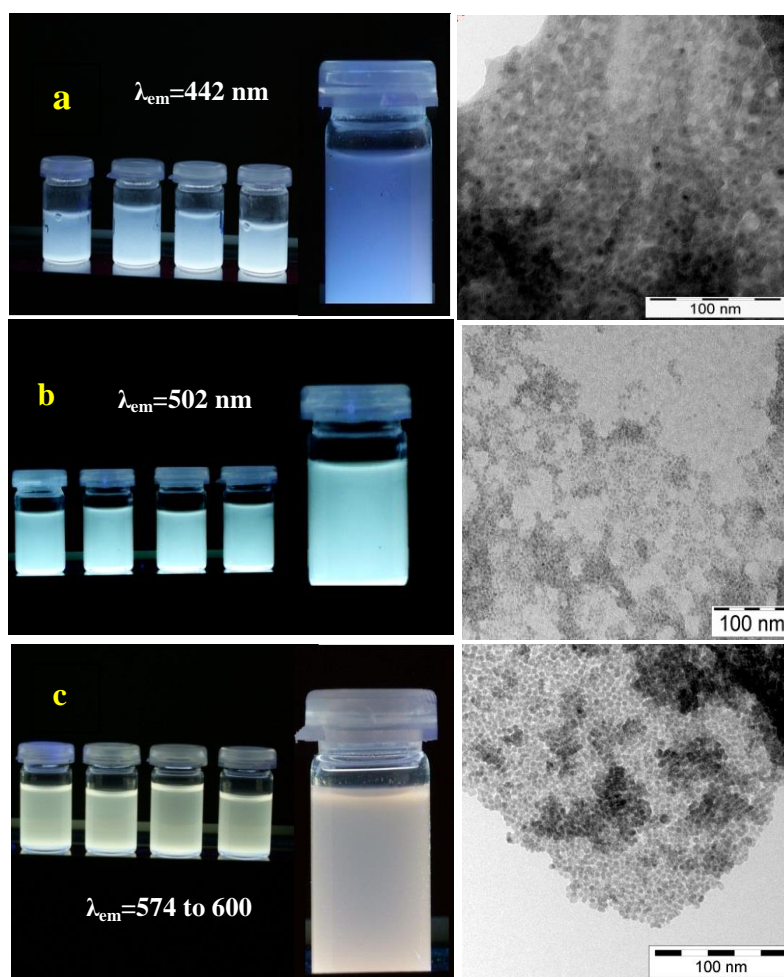


Figure 67 Visible emissions of a) ZnO-2, b) ZnO-3 and c) Acetate@ZnO.

core(ZnO)-shell(Oleate) like structure which was detected by NMR analysis (Figure 69, Figure 70 and Figure 72) and TEM images. TEM images clearly showed the core/shell morphology of the quantum dots with a homogeneous coverage and remarkably monodispersed quantum dot structures with same particle size. Calculated particle sizes and their statistical analysis have also supported this monodispersed distribution.

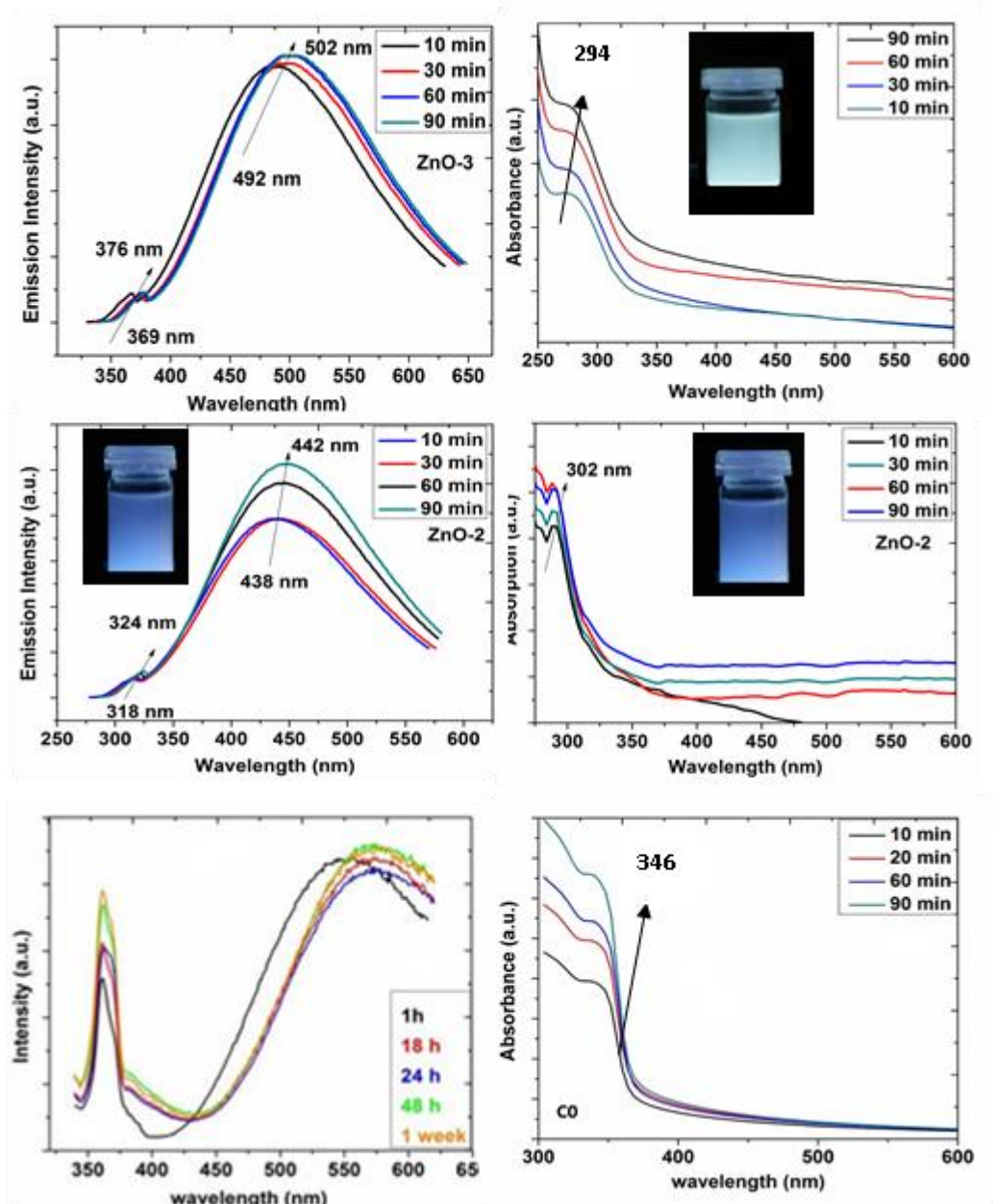


Figure 68 Optical properties of ZnO-2, ZnO-3 ve ZnO-4, Inset images represent visible emission colour of the quantum dots.

Especially TEM images revealed that Oleate@ZnO QD's have an organic shell which is around 3.5-4 nm in thickness averagely (Figure 73) . Interestingly, during this organic shell investigation FT-IR peaks (Figure 71) showed only two main peaks (at 1552 and 1402 cm^{-1}) which may arise from the regular orientation of oleate groups on the surface. Oleate groups also govern the emission process by controlling the surface defects. TEM and HR-TEM images of the ZnO-1 QD's have already presented in Figure 60 with selective area electron diffraction (SAED) pattern and QD's crystal structure have been

4 Results and Discussion

detected as wurtzite by measuring their d-spacing of [002] facets as 0,26 nm. Same observations have been confirmed in ZnO-2, ZnO-3 and ZnO-4 by measuring the same fringes (Figure 74).

4.1.4.2 NMR Measurements for Identification of Oleate Ligand

Identification of the oleate groups on the surface of the ZnO quantum dots have been conducted by FT-IR and NMR measurements which is essential for the ligand recognition^[113-114].

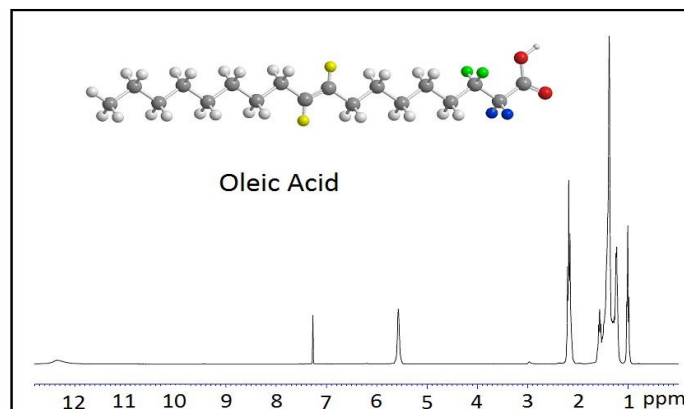


Figure 69 ^1H NMR for the $\text{Zn}(\text{Oleate})_2$ precursor.

Since $\text{Zn}(\text{Oleate})_2$ complex was used as starting material, complete analysis for the pure ligand (oleic acid) was necessary. Oleic acid contains simply a double bond on the carbon atoms number 9 and 10 which can be easily seen as singlet at around 4,5 ppm. Additionally carboxylic acid hydrogen appears at 12 ppm as a broad singlet. Hydrogen atoms which are close to carbonyl group can be differentiated due to the polar character of the carbonyl group and its environmental effects on the hydrogen atoms. Neighboring hydrogen atoms to carbonyl is at 2,1 ppm. This is quite a common behavior of these hydrogen atoms in the NMR characterizations.

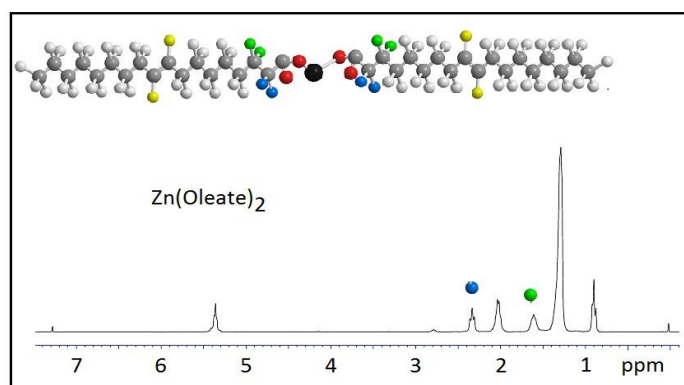


Figure 70 NMR investigation of ZnO quantum dot precursor $\text{Zn}(\text{Oleate})_2$.

4 Results and Discussion

Since all the other hydrogen atoms are more or less similarly effected from the environment they appear as a multiplet between 1 and 2 ppm as presented at Figure 69. NMR solvent CDCl_3 appears at 7,4 ppm. When this capping ligand oleic acid was transformed into the molecular precursor $\text{Zn}(\text{Oleate})_2$ a number of changes have been observed in the NMR spectra due to its coordination to the metal center. The resonance peak of the double bond protons ($\text{CH}=\text{CH}$) slightly shifted to 5,36 ppm as other resonance peaks of the methylene ($-\text{CH}_2$) protons. Methylene protons ($-\text{CH}_2$) which are adjacent to the carbonyl ($-\text{C}=\text{O}$) group appears at 2,34 ppm and β -methylene protons ($-\text{CH}_2$) shifted to the 1,60 ppm due to the ionic character of the zinc-carbonyl bonding. After synthesis, ^1H -NMR spectra of oleate capped ZnO QD's clearly shows the hydrophobic nature of the surface modification. In case of $\text{Oleate}@/\text{ZnO}$ QD's, oleate ligand has attached onto the surface which is detected by its asymmetric and symmetric carbonyl stretching peaks (Figure 71) at 1564 and 1405 cm^{-1} which is different those of free ligand.

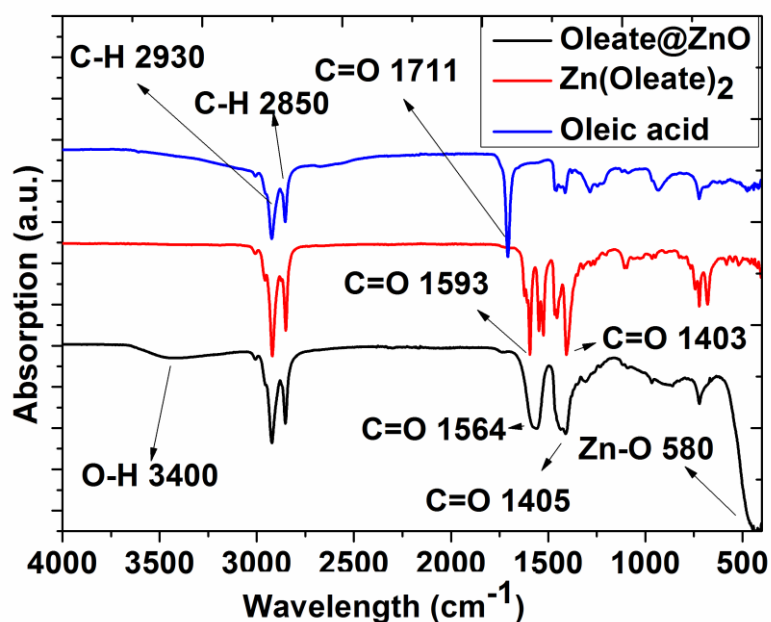


Figure 71 FT-IR observation of transformation of molecular precursor in the $\text{Oleate}@/\text{ZnO}$ QD.

In $\text{Oleate}@/\text{ZnO}$ QD's, oleate ligand has attached onto the surface which is detected by its asymmetric and symmetric carbonyl stretching peaks at 1564 and 1405 cm^{-1} which is different from molecular precursor itself. In the range starting from 585 till 470 cm^{-1} we have found it as reported for the $\text{Zn}(\text{CH}_3\text{COO})_2 \cdot 2\text{H}_2\text{O}$ ^[68].

4 Results and Discussion

Even though QD's purification process involves hexane washing, this spectra is a clear evidence that hexane treatment for the precipitation of the ZnO QD's leaves no residue that would appear at 0,85 and 1,23 ppm. The NMR spectrum of Oleate@ZnO QD's (Figure 72) exhibited broadening of the NMR peaks, due to interactions of protons which are adjacent to the carbonyl groups (especially α and β protons) with the ZnO QD's. The methylene protons ($-\text{CH}_2$) which are adjacent to the carbonyl ($-\text{C}=\text{O}$) group and β -methylene protons ($-\text{CH}_2$) almost disappeared because the proton motion of the oleate methylenes under the

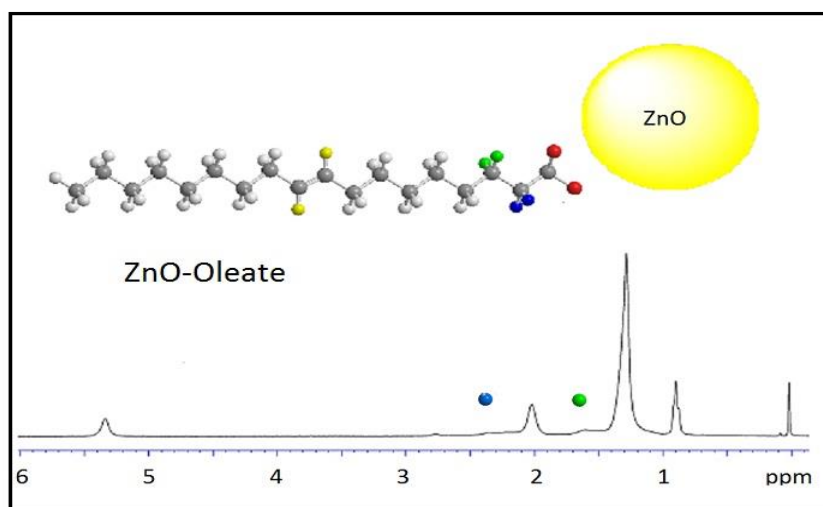


Figure 72 NMR investigation of Oleate@ZnO QD's.

effect of this local inhomogeneities is highly restricted. Since proton motion is restricted because of the attachment onto the ZnO QD's, effect of the magnetic field on these methylene proton relaxations become only slightly observable and causes disappearance or extreme broadening of the corresponding peaks. This is another clear evidence of oleate modification for ZnO QD's which revealed very interesting results when their visible emission characteristics were investigated. The highly bulky oleate groups provide surface coverage which is easily detected also by FT-IR spectroscopy.

4.1.4.3 Ultrastability and Agglomeration Free Feature of Oleate@ZnO QD's

As previously pointed out, results showed that, $\text{Zn}(\text{Oleate})_2$ based quantum dots form core(ZnO)-shell(Oleate) like structure, which was detected by NMR and FT-IR analysis and TEM images like below. Especially TEM images revealed that Oleate@ZnO QD's can form an organic shell which is around 3.5-4 nm in thickness.

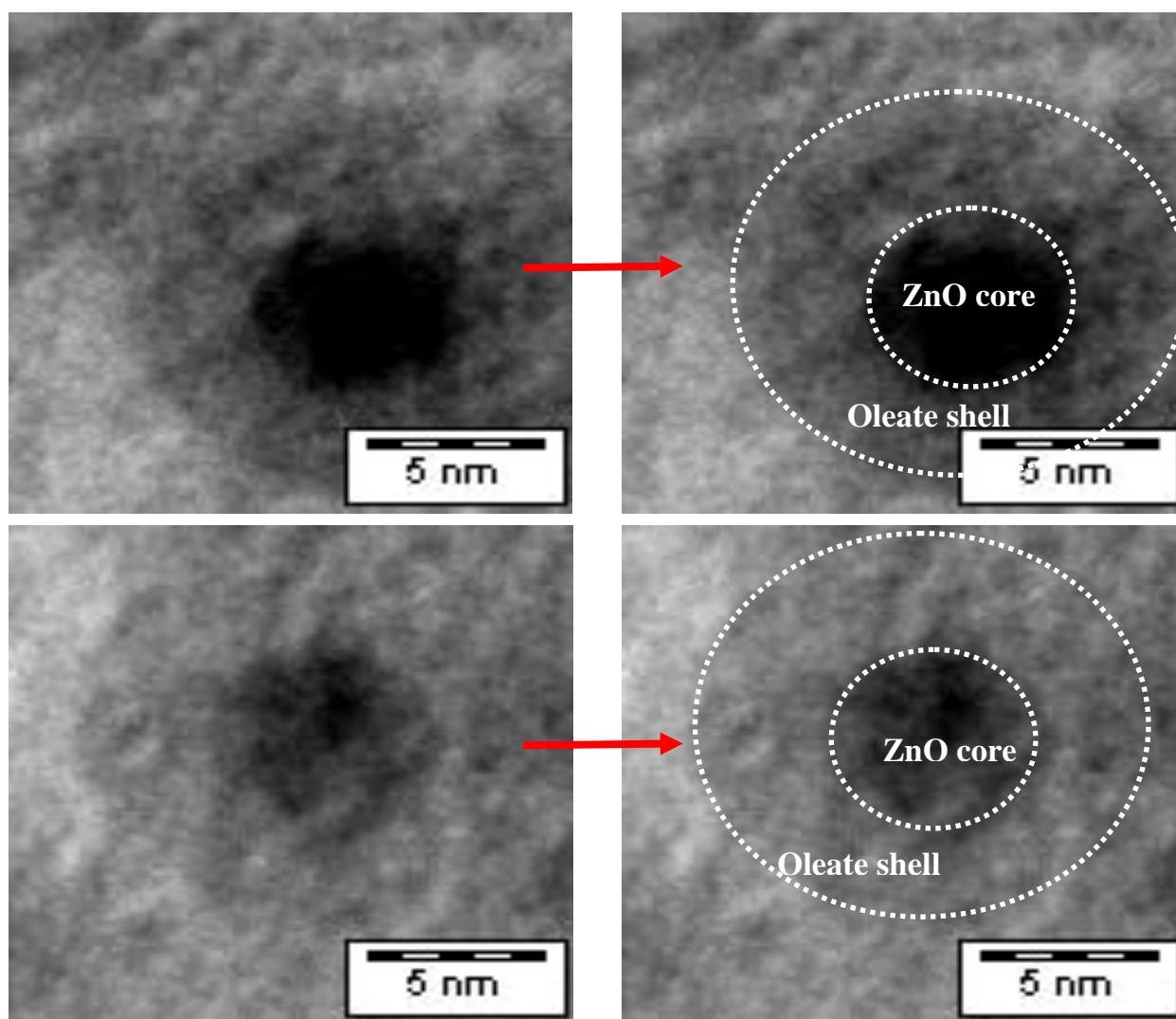


Figure 73 Core-shell structure of the Oleate@ZnO QD's for the synthesized Oleate@QD's.

Interestingly, during this organic shell investigation FT-IR peaks showed only two main peaks (at 1552 and 1402 cm^{-1}) which may arise from the regular orientation of oleate groups on the surface as discussed before. TEM images clearly showed that there is a lighter coverage (**Figure 73**) on the ZnO quantum dots (**Figure 74**). Since NMR and FT-IR investigations already proved the oleate availability, this deposition on the quantum dot surface provide amazing stability to the ZnO QD's. Generally oleate groups are considered as slightly weak ligand for the protection of the surface but due to the concentration and careful reaction conditions a new kind of protection was achieved. This protection provides an amazing stability and agglomeration free Oleate@ZnO QD's. Inadequate protection of the ZnO surfaces is detrimental for the optical properties since proximal surface defects are not protected. Since defects

4 Results and Discussion

gradually disappear, PL efficiency of the quantum dots disappears at the same time. Core shell structure of the Oleate@ZnO QD's was deeper by analyzing their ligand removal features. Since oleate is a carboxylic acid attached to the surface the metal oxide structure we can substitute or remove this protection for example by heating or phase transfer reactions. Figure 71 reveals the TEM result of the heated Oleate@ZnO QD's. As expected at 300 °C oleate groups have been removed.

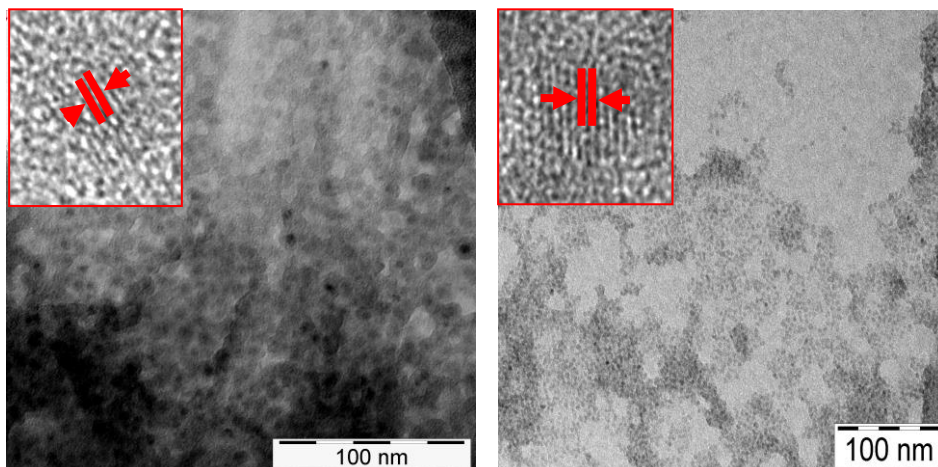


Figure 74 TEM and HR TEM images of ZnO-2 (left) and ZnO-3 right.

Surface of the ZnO quantum dot can be seen easily in Figure 71. This also affects the crystallinity of the quantum dots as observed in the XRD patterns in **Figure 76** and **Figure 77**. As seen clearly from the TEM images, surface covering oleate groups has been removed successfully and this led to formation of the uncovered quantum dots that allowed to measure the quantum dot size (**Figure 75**).

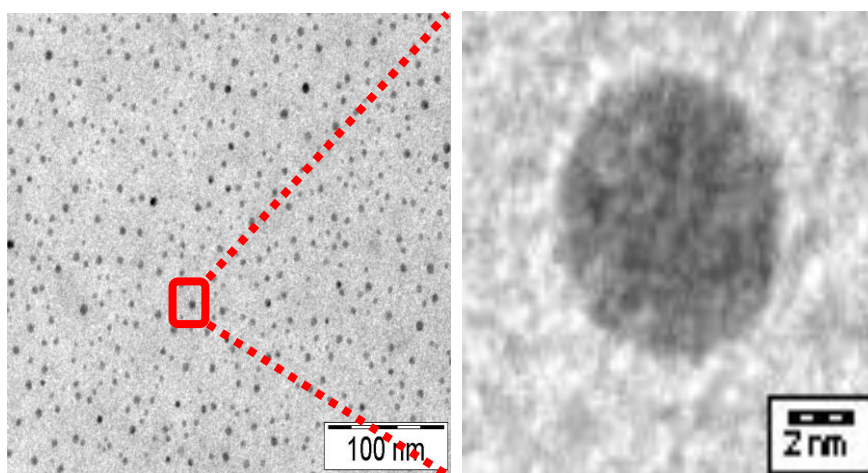


Figure 75 TEM investigation of oleate removal for ZnO-1.

4 Results and Discussion

XRD patterns also reveal the better crystallinity of the heat treated quantum dots.

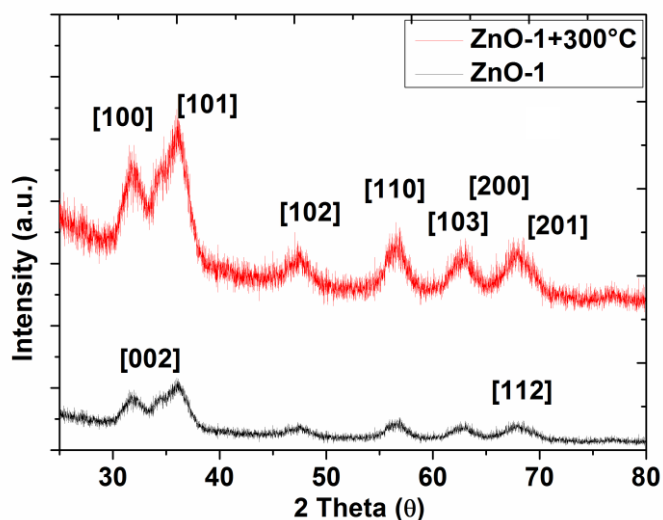


Figure 76 XRD patterns of ZnO-1 before and after heat treatment.

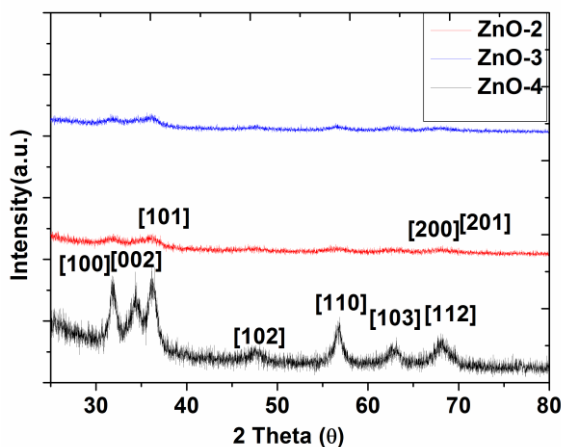


Figure 77 XRD patterns of the Acetate@ZnO and ZnO-2, ZnO-3.

Even though [002] peak is not perfectly sharp, other peaks of the wurtzite structure were identified properly. For comparison of the agglomeration behavior we can check TEM images as given in Figure 78.

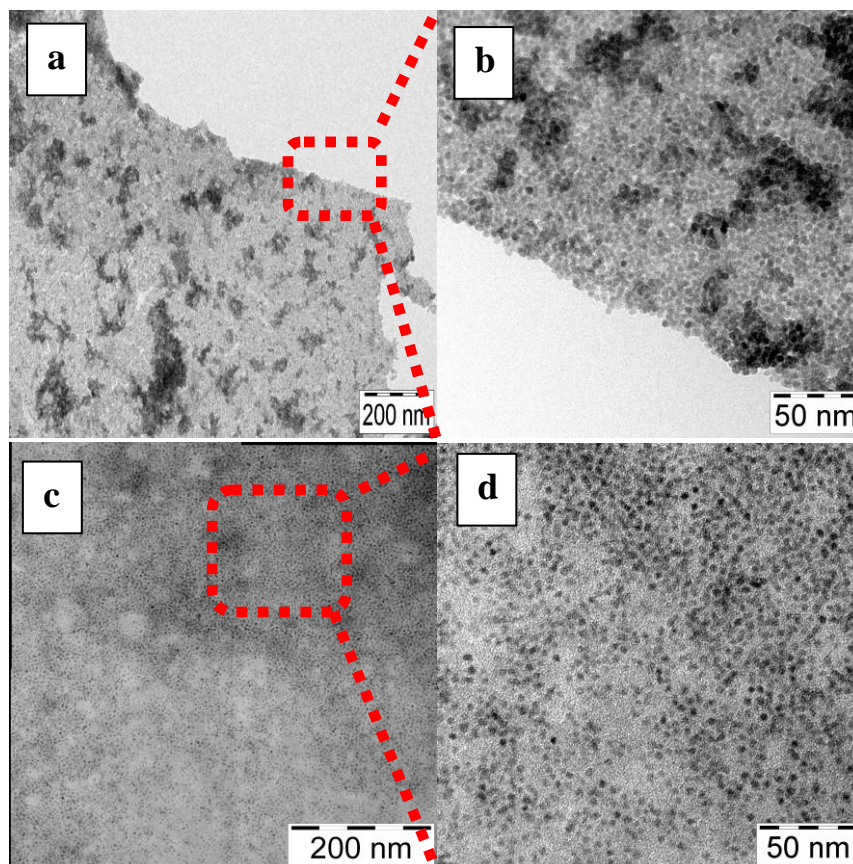


Figure 78 Comparison of the agglomeration behavior of a b) Acetate@ZnO and c-d) Oleate@ZnO QD's.

Since Acetate@ZnO QD's have no proper protection they agglomerate and form a quantum dot monolayer as presented. Here again we compare the Acetate@ZnO QD's with Oleate@ZnO QD's and see that due to the oleate factor as-synthesized quantum dots have an amazing non-agglomerating behavior.

4 Results and Discussion

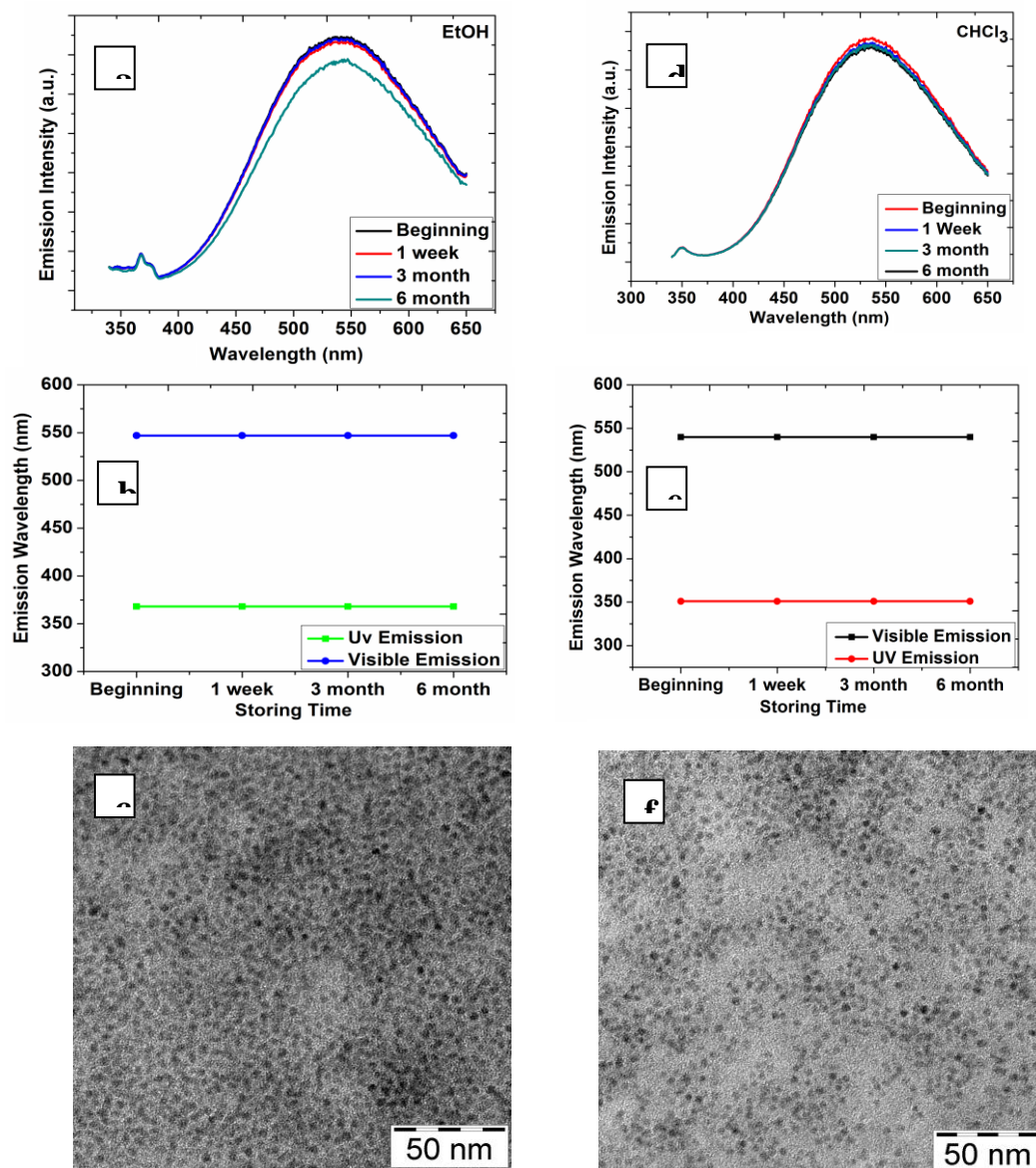


Figure 79 Stability observation of the Oleate@ZnO QD's in EtOH (a-b-c) and CHCl (d-e-f) during 6 month with their TEM analysis after storage.

It is seen clearly that no attaching quantum dots available. Oleate ligand brings an ultrastability to the ZnO quantum dots (Figure 79). Their visible emission character do not show change upon storage. Even after storing no agglomeration occurs as presented in TEM images in Figure 79. Since we have used different amount of ratios for the Oleate@ZnO synthesis we obtain different amount of surface ligand loadings as presented in Figure 80. TGA analysis of the Oleate@ZnO QD's (ZnO-1, ZnO-2, ZnO-3) showed physical and chemical adsorbed ligands and water for Acetate@ZnO QD's (ZnO-4) as their mass removal shows 2 and 3 main steps respectively. For ZnO-4 until 250 °C water

and solvents if available and other physically adsorbed ligands are removed (% 8-9) whereas chemically bonded acetate groups are removed at 435 °C, (% 8).

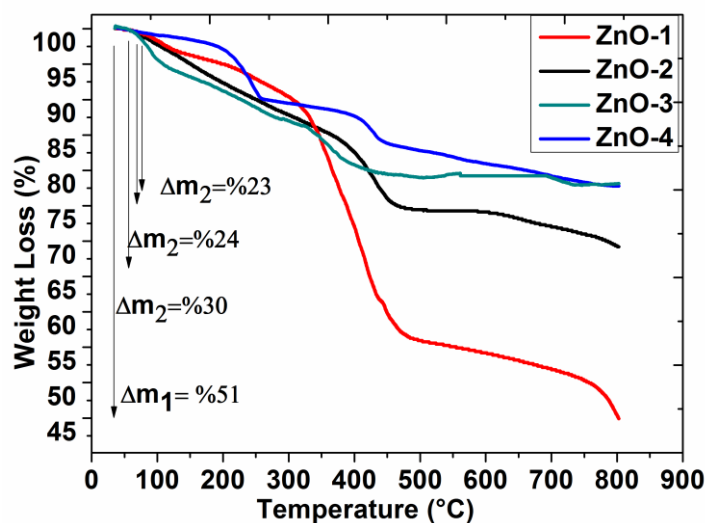


Figure 80 TGA analysis of oleate loading for ZnO QD's.

After this point, small difference in weight detected until 800 °C which means a complete removal of all organic species (% 7). For ZnO-1 nanoparticles there are 2 main steps observed composed of partial and full oleate removal. Since oleate group has a higher molecular weight, mass removal causes a big difference with a small amount of possible adsorbed solvent molecules as seen in ZnO-1. Until 475 °C % 41 of the total removal has been completed and until 800 °C this increased to %51 for ZnO-1. Total oleate loading is % 30 for ZnO-2 which only %25 of full loading till 475 °C is removed and the rest (%5) takes until 800 °C. As for ZnO-3 %19 of total oleate loading is removed until 475 °C and leaves only %5 which will be removed until 800 °C.

4.1.4.4 Phase Transfer Synthesis for Water Soluble ZnO QD's and other techniques for visible light emission manipulation

Storing the ZnO QD's has its own difficulties but as previously mentioned, Oleate@ZnO brings a new concept for the quantum dot storage.

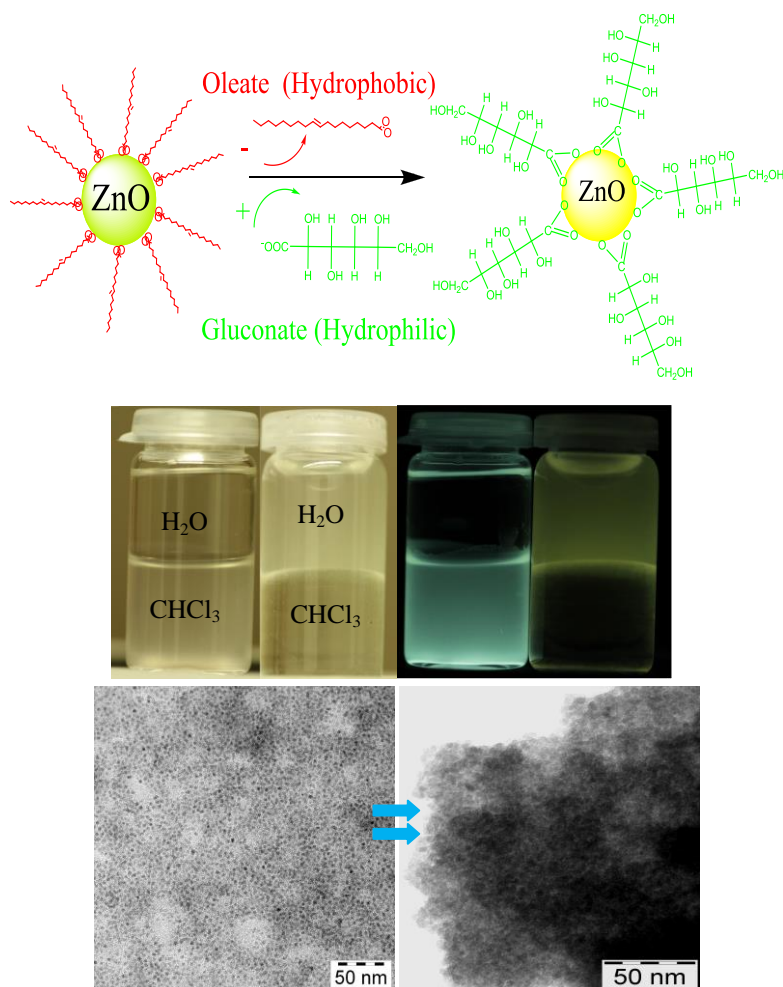


Figure 81 a)Oleate@ZnO QD's to Gluconic@ZnO QD b)Appearance before and phase transfer under UV illumination ($\lambda_{\max}= 354$ nm) c) TEM images before and after phase transfer with gluconic acid.

It was observed in the controlled experiments that ZnO QD's visible emission with the same intensity even after several months but it is possible modulate (switch to another wavelength or quench its visible light emission) by using phase transfer or encapsulation method. In phase transfer method we can simply transfer ZnO QD's (Figure 81) from apolar (for example CCl₄) solvents into the aqueous phase and use of this solutions for ink-jet printing or nanocomposite structure applications. This allows to obtain ZnO QD's that are intractable even after several weeks and can be modified as per requirements of further studies or applications. Using different ligands can cause quenching or extremely lowering the visible light emission. Another method is encapsulating these quantum dots in the silica structures. Since we have completely masked/repared the defect structure almost no visible emission is seen even though UV emission is still present and observable.

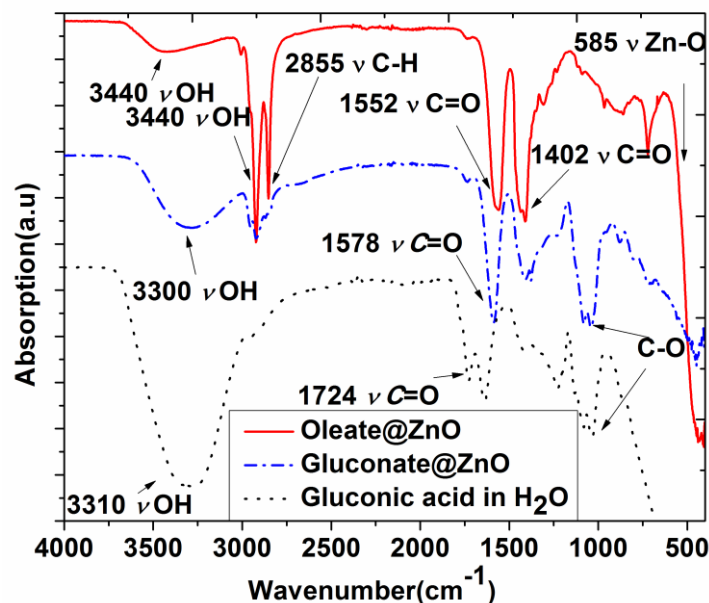


Figure 82 FT-IR confirmation of the phase transfer for gluconic acid

Figure 82 is the FT-IR confirmation of the transfer of Oleate@ZnO QD's from organic into aqueous phase by gluconic acid phase transfer reaction. Driving force of this substitution is the removal of oleate group with a lower pKa value acid ligand, gluconic acid in this case. When we compare the pKa values of the oleic acid (pKa: 9.85) and gluconic acid we conclude that gluconic acid can attach to the surface in salt like interaction. This has also been proved by NMR investigation (Figure 83) showing a salt like Zn-gluconate bonding. When carboxylic acid ligands with pK_a values smaller than pKa: 9.85, ligands have the pKa values smaller than pKa: 9.85 are introduced, reaction provides phase

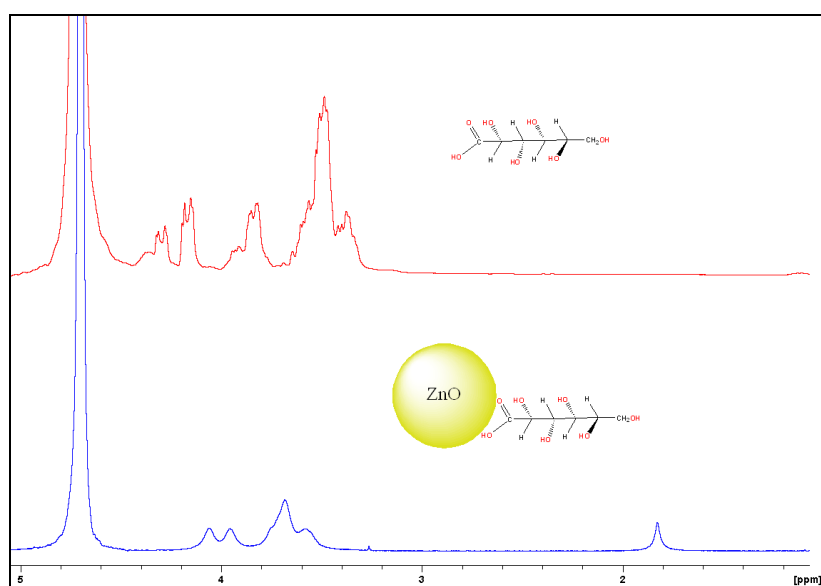


Figure 83 Salt like attachment of gluconate after phase transfer synthesis.

4 Results and Discussion

transfer for the Oleate@ZnO QD's. This concept can cause small problems if introduced ligand is extreme in concentration. The effect of pKa values has been proved by mandelic acid (pKa: 3.41) and also polyfunctional carboxylic acids like citric acid (pKa1:2.8, pKa2:4.1 and pKa3:5.3) as phase transfer has been confirmed by their FT-IR spectras (not shown). The pKa values closer to 9.85, cause difficulties since reaction requires substitutional hydrogen transfer. An important point is anticipation of ZnO QD aggregation after phase transfer. Due to its highly hydroxyl containing nature, gluconic acid caused an aggregation as evidenced clearly in the TEM (Figure 81) image and FT-IR spectra after phase transfer. This is an important concept since extreme agglomeration can cause decrease in the emission properties. TEM image of the phase transfer product, revealed its agglomeration due to the intermolecular interactions of gluconate ligand. Hydroxyl groups on the gluconic acid provided water solubility but due to the extreme hydrogen bonding and van Der Waals interactions TEM images reveal the embedded ZnO QD's in gluconate medium. After phase transfer, spectral position (542 nm) of the visible emission (not shown) for the Gluconate@ZnO QD's showed a slight bathochromic shift (emission $\lambda_{\text{max}}=547$ nm) as compared to Oleate@ZnO QD's which confirmed by their visible emission analysis. In the phase transfer image of Oleate@ZnO QD's, due to the organic nature of the environment (CHCl_3) visible emission seen as greenish-yellow even though aqueous solution of the gluconic modified ZnO QD's seem profoundly yellow.

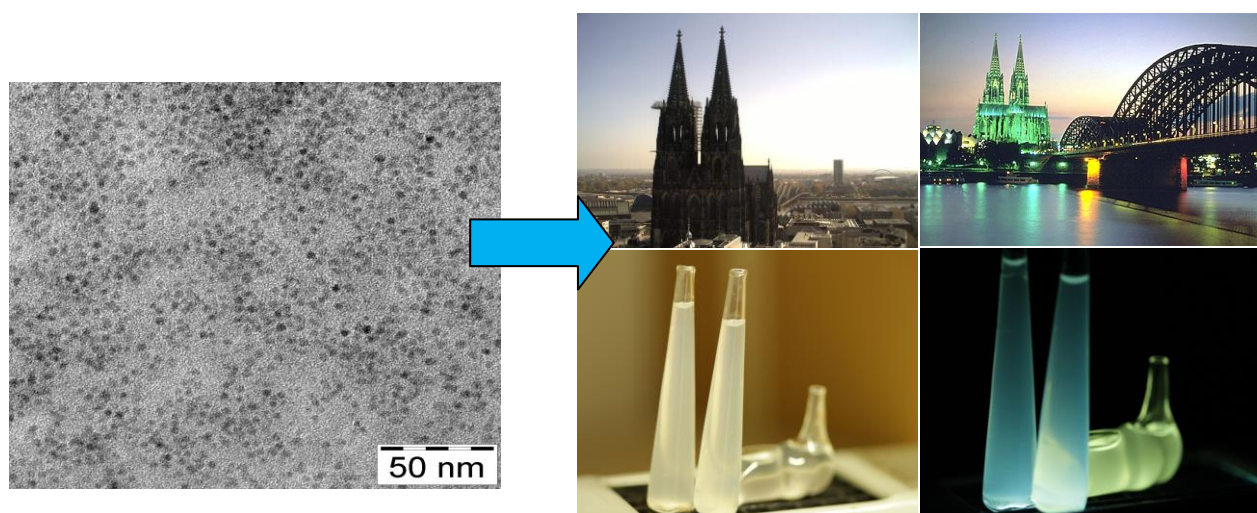


Figure 84 ZnO QD's solutions for different visible light emissions.

Intensity of the visible emission has been slightly decreased. This possibly arises due to the substitution of the surface ligand and decrease in the oxygen

4 Results and Discussion

deficiencies on ZnO QD's by substitution. Storage of these phase transferred QD's led agglomeration on the bottom of the tube since they are not protected by a long chain surface agent. FT-IR investigation also established the ligand change by functional group detection. For manipulating the visible light emission (Figure 84) encapsulation has been achieved for the ZnO quantum dots in the silica shell. Results show that visible light emission of the quantum dots disappeared. This can be attributed to;

- Extreme huge size (200 nm) of the encapsulation spheres when compared to ZnO QD's
- Saturation of the ZnO surface defects by silica
- Attack of basic component (OH^-) to the surface of the quantum dots

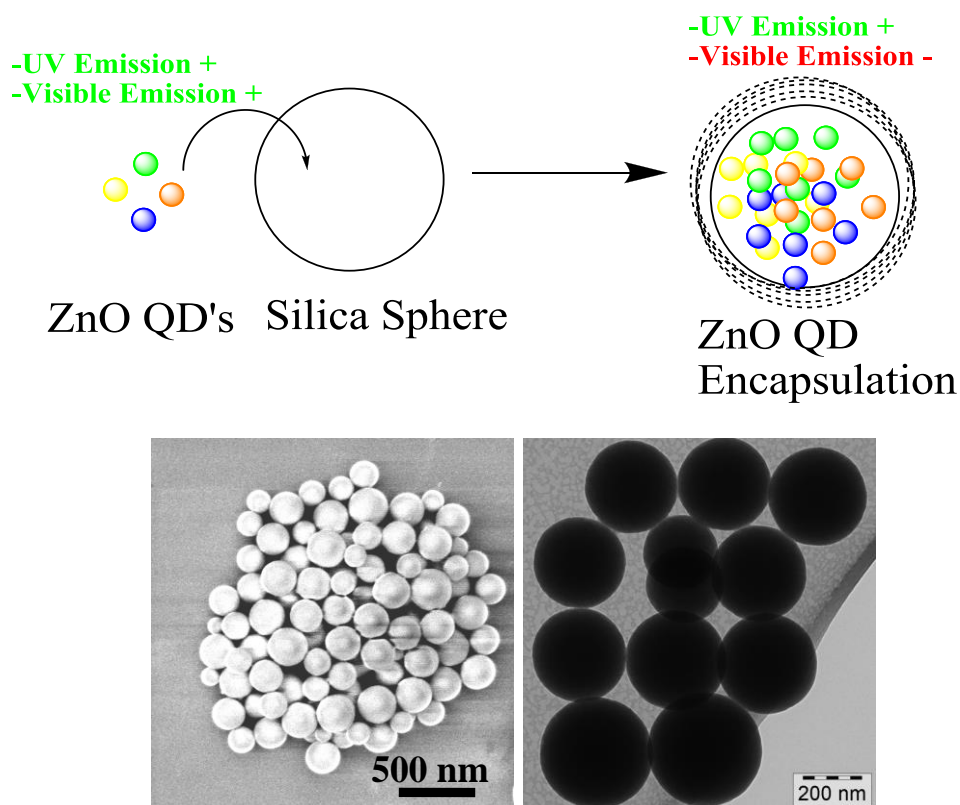


Figure 85 Silica encapsulation causes quenching in visible light emission.

As highlighted before, for the encapsulation a basic mixture has been utilized. This mixture may cause several variations on the introduced ZnO QD's. Since encapsulation process (Figure 85) starts with pH arrangement, basic reaction environment causes defect saturation and therefore addition of the silica shell precursor encapsulates the quantum dots and visible emission vanishes. SEM images and TEM investigation of the as-synthesized silica spheres provided no

detailed information about the ZnO quantum dots (Figure 85). Even though (w/w) 5% addition into the silica shell from the ZnO quantum dots, did not show any sign from the visible light emission. Interestingly UV emission is always detectable and its spectral position does not change during encapsulation. SEM and TEM images showed that encapsulated Oleate@ZnO QD's in highly spherical silica spheres and their visible emission peak is not visible anymore (not shown). Still we can simply detect the UV emission which is a clear proof for the encapsulation reaction. Even though UV emission provides a proof investigated TEM images are not providing enough support for the clear evidence. Due to the extremely small size of the quantum dots they are not detectable on the encapsulation spheres.

4.1.5 Nanomaterials and Discussion of Ligand@ZnO QD's

Due to their visible light emission and antibacterial property, size dependent selective UV absorption characters, ZnO QD's have been used for many material applications.

4.1.5.1 Cytotoxicity and Cell Labeling by Ligand@ZnO QD's

After phase transfer process aqueous solution of the gluconate@ZnO QD's were used in labeling of Human Embryonic Kidney 293 (HEK 293) cells. Cytotoxicity level of the gluconate@ZnO QD's on HEK 293 cells was already determined by the 3-(4,5-dimethylthiazol-2-yl)-2,5-diphenyltetrazolium bromide (MTT) assay (Carl Roth, Karlsruhe, Germany). According to the process, formazan crystals that formed were solubilized with 4mM HCl in isopropanol which contains 0,1% Tergitol solution (Sigma Aldrich, Steinheim, Germany). Different amount of gluconate@ZnO QD's (10µg/ml, 30 µg/ml, 50 µg/ml, 100 µg/ml) added into 20µl MTT for the each well and incubation has been carried out at 37°C for 4h. After removal of medium 200µl MTT solvent was added to each well and mixed. The absorbance was read at 620 nm by enzyme-linked immunosorbent assay (ELISA) (Elx800, Biotek). The results were computed in relation to an untreated control. It is already known that ZnO nanoparticles show dose dependent cellular toxicity. By using the same method HEK 293 cells have been treated by introducing gluconate@ZnO QD's (20µg/ml) incubating them at 37°C in 2 hours.

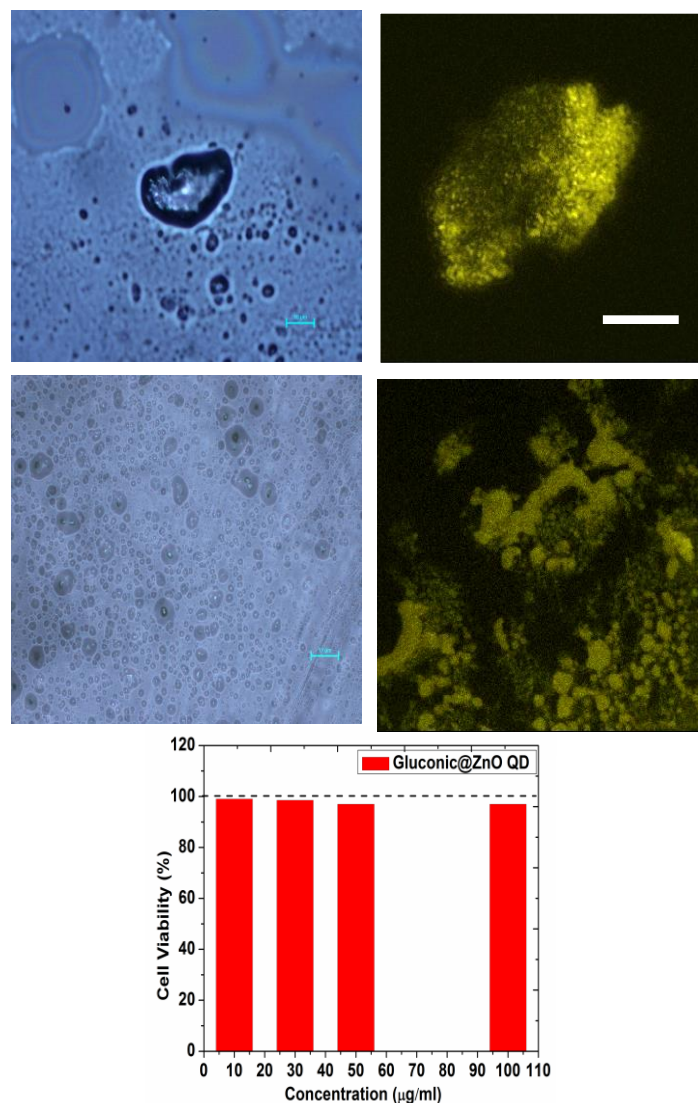


Figure 86: a) Confocal images of the HEK cells after 2h incubation b) MTT test for the cell viability during 4h with different dosing.

Since ZnO QD's can not directly diffuse into the cell's and therefore can not be available inside due to their high pH dependent dissolution character, synthesized D's provide us an easy method for the cell labeling and an easy application as addition to the previous fabrication and applications of the ZnO QD's.30-35 MTT results already revealed viability loss only around % 3-5 during 4 hours treatment as presented in Figure 9. Prepared HEK 293 cells were mounted on glass slides with gelvatol and confocal images of the HEK cells were obtained under the particles corresponding excitations. It is really hard to obtain water mixture with Oleate@ZnO but gluconate modification provides water solubility. Same anticipation can also be made for the cysteine modified quantum dots. Their cytotoxicity degree is remarkably low and their usage for cell labeling gives positive results as presented in Figure 86.

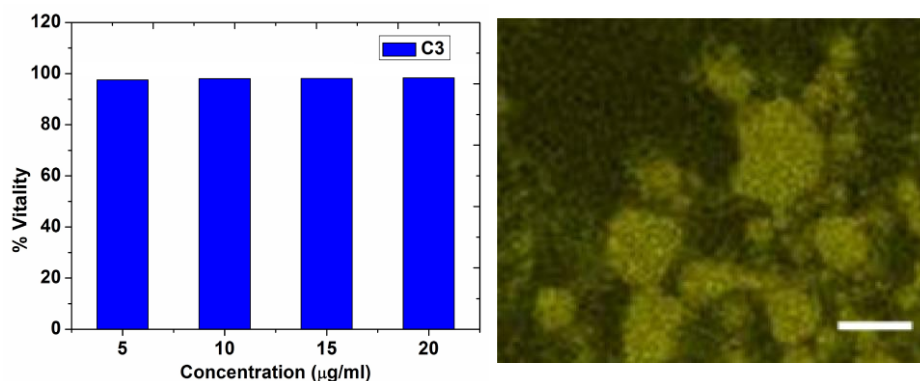


Figure 87 Cysteine capped ZnO cell labeling and cytotoxicity.

Visible light emission of the cysteine-capped ZnO QDs was used in labeling of human embryonic kidney 293 (HEK 293) cells (Figure 87). Cytotoxicity of cysteine-capped ZnO QDs on HEK 293 cells was determined by the 3-(4,5-dimethylthiazol-2-yl)-2,5-diphenyltetrazolium bromide (MTT) assay (Carl Roth, Karlsruhe, Germany) as explained before. After exposure to the different amounts of cysteine-capped ZnO QDs (5, 10, 15, and 20 µg/mL), 20 µl MTT solution was added to each well and incubated at 37 °C for 2 h. The medium was removed and 200 µl MTT solvent was added to each well and mixed thoroughly. The absorbance was read at 620 nm by enzyme-linked immunosorbent assay (ELISA) (Elx800, Biotek, Germany). The results were computed in relation to an untreated control. In previous reports it has been revealed that ZnO nanoparticles show dose dependent cellular toxicity during 24 and 48 h incubation. In this study, HEK 293 cells have been treated in the same manner by introducing C3 quantum dots (20 µg/mL), incubating them at 37 °C but in shorter times 1–2 h. MTT assay test revealed that only 5–8% of the cell viability loss was observed during 2 h treatment.

4.1.5.2 Selective UV-A (400-315 nm) and UV-B (315-280) Region Protection by ZnO QD's and Antibacterial, Transparent, Hybrid Nanocomposites

Due to the size dependent UV absorption and antibacterial properties of the as-synthesized quantum dots, it is possible to embed these quantum dots into the inorganic organic hybrid polymers for UV protective transparent coatings, visible light emitting material synthesis and nanocomposites. Since zinc release provides antibacterial properties, quantum dot introduced formulations have been prepared and analyzed thoroughly after quantum dots introduced into the nanocomposite structures. Additionally, ZnO QD's may absorb the UV light in the thin films for the transparent UV protective surfaces on different substrates.

4.2 Anisotropic ZnO Nanoparticles by Heating Up Method

Heating up method is highly effective way to synthesize monodispersed nanocrystals^[115-129]. Especially for the metal oxide nanocrystals it is easier and controllable. In this section it has been given the details of the heating up method and anisotropic ZnO nanocrystal synthesis for the surface modification and cytotoxicity applications.

4.2.1 Basics of ZnO Heating Up Method

Previously characterized molecules or mixtures are heated up to 250-350 °C and this process basically utilizes the precipitation of decomposed precursors in organic solutions for the formation of nanostructures. Proper high temperature solvents and precursors helping the nanocrystal formation are basic components. Generally long-chain hydrocarbons such as 1-octadecene or other high boiling solvents are used as reaction medium. Contrary to hot injection method there is no additional precaution that abruptly induces high supersaturation. This is done in hot injection method for the anisotropic nanocrystal formation. Precursors are analysed before the reaction for the completion of before to do operations. Especially reaction kinetics should be investigated since so far heating up procedure have been used for the nanocrystals starting from the metal carboxylates^[125]. It is well known that metal carboxylate complexes thermally decompose at temperatures near 300 °C or proper higher temperatures to produce metal oxide nanocrystals and additionally some other compounds like CO, water, ketones, esters, amides and various hydrocarbons. We can simplify the metal carboxylate decomposition by assuming that they are forming the side compounds after the reaction

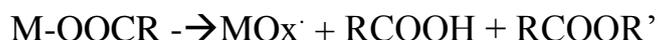


Figure 84 Thermal decomposition of metal carboxylate precursor.

It is known that highly energetic intermediate nanostructures are produced during the heating process and as a result of that intermediate, structures form non soluble oxo clusters which is obtained finally as nanoparticles. These nanoparticles have their own specific character and nanostructure due to the unique preparation technique. Additionally these intermediates can be directly controlled by the surface directing agents or surfactants.

4.2.2 Plate like and and Pyramidal ZnO Nanoparticles by Heating Up

For a proper control of the reaction, it is important to identify which temperature is proper for the decomposition of the precursor mixture.

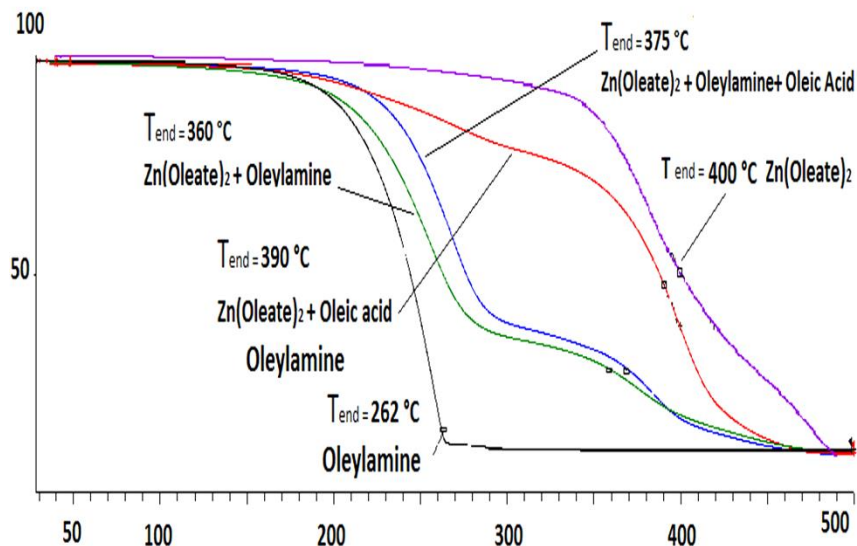


Figure 88 Thermal decomposition profiles of precursor mixtures.

When this onset is properly found, this temperature is used for the nanocrystal synthesis. The TGA curves of the different precursor compositions showed that main thermal decomposition occurs in two main steps (Figure 88). The weight loss occurred below 250 °C can be attributed to the dehydration of adsorbed water or humidity and solvent removal if available. Evaporation of the volatile organic components is easily understood by a broad endothermic peak observed also around 260 °C.

For the proper decomposition temperature detection of the precursors 5 different compound and mixture were analysed namely; Zn(Oleate)₂, Oleylamine, Zn(Oleate)₂+Oleylamine+Oleic Acid, Zn(Oleate)₂+Oleic Acid, Zn(Oleate)₂+Oleylamine.

4 Results and Discussion

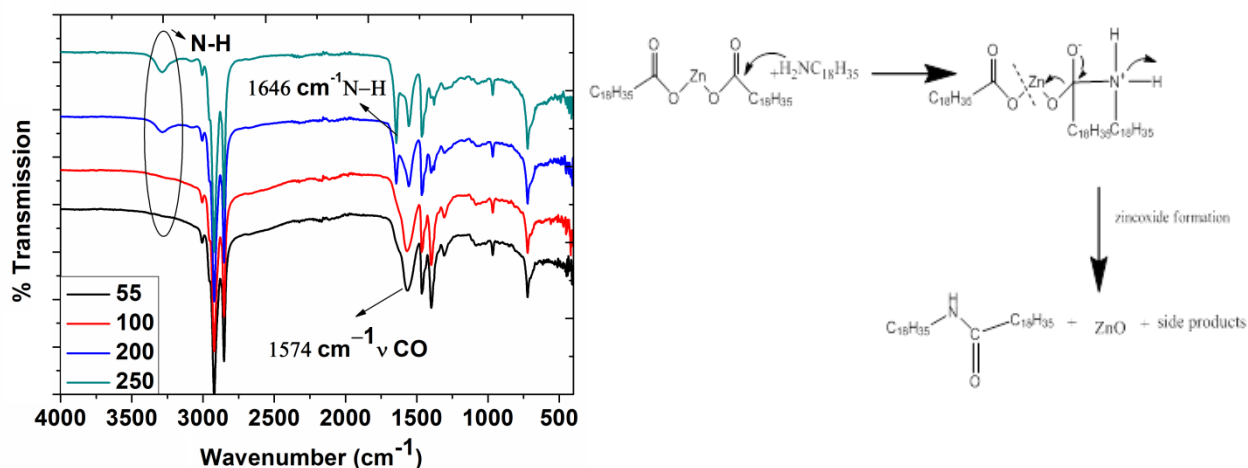


Figure 89 Decomposition mechanism of ZnO precursor and FT-IR observation

Oleylamine thermogravimetric analysis (black) shows a weight loss starting from around 60 °C and continues until 260 °C. After this temperature a slight prominent exothermic peak is observed which can be attributed to the residual organic groups. Zn(Oleate)₂+Oleylamine (green) and Zn(Oleate)₂+Oleylamine+Oleic Acid (blue) thermogravimetric peaks are almost similar which is only differentiating slightly in their shape. On the other side Zn(Oleate)₂+Oleylamine+Oleic Acid (blue) composition continues to lose weight until near 390 °C. This aspect can be explained by the new formed composition and its relative resistance against thermal decomposition. Addition of oleylamine triggers the decomposition of the Zn(Oleate)₂ complex starting from around 210 °C which is confirmed by FT-IR observation (Figure 89) of the precursor mixtures. All three oleylamine ligand containing curves of the mixtures start to decompose by thermally via insertion of amine functional group and its attack onto the carbonyl function leading to the amide formation. In the absence of the oleylamine precursor, precursor mixture is highly resistant to the thermal decomposition which requires high nucleation and growth temperature. As a result, it has been thought that a thermal decomposition which is fixed around 290-300 °C would provide ZnO uniform crystals.

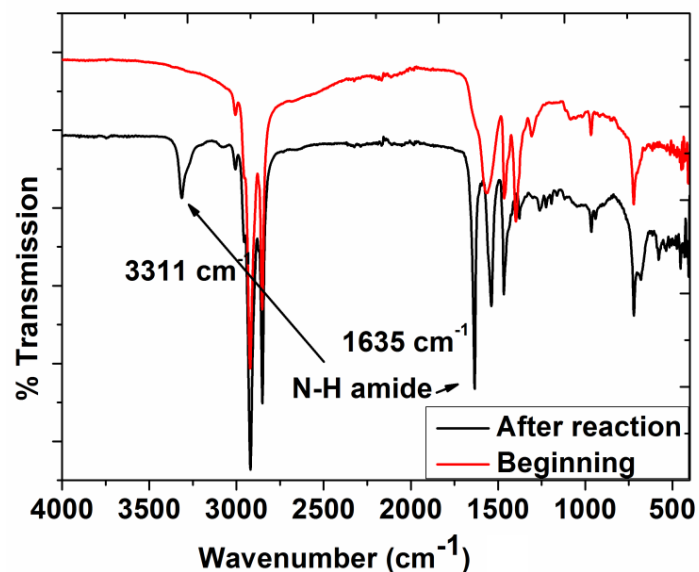


Figure 90 FT-IR spectra for the comparison of beginning and final composition.

In Figure 90 FT-IR spectroscopy clearly showed that amide formation is occurred as expected. Especially N-H stretching for the amide band is clearly seen with other molecular movements in 1635 cm^{-1} and 3311 cm^{-1} . After completion of the heating up method, they have been precipitated with ethanol and washed many times with EtOH and acetone respectively.

4.2.3 Distorted Examples of Anisotropic ZnO Nanoparticles by Heating Up Method

According to the TEM investigation for the nanoplates, diameter and length values have been detected. They have been found as 25 nm in length and 12 nm in diameter (Figure 92). This unveils the concept of proportioned growth for the ZnO nanocrystals. Plate nanostructures have formed agglomerations as seen in the TEM images and they are monodispersed in size and geometry. Deeper analysis and magnified images clearly showed that nanoplates have flat tips in addition to slightly distorted morphologies (Figure 91).

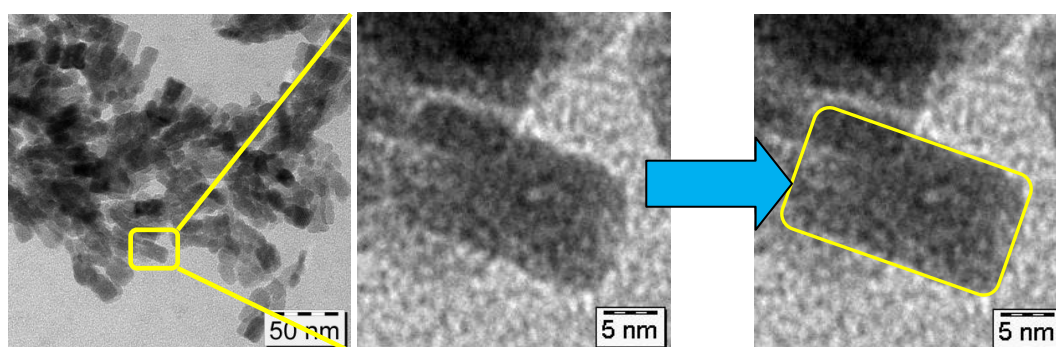


Figure 91 Nanoplate morphology for the ZnO nanoparticles.

4 Results and Discussion

During the synthesis of nanoplates, temperature has been kept at the corresponding decomposition temperature (285-290 °C) and fluctuations in the temperature has been prevented. During nucleation and growth process of the ZnO nanocrystals it has been proved that oleic acid provides a great “steric hindrance” which inhibits the formation of new planes onto the initial nuclei^[129].

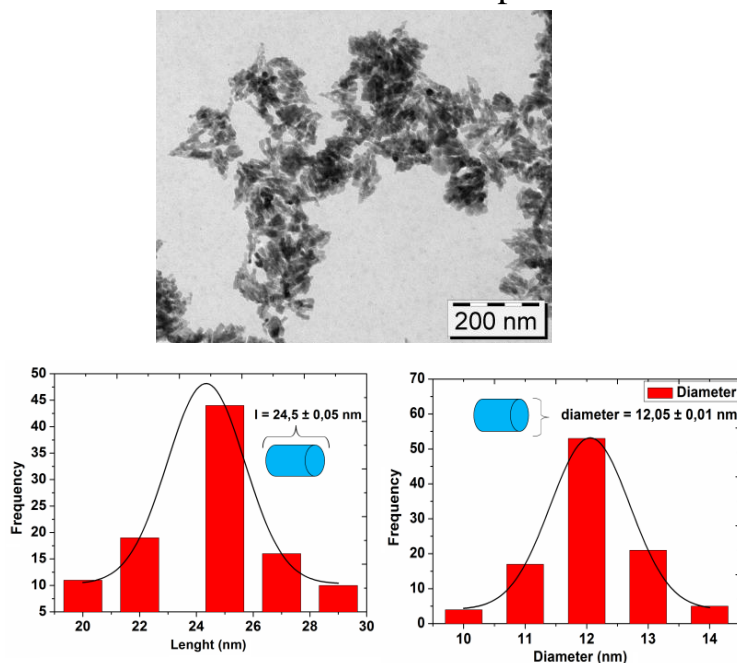


Figure 92 TEM investigation of the nanoplates diameter and length.

If the oleic acid is used as only capping agent it was revealed that high polar structure of the ZnO nanostructure is driven by its components and instead of elongated structures we obtain plate like nanoparticles. Another ligand and morphology controller is oleyl amine for the final structure.

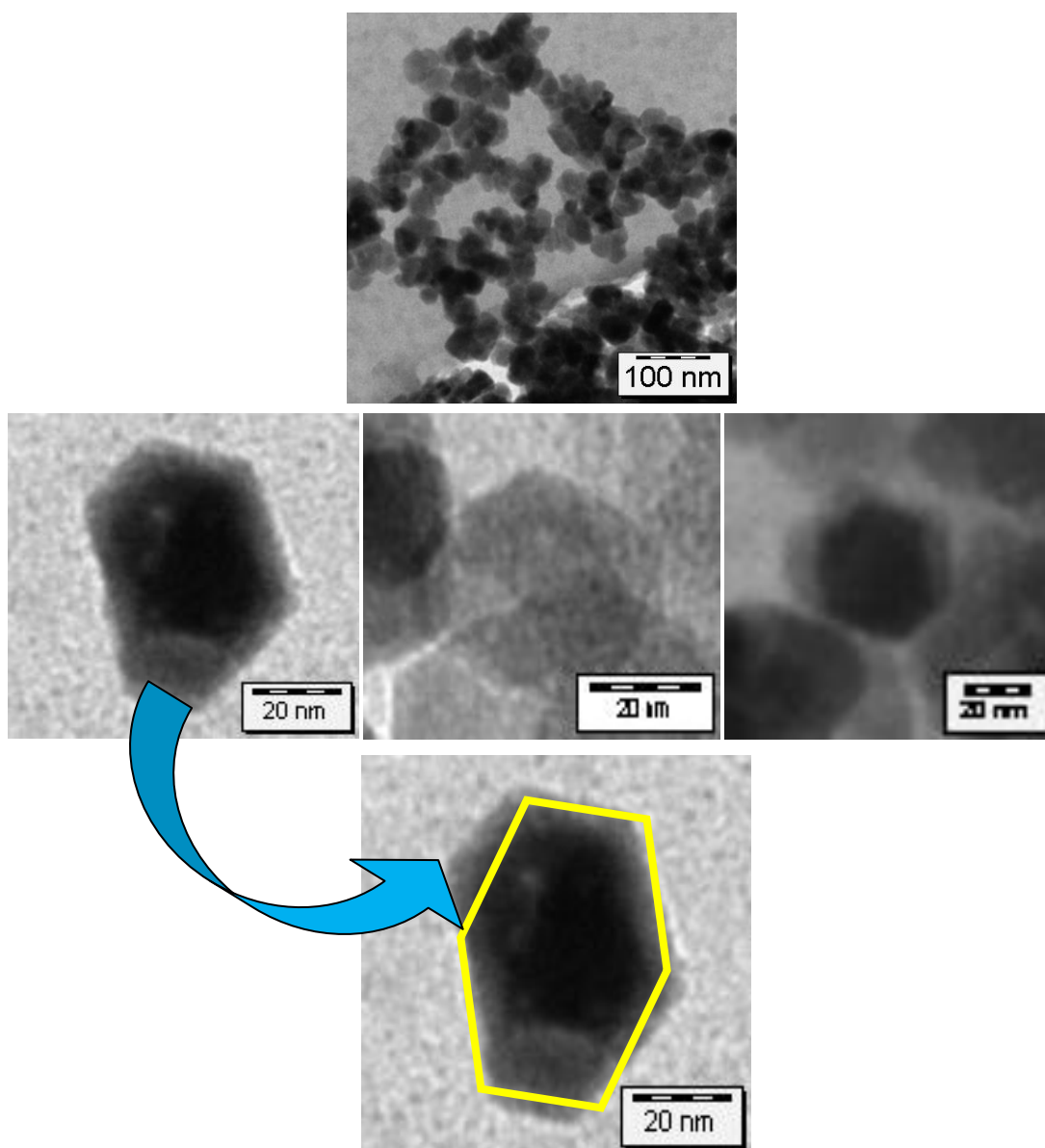


Figure 93 Hexagonal morphology of the ZnO nanocrystals.

ZnO crystal is basically highly polarized and contains chemically active Zn^{2+} terminated [0001] polar surface and naturally O^{2-} terminated [0001-] polar but inert side. Therefore decomposed precursor zinc oleate provides constituent Zn^{2+} cation which deposited on the ZnO core while negatively charged alkyl chain strongly bound on the highly polarized Zn^{2+} surface. In order to synthesis of uniform particles, entire process must be kept under the control. While nanocrystals are being formed, inhibition of the other new nanocrystal formation during growth procedure is the key point for the monodispersed nanocrystal synthesis. Therefore by this synthesis method by applying the given proportion we have obtained nanocrystals which have cylindrical structures due to the anisotropic growth control of the ligands. When another another precursor

4 Results and Discussion

proportion is used for the synthesis of another anisotropic nanocrystals, we have seen that, after the TEM investigation, it was possible to obtain hexagonal structure (Figure 93) and its distorted examples (Figure 94) with like pyramidal and nanorod type nanocrystals which are to be shown later. ZnO has a natural habit to grow in hexagonal structure. Therefore even though we try to vary the conditions of growth deeply by applying different ligands, we observed easily that hexagonal nanocrystals are easily produced if there is vigorous manipulation conditions. By examining these nanocrystals it has been found that crystal sizes were also around 25-30 nm and it was easy to see the hexagonal edges. It is easily noticeable that crystals are not perfectly hexagonal but edges are seemed to have very sharp morphologies.

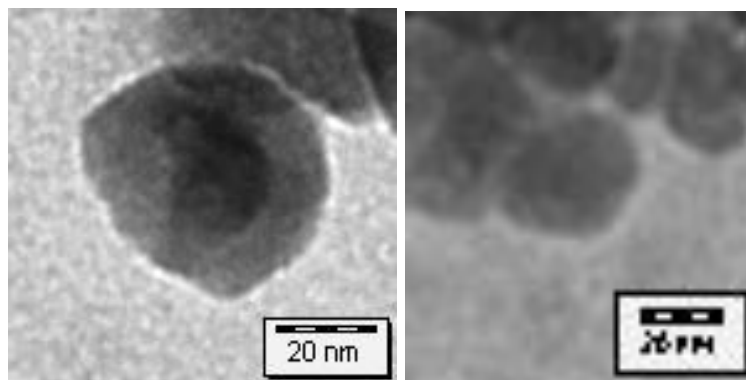


Figure 94 Distorted hexagonal nanocrystals of the ZnO.

This is clearly seen in Figure 93. Still there are some crystals which are seen like their sharp edges are consumed during the crystal growth and these crystals are starting to become more and more curvy as presented in Figure 94.

TEM investigations have also revealed that these distorted hexagonal structures are equal in proximity during the formation of other morphologies. Nanoparticle size investigation has been done by TEM images and it has been found that nanocrystal sizes are about 35 nm average but there are many other particles like 42 nm and 29 nm which reveals undesired formation of slightly monodispersed crystals (Figure 95).

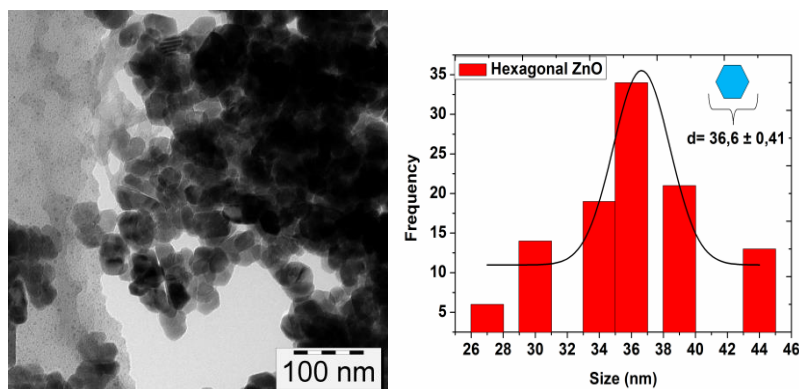


Figure 95 Particle size distribution of the ZnO-distorted hexagonal nanoparticles.

There are remarkably much particle which are bigger or smaller than average particle size. Therefore uniformity in the size and shape has not been perfectly observed. Precursor variation led also pyramidal or triangle shaped nanocrystals. These nanocrystals show monodispersed behavior as TEM investigation presented in Figure 96. Additional one concept is the nanoparticle attachment due to the surface interactions. Since we used acidic and amine type ligands they cause interparticle interaction and nanoparticle surfaces therefore attached to each other in order to decrease the surface energy.

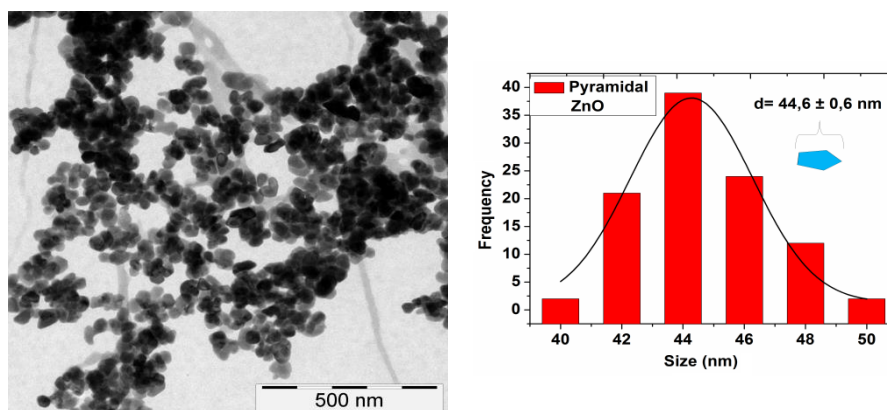


Figure 96 Particle size distribution of the pyramid like ZnO NP's.

After cleaning procedure nanoparticles are washed with acetone several times for TEM (Figure 97) but it should be always noted that nanoparticles have -OH groups on the surface. These groups cause also an easy interparticle attachment for the projected nanocrystals.

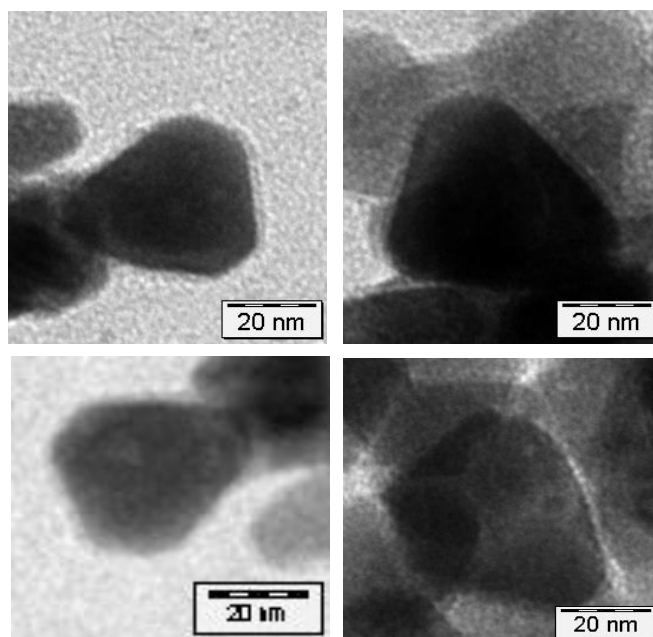


Figure 97 TEM investigation of the pyramidal ZnO nanocrystals.

Since ZnO nanostructures are simply deformed examples of the hexagonal crystals it was possible to observe other morphological nanocrystals as presented in the Figure 98.

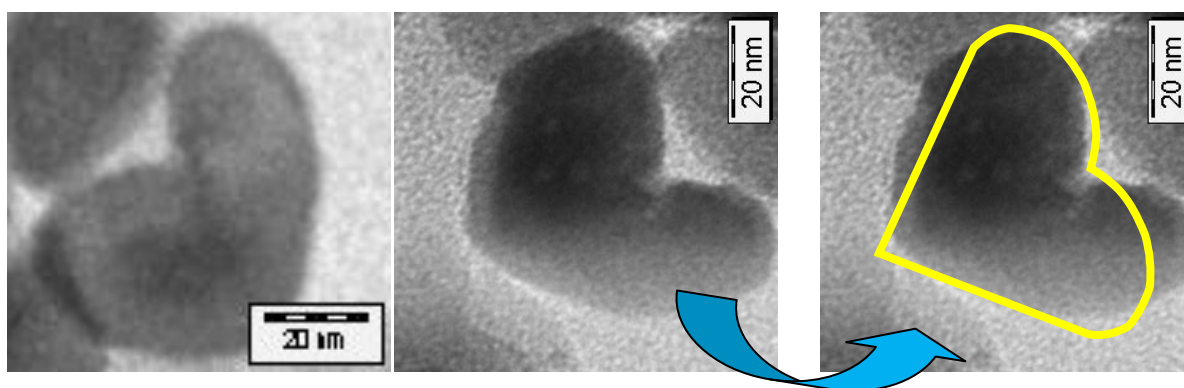


Figure 98 Heart shaped assembly from pyramidal ZnO nanoparticles.

Enlargement of the nanocrystals in TEM revealed that when morphology evolution is investigated, some faces of the hexagonal nanostructure seems more energetic than the other faces. Therefore these faces are growing faster than the other ones and form anisotropic pyramid shaped nanocrystals.

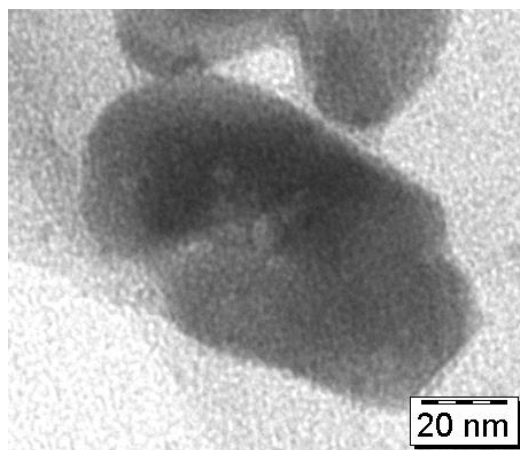


Figure 99 Nanoparticle twins of the pyramidal ZnO NP's.

Pyramid shaped nanoparticles have been also exhibiting some self assembly nanoarchitectures as it has been showed in Figure 98 and Figure 99. During the growth of the nanoparticles, when small nanocrystals come together they may attach to each other with different positions to yield heart or twin type morphologies. Detailed investigation has been revealed that if they attach to each other like head to head then it is seen heart shape but when they attach to head to feet then it is seen twin shaped nanoparticles. These type of interactions for self assembly is because to lower the surface energy and form a stable structure during the formation. When particles lower their facial energy and activity by doubling themselves under suitable conditions they generally act in the favor of less energetical state. As presented when energetical situation is proper is also possible that nanocrystals. If reaction mechanism of the Zn(Oleate)₂ precursor is investigated, results clearly revealed that amine is attacking onto the carbonyl structure, but it should be anticipated that due to the sterical hindrance amine attack decomposes the precursor into the final material very slowly. In order to facilitate the amine attack, oleyl amine attack onto the sterically less Zn(CH₃COO)₂·2H₂O precursor has been studied. In this case the precursor molecule contains water and therefore it should be degassed and kept at proper temperature before the amine attack starts. For this reason precursor has been dissolved in amine and mixture has been kept at 130 °C degree for 1 hour in order to remove the water. After one hour reaction mixture has been heated up to 250 °C degree for the metal oxide formation.

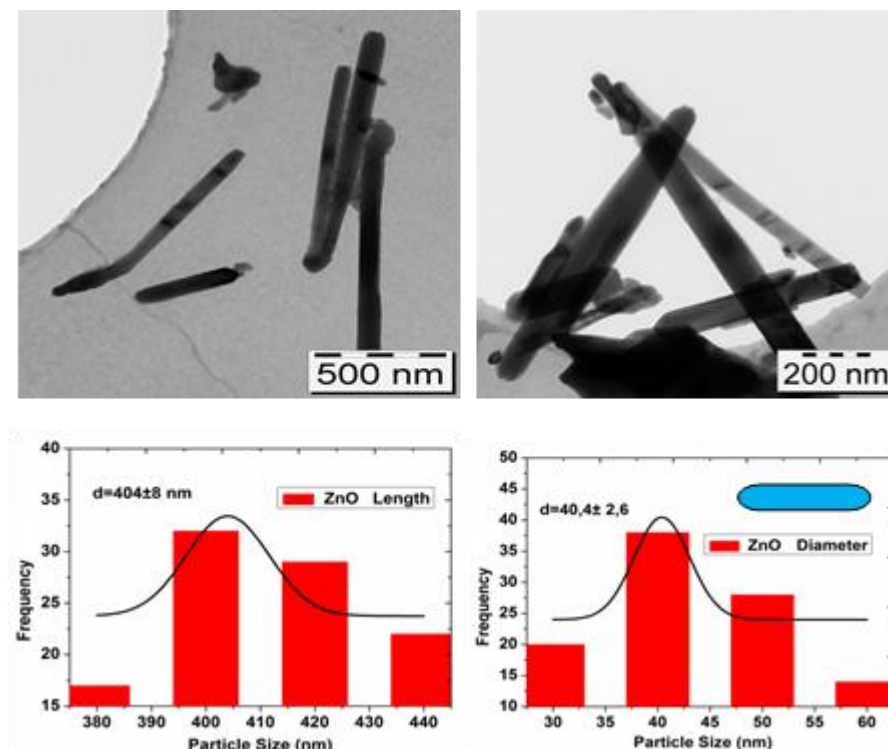


Figure 100 TEM and particle size investigation of the ZnO nanorods.

As expected ZnO formation requires less energy for the sterically less hindered molecule. Therefore we do not need to go to the higher temperatures like 300 °C. TEM investigation of this attempt provided elongated ZnO nanorods Figure 100 within the nano range. According to the TEM investigation nanorods have an average 420-440 nm length and 30-40 nm diameter in size. Even though these magnitudes are in the nanometer range, it has been also observed that some nanorods are exceeding micrometer range. This situation reveals that during decomposition either time can be elongated or the amount of the oleylamine can be changed. If synthesized nanorods are analysed thoroughly it is seen that, tips of the nanorod structures are much sharper than the middle of the nanorods. But still structures do not exhibit bullet like type of morphology.

4.2.4 Crystallinity and surface modification of the Anisotropic ZnO nanostructure

In the Figure 101, XRD pattern of the as-synthesized ZnO nanorod has been given.

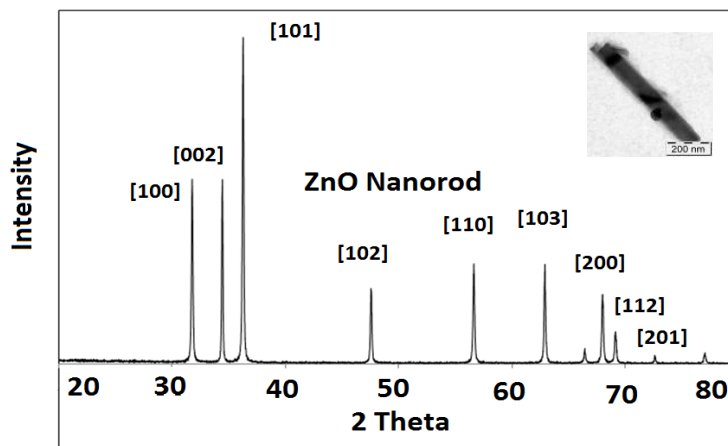


Figure 101 XRD pattern of the as-synthesized ZnO Nanorod.

All obtained XRD patterns of ZnO nanocrystals can be matched with JCPDS= 36-1451. Pattern in Figure 101 shows an extremely sharp peaks and [101] face of the pattern is higher in intensity if compared to other peaks. This actually shows the elongated character of the ZnO nanostructures. Same phenomena is observed in the ZnO nanoplates and if we compare the results, as expected [101] peak is simply higher in intensity. Still it should be noticed that [101] intensity of the nanorod structure is remarkably higher than the nanoplate (Figure 102) structures.

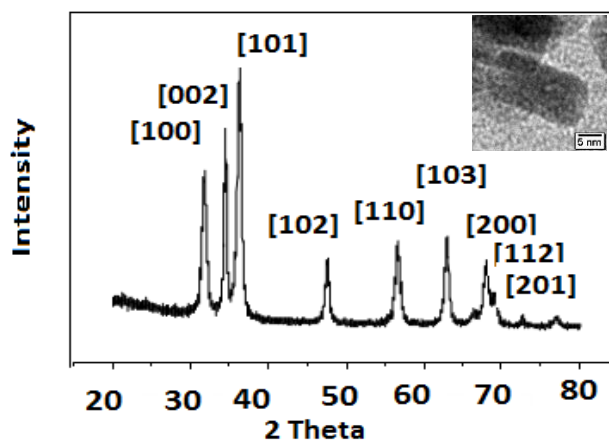


Figure 102 XRD pattern of the nanoplate like ZnO.

4 Results and Discussion

As seen again in the Figure 102, nanoplates have also [002] patterns which is higher in intensity than the [001]. Comparison of the same patterns with the pyramidal ZnO nanoparticles resulted that most

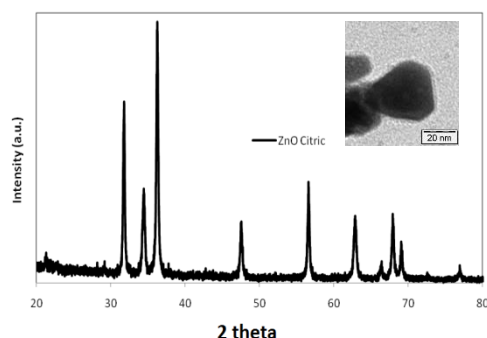


Figure 103 XRD pattern of the pyramidal ZnO.

is the lower intensity of the [002] peak. [101] is still the highest peak but there is another difference. Generally if we have elongated nanostructures [002] peak is not lower in intensity than the [100] peak. Strangely for the pyramidal nanostructures (Figure 103) it has been found that [002] is comparatively lower in intensity when we directly compare with nanorods and nanoplates. Therefore [002] intensity order can be written as ; nanorod > nanoplate > nanopyramidal . Other hexagonal nanostructure (Figure 104) shows the more or less the same pattern as in the nanopyramidal structure but comparatively [100] peak is higher in intensity if we compare it with the [110] peak of the nanopyramidal structures.

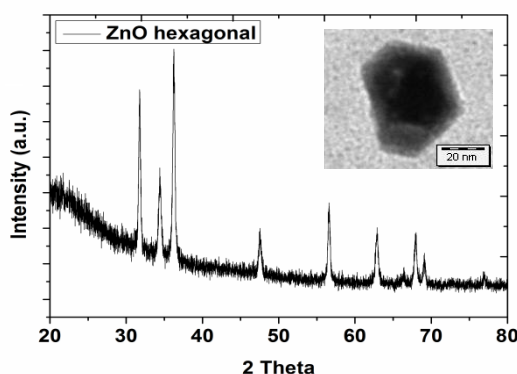


Figure 104 XRD pattern of the distorted hexagonal ZnO nanostructure.

XRD investigation of the synthesized nanostructures clearly revealed the selective facet growth of the ZnO. In addition to that for cytotoxicity and gene expression investigations and photocatalytic activity testing of these obtained nanocrystals have been conducted by naked and modified nanocrystals for understanding the different carboxylic acid ligands on the material properties.

4 Results and Discussion

List of the modification has been given in the Table 5. Surface modification of the ZnO nanocrystals is extremely important for the water solubility, functional group attachment, nanobiological applications and catalysis. In quantum dot synthesis chapter, it has been shown that oleate group plays an important role for the extreme stability of the quantum dots by forming so called core/shell structure and protecting the surface from external attacks. In this thesis synthesized nanocrystals have been modified with many functional carboxylic ligands for the same targets. Thermal analysis and FT-IR investigation provides great information for the organic modification of the nanocrystals. Additionally NMR has been employed for the mandelic acid modification for showing the peak broadening effect for the salt like surface modifications of the nanocrystals. Optical and aqueous properties have also been listed accordingly.

Table 5 Modification list for the ZnO nanocrystals.

Nanocrystal	Ligand
ZnO nanorod	Folic acid
ZnO nanopyramid	Citric acid
ZnO nanoplate	Mandelic acid
ZnO hexagonal	Mandelic acid

4.2.5 Optical, thermal and aqueous properties of the surface modified ZnO nanocrystals

Nanocrystal modification was confirmed by FT-IR analysis, photochemical activity measurement and TG-DTA analysis. NMR spectrums of mandelic acid modified ZnO nanoparticles have been measured for showing the salt-type surface modification effect on the ZnO nanocrystals.

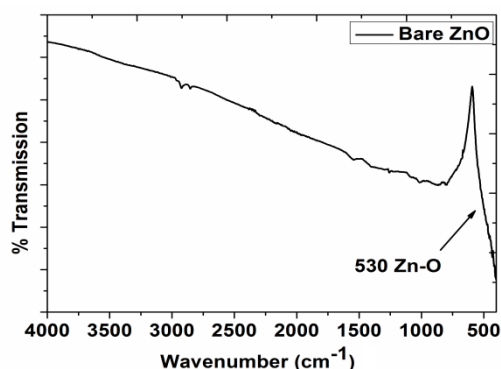


Figure 105 FT-IR spectra for the bare ZnO nanocrystals.

4 Results and Discussion

In the FT-IR method surface modification agent alone (Figure 105) and surface modified ZnO nanocrystal FT-IR spectra is recorded and overlapped in order to identify the molecular peak differences throughout the modification. In bare ZnO nanocrystal, FT-IR spectra was, as expected, containing only metal-oxygen Zn-O bands appear in the fingerprint region. Adsorbed organic molecules caused by washing /cleaning process or adsorbed by the crystal formation has also very weak and broad peak at 1500-1100 cm^{-1} region. Since carboxylic acid molecules are used for the modification $\nu(\text{C}=\text{O})$ stretching peak of the carboxylic acid should be tracked since its remarkable shift shows the salt type modification on the ZnO surfaces. Folic acid (Figure 106), citric acid (Figure 107) and optical (Figure 108) and NMR effect for mandelic acid (Figure 106) pictures show these highly used ligands for the nanoparticle control and surface modulation. In the pure mandelic acid spectra carbonyl stretching band appears at 1708 cm^{-1} which is quite characteristic for the carboxylic acid structures but after the surface modification of the ZnO nanocrystals, this band shifts to the 1592 cm^{-1} proving the Zn-mandelate complex structure and surface modification of the ZnO nanocrystal. Same situation is valid for the citric acid. Carbonyl asymmetrical stretching shifts to 1582 cm^{-1} and 1410 cm^{-1} for the symmetrical stretching.

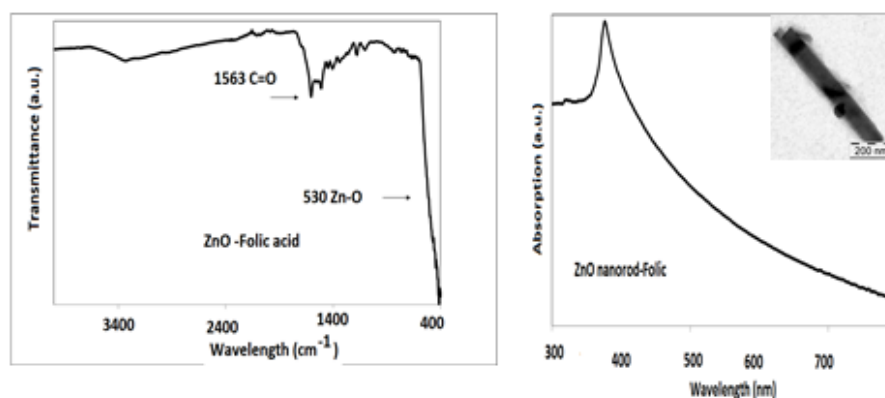


Figure 106 FT-IR and UV Vis- absorption spectra of the folic acid modified ZnO Nanorods.

Folic acid acid modification on the ZnO can be confirmed by N-H (1617 cm^{-1}) and carbonyl (1563 cm^{-1}) group shifting by the electron density of the ZnO surface. Optical absorption characteristics do not change remarkably since a shift in the UV absorption means a particle size variation.

4 Results and Discussion

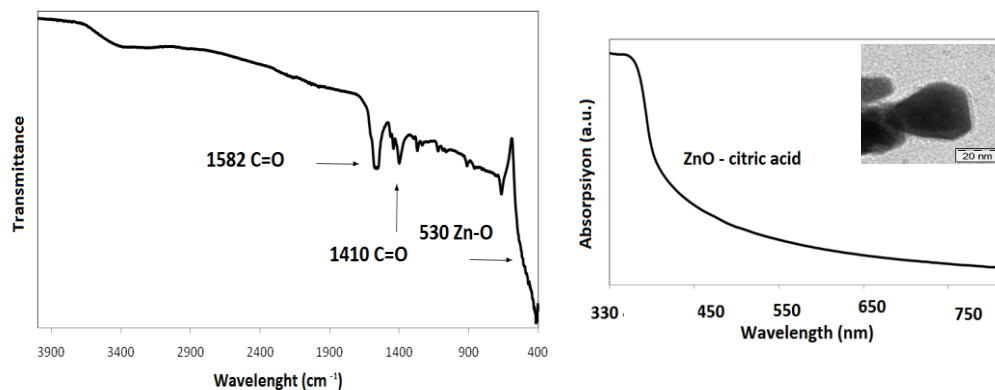


Figure 107 FT-IR and UV –Vis absorption spectra of the citric acid modified nanopyrramids.

UV Vis spectras of the modified nanoparticles show a λ_{\max} = 380 nm, 356 nm and 352 nm respectively for the Folic@ZnO nanorod, Citric@ZnO nanopyramid, Mandelate@ZnO nanoplates.

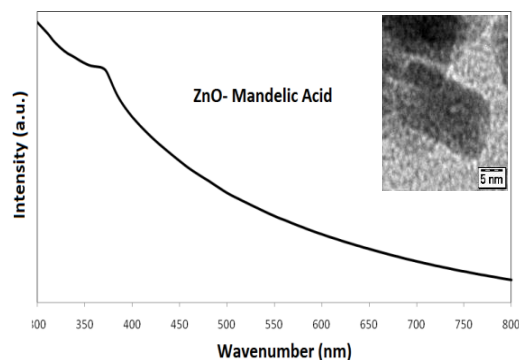


Figure 108 UV Vis spectrum for the Mandelate@ZnO nanoplate.

As seen in the ^1H NMR spectra, if organic ligands mandelate attaches to the surface of the nanoplate, a broadening is observed in the peaks due to the higher electron density on the nanoparticle surface. Especially NMR spectra (in DMSO) in the below (ZnO-mandelic), clearly shows even a broadening in the aromatic groups at the chemical shift 7.3.

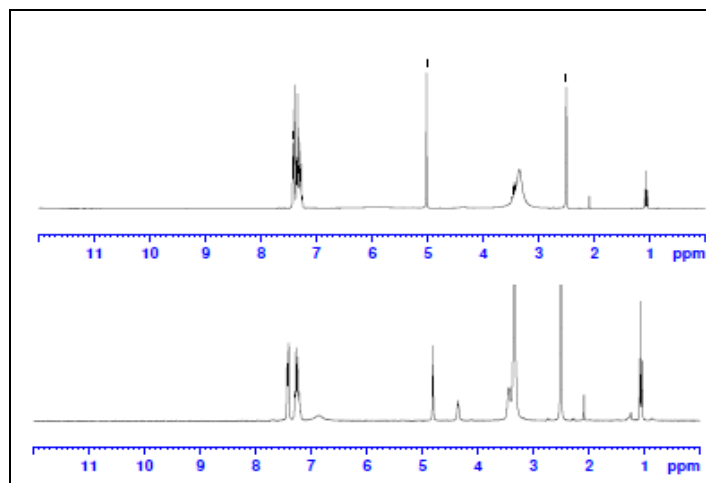


Figure 109 NMR spectra for mandelic acid modification of ZnO nanoplates.

They seem clearly splitted into two symmetrical appearance. Since mandelic acid molecules are on the nanocrystals magnetic field relaxation takes a slightly little more time. This causes the broadening and it is visible in the NMR spectra. There is one interesting point about the surface modification. If modification ligand is used more than necessary there is a surface corrosion which has been detected by TEM investigation.

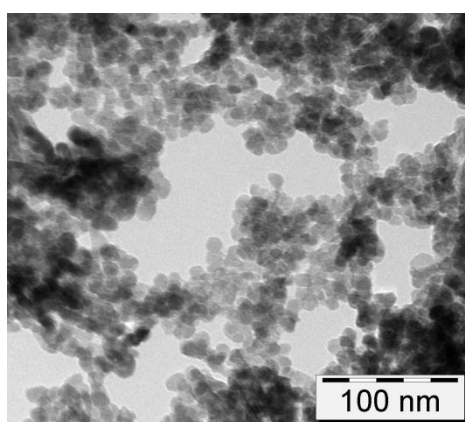


Figure 110 TEM investigation of the mandelic acid modified ZnO nanoplates.

Nanoplate structures have lost their plate like morphology due to the dissolution by mandelic acid. Investigated nanoparticle size is nearly reduced 1 nanometer which has been detected by statistical evaluation unting aftersurface modification.

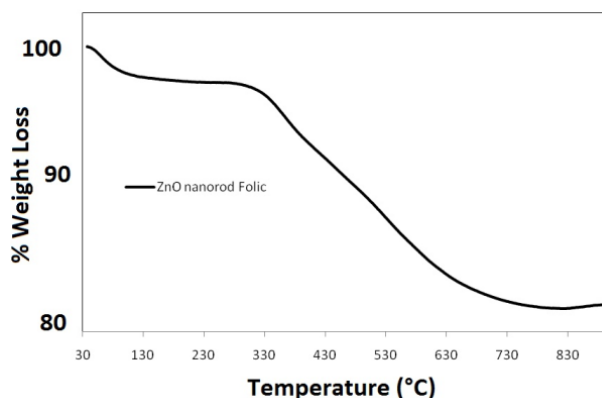


Figure 111 Thermal weight loss of the folic acid modified ZnO nanorods.

Additionally TEM investigation for the modified nanoparticles showed that oriented attachment of the nanoplate structures are hardly visible due to the dissolution. Nanoparticles are seen transformed into spherical morphology (Figure 110) which is detectable easily. Statistical particle size analysis resulted that average size is reduced almost 1 nanometer.

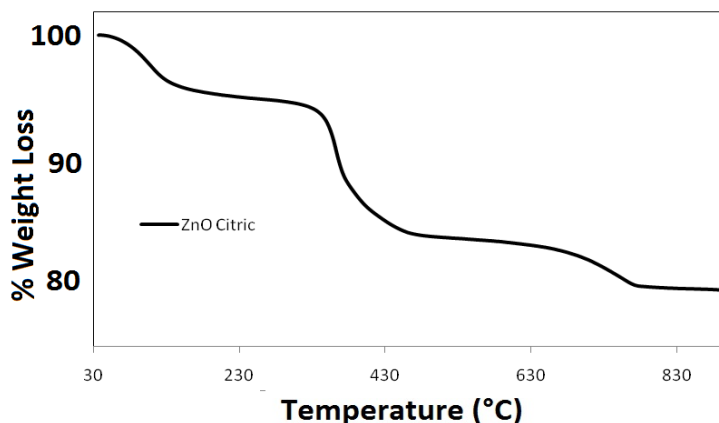


Figure 112 Thermal decomposition pattern of the citric acid modified ZnO nanopyramids.

Citric acid modified ZnO nanopyramids have shown 3 step decomposition which can be attributed to the multiple decomposition of the organic ligand and adsorbed volatile components. As FT-IR also detected, thermal decomposition pattern clearly reveals the organic attachment onto the ZnO nanocrystals. Especially weight loss between the 200 and 800°C is a fair sign for the organic molecule loaded on nanocrystals.

4.2.6 Ligand@ZnO Nanostructures as Nanobiotechnology Nanomaterials

Synthesized nanocrystal structures have been used for the gene regulation, cytotoxicity assessment and photocatalytic activity measurements. Especially after surface modification water soluble nanocrystals have been used for the cell – particle interactions. Since for the nanotoxicologic investigations and theranostic applications surface of the nanocrystals must be modulated and they should be made water soluble, surface modification concept is a vital point for the nanocrystal processing. As presented before, nanocrystal surfaces of the ZnO have been modified many proper ligands to make them water soluble and tested against to immune cells for the investigation of nanomaterial-cell interactions. Results clearly showed that, unmodified nanocrystals are relatively more toxic than the modified nanocrystals. Degree of surface protection depends of the bonding type between the ligand and crystal. If ligand attaches to the ZnO surface by an ether bond and covers the whole surface for the full protection, it is possible to observe decrease in the nanotoxicity.

4.2.6.1 Ligand Effect for the Nanotoxicity and Gene Regulation

As mentioned, surface of the ZnO nanocrystal is composed of weakly bonded atoms and they need to be protected by an external ligand which interacts with the surface atoms and covers them against dissolution. If ZnO nanocrystals are used in the slightly basic conditions, it is widely known that this medium causes dissolution from the ZnO nanoparticles as ICP-MS (Inductive Coupled Plasma-Mass Spectroscopy) or AAS (Atomic Absorption Spectroscopy) methods can detect. Detection of the released zinc cation from the nanoparticles surface can be correlated with the corresponding nanotoxicity data. In a previous publication, it has been highlighted that if the release amount of Zn cation is high, nanotoxicity of the nanoparticles were also considerably high. This led us to a new model as presented in Figure 113^[130-131].

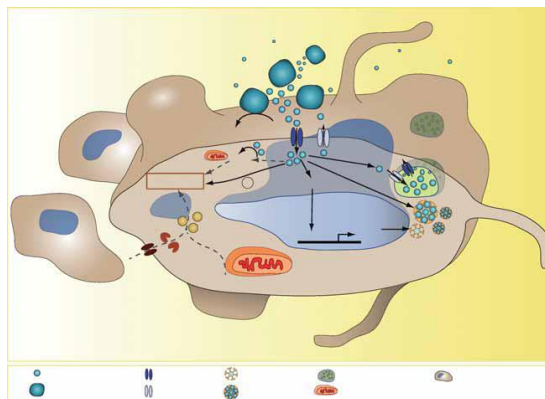


Figure 113 : Schematic representation of some key events of ZnO toxicity in Jurkat cells. The illustration combines results of this study on ZnO NPs and some of the existing knowledge on zinc ions. Zn(II) ions are predominantly released from ZnO NPs extracellularly and are taken up by cells likely by zinc transporters of the ZIP family. Excess free Zn(II) in the cells is stored in zincosomes and binds to MT, which are highly upregulated in Zn(II)-overloaded cells. If the amount of intracellular Zn(II) is too high, the cells undergo apoptotic cell death not via the classical extrinsic or mitochondrial apoptosis pathways (dashed gray lines) but through a yet unknown alternative, caspase-independent pathway that is independent of the formation of ROS. Casp: caspase; FasR: Fas receptor; MRE: metal response element; MT: metallothionein; MTF-1: metal-regulatory transcription factor-1; ROS: reactive oxygen species; Zip: Zrt- and Irt-like proteins (SLC39); ZnT: zinc transporters (SLC30); Zn(II): zinc ions^[131].

Gene expression results have also showed that when the amount of zinc release is increased there was a small change in regulation and variations. Release of the zinc cations has been detected by zinc sensitive fluorescence dye Zincoin. As the nanoparticle concentration increases with time, observation under the confocal microscopy shows the increasing zinc dissolution from the nanoparticles as presented in Figure 114.

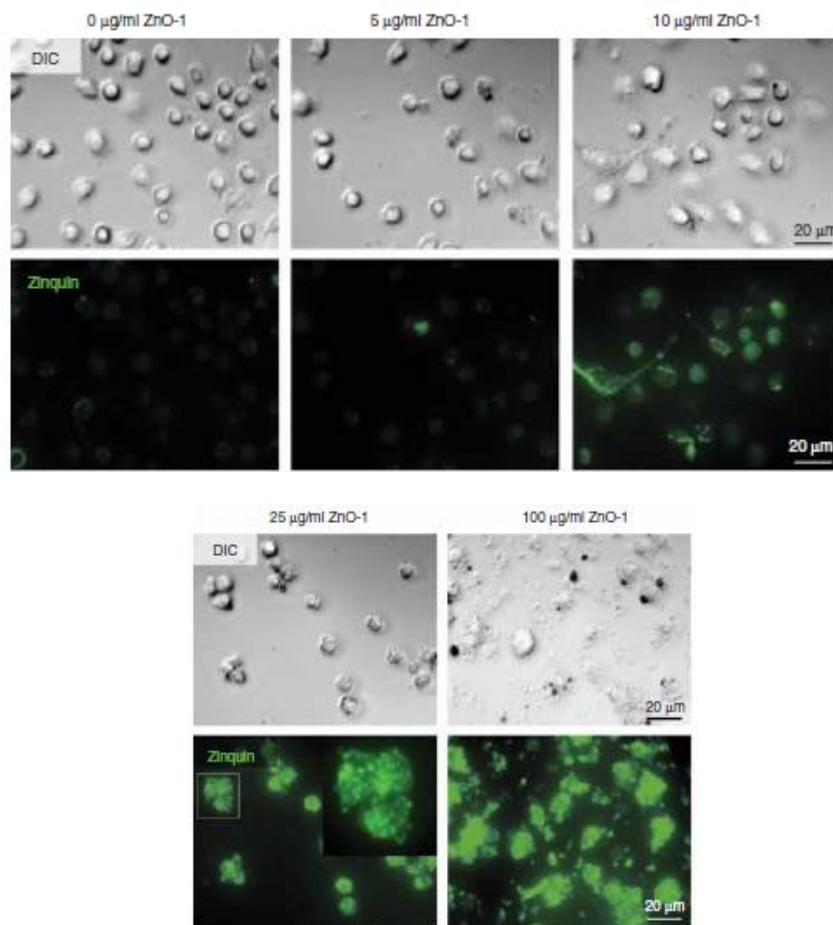


Figure 114 Increasing amount of dissolution by the increasing amount of zinc species^[131].

4.2.6.2 Cell Labeling by Fluorescein modified ZnO nanoplates

Nanoplate and nanopyramid ZnO structures have been modified with widely known fluorescein ligand to use the nanoparticles for the cell labeling applications. After synthesis and characterization, fluorescein attached nanoplates have been used for the labeling applications of the HEK cells by confocal microscopy.

Confocal images showed that nanoparticles are easily attached to the surface of the nanoparticles. Surface modified ZnO nanoplates have been used for this application. After HEK cells have been prepared in the cell medium, fluorescein loaded ZnO nanocrystals have been introduced and cells and for the real time testing they have been stored for 2 hours.

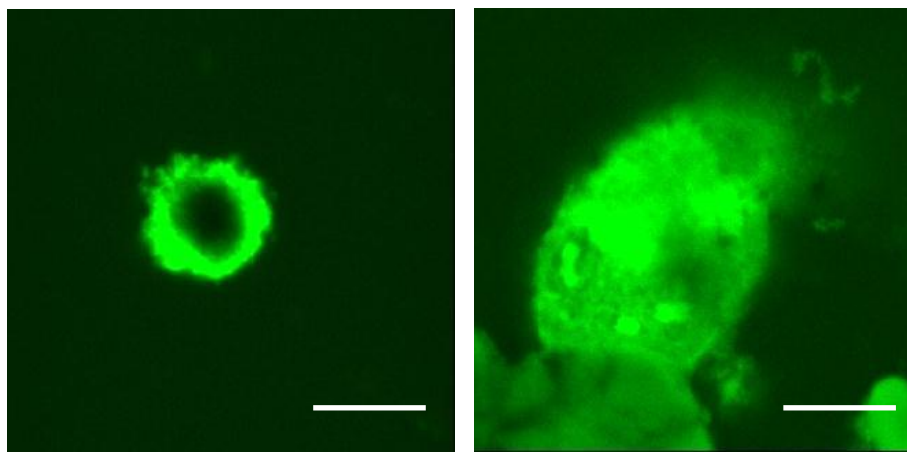


Figure 115 Fluorescein@ZnO nanoplate/nanopyramid cell labeling (bar=10 micrometer).

For the confocal microscopy analysis, prepared nanoparticle attached cells have been immobilized on glass. After excitation, fluorescein attached nanoparticles clearly showed that cells are labeled (Figure 115).

4.2.6.3 Photocatalytic activity of the nanostructures for the decomposition of methylene blue

Effect of the modification on the nanoparticle photocatalysis has been studied by methylene blue (MB) dye. Naked and surface modified ZnO nanocrystals have been tested by UV illumination to test their decomposition capacity for the simply an oxidation mechanism for the organic compounds. Obtained ZnO photocatalytic activity results (Figure 116) showed some fundamental points in the ligand modified ZnO photocatalysis;

- i) Naked ZnO nanoparticles shows always higher photocatalytic activity when compared to its organic acid ligand modified nanoparticle form
- ii) If surface ligand concentration is higher than usual necessary limits on nanoparticle surface and if they attached with ester or ether bond to the particle, (more than % 30-35) this causes high surface deactivation and decrease in photocatalytic activity.

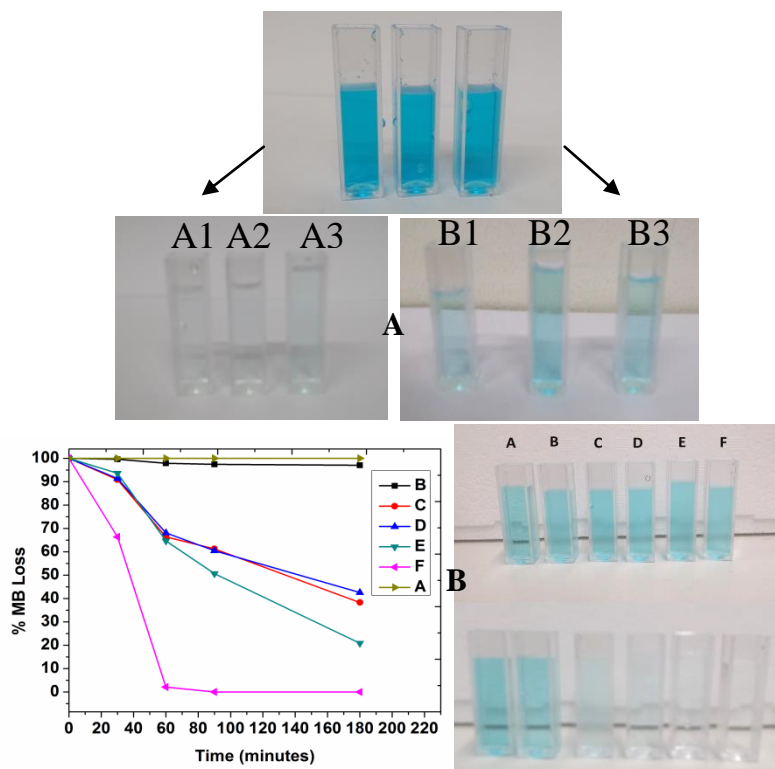


Figure 116 Photocatalytic activity of ligand modified ZnO nanoparticles (Top A, from left to right B1:Mandelate@ZnO Nanoplate and A1: Bare ZnO Nanoplate, B2: Mandelate@Hexagonal ZnO NP and A2: Bare Hexagonal ZnO NP, B3: Citrate@ZnO Nanopyramids and A3:Bare ZnO Nanopyramids (bare particles gave better activity) Below B, A: blank sample, B:Oleate@ZnO QD, C:Mandelate@ZnO Nanoplate, D: Mandelate@Hexagonal ZnO NP, E: Citrate@ZnO Nanopyramid, F= Folate@ZnO Nanorod).

- iii) Extremely small ZnO quantum dots (<6 nm) show almost no photocatalytic activity due to their complete surface protection by long alkyl chain (oleate) since they may form complex structures like core/shell.
- iv) Clear evidences showed that if salt type surface modification is available on the particle surface, at the end of photocatalytic activity tests, ligands may be removed from the surface during catalytic process. Therefore some anomalies are seen in the photocatalytic activity.
- v) Nanorods have shown better photocatalytic activity when compared to 30-40 nm distorted hexagonal ZnO examples of nanoparticles. This is possible due to the inefficient surface coverage of the nanorod structure which facilitates the active radical and/or exciton formation and transportation of these species to the nanoparticle surface.

4.3 Synthesis of Visible Light Active, Multibranched TiO₂ Nanostructures by Hot Injection Method

Hot injection method is generally used for the fabrication of monodispersed chalcogenide type of nanostructures which is capable of the visible or IR light emission^[133-134]. Hot injection method have been applied for the production of complex nanostructures of the metal oxide TiO₂ which is not easy to obtain by other nanosynthetic techniques^[135-136]. In hot injection synthesis, after the production of quantum dot or nanocrystal many modifications can be achieved as classified below^[49];

- a) Growth control with surfactants other than TOPO: For the surface modification TOPO and TOP are most used surfactants due to its capability of resist up to high temperatures. By varying this parameter crystal properties are changed.
- b) Ligand exchange after synthesis: The surface properties and chemical interaction character of as synthesized high-quality nanocrystals can be further modified by post-preparation methods by the ligand exchange or phase transfer reactions. This is for the modification of particle biocompatibility or quantum yield of the nanocrystals.
- c) Inorganic passivating shells: Optical features can be positively increased by the synthesis of another type of nanocrystal which is grown additionally on top of the fabricated nanocrystal. There should not be a big mismatch in the core/shell interface. Also thin shells can produce defect structures which is not desirable and should be prevented.
- d) Synthesis of nanocrystals with a non-spherical shape: If the total growth rate is slow then nanocrystals form generally a spherical structure which minimizes the surface area. This is the necessity of thermodynamics. If we can manipulate growth conditions of nanocrystals in a way that different crystal facets grow with different growth rates then it is possible to fabricate highly anisotropic nanocrystals with hot injection method. Nanocrystal shape control is under the kinetic control and heterogeneous equilibrium of the coordinating molecules (chemisorbed versus dissolved) that is different for different crystal facets.
- e) Alternative precursors and/or solvents: Hot injection solvents are generally toxic organometallic precursors and coordinating solvents. They have been investigated at the beginning of the method evolution. If alternative

solvents are used like fatty acids, amines or even non coordinating solvents such as octadecene it is also possible to modify the crystal structures.

4.3.1 Thermogravimetric Analysis of TiO₂ Precursor for Hot Injection Method

For the hot injection synthesis synthesis of TiO₂ nanostructures (Figure 117) we should define the decomposition profile of the titanium liquor for the nanostructure fabrication. Thermogravimetric analysis provide a very useful information of the precursor mixtures before hot injection or thermal decomposition procedures since they need a temperature definition for the proper injection time. If necessary injection is done under inappropriate conditions, desired nanoparticle formation control, anisotropy or kinetic conditions can be concluded with irregularity in nanoparticle monodispersity or anisotropic growth direction. Therefore injection temperature is examined and analyzed for a proper controlled anisotropic nanoparticles.

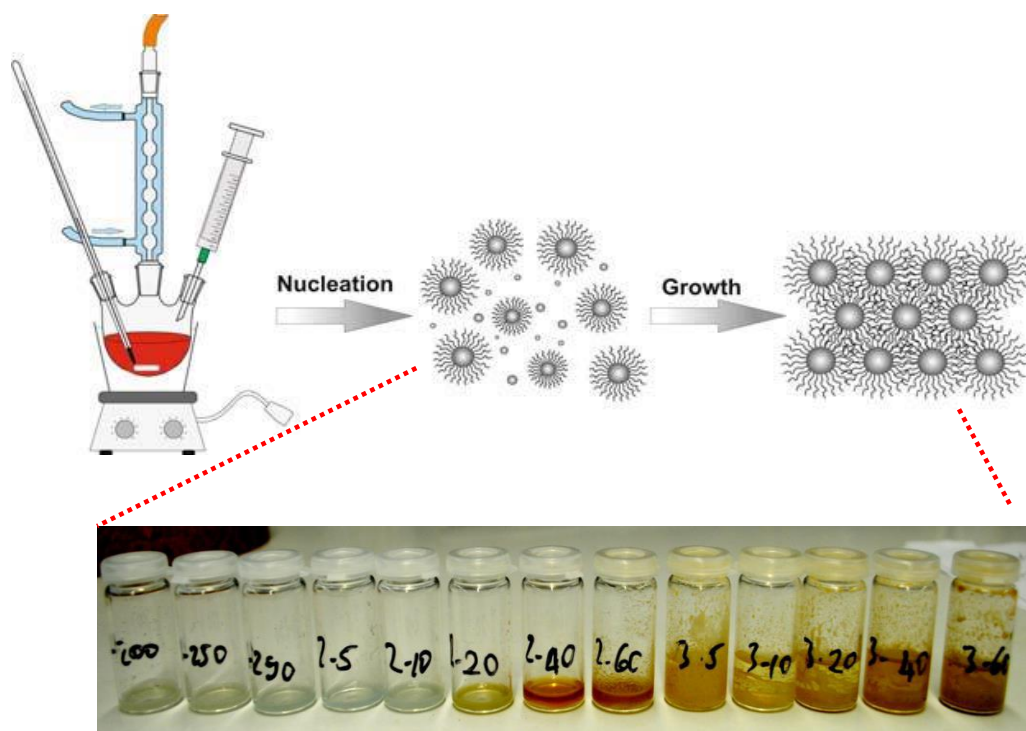


Figure 117 TiO₂ precursor mixture evolution during the hot injection synthesis.

Since used ligands (oleylamine and oleic acid) have different affinity for attaching onto the different titanium facets in the early stages of nanocrystal formation, decomposition profile of the precursor liquor gives a basic idea for the behavior of the formed primitive nanocrystals or nucleus during decomposition phase.

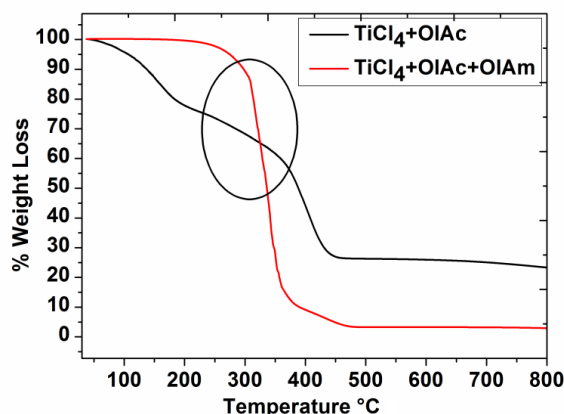


Figure 118 TGA decomposition profile of Ti precursor mixtures.

Decomposition curves for the TiO_2 precursors showed that while Oleic acid Ti-precursor is following a multistep decomposition (Figure 118) it was possible to obtain one step decomposition by the addition of oleylamine into the mixture.

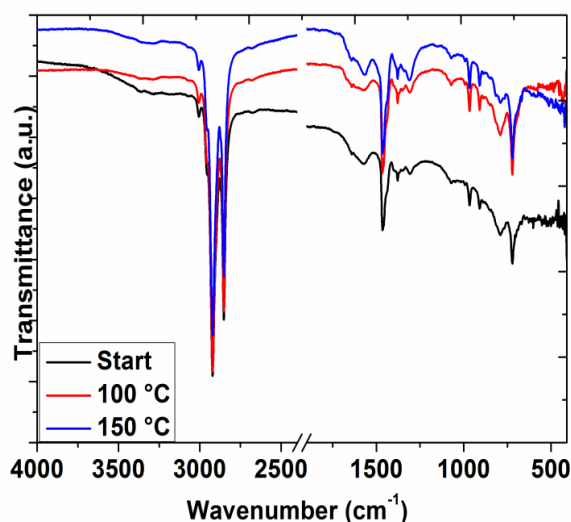


Figure 119 FT-IR confirmation of the amide formation until 150 °C.

Theoretically if there is only oleic acid present in the mixture first step should be a transition situation which produces highly reactive intermediate species. It should be noted from the FT-IR investigation in Figure 119 and Figure 120 that, precursor mixtures have very different decomposition Especially analysis of the triple mixture as seen in Figure 118 resulted that total decomposition and nanoparticle formation occurs starting from the 280 °C. As can be seen from the analysis of FT-IR spectra that during thermal decomposition reaction, amide formation which is formed by amine attack to carbonyl group triggers the TiO_2 formation. This reaction basically starts at 200-250°C range as presented in Figure 120.

4.3.2.1 Synthesis and Morphology Investigation of Visible Light Active Spherical TiO₂

For the spherical visible light active nanoparticle synthesis^[137, 82] we have used started to mix the oleylamine, oleic acid and octadecene and heat them up to 120 °C under vigorous N₂ gas protection. We keep the precursor mixture at this temperature for the removal of water molecules if available. After this point TiCl₄ precursor has been added into the reaction mixture and mixture has been heated up to 300 °C with a heating rate of 10 °C per minute. Reaction mixture has been kept at this temperature and pre-defined amount of injections have been made.

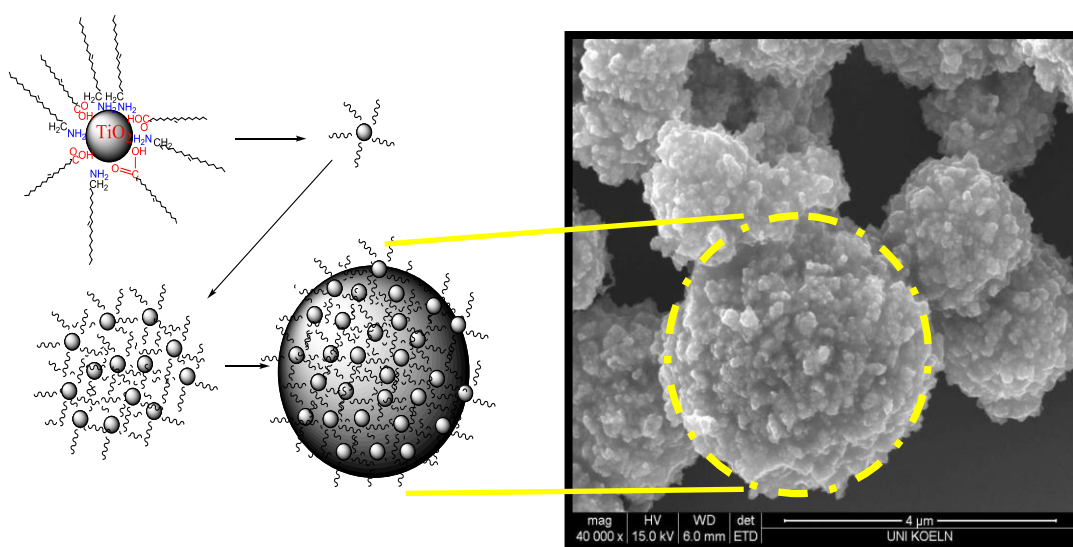


Figure 121 Self assembly formation of the spherical TiO₂ nanoparticles.

When another defined mmol amount of Ti precursor injection has been performed into the reaction system together with the other components, spherical self assembled nanoparticles have been formed. According to the SEM images, nanoparticles are forming spherical balls. This is due to the extreme amount of surfactants. Since long chain oleic acid and oleyl amine is available, after decomposition and particle formation they attach to each other for these self assembly structures as presented in Figure 121. These balls are clearly evolved from the surface modified TiO₂ nanoparticles due to the extreme amount of long chain oleyl ligands. Nanoparticles are formed but organic long chain and extreme concentration of this long chains favor the ball like self assembly.

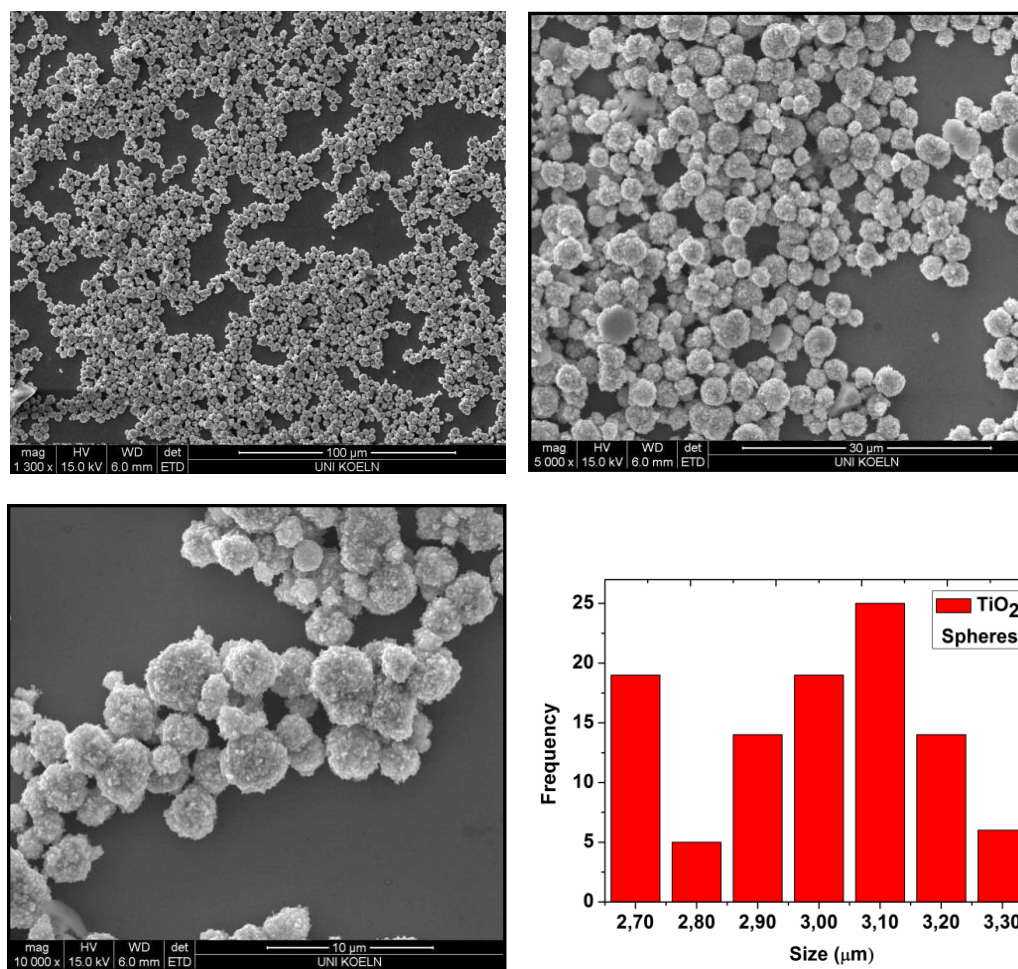


Figure 122 Self assembly spheres of TiO₂ and their size distribution.

One interesting point of these nanoparticles, under SEM investigation it has been clearly shown that, these balls are comprised of smaller particles. TEM investigation of the spherical nanoparticles before and after the injection showed that there is no big difference possibly due to the hindrance of the organic pool as presented in TEM. Primary particle size is about 30 nanometer. These ball like self assembly structures are having an average size distribution of 3,10 micrometer which has been contributed by nanoparticles. Real size detection has been done by a detailed statistical analysis of the SEM figures as presented in Figure 122. As clearly seen in the figures, small nanoparticles have formed morphologically spherical and various sizes of organically modified ball like nanostructures. Interestingly enough, color of the fabricated nanocrystals was stangely orange-deep yellow. Comparison of this deep yellow-orange color of the spherical TiO₂ assemblies with commercial TiO₂ P-25 enlightened the difference between the commercial and as-synthesized particles. According to the literature^[138-140] this type of color arises when TiO₂ is doped with a non

metallic (especially N) anion. Images obtained from the literature are clearly showed that when N is a dopant color of the TiO₂ nanocrystals evolve from pale yellow to the deeper yellow-orange. In order to analyze this issue we calculated the band gap energy of the TiO₂ nanocrystals as presented below.

4.3.2.2 Band Gap Calculation of Spherical TiO₂ Nanostructures

Dark yellow colored nanocrystals are clearly different from the commercially available P-25 white nanoparticles. When they are deeply compared, it is widely known that %70 anatase and %30 rutile mixture of the commercial nanoparticles have the band gap of 3,2 eV. This is clearly in the UV range. But when fabricated spherical nanoparticles UV-Vis absorption properties are measured and required calculations made, it has been found that band gap of the fabricated nanocrystals was in the visible range as $E_g = 2,39$ eV (Figure 123). According to Kubelka- Munk function it is possible to calculate the band gap characteristics of a metal oxide nanoparticle. In this procedure absorption spectra is recorded and transformed into energy units by required calculations.

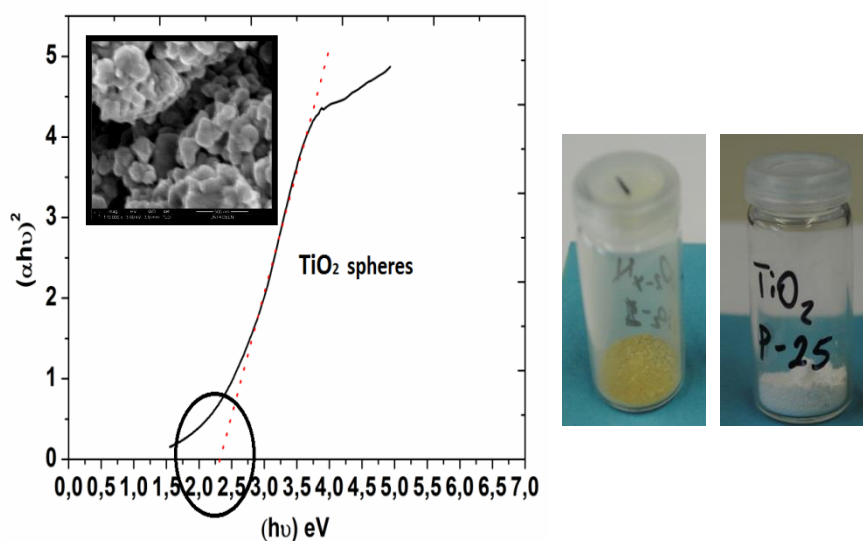


Figure 123 Band Gap calculation and SEM images of TiO₂ nanoparticles and color comparison of spheres with P-25.

4.3.3 Crystallinity, Surface and Thermal Properties

Fabricated nanoparticles showed anatase crystal structure. Due to the low intensity of the peaks nanoparticles have been heated to 300 °C for overnight to increase the crystallinity but similar patterns have been observed as presented in Figure 124.

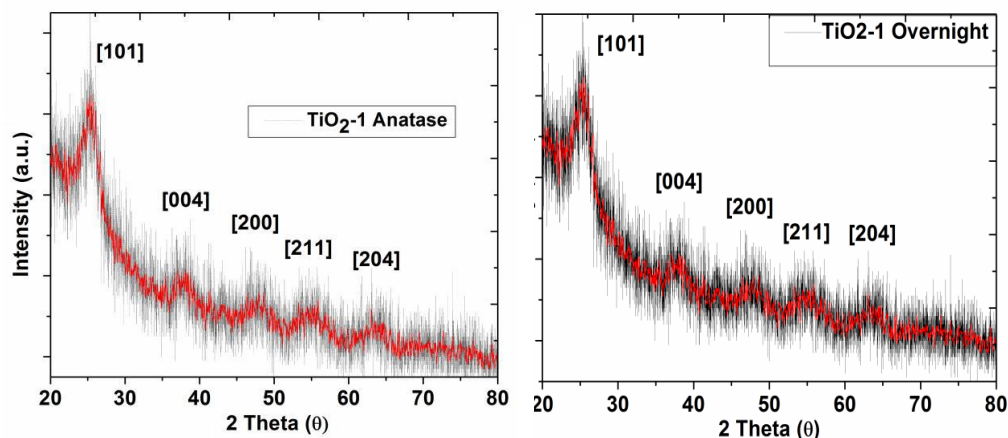


Figure 124 XRD patterns of the spherical TiO₂ nanoparticles.

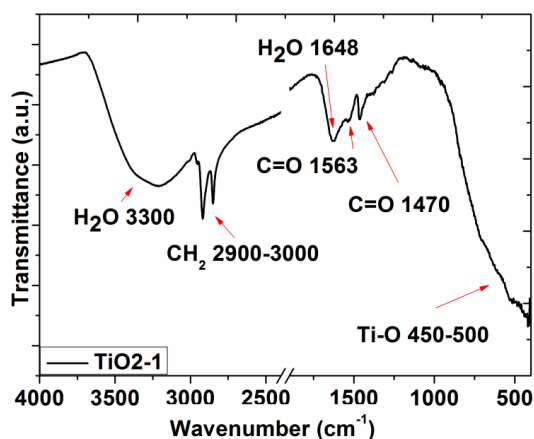


Figure 125 FT-IR investigation of the spherical TiO₂ nanoparticles.

Analyzed peaks established that crystalline structure is anatase and no rutile modification has been detected. Still due to the extreme organic surfactant loading, surface features should be investigated for the further understanding. FT-IR spectra (Figure 125) of the spherical nanocrystals has revealed the organic oleate groups and small amount of water molecules attached on the surface. Zeta potential measurements pointed that these nanocrystals have around -12 mV as a surface charging which can contribute the these self assembly structures. High organic content on the nanoparticle surface resulted also high weight loss during the thermal analysis and EDX resulted only Ti and O atoms as presented in Figure 126.

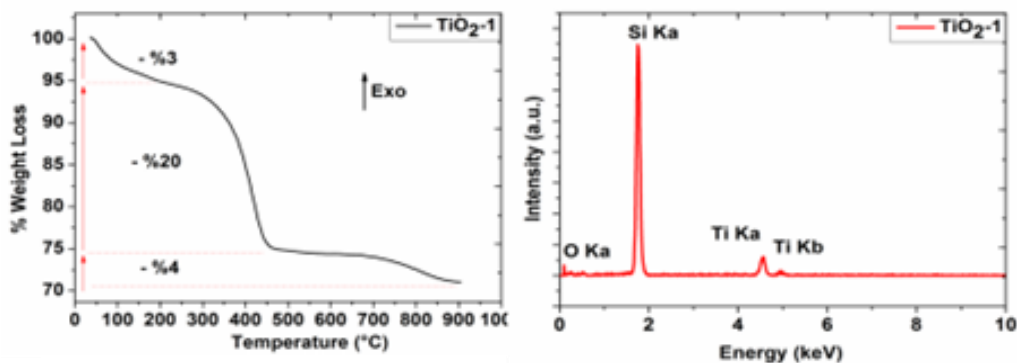


Figure 126 Thermogravimetric analysis and EDX of the spherical TiO₂ nanoparticles.

%27 weight loss from the thermal analysis of nanoparticles and carbonyl and CH groups which are visible in FT-IR spectra which presented before, proves the organic loading.

4.3.4 Visible Light Active, Multibrached TiO₂ NR by Hot Injection Method

In order to investigate nanoparticle evolution for TiO₂ another injection experiments have been performed. Due to the excessive amount of injection in previous section resulted spherical particles, it has been applied only 3 fold more of Ti precursor during the injection process. Hot injection method served as a morphology and crystallinity manipulator as injected precursor provided elongated nanostructures. Most important mark of this reaction is that, injected mixture has been given very slowly to the reaction (about half an hour) mixture, so that monomer flux for the kinetic control can be arranged accordingly.

4.3.4.1 Synthesis and Crystallinity of Visible Light Active Multibranched TiO₂ Nanostructures

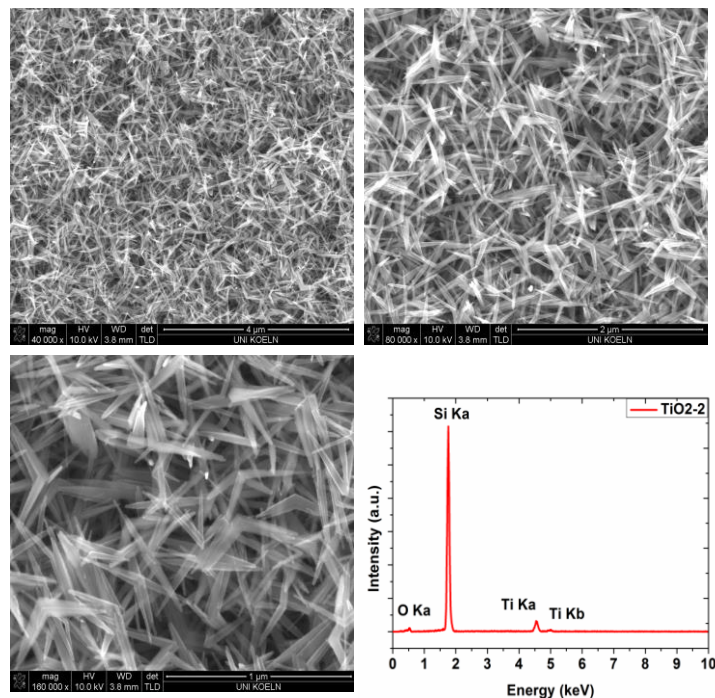


Figure 127 SEM images of the multibranched TiO₂ nanocrystals and EDX investigation.

After hot injection synthesis, 3 fold injected particles have been analysed by SEM. Results unveiled the elongated nanocrystal morphology. Interestingly, elongated nanostructures (Figure 127) have been showing multibranched geometry which arises from the kinetical control of the nanoparticle synthesis. Presented EDX result revealed that the composition of the elongated nanostructures showing only titanium and oxygen. This is a clear evidence of the pure TiO₂ nanocrystals which is also showing the visible light activity. Compared with P-25 it is quite visible that the nanocrystals are remarkably different and very close to deep yellow orange (Figure 128) which means the visible light absorption. UV spectra and band gap analysis of the elongated nanocrystals revealed $E_g=2,34$ eV band gap energy which is in the visible range of the electromagnetic spectra.

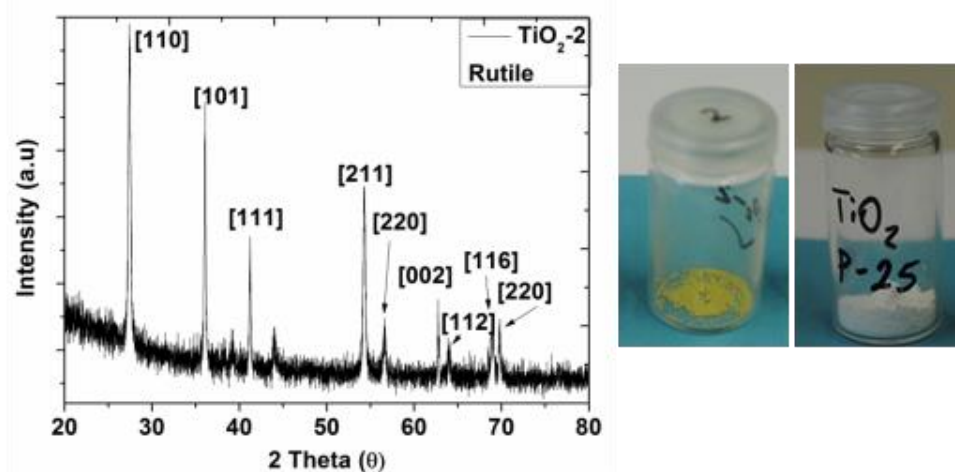


Figure 128 XRD spectra and color difference of elongated TiO_2 .

XRD spectra of the elongated TiO_2 (Figure 128) nanostructures showed an interesting results since it seems that the elongated nanocrystals have rutile crystal pattern. There are only 2 peaks which are not matching with the rutile peak list and they are very low in intensity compared to rutile peaks. Still peak at about 38 can attribute to anatase and peak at 44,8 can be attributed to brookite crystal structure. Since there is no other supporting data on these crystal structures it can be simply accepted that they are artifacts. It is extremely interesting phenomena due to the anatase to rutile transformation. As in another reaction it has been heated only precursor mixture without further injection. Crystal structure of these nanocrystals were also anatase and more or less the same with spherical nanocrystals. But as indicated here, well arranged and slow injection seems changed the crystal structure from anatase to rutile. There is no other parameter but concentration which transforms the crystal structure from anatase to rutile. By hot injection this direct crystal transformation for the TiO_2 nanostructures has been observed.

4.3.4.2 TEM Investigation of the Multibranched, Visible Light Active TiO_2

Due to the highly anisotropic character of the TiO_2 nanostructures TEM and HR-TEM analyses provided additional information about the fabricated nanocrystals. General results revealed that TiO_2 nanostructures have the elongated bullet like and they seemed clearly attached selectively to each other. When it is focused to size distribution, angle distribution between attached nanorods, multibranched gallery of the nanocrystals, one can get the information that nanorods are slowly transforming themselves to the multibranched nanostructures as the time continues. Therefore basically it is possible to define three fundamental rules for the elongated TiO_2 nanostructures which will be

analysed. Since elongated nanorods have bullet like structures it was possible to detect the sharp tips and larger bottom of the nano rod shaped structures.

4.3.4.3 Fundamental Nanorod Morphology for the TiO_2 Nanostructures

Detailed TEM investigation revealed that basic rule for the TiO_2 nanorods, is they form elongated bullet like nanostructures which one side is sharp and other side is broad.

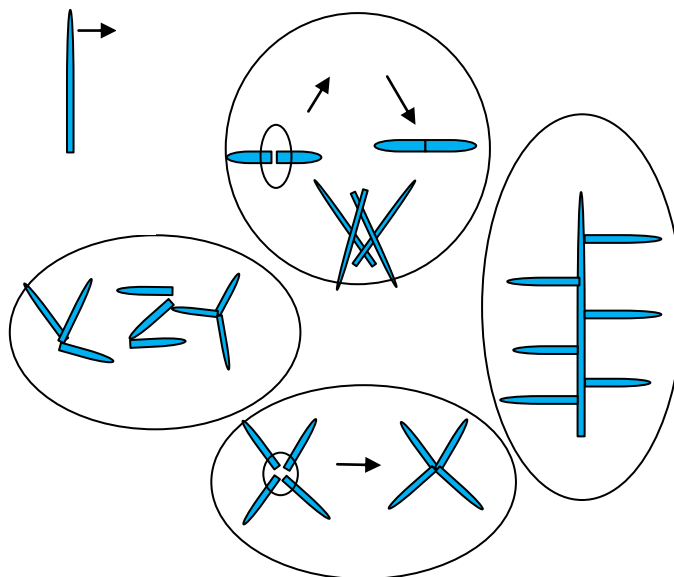


Figure 129 Schematic perspective of multibranching in the TiO_2 nanostructures. Elongated nanoparticles also form dipod, tripod, tetrapod and multipod like structures

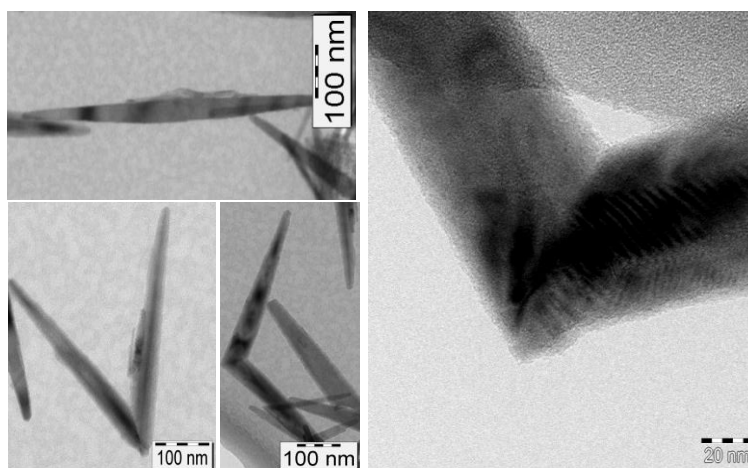


Figure 130 Dipod like TiO_2 nanostructures.

(Figure 129). According to the TEM investigation, sharper tips of the elongated nanostructures are always visible and larger bottoms are attaching to each other

4 Results and Discussion

to form multipod geometries. Dipod like structures basically formed with two elongated bullet like nanorods. Due to the attachment orientation, dipods can be two side sharp rod or V type morphology as shown in Figure 130.

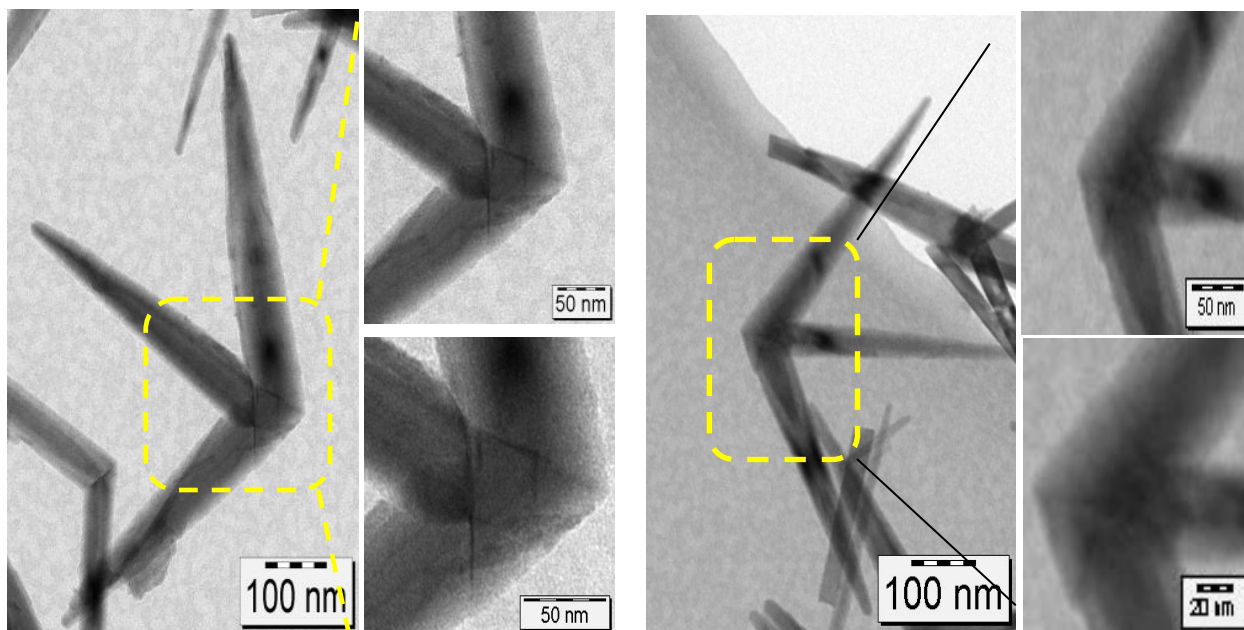


Figure 131 Tripod like nanostructures of TiO_2 .

Tripods are generally have the morphology (Figure 131) that all rods are oriented into the same axis which forms a shape like Poseidon's trident. Y shape has also been observed but trident was more abundant. Tetrapod geometry has basically 3 different orientation. First (T1) one is a visible X shape which all arms are (with very small angle variation) in the same plane (Figure 132). Second orientation (T2) shows that only one of the arms has been grown up on the z axis while other three arms are on the same plane. Therefore it looks a tetrahedral geometry when if the edges are drawn but angles between the arms were not perfectly matching with the expected geometry. Third orientation (T3) revealed the geometry that if not only one but two of the arms grown up on the two other arms while the latter are in the same plane. Grown arms of the particles are not in the same geometric plane if compared to each other.

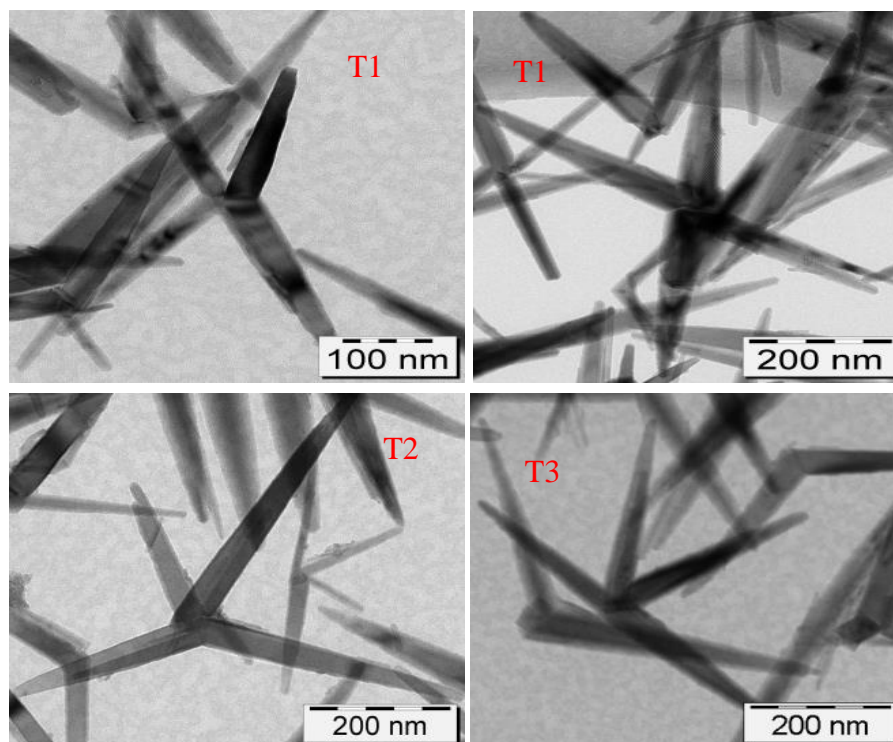


Figure 132 Examples of tetrapod like TiO_2 nanostructures.

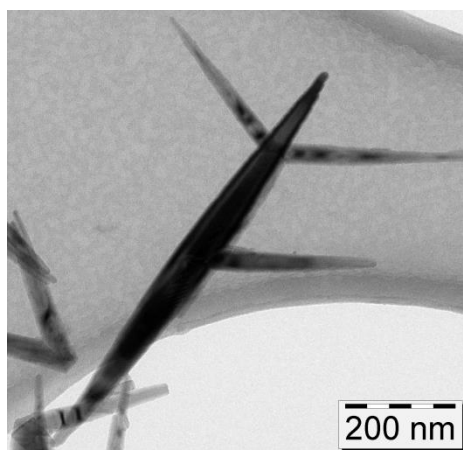


Figure 133 Obtained multipod TiO_2 Nanostructures.

In addition to the dipod, tripod, tetrapod structures multipod nanostructures have been also observed as presented in Figure 133. Multipod structure is like tetrapod but the main skeleton seems that it is thicker and longer than the side arms. Since in previous examples of the multipod structures, arms are completely same in size and thickness, this new structure provides another example for the multipod fabrication. Side arms orientation is in the same direction when they are in the same side of the main skeleton but also opposite arms represent a symmetrical perspective. Synthesis of these elongated nanostructures have been classified according to their morphology.

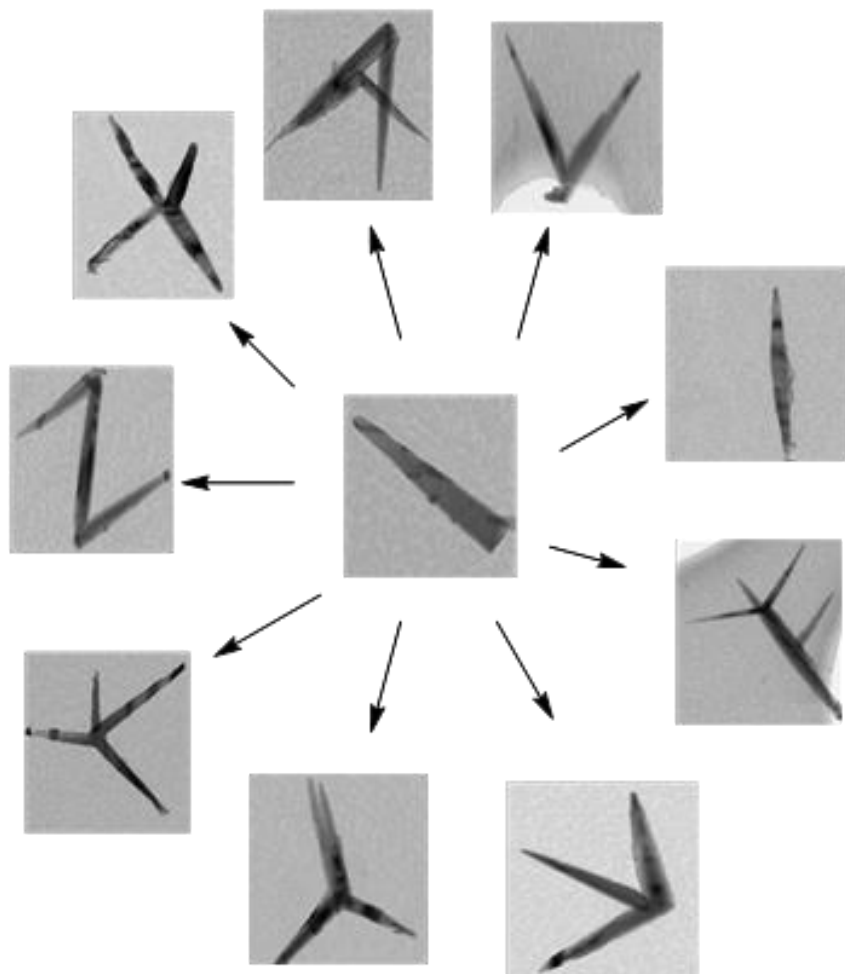


Figure 134 Fabricated alphabet nanogallery of TiO_2 without size bars.

This classification with TEM images have been presented in Figure 134. This is the gallery of the elongated TiO_2 nanostructures or can be accepted as some parts of the Latin alphabet as nanorods clearly seen as in the form of capital letters from alphabet.

Detailed TEM investigation have shown that V shape is the most available form among the fabricated nanostructures. If we also assume that nanorod shaped structures belong to same family with V shape which means dipodic morphology, 60 % of the of the whole multipod geometry are in the dipodic state (Figure 135).

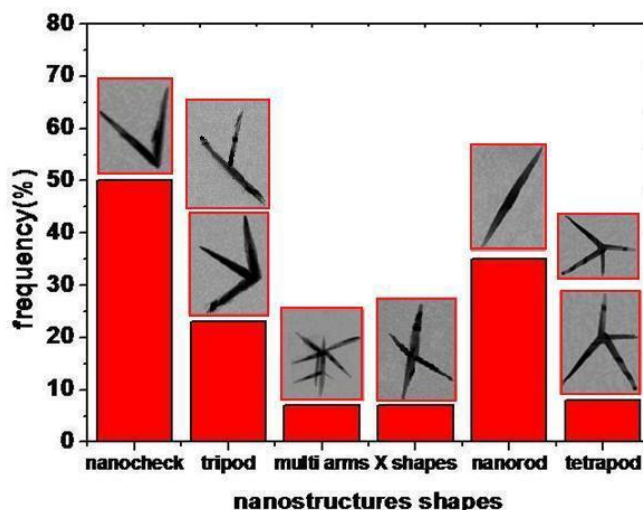


Figure 135 Proximity of the different TiO₂ nanostructures.

Tripod like, tetrapod like structures and after that multiple branched structures follow the proximity order respectively. Formation mechanism of these nanorods have been rarely observed and reported as twinning mechanism or selective facet growth. Both of the mechanisms can be observed here by analyzing the TEM images.

4.3.4.4 Angle Between the Attaching Nanorods

According to the detailed TEM analysis it has been detected that V shaped dipod structures have some specific angles between the arms^[137].

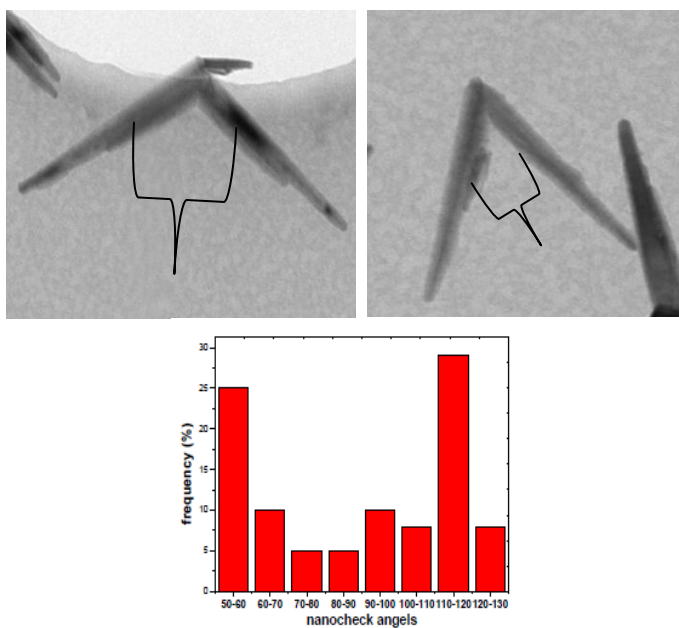


Figure 136 Angle distribution between the V shaped dipod structures.

4 Results and Discussion

The angle between two elongated arm actually follows a regularity in high percent.

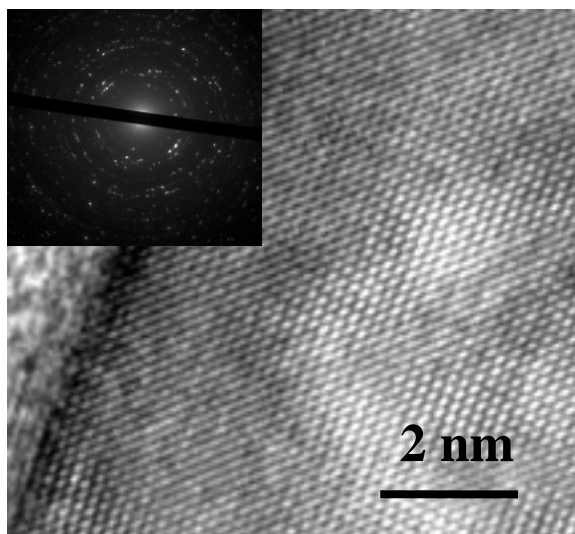


Figure 137 HR-TEM image and SAED pattern of the TiO_2 nanorods.

This angles are between 50-60 and 110-120 degree. This can be explained by the truncated growth of the primer crystal. Since truncated nanostructures have energetically more active facets, during the kinetical growth under the monomer flux control, more energetic facets grow faster than lower energetical facets. This lead V type morphology and since angles between these facets are in the similar values, this angles can be anticipated. This bimodal distribution of the angles are averagely 65 and 120 degree respectively. They intensively adapt into two angles as shown in the corresponding morphology in Figure 136.

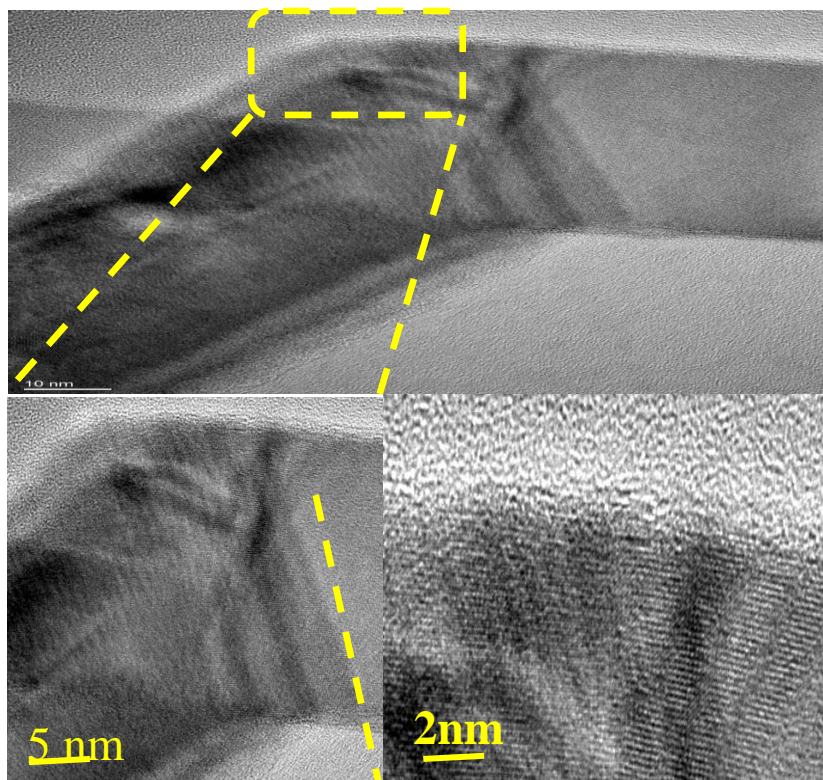


Figure 138 HR TEM investigation for the junction points.

HR TEM investigation of the elongated nanostructures shows clear crystal orientation and atomic orientation (Figure 137). Rutile crystal structure has been detected by facet corresponding [001] fringes of the nanocrystals (Figure 138) the rutile phase. As shown in Figure 138, there is a continuation in the crystal structures which confirms of the TiO_2 without other phases.

4.3.4.5 Possible Formation Mechanism for the TiO_2 Multibranching Nanostructures

Alivisatos^[46] has shown in a previous study that that growth of the multibranching TiO_2 nanocrystals depend on the truncated cores and growth proceeds from highly energetic facets as shown in Figure 139.

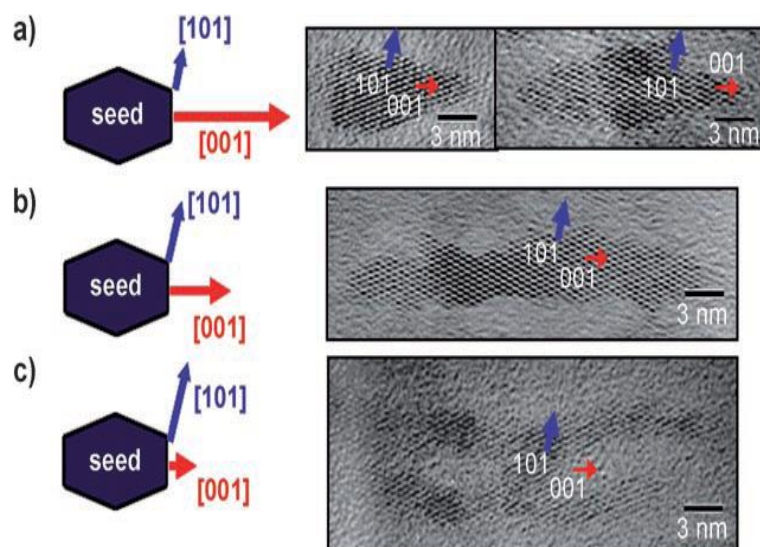


Figure 139 Shape evolution of TiO₂ nanocrystals through the surface energy modulation effect by using surface selective lauric acid (LA) surfactants. a) Bullet- and diamond-shaped nanocrystals are formed at low LA concentration. b,c) At higher LA concentrations rods (b) and branched rods (c) are formed. Beginning precursor mixture for TiO₂ formation forms transient carboxylic acid complexes of the titanium and amine. These structures perform condensation reactions in the acidic media since attachment to the titanium requires hydrogen removal and therefore reaction medium is extremely acidic (<2 pH). Under these conditions with the help of amine and oleic acid ligands form kinetic control instead of random growth (Figure 140) ^[46].

We can simply propose that results are arises from a growth regime where thermodynamic pathways, related to the crystal-structure-directing effect of the initially nucleated seeds. Therefore surface energy variation causes a kinetic control due to the controlled high monomer flux. Crystals showed clearly that in the early stages of the reaction crystals Especially with diffusion-limited monomer flux and surfactant-induced stabilization causes elongated nanocrystals with kinetic control. For the mechanism investigation aliquot has been taken from the early stage growth of the nanorods.

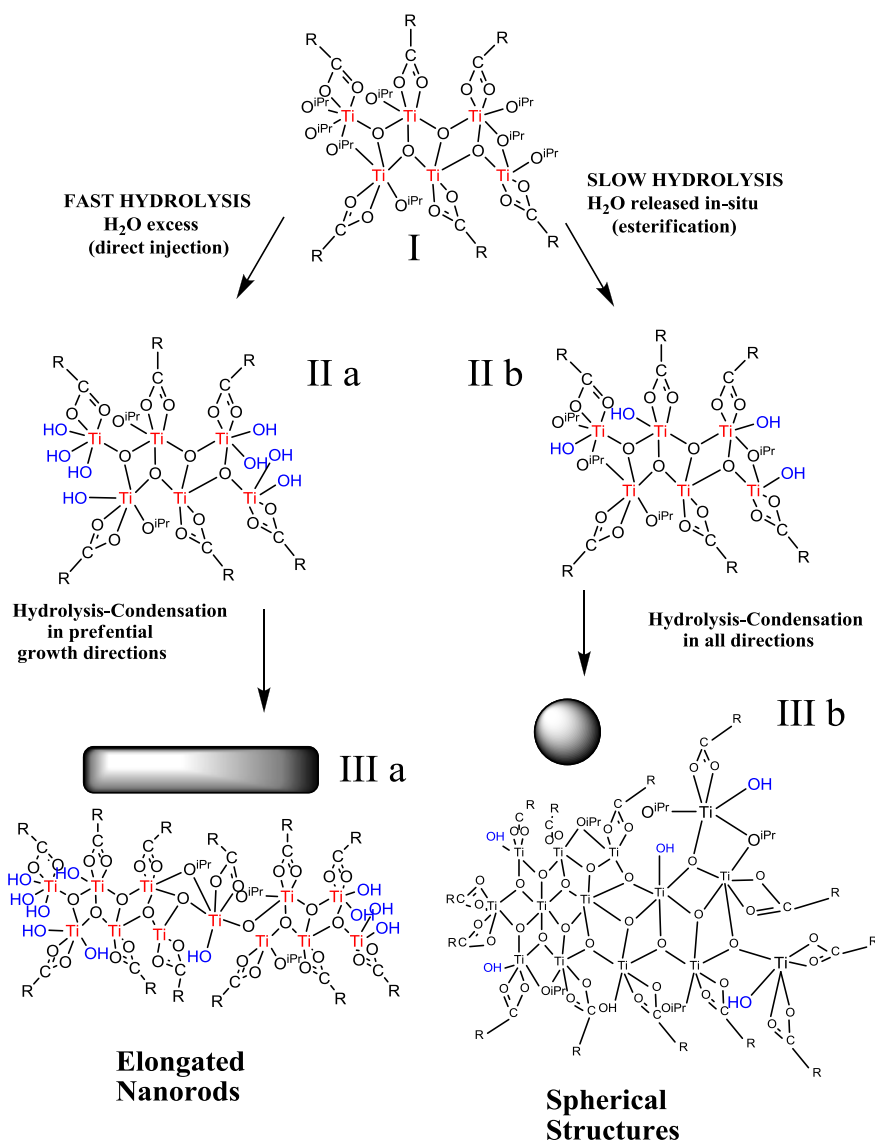


Figure 140: Titanium alkoxide for the elongated nanostructures^[83].

(Figure 141) have cube like or truncated shapes which is to be grown later with a kinetic control. Investigated TEM images showed that synthesized nanocrystals are generally showing distorted truncated nanostructures with different geometrical edges. Cubes or trigonal pyramids or elongated square pyramids are visible. This shapes are the clear proof for the kinetic control and ligand modulated crystal shape evolution. Since TiCl_4 has been used as precursor, during the injection process pH value of the solution is extremely low as evidenced by qualitative examination of the solution after the injection and during the reaction. Additionally, HCl is available also in gas form which allows low pH value in all locations of the reaction flask. Therefore reaction is programmed for a kinetic control and elongated nanorods have been obtained.

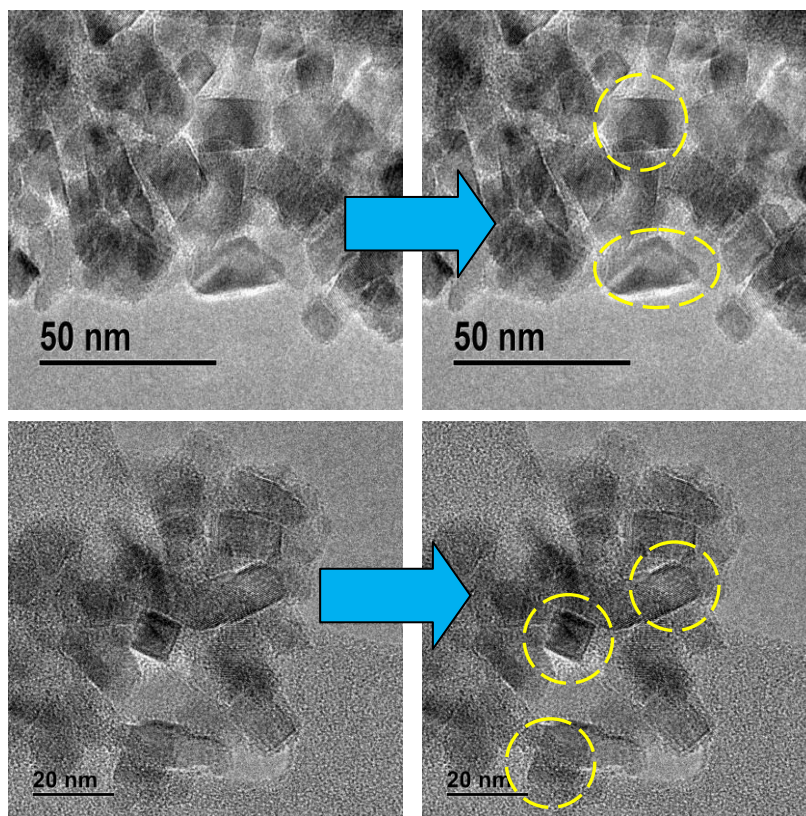


Figure 141 Distorted truncated and cube like truncated structures in the early stages of nanorod formation.

4.3.4.6 Nanomaterial Applications of Spherical and Multibranched Visible Light Active TiO₂ Nanostructures

Synthesized nanostructures have been used for the visible light photocatalysis and for the decomposition of organic dye methylene blue. For this aim solar illuminator as visible light source has been used as presented in Figure 142.

4.3.5 Solar Light Driven Photocatalysis of Visible Light Active TiO₂

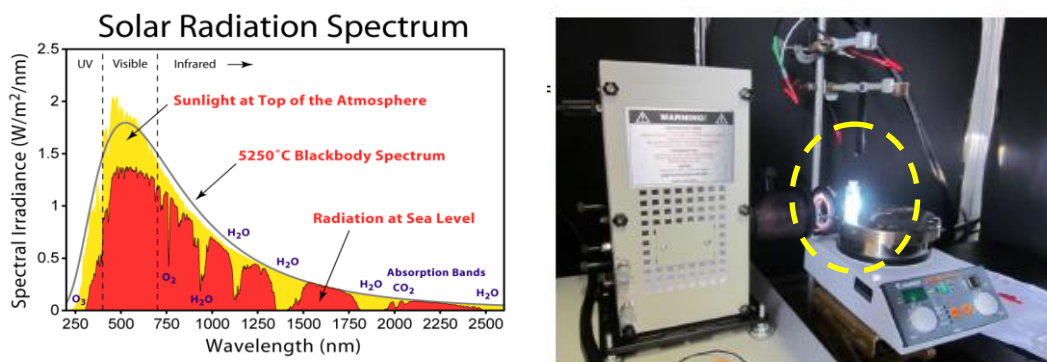


Figure 142 Solar light spectrum and solar driven visible light photocatalysis. Fabricated nanocrystals have been mixed with the defined concentration of methylene blue dye. This stock solution has been used for the visible light

4 Results and Discussion

photocatalysis during the decomposition of methylene blue (Figure 143) solutions. It has been showed that synthesized visible light active TiO₂ nanostructures show remarkable photocatalytic activity as compared to commercial P-25 TiO₂. Organic dye solutions have been cleaned within a very short time which is almost impossible by the commercial P-25 nanoparticles. Multibranched nanorods show slightly higher activity when compared to spherical nanoparticles. Especially photocatalytic activity of TiO₂ has been enhanced about %60 when compared to P-25. This is the proof for the nitrogen availability in TiO₂.

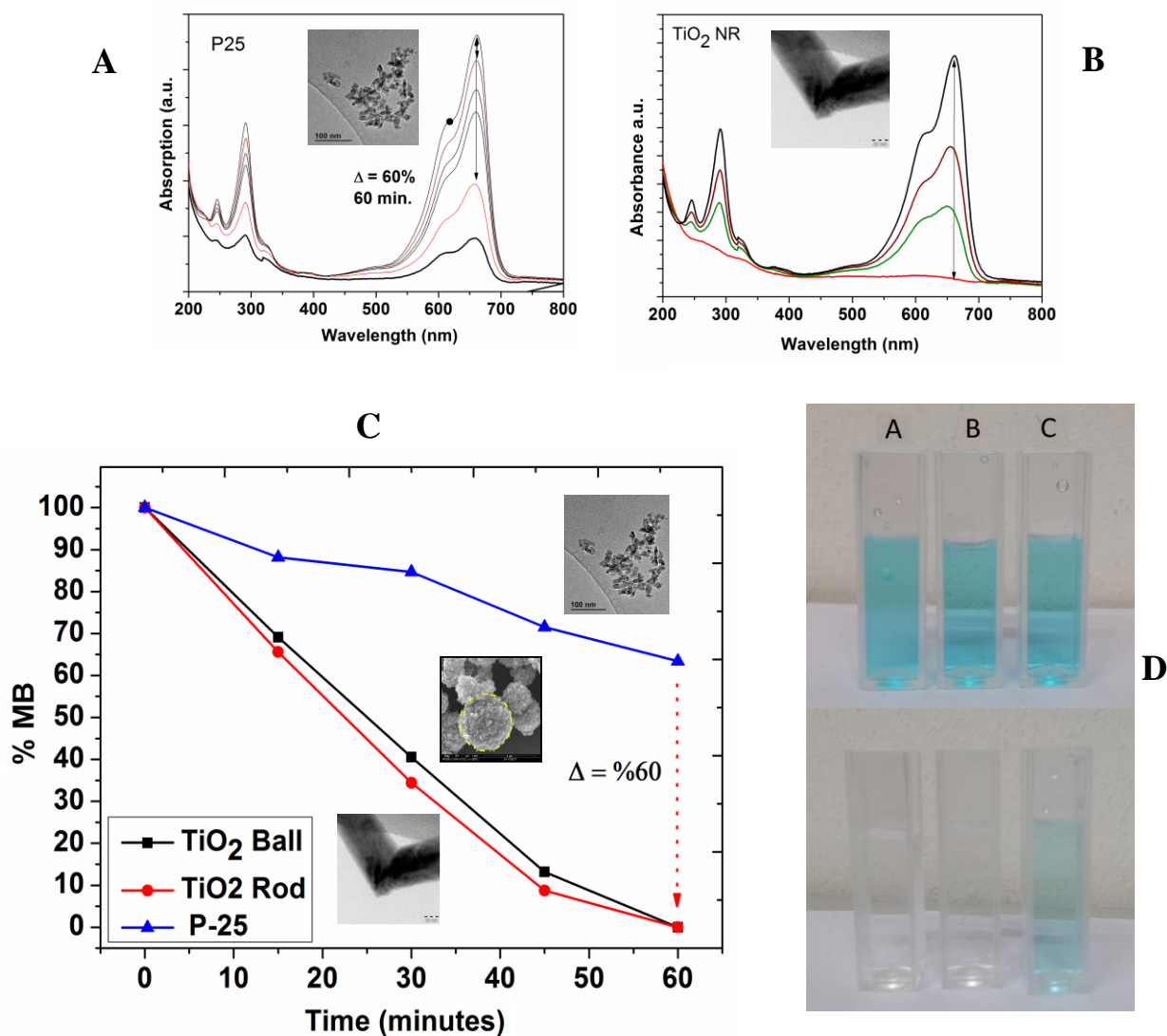


Figure 143 Photocatalytic comparison activity of of P-25, TiO₂ Rod and TiO₂ Spheres by solar light (A: decomposition of MB by P-25, B: decomposition by TiO₂ NR, C-D: comparison of activities, visual observation of MB decomposition).

4.4 Metal Oxide / Polymer Nanocomposites

Metal oxide nanoparticles are widely used for the MO_x/polymer nanocomposites due to their optical^[142-143], emission^[144-145], photocatalytic^[146-148], antibacterial^[149-152] and hydrophilic-hydrophobic^[153-154] features. Accordingly, analysis and material properties of ZnO-TiO₂/Polymer hybrid nanocomposites for light emission, antibacterial activity, superhydrophilic surface and selective UV protection properties.

4.4.1 Hybrid Inorganic Organic Polymer/MO_x Nanocomposites

Inorganic organic hybrid nanocomposites have been used for their enhanced thermal^[155], anti scratch^[156], anti abrasive^[157] and chemical durability^[158] features.

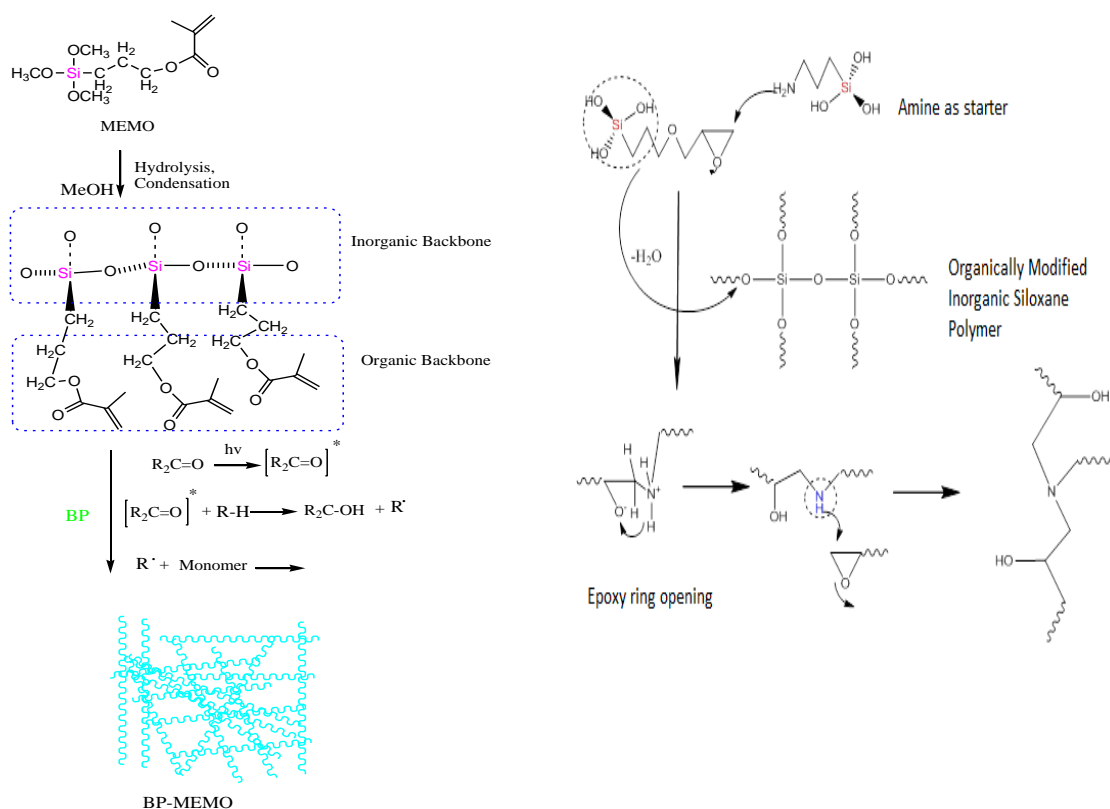


Figure 144 Hybrid nanocomposite preparation techniques left) UV curable right) epoxy amine.

Introduced nanoparticles are attached into the growing silica network by hydroxyl or alkoxy groups^[159-160]. Since alkoxy silane acts also as surface modifier with the contribution of other polymers nanoparticle dispersion is in the nano level (Figure 144). Particle introduction basically can be done by two different method;

4 Results and Discussion

- a) In situ nanoparticles formation ; where nanoparticle spontaneously is formed in the hybrid network during hydrolysis and condensation reactions
- b) Direct introduction; where the nanoparticles are synthesized somewhere else and introduced into the nanocomposite network during the hydrolysis, condensation and polymerization processes.

Co-polymers in addition to alkoxy-silanes provide additional thermal, optical and flexibility features to the nanocomposite.

4.4.1.1 TiO₂ Nanowire/Epoxy-amine Superhydrophilic Nanocomposite

For the synthesis of superhydrophilic surfaces, 10 M, 100 ml NaOH, has been mixed with 2 gr P-25 nanoparticles and ultrasonically dispersed. After that 30 ml from this mixture has been placed into the hydrothermal tube and reaction has been conducted at 150 °C about 48 hours. Obtained nanostructure has been washed with excessive water, EtOH and acetone respectively and dried in vacuo. There are very similar synthesis methods for the nanowire synthesis in the literature^[161-162]. SEM images of the fabricated material showed that TiO₂ (Figure 145) was a nanowire type material. For the fabrication of superhydrophilic nanocomposite coatings, it has been prepared a nanocomposite of alkoxy-silane and with nanowires. For the synthesis of nanocomposite, a mixture of Glycidylpropyl trimethoxysilane and water with diluted HCl

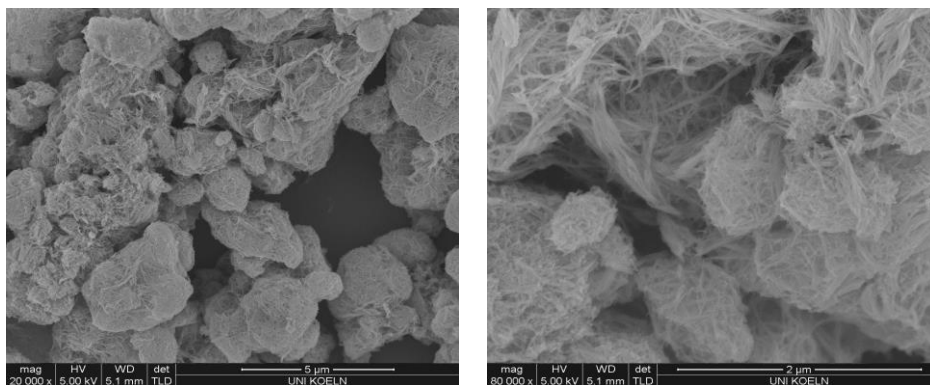


Figure 145 TiO₂ Nanowires by hydrothermal method by self dissolution of TiO₂ nanoparticles.

(GLYMO)/Tetraethoxysilane (TEOS) mixture has been prepared at 1/10 proportion for the nanocomposite formulation and stirred for the homogeneity



Figure 146 Superhydrophilic nanocomposite coatings on glass (surface angle <math>< 5^\circ</math>).

and %10 w/w TiO_2 nanowire compared to polymer total weight has been added and homogeneously dispersed. After hydrolysis and condensation reactions about 3 hours, aminopropyl trimethoxysilane has been added as an amount of %10 mol amount of total epoxy compound. Prepared reaction mixture has been coated onto the glass slides with spin coating method with 2000 rpm 15 second. Nanocomposite coatings have been cured at 150°C , 10 minutes. Observation of contact angles after synthesis showed that droplets formed a contact angle which is lower than 5 degree (Figure 146). These hybrid coatings can be coated onto glass, metal or plastic surfaces for superhydrophilic film applications.

4.4.2 Polymer and ZnO QD Nanocomposites

Oleate@ZnO quantum dots have been phase transferred with gluconic acid and washed with EtOH and acetone respectively and dried 24 h in an oven at 80°C . In another flask methacryloxypropyl trimethoxysilane has been hydrolysed with 0,1 M HCl and gluconic acid modified ZnO quantum dots have been introduced into this mixture with different variations.

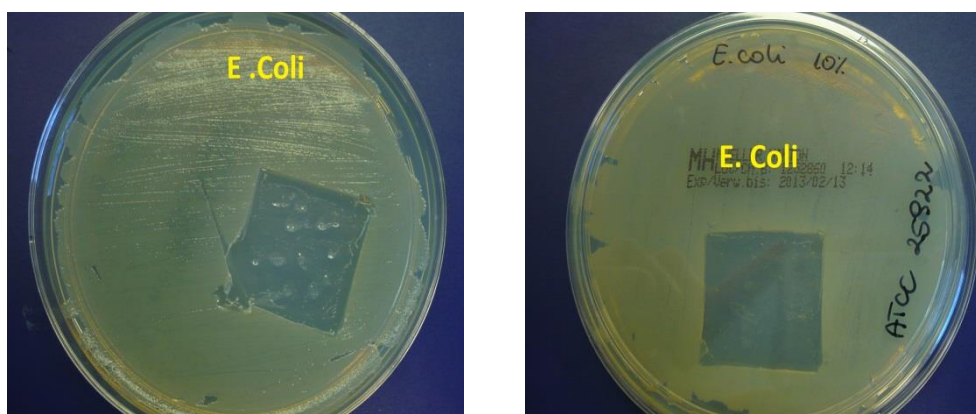


Figure 147 %5 (left) and %10 (right) percent ZnO QD containing nanocomposite coatings antibacterial testing.

4 Results and Discussion

After addition of radical starter with %3 (benzophenone) transparent nanocomposite mixtures have been obtained which were coated onto the glass substrates with the spin coating method as 2000 rpm, 10 second. After that UV lamps have been used for curing the nanocomposites with 354 nm. After 20 minutes nanocomposite coatings have also been cured within an oven thermally at 150 °C, 10 minutes. These coatings have been tested against to a broad band bacteria such as; E.Coli, S. Aureus, MRSA, Salmonella which are similar to previous studies^[163-164]. It has been shown that quantum dot embedded nanocomposite coatings are completely transparent, showing broadband antibacterial activity and quite durable against chemicals. Therefore growth of extremely dangerous bacterias like E.Coli and can be prevented with different ZnO concentration as shown in Figure 147. Same nanocomposite coating system with %5 and %10 ZnO QD concentration is also efficient against to S. Aureus and P. Aeruginosa bacterias (Figure 148).

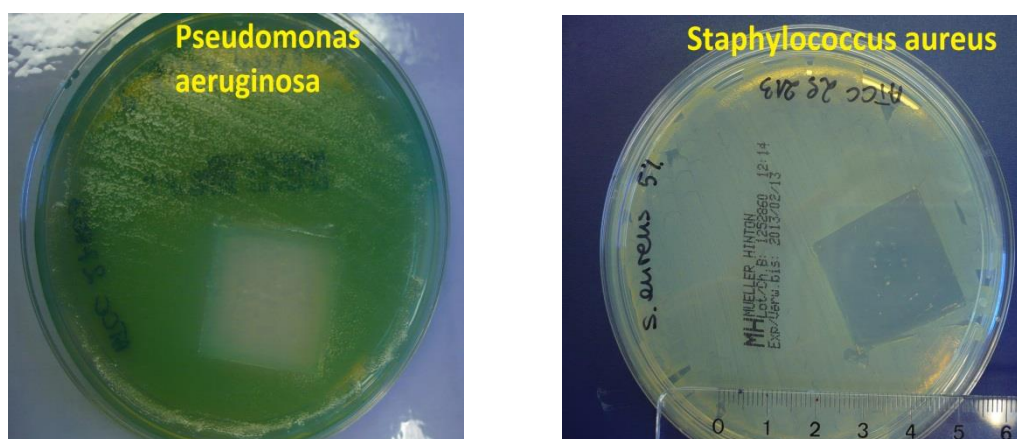


Figure 148 Antibacterial test for 5% ZnO QD containing nanocomposite against to Pseudomonas Aeruginosa (ieft) and S. Aureus (right).

Prepared coatings systems have been tested on the glass samples after curing the spin coated films. Results showed that obtained water soluble ZnO quantum dots can be homogeneously dispersed and coated onto the glass samples for antibacterial applications.

4.4.2.1 Selective UV Protective Transparent ZnO/Hybrid Nanocomposites

Since fabricated ZnO and TiO₂ nanoparticles have specific UV absorption capacs, it is possible to use especially ZnO QD's for the Uv filtering transparent nanocomposites. For this aim, ZnO quantum dots have been firstly prepared and introduced into the hybrid nanocomposite structures. Since quantum dots extremely small, they do not form agglomerates and therefore

coating seems transparent which is decoratively desirable. Synthesized nanocomposite formulations can be applied on any surface for the UV protective transparent nanocomposite materials due to the quantum dot absorption features. Since quantum dot size selectively filters wavelengths, whole coatings can be used for the same reason.

4.4.3 Biodegradable PLA/Metal Oxide Nanocomposites

Biodegradable PLA polymer attracting big interest in the last decade. Since its synthesis is done huge amounts in the world for the different aims it is possible to modulate the PLA polymers by fabricating nanocomposite structures. They have been generally applied as coating for the glass and metal surfaces.

4.4.3.1 PLA/MEMO/ZnO QD Nanocomposites

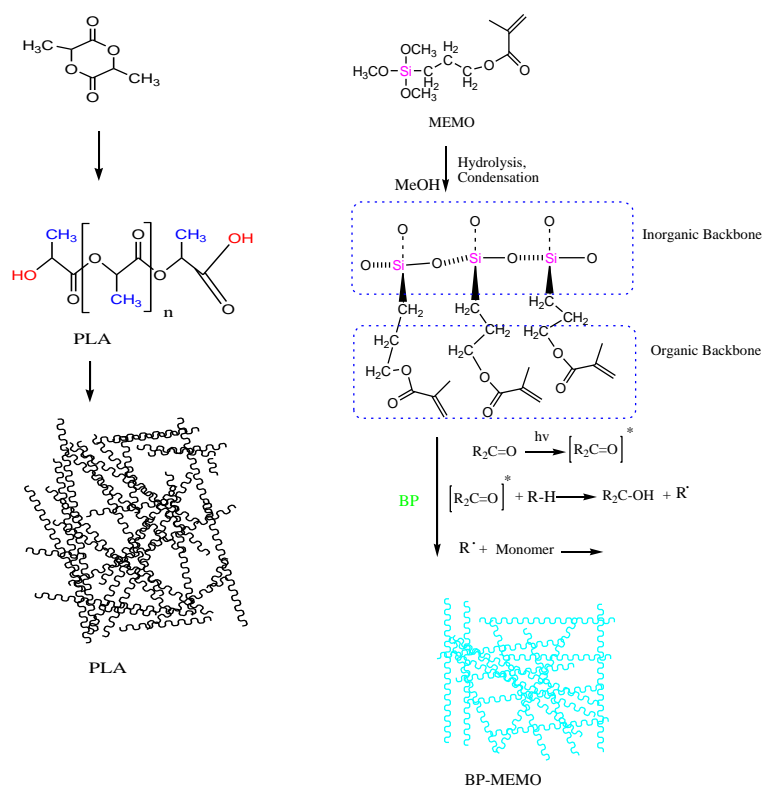


Figure 149 PLA/MEMO hybrid nanocomposite preparation.

PLA is an incredibly important polymer since it degrades in the nature and its products and nanocomposites can be improved mechanically and chemically.

As an example ZnO QD embedded PLA nanocomposites have been prepared with co-polymerization of UV curable alkoxy silane MEMO (methacryloxypropyl trimethoxysilane) as shown in Figure 149. During synthesis and homogenization, ZnO quantum dots have been introduced into the

4 Results and Discussion

polymer structure for obtaining visible light emitting nanocomposite materials (Figure 150).

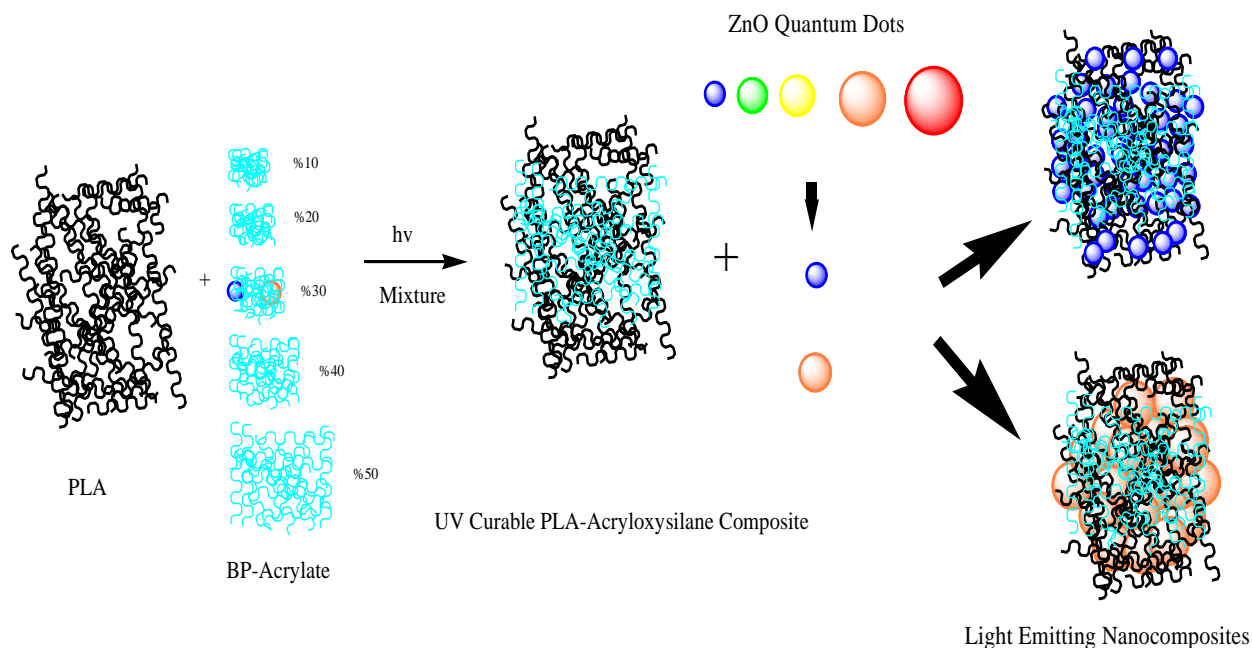


Figure 150 ZnO QD addition into the PLA/MEMO nanocomposite structures for light emitting nanocomposites.

Introduction of the ZnO quantum dots into the hybrid system can be done by dispersing them in the solvents of the nanocomposite system prior to PLA/MEMO co-polymers like in EtOH or H₂O.

FT-IR analysis (Figure 151 and Figure 152) clearly showed that polymerization of double bond can be tracked by disappearing of corresponding peak as also shown in [165].

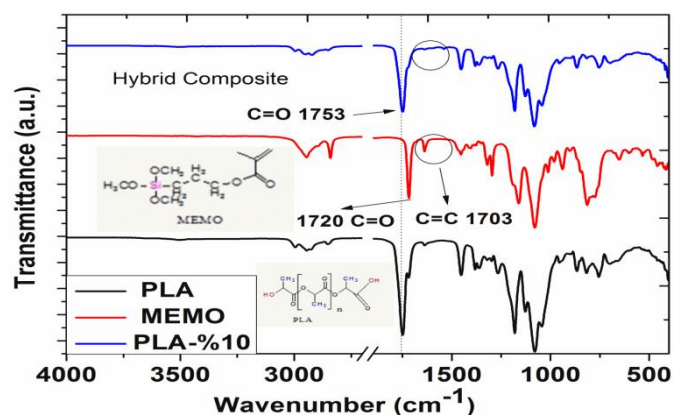


Figure 151 FT-IR investigation of UV curable PLA/MEMO nanocomposite mixtures.

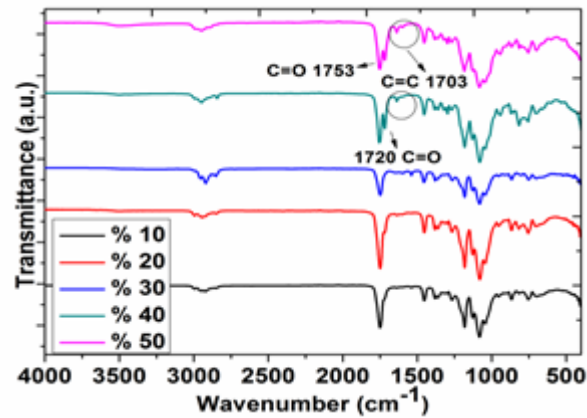


Figure 152 Effect of UV curing for the PLA/MEMO nanocomposite structure.

Analysis showed that after %30 MEMO addition, UV curing confronts with viscosity and time period problems which cause long term curing (more than 30 minutes) necessity. Therefore addition of increasing amount of MEMO (Figure 152) should be more carefully analysed in sense of disappearing double bond peak. Prepared nanocomposite structures have been coated onto the glass substrates and surface characteristics have been analyzed.

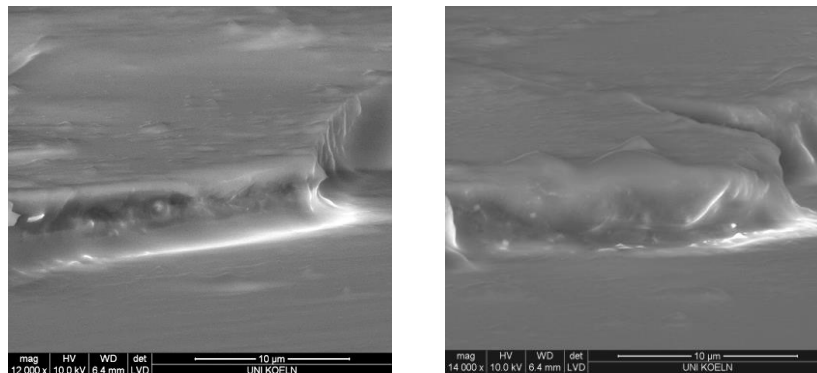


Figure 153 Deformation by e-beam for the PLA/%10 MEMO nanocomposite

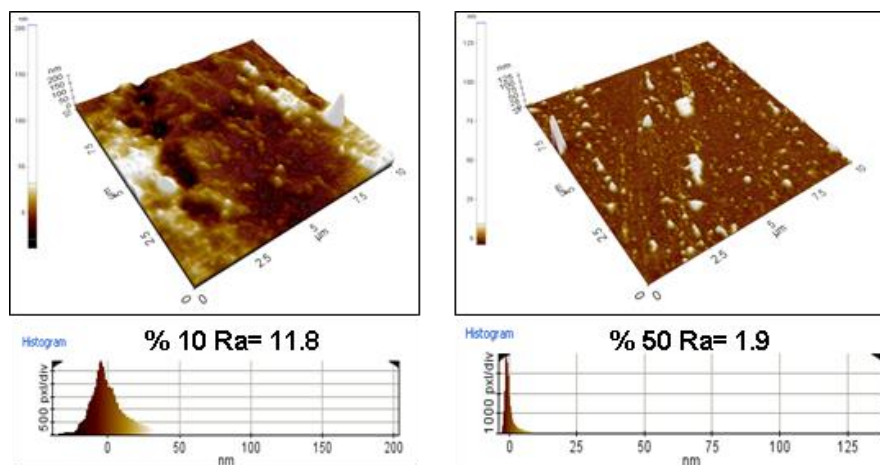


Figure 154 Change of roughness from PLA/%10 MEMO to PLA/%50 MEMO.

4 Results and Discussion

SEM investigations revealed that if only %10 MEMO is introduced into the PLA, thermal durability of the nanocomposite is still inefficient for analysis under SEM and this situation can be very easily observed in the corresponding SEM image (Figure 153) where nanocomposite coating is deformed after contacted to e-beam. AFM investigation (Figure 154) and SEM images (Figure 155) clearly revealed that average surface roughness decreases as MEMO content increases due to the effective film forming character of the MEMO. Prepared nanocomposite structures have been coated onto the glass substrates and surface characteristics have been analyzed. Transparency of the nanocomposite structure found quite proper for the daily applications even at the %50 MEMO content (Figure 156). Additionally, increase of MEMO content in the nanocomposite formulation increases the resistance against to water diffusion as shown in Figure 157. Introduction of %2 ZnO quantum dot amount into the hybrid nanocomposite resulted as visible light emitting materials but had no remarkable effect on the regular biodegradation (Figure 158).

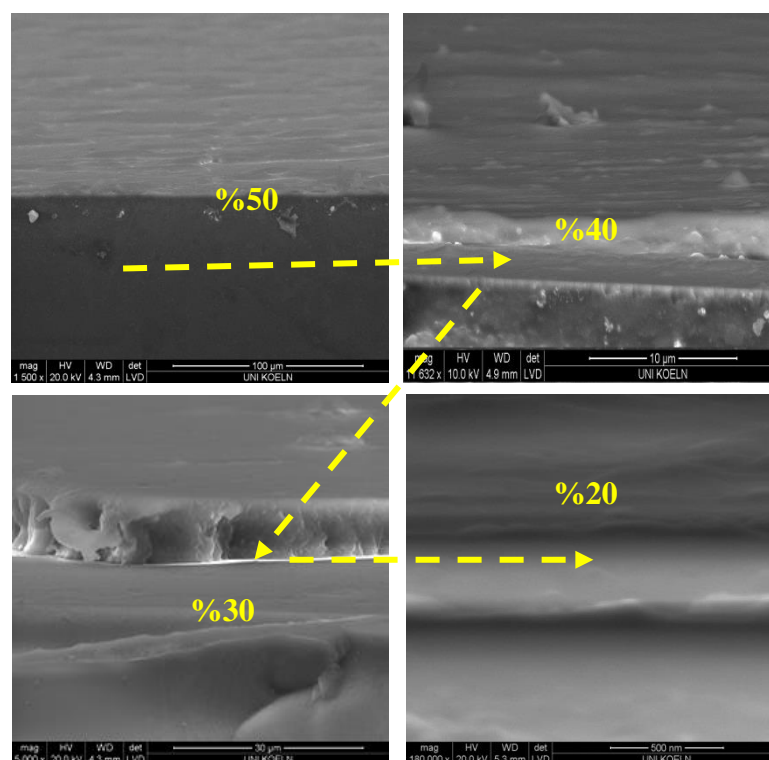


Figure 155 Cross sectional SEM analysis with increasing MEMO content (from %20 to %50 respectively).

ZnO quantum dots with different particle size can provide visible light emitting nanocomposite materials as shown in Figure 159. Blue, yellow and even orange colour emitting hybrid nanocomposites have been obtained. But due to the

defect oriented visible emission other particles like $\text{Eu@In}_2\text{O}_3$ should be used for the red emitting nanocomposites.

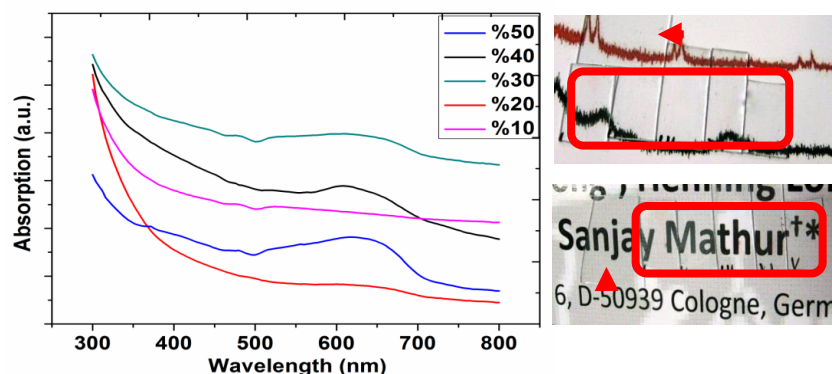


Figure 156 Transparency of the %30 MEMO/PLA nanocomposite polymer.

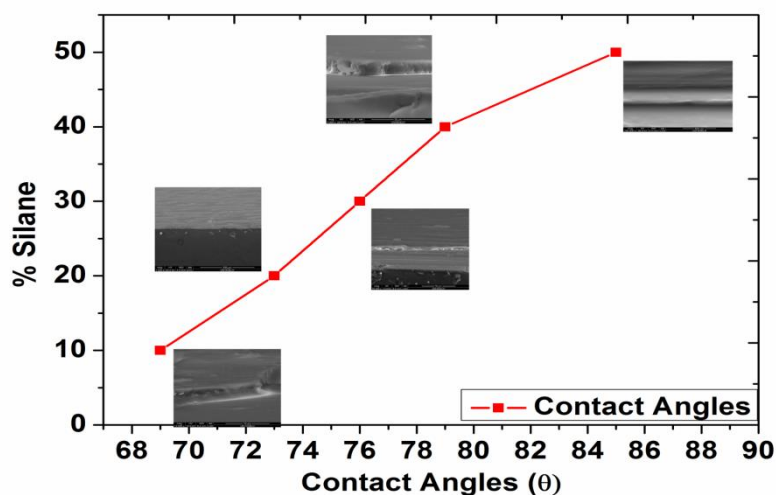


Figure 157 Contact angle increase with increasing MEMO content.

Distribution of the metal oxide particles can be detected by FIB technique after analysis of frozen nanocomposites. Since back scattering features are different for polymer and $\text{Eu@In}_2\text{O}_3$ nanoparticles, it is possible to differentiate the particles as white items distributed in the nanocomposite structure as shown in Figure 160. Introduced nanoparticles provide visible light emission for the whole structure in nanocomposite but there are solid and porous part of the final material as seen in Figure 161.

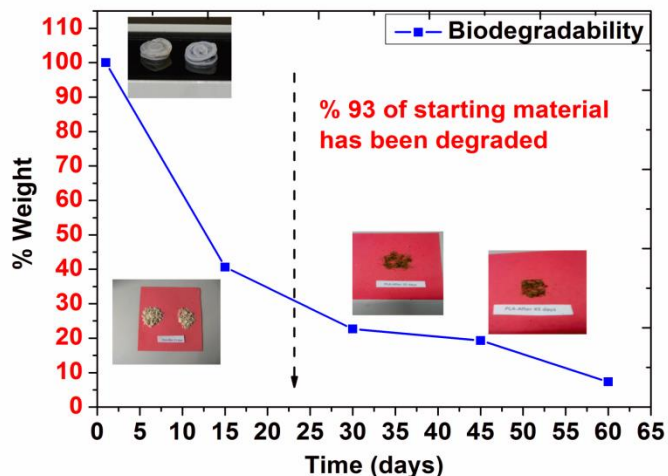


Figure 158 PLA biodegradation with a commercial compost formulation.

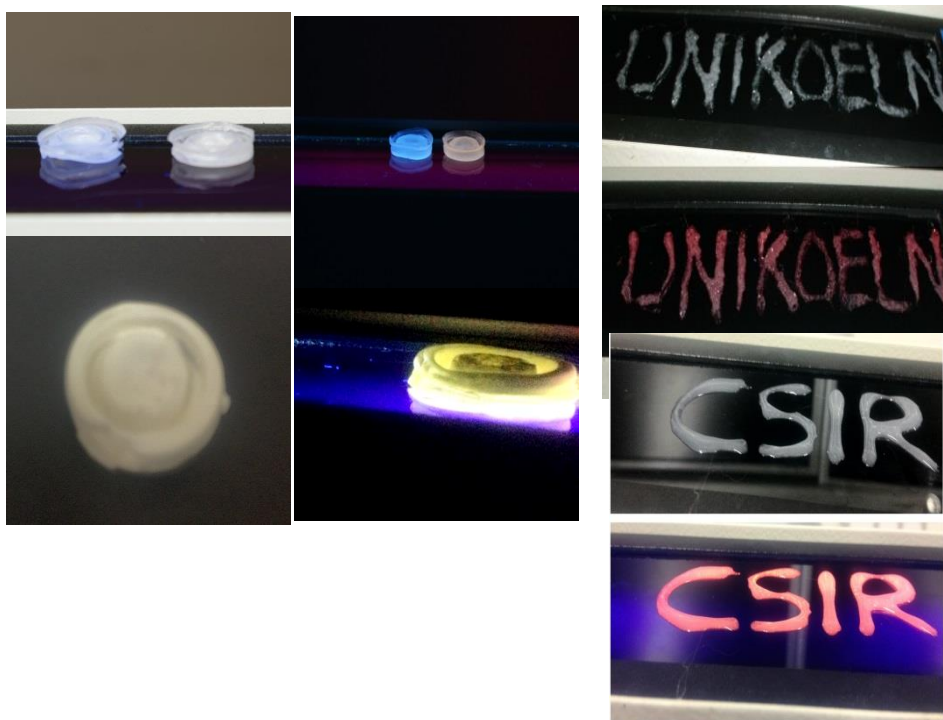


Figure 159 Solid state light emitting nanocomposites.

Since distribution of the nanoparticles is vitally important for the homogeneous emission features, this FIB-backscattering method should have been developed for the visible and detailed detection of the nanoparticles distributed in the organic polymer.

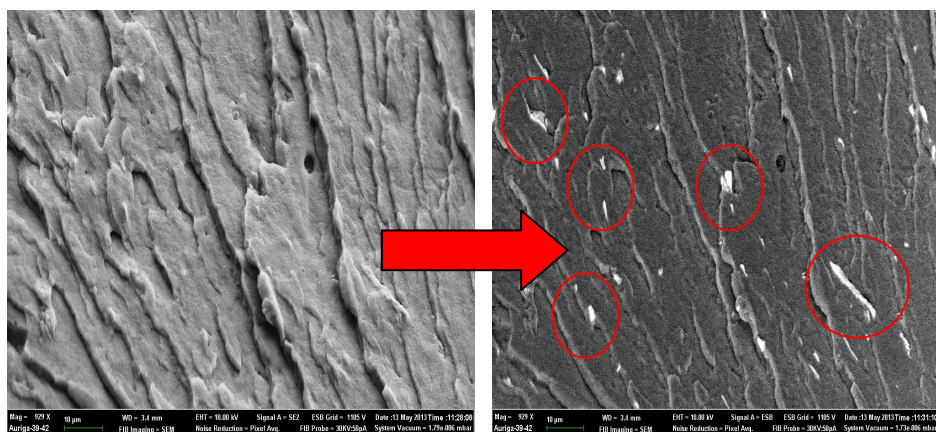


Figure 160 FIB-Back scattering images of metal oxide/PLA for observing particle dispersion.

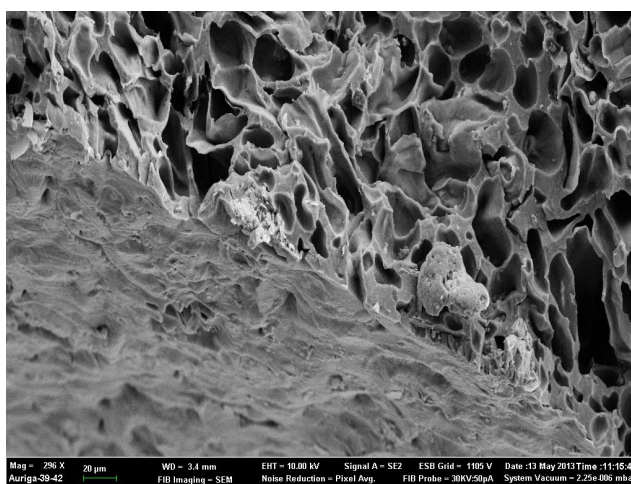


Figure 161 FIB image of liquid N₂ frozen MO_x/PLA nanocomposite structure.

SEM images therefore resulted huge amount of description possibilities for the particles. According to these images it has been detected that particles are available both in this porous and solid structure inside the nanocomposite. Therefore distribution has been achieved successfully. Therefore this method can be generalized for any kind of particle dispersed in the organic polymer. Colour difference (which can also be modulate and selected as red, green or other) provide the positions of the particles stabilized by polymer backbone. Still they do not lose their light emitting character. One drawback of this method is the size limitation. Since there would be a need of high resolution for quantum dot dispersed polymers either we need to find high agglomerations of quantum dots or fill the whole system with the solid particles.

4.4.4 ZnO QD@Clay Nanocomposites For Light Emitting Clays

Since size dependent emission can be used for visible light emitting colorful structures , clays with ZnO quantum dots have been prepared.

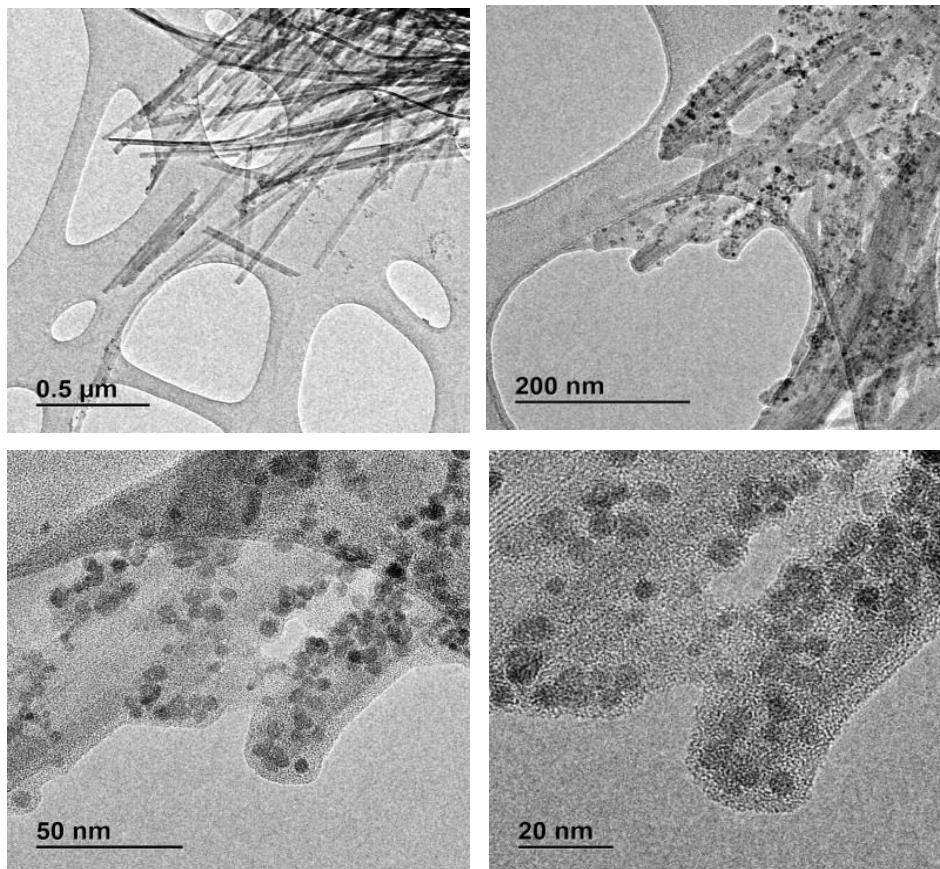


Figure 162 ZnO QD@Nanorod Clay Nanocomposites.

One example is nanorod shaped clay structure (Attapulgite) which has been decorated with ZnO quantum dots as shown in Figure 162.

It is clear that ZnO quantum dots are sitting on the clay structure and therefore, they would provide corresponding visible light emission. It was possible to observe clay nanocomposites emitting visible light from blue to yellow by different size of ZnO quantum dots. Same quantum dots can be also used for the decoration of plate like clays as shown in Figure 163.

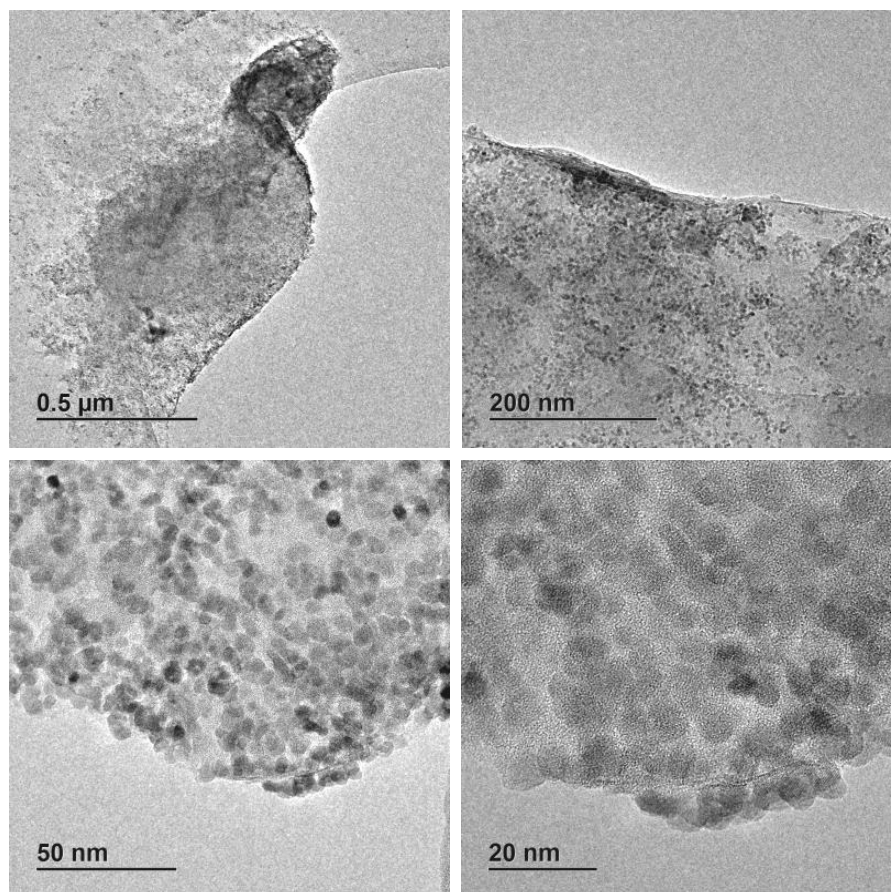


Figure 163 ZnO QD decoration for the plate like clays.

TEM and HRTEM analysis showed that ZnO quantum dots were changing from 2-7 nm in size. Measurement of [002] fringe of the ZnO has proved the composition of ZnO. An interesting observation obtained is that ZnO quantum dots were only growing on the clays but not separately. This phenomena is actually offers the mechanism of the ZnO growth on the clay structure. In the beginning $\text{Zn}(\text{CH}_3\text{COO})_2 \cdot \text{H}_2\text{O}$ is adsorbed by the clay and concentration of the zinc is increased on the clay surfaces. This local concentration difference causes that growth of the ZnO should propagate on the clay surfaces. Homogeneous feeding of the zinc cation and basic environment provides a homogeneous formation of the quantum dots attached on the surface of the clays as presented in the TEM images. This kind of clay based growth of the nanoparticles can be used for the other metal oxide nanoparticles and nanocomposites^[166-170].

5 Conclusions and Outlook

In this part complete thesis has been shortly analyzed and future study points have been highlighted. Since obtained nanostructures revealed that they allow us the molecular manipulation for the anisotropy and band gap engineering future aims should be targeted.

5.1 Conclusions

As emphasized before, ZnO and TiO₂ nanomaterials occupy broad band applications in the material science. Due to their relatively low band gap, low cost, easy manipulation and doping for optical application features, they attract enormous interest nowadays. Hence, focus on the extremely low size (quantum dots) and anisotropic morphology of these two metal oxide can trigger the large amount of quantum dot or anisotropic particle production with desired optical and doping properties.

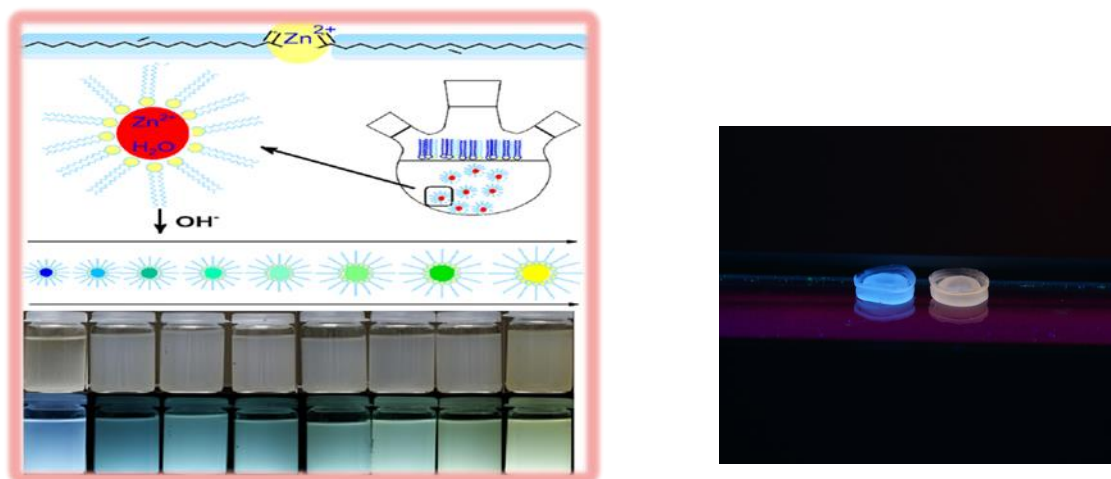


Figure 164 Oleate@ZnO QD's and solid state light emitting nanocomposites.

ZnO has been synthesized by heating up and modified sol gel chemistry. It has been found that surface modification of the ZnO QD's govern the quantum dot/nanoparticle stability and surface defects which are responsible for the tunable visible light emission. In addition to the common acetate modified synthesis of ZnO quantum dots, molecular ligands such as cysteine, oleate manipulates the surface character and emission properties as presented in Figure 164. This implies that surface modification and defect control can be achieved by using long chain structures which prevents the widely known red shift. Long chains can be adsorbed on the quantum dot surface chemically or physically but this ligand should be electively long to achieve the homegenity and long term

5 Conclusions and Outlook

stability. Anisotropic ZnO nanoparticles basically follow the hexagonal formation rules due to its crystal growing habit but precursor type and ligand proportions can easily modify the obtained nanostructure as shown in Figure 165.

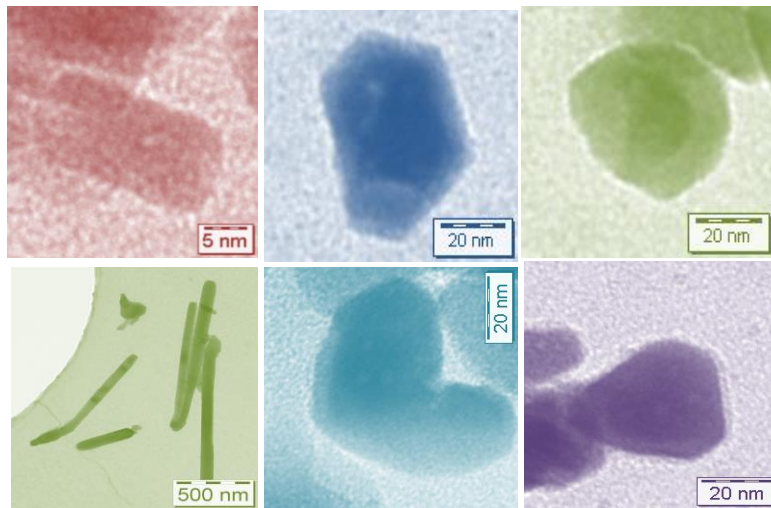


Figure 165 ZnO morphology gallery obtained by heating up method.

By manipulation of the ligand mixtures and different temperatures it is possible to form a table for the anticipation of the nanocrystals after a detailed TEM investigation. Anisotropy is highly dependent on these selectively adsorbing ligands and in addition to the amine and carboxylic acid group other functional groups like thiol or halogenides can provide many different anisotropic nanoparticles which showing different toxicity, stability, optical and morphological properties. Since hexagonal growth habit is set for the ZnO nanoparticles, it is possible to obtain distorted hexagonal morphology. By different ligands these morphologies can be manipulated and oriented attachment or self assembly processes can be observed for the fabrication of extremely unusual complex structures. Another anisotropic morphology fabrication is made for the TiO₂. Hot injection method has been first time used in order to synthesize visible light active ($E_g = 2,3$ eV), multibranch or spherical nanoparticles.

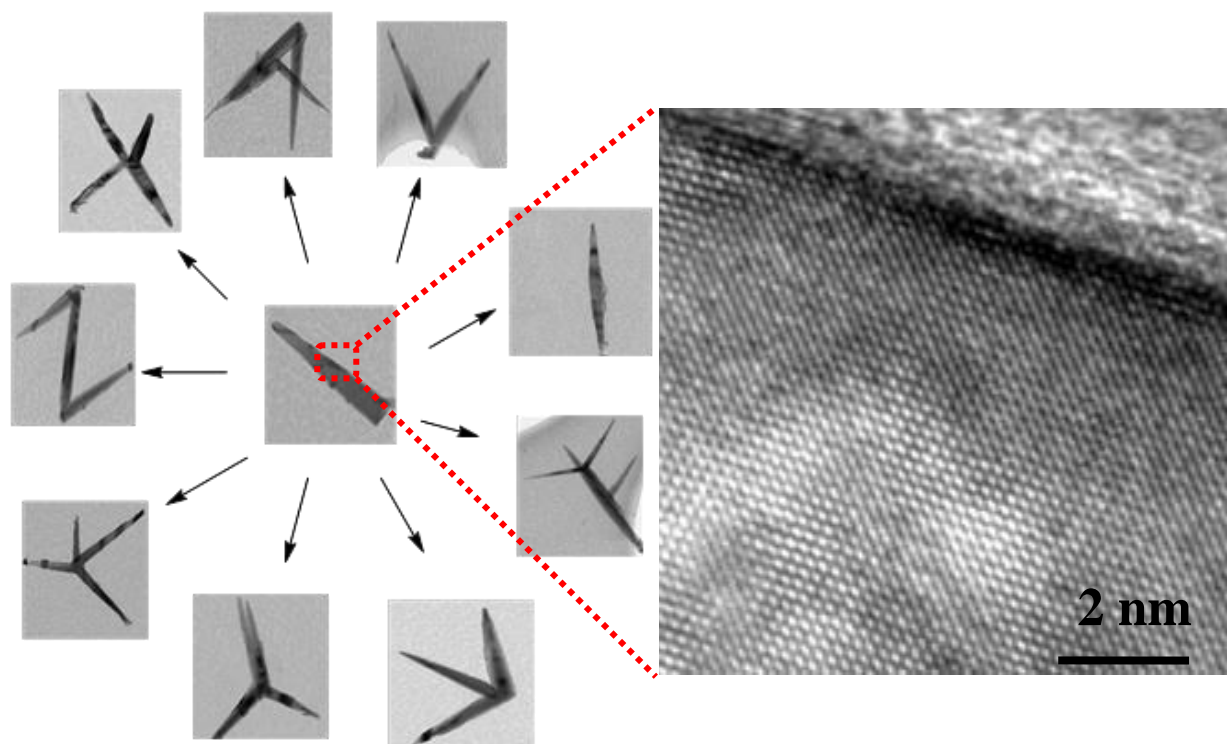


Figure 166 TiO₂ morphology gallery and HR-TEM of TiO₂ by Hot Injection.

Spherical morphology of the nanoparticles form micron sized self assembled (3 micrometer) balls which composed of nanoparticle self alignment from the long chain modified nanoparticles. Their band gap is in the visible range which has been also confirmed by band gap calculation and photocatalytic experiments. If we control the hot injection method to synthesize elongated nanostructures of TiO₂, it has been observed that multibranch nanorods, V shaped particles, tripods, tetrapods are formed within some pre confirmed rules. These nanorods show better photocatalytic activity properties as compared to commercially available P-25 TiO₂. Accordingly hot injection method can be used for the other metal oxide nanostructure synthesis. It may be possible to obtain attached metal oxides with different band gap and composition as shown in Figure 166.

5.2 Outlook and Future Prospects

High temperature liquid systems for the anisotropic nanoparticle preparation are very attractive fabrication methods even though their drawbacks like high boiling point solvents or hard heating control for reactions. It has been concluded that by manipulation of the precursor ligands, concentration and temperature for further modulation of the anisotropy it is possible to produce extremely attractive nanostructures for nanoelectronics, theranostics and

5 Conclusions and Outlook

catalytic applications. Therefore other systematic investigations should be done for the predictable extremely hard geometrical shaped metal oxide nanoparticles. Cytotoxicity, gene regulation and investigations on nano-biological interactions should be expanded for the further understanding of the nano-human interface and reciprocative behaviours. Since modified sol-gel method has also provided ultrastable visible light emitting systems one can easily focus on the other nanoparticle systems for the long term stability and easy to manipulate quantum dots for the industrial applications.

6 References

- [1] *TiO₂ Nanotube Arrays: Synthesis, Properties, and Applications*, Synthesis, Properties, and Applications, Grimes, Craig A., Mor, Gopal K., Springer, 2009
- [2] Zallen, R.; Moret, M. P., *Solid State Commun.* 2006, 137, 154.
- [3] Zhong Lin Wang, *J. Phys.: Condens. Matter*, 2004, 16, 829
- [4] *Zinc Oxide: Fundamentals, Materials and Device Technology*, Prof. Dr. Hadis C Morkoç, Ümit Özgür, Wiley-VCH Verlag GmbH & Co. KGaA, 2009
- [5] *Zinc Oxide Bulk, Thin Films and Nanostructures Processing, Properties and Applications* Edited by: Chennupati Jagadish and Stephen Pearton, Elsevier, 2006
- [6] Anderson Janotti and Chris G Van de Walle, *Rep. Prog. Phys.*, 2009, 72, 126501
- [7] Hyungkyu Han, Taeseup Song, Eung-Kwan Lee, Anitha Devadoss, Yeryung Jeon, Jaehwan Ha, Yong-Chae Chung, Young-Min Choi, Yeon-Gil Jung, and Ungyu Paik, *ACS Nano*, 2012, 6 (9), 8308–8315
- [8] Sunandan Baruah, Sudarson Sekhar Sinha, Barnali Ghosh, Samir Kumar Pal, A. K. Raychaudhuri, Joydeep Dutta, *J. App. Physc.*, 2009, 105, 074308
- [9] Amy L. Linsebigler, Guangquan. Lu, John T. Yates *Chem. Rev.*, 1995, 95 (3), 735–758
- [10] *TiO₂ Photocatalysis: Fundamentals and Applications*, Akira Fujishima, Kazuhito Hashimoto, Toshiya Watanabe, Bkc, Incorporated, 1999
- [11] Qiong Sun, Yang Li, Xianmiao Sun, and Lifeng Dong, *ACS Sustainable Chem. Eng.*, 2013, 1 (7), pp 798–804
- [12] Yu-Cheng Chang, Han-Wei Wu, Hsuen-Li Chen, Wen-Yun Wang and Lih-Juann Chen, *J. Phys. Chem. C*, 2009, 113 (33), pp 14778–14782
- [13] Nguyen Khac Huu, Dae-Yong Son, In-Hyuk Jang, Chang-Ryul Lee, and Nam-Gyu Park, *ACS Appl. Mater. Interfaces*, 2013, 5 (3), pp 1038–1043
- [14] Hao Ming Chen, Chih Kai Chen, Yu-Chuan Chang, Chi-Wen Tsai, Ru-Shi Liu, Shu-Fen Hu, Wen-Sheng Chang and Kuei-Hsien Chen, *Ang. Chemie.*, 2011, 122, (Issue 34), 6102–6105,

6 References

- [15] Shuyan Gao, Xiaoxia Jia, Shuxia Yang, Zhengdao Li, Kai Jiang , J.Solid State Chem.,2011,184,764-769
- [16] Kazuhiko Maeda, Naoyuki Sakamoto, Takahiro Ikeda, Hajime Ohtsuka, Anke Xiong, Daling Lu, Masayuki Kanehara, Toshiharu Teranishi and Kazunari Domen, Chemistry - A European Journal, 2010,16,7750–7759
- [17] Hao Ming Chen, Chih Kai Chen, Ming Lun Tseng, Pin Chieh Wu, Chia Min Chang, Liang-Chien Cheng, Hsin Wei Huang, Ting Shan Chan, Ding-Wei Huang, Ru-Shi Liu and Din Ping Tsai, Small, 2013, 9,2926–2936
- [18] Daimei Chen, Zhongyi Jiang, Jiaqing Geng, Qun Wang, and Dong Yang Ind. Eng. Chem. Res., 2007, 46 (9), 2741–2746
- [19] M. L. Curri,R. Comparelli,M. Striccoli, A. Agostiano, Phys.Chem.Chem.Phys., 2010, 12, 11197–11207
- [20] Seungwoo Lee, Hong Suk Kang and Jung-Ki Park, Advanced Materials, 2012,24, 2069
- [21] Tapan K. Sau, Andrey L. Rogach, Frank Jäckel, Thomas A. Klar and Jochen Feldmann,Advanced Materials, 2010, 22, 1805–1825,
- [22] R. Wüest, Photonics and Nanostructres. 2009,7, 212-219,
- [23] L. J. Guo,Advanced Materials, 2007, 19, 495–513,
- [24] J. González-Benito, G. González-Gaitano, Macromolecules, 2008, 41 (13), 4777–4785
- [25] Tan Xing, Jaka Sunarso, Wenrong Yang, Yongbai Yin, Alexey M. Glushenkov, Lu Hua Li, Patrick C. Howlett, Ying Chen, Nanoscale, 2013,5, 7970-7976
- [26] Claudio L. De Castro, Brian S. Mitchel, Synthesis, Functionalization and Surface Treatment of Nanoparticles,Edited by M.-I. Baraton, 1-15, 2002
- [27] Gupta A , Arora A , Menakshi A , Sehgal A , Sehgal R . Nanotechnology and Its Applications in Drug Delivery: A Review . WebmedCentral:International Journal of Medicine and Molecular, Medicine 2012;3(1)
- [28] Indrani Banerjee, Ravindra C. Pangule and Ravi S. Kane, Advanced Materials, 2011, 23,690–718,

6 References

- [29] Xiangbo Meng, Xiao-Qing Yang and Xueliang Sun, *Advanced Materials*, 2012,24, 3589–3615,
- [30] Christine Ogilvie Robichaud, Dickson Tanzil, Ulrich Weilenmann, and Mark R. Wiesner ,*Environ. Sci. Technol.*, 2005, 39 (22), 8985–8994
- [31] Brian H. Northrop, Yao-Rong Zheng, Ki-Whan Chi and Peter J. Stang *Acc. Chem. Res.*, 2009, 42 (10), 1554–1563
- [32] Saumyakanti Khatua, Pramit Manna, Wei-Shun Chang, Alexei Tcherniak, Eric Friedlander, Eugene R. Zubarev and Stephan Link, *J. Phys. Chem. C*, 2010, 114 (16), 7251–7257
- [33] Somobrata Acharya, Jonathan P. Hill and Katsuhiko Ariga, *Advanced Materials*, 2009,21,2959
- [34] Sanjay Mathur, Hao Shen, Jessica Altmayer, *Rev. Adv. Mater. Sci.*, 2007, 15,16-23
- [35] Wei Zhou, Jianbo Wu, and Hong Yang, *Nano Lett.*, 2013, 13 (6), pp 2870–2874
- [36] Idalia Bilecka, Markus Niederberger, *Nanoscale*, 2010,2, 1358-1374
- [37] Jonathan M. Patete, Xiaohui Peng, Christopher Koenigsmann, Yan Xu, Barbara Karn and Stanislaus S. Wong , *Green Chem.*, 2011,13, 482-519
- [38] Singanahally T. Aruna, Alexander S. Mukasyan, *Current Opinion in Solid State and Materials Science* , 2008,12 44
- [39] Victor K. LaMer, Robert H. Dinegar, *JACS*, 1950, 72(11),4847-4854.
- [40] R. Viswanatha and D.D. Sarma, *Nanomaterials Chemistry*, . Edited by C.N.R. Rao, A. Müller, and A.K. Cheetham ,2007 WILEY-VCH Verlag GmbH & Co. KGaA, Weinheim, page 139
- [41] Yugang Sun ,*Chem. Soc. Rev.* , 2013, 42, 2497-2511
- [42] I.M. Lifshitz, V.V. Slyozov, *J. of Phys. Chem. Solids*, 1961, 19 (1–2): 35–50
- [43] http://en.wikipedia.org/wiki/Ostwald_ripening (last visited 22.10.2013)
- [44] Andrea R. Tao, Susan Habas, and Peidong Yang, *Small*, 2008,, No.3, 310–325
- [45] Young-wook Jun, Jin-sil Choi, Jinwoo Cheon, *Angew. Chem. Int. Ed.*,2006,45,3414 – 3439

6 References

- [46] Jun YW, Casula MF, Sim JH, Kim SY, Cheon J, Alivisatos AP., *J Am Chem Soc.* ,2003,125(51):15981-5.
- [47] C. B. Murray, D. J. Norris, and M. G. Bawendi, *JACS*, 1993,115, 8706–8715,
- [48] Z. A. Peng and X. Peng, *JACS*,2001,123, 183–184
- [49] Niederberger, Markus, Pinna, Nicola ,*Metal Oxide Nanoparticles in Organic Solvents*, Springer, 2009, (Surfactant-Assisted SynthesisNiederberger, Markus; Pinna, Nicola)
- [50] Kwon, S. G. and Hyeon, T. , *Small*, 2011 ,7: 2685–2702
- [51] *Sol-gel Science: The Physics and Chemistry of Sol-gel Processing*, C. Jeffrey Brinker, George W. Scherer, 1990, Gulf Professional Publishing
- [52] <http://biomaterials.kaist.ac.kr/research/research.htm> (last visited 22.10.2013)
- [53] H.Schmidt., H. Wolter, *J. Non-Cryst. Solids*, 1990,121, Issues 1–3, Pages 428–435
- [54] Dr. Eva Hemmer , Ph.D. Thesis, 2008, University of Cologne
- [55] S. Mathur and H. Shen, *Inorganic nanomaterials from molecular templates*, in H. S.Nalwa, ed. *Encyclopedia of Nanoscience and Nanotechnology* 4, pp. 131–191,American Scientific Publisher, 2004.
- [56] Clément Sanchez, Beatriz Julián, Philippe Belleville,Michael Popall, *J. Mater. Chem.*, 2005,15, 3559-3592
- [57] B.M. Novak, *Adv. Mater.* 1993, 5,422
- [58] *Hybrid Materials: Synthesis, Characterization, and Applications*, Guido Kickelbick (Editor), 2007, Wiley
- [59] *Nanocomposites - New Trends and Developments*, Edited by Farzad Ebrahimi, InTech, Chapter 1, *Polymer/ Clay Nanocomposites: Concepts, Researches, Applications and Trends for The Future* by Priscila Anadão, 2012
- [60] *Nanotechnology and Nanomaterials » "Advances in Diverse Industrial Applications of Nanocomposites"*, edited by Boreddy Reddy,2011,Intechopen , Chapter 7, Ali Olad *Polymer/Clay Nanocomposites*

6 References

- [61] A.B. Djurišić, A.M.C. Ng, X.Y. Chen, *Prog. Quant.Electr.*2010,34, 191–259
- [62] Kelly M. Whitaker, Maxim Raskin, Gillian Kiliani, Katja Beha, Stefan T. Ochsenein, Nils Janssen, Mikhail Fonin, Ulrich Rüdiger, Alfred Leitenstorfer, Daniel R. Gamelin, and Rudolf Bratschitsch, *Nano Lett.*, 2011, 11 (8),3355–3360
- [63] Alejandro J. Gimenez, J. M. Yáñez-Limón, and Jorge M. Seminario, *J. Phys. Chem. C*, 2011, 115 (1), 282–287
- [64] Ranu K. Dutta, Prashant K. Sharma, Richa Bhargava, Naresh Kumar and Avinash C. Pandey, *J. Phys. Chem. B*, 2010, 114 (16), 5594–5599
- [65] Manoj Raula, Md. Harunar Rashid, Tapas K. Paira, Enakshi Dinda and Tarun K. Mandal, *Langmuir*, 2010, 26 (11), 8769–8782
- [66] Shirish H. Sonawane, Boon M. Teo, Adam Brotchie, Franz Grieser and Muthupandian Ashokkumar, *Ind. Eng. Chem. Res.*, 2010, 49 (5),2200–2205
- [67] Sung-Hae Lee, Se-Hoon Han, Hyun Suk Jung, Hyunjung Shin and Jagab Lee, Jun-Hong Noh, Sangwook Lee and In-Sun Cho, Jung-Kun Lee, Jinyoung Kim, Hyunho Shin, *J. Phys. Chem. C*, 2010, 114 (15), 7185–718
- [68] Eric A. Meulenkamp, *J. Phys. Chem. B*, 1998,102,5566
- [69] Soon Gu Kwon and Taeghwan Hyeon , *Acc. Chem. Res.*, 2008, 41 (12), pp 1696–1709
- [70] Markus Niederberger, *Acc. Chem. Res.*, 2007, 40 (9), 793–800 (and references therein)
- [71] Xiaobo Chen and Samuel S. Mao, *Chem. Rev.*, 2007, 107 (7), pp 2891–2959
- [72] Marchand R., Brohan L., Tournoux M., *Mater.Res.Bull.*,1980,15 (8): 1129–1133
- [73] Latroche, M; Brohan, L; Marchand, R; Tournoux, J.*Solid State Chem*, 1989,. 81 (1): 78–82
- [74] Akimoto, J.; Gotoh, Y.; Oosawa, Y.; Nonose, N.; Kumagai, T.; Aoki, K.; Takei, H., , *J.Solid State Chem* 1994, 113 (1): 27–36
- [75] Simons, P. Y.; Dache, F., *Acta Crystallographica*, 1967, 23 (2): 334–336.

6 References

- [76] Sato H. , Endo S, Sugiyama M, Kikegawa T, Shimomura O, Kusaba K, Science, 1991, 251,4995,786–788
- [77] Dubrovinsky, LS; Dubrovinskaia, NA; Swamy, V; Muscat, J; Harrison, NM; Ahuja, R; Holm, B; Johansson, B, Nature, 2001, 410 (6829): 653–654
- [78] Dubrovinskaia N A, Dubrovinsky L S., Ahuja R, Prokopenko V B., Dmitriev V., Weber H.-P., Osorio-Guillen J. M., Johansson B, Phys. Rev. Lett.,2001, 87 (27 Pt 1): 275501
- [79] Mattesini M, de Almeida J. S., Dubrovinsky L., Dubrovinskaia L, Johansson B., Ahuja R., Phys. Rev. B 2004 ,70 (21): 212101
- [80] Sorapong Pavasupree, Yoshikazu Suzuki, Susumu Yoshikawa, Ryoji Kawahata, J. Solid State Chem, 2005, 178 3110–3116
- [81] Chien-Cheng Tsai and Hsisheng Teng, Chem. Mater., 2006, 18 (2), 367–373
- [82] Raffaella Buonsanti, Elvio Carlino, Cinzia Giannini, Davide Altamura, Luisa De Marco, Roberto Giannuzzi, Michele Manca, Giuseppe Gigli, and P. Davide Cozzoli, J. Am. Chem. Soc., 2011, 133 (47), 19216–19239
- [83] P. Davide Cozzoli, Andreas Kornowski, and Horst Weller, J. Am. Chem. Soc., 2003, 125 (47), 14539–14548
- [84] Raffaella Buonsanti, Vincenzo Grillo, Elvio Carlino, Cinzia Giannini, Tobias Kipp, Roberto Cingolani and Pantaleo Davide Cozzoli, J. Am. Chem. Soc., 2008, 130 (33), pp 11223–11233
- [85] Arslan, Osman; Arpac, Ertugrul; Sayilkan, Hikmet, J.ournal of Inorg. and Org. Polymers Mat. ,2010, 20, 284-292
- [86] <http://photochemistryportal.net/home/index.php/2009/09/30/metal-oxide-photocatalysis/> (last visited 22.10.2013)
- [87] Martin W.G. Hoffmann, Alaa Eldin Gad, J. Daniel Prades, Francisco Hernandez-Ramirez, Raquel Fiz, Hao Shen, Sanjay Mathur, Nano Energy, 2013, 2, 514–522
- [88] Tobias Voss, Geoffry T. Svacha, and Eric Mazur, Sven Müller and Carsten Ronning, Denan Konjhodzic and Frank Marlow, Nano Lett., 2007, 7 (12), 3675–3680

6 References

- [89] Yu-Hsiang Sung, Wen-Pin Liao, Dian-Wei Chen, Chun-Te Wu, Geng-Jia Chang and Jih-Jen Wu, *Advanced Functional Materials*, , 2012,22,3808
- [90] Rupesh S. Devan, Ranjit A. Patil, Jin-Han Lin and Yuan-Ron Ma,*Advanced Functional Materials*,2012,22, 3326–3370
- [91] H.-M. Xiong, Z.-D. Wang and Y.-Y. Xia ,*Adv.Mater.*, 2006,18,748–751,
- [92] S. Li, M. S. Toprak, Y. S. Jo, J. Dobson, D. K. Kim and M. Muhammed ,*Adv.Mater.* 2007,19,4347–4352,
- [93] Pavle V. Radovanovic, Nick S. Norberg, Kathryn E. McNally, and Daniel R. Gamelin,*J. Am. Chem. Soc.*, 2002, 124 (51), 15192–15193
- [94] Xiaosheng Tang, Eugene Shi Guang Choo, Ling Li, Jun Ding and Junmin Xue,*Langmuir*, 2009, 25 (9), 5271–5275
- [95] Luyuan Zhang, Longwei Yin, Chengxiang Wang, Ning lun, Yongxin Qi and Dong Xiang,*J. Phys. Chem. C*, 2010, 114 (21), 9651–9658
- [96] Ying-Song Fu, Xi-Wen Du, Sergei A. Kulinich, Jian-Sheng Qiu, Wen-Jing Qin, Rui Li, Jing Sun, and Jim Liu, *J. Am. Chem. Soc.*, 2007, 129 (51), pp 16029–16033
- [97] Huan-Ming Xiong,*J. Mater. Chem.*, 2010,20, 4251-4262
- [98] A. Van Dijken, E.A. Meulenkaamp, D. Vanmaekelbergh, A. Meijerink, *J. Phys. Chem. B*, 2000,104, 1715
- [99] A. van Dijken, J. Makkinje, A. Meijerink, *J. Luminesc.*, 2001,92., 323-328
- [100] A van Dijken, E.A Meulenkaamp, D Vanmaekelbergh, A Meijerink, 2000,*J. Luminesce.* 87–89, 454-456
- [101] Lubomir Spanhel, Marc A. Anderson,*J. Am. Chem. Soc.*, 1991, 113 (8), 2826–2833
- [102] Q. Wu, X. Chen, P. Zhang, Y. Han, X. Chen, Y. Yan, and S. Li:*Cryst. Growth Des.* 2008, 8,3011)
- [103] P. Gerstel, R.C. Hoffmann, P. Lipowsky, *L.P.H. Chem. Mater.*,2006,179, 18
- [104] O. Arslan, A.P. Singh, L. Belkoura, S. Mathur, *Journal of Materials Research*, 2013, 28,1947-1954
- [105] L. Qu,; X.Peng, *J. Am. Chem. Soc.* 2002,124,2049;

6 References

- [106] G.A. Beane, A.J. Morfa, A.M. Funston, P.Mulvaney, *J. Phys. Chem. C* 2012, 116,3305
- [107] J. Cui, *J. Phys. Chem. C* 2008, 112,10385
- [108] X. Tang, E.S.Guang Choo, L. Li, J. Ding, J. Xue, *Langmuir*, 2009, 25,5271;
- [109] H. Zeng, G. Duan, Y. Li, S.Yang, X. Xu, W.Cai, *Adv. Funct. Mat.* 2010, 20,561
- [110] Devan, R.A. Patil, J.Lin,Y. Ron Ma, *Adv. Funct. Mat.* 2012,22,3326
- [111] Q. X. Zhao, P. Klason, M.Willander, H. M. Zhong, W. Lu, J. H. Yang, *Appl. Phys. Lett.* 2005,87, 211912.
- [112] Swift Synthesis of Ultrastable Oleate@ZnO Quantum Dots as Visible Light Emitters, O.Arslan, L. Belkoura, S.Mathur, *J. Adv. Funct. Mat.*, 2013, submitted article
- [113] O. Kohlmann, W. E. Steinmetz, X. A. Mao, W. P. Wuelfing,A. C. Templeton, R. W. Murray, C. S. Johnson, *J. Phys. Chem. B* 2001, 105, 8801–8809
- [114] A. Hassinen, I. Moreels, C.de Mello Donega, J.C. Martins, Z. Hens, *J. Phys. Chem. Lett.* 2010, 1, 2577
- [115] Likun Pan, Xinjuan Liu, Zhuo Sun and Chang Q. Sun , *J. Mater. Chem. A*, 2013,1, 8299-8326
- [116] Hashem Shahroosvand and Mahsa Ghorbani-as, *Cryst EngComm*, 2012,14, 8199-8207
- [117] Chih-Cheng Lin, Yuan-Yao Li, *Mater. Chem.Phys.* 2009,113, 334-337
- [118]
- [118] Yang Yang, Huilan Chen, Bin Zhao, Ximao Bao, *J. Cryst.Growth*, 2004,263,447-453
- [119] C.W. Yao, H.P. Wu, M.Y. Ge, L. Yang, Y.W. Zeng, Y.W. Wang, J.Z. Jiang,,*Materials Letters*, 2007,61, 3416-3420
- [120] Lu Ren, Tingting Tian, Yuanzhi Li, Jianguo Huang, and Xiujian Zhao, *ACS Appl. Mater. Interfaces*, 2013, 5 (12), pp 5861–5867
- [121] P. Davide Cozzoli, M. Lucia Curri, and Angela Agostiano, Gabriella Leo and Mauro Lomascolo, *J. Phys. Chem. B*, 2003, 107 (20), pp 4756–4762

6 References

- [122] P. Davide Cozzoli, Andreas Kornowski, and Horst Weller, *J. Phys. Chem. B*, 2005, 109 (7), pp 2638–2644
- [123] Christian Cavelius, Karsten Moh, and Sanjay Mathur, *Crystal Growth & Design*, 2012, 12 (12), pp 5948–59
- [124] Markus Niederberger, *Acc. Chem. Res.*, 2007, 40 (9), pp 793–800
- [125] Eva Hemmer, Yvonne Kohl, Victoria Colquhoun, Hagen Thielecke, Kohei Soga and Sanjay Mathur, *J. Phys. Chem. B*, 2010, 114 (12), pp 4358–4365
- [126] I.M. Grabs, C. Bradtmöller, D. Menzel, G.Garnweitner, *Crystal Growth & Design*, 2012, 12 (3), pp 1469–1475
- [127] Jing Mao, Xiao-Lei Li, Wen-Jing Qin, Kai-Yang Niu, Jing Yang, Tao Ling and Xi-Wen Du *Langmuir*, 2010, 26 (17), pp 13755–13759
- [128] Idalia Bilecka, Pierre Elser and Markus Niederberger, *ACS Nano*, 2009, 3 (2), pp 467–477
- [129] Sang-Hyun Choi, Eung-Gyu Kim, Jongnam Park, Kwangjin An, Nohyun Lee, Sung Chul Kim, and Taeghwan Hyeon, *J. Phys. Chem. B*, 2005, 109 (31), pp 14792–14794
- [130] S.Tuomela,R.Autio,T. Buerki-Thurnherr,O.Arslan,A.Kunzmann, B.Andersson-Willman,P. Wick, S. Mathur,A. Scheynius,H.F. Krug,B.Fadeel,R. Lahesmaa, *PloS One*, 2013, 8, e68415
- [131] Buerki-Thurnherr, Tina; Xiao, Lisong; Diener, Liliane; Arslan, Osman; Hirsch, Cordula; Maeder-Althaus, Xenia; Grieder, Kathrin; Wampfler, Bruno; Mathur, Sanjay; Wick, Peter; Krug, Harald F. , *Nanotoxicology* , Volume 7 (4) – Jun 1, 2013
- [132] Hirsch, C.; Buerki-Thurnherr, T.; Xiao, L.; Arslan, O.; Wampfler, B.; Mathur, S.; Roesslein, M.; Wick, P.; Krug, H. F., *Toxicology Letters* 06/2012; 211(S), S41-S41:211(S), S41-S41
- [133] Gdor I, Sachs H, Roitblat A, Strasfeld DB, Bawendi MG, Ruhman S. Exploring Exciton Relaxation and Multiexciton Generation in PbSe Nanocrystals Using Hyperspectral Near-IR Probing. *ACS Nano* 2012, 6: 3269-3277.

6 References

- [134] Choi HS, Ipe BI, Preeti M, Lee H, Bawendi MG, Frangioni JV. Tissue- and Organ-Selective Biodistribution of NIR Fluorescent Quantum Dots. *Nano Letters* 2009, 9: 2354-2359.
- [135] Raffaella Buonsanti, Elvio Carlino, Cinzia Giannini, Davide Altamura, Luisa De Marco, Roberto Giannuzzi, Michele Manca, Giuseppe Gigli, P Davide Cozzoli, *JACS*, 2011; 133(47):19216-39
- [136] L. Marco, M. Manca, R. Buonsanti, R. Giannuzzi, F. Malara, P. Pareo, L. Martiradonna, N. M. Giancaspro, P. Davide Cozzoli, G. Gigli, *J.Mater.Chem.* 2011; 21(35):13371-13379.
- [137] Kunlun Ding, Zhenjiang Miao, Baoji Hu, Guimin An, Zhenyu Sun, Buxing Han, and Zhimin Liu, *Langmuir*, 2010, 26(12), 10294–10302
- [138] Xiaobo Chen, and Clemens Burda, *J. Am. Chem. Soc.* 2008, 130,, 5018–5019
- [139] Tushar C. Jagadale, Shrikant P. Takale, Ravindra S. Sonawane, Hrushikesh M. Joshi, Shankar I. Patil, Bharat B. Kale and Satishchandra B. Ogale, *J. Phys. Chem. C*, 2008, 112 (37), pp 14595–14602
- [140] Wei Guo, Yihua Shen, Liqiong Wu, Yurong Gao, and Tingli M, *J. Phys. Chem. C*, 2011, 115 (43), pp 21494–21499
- [141] Robert Menzel, Ben F. Cottam, Sabina (Chyla), Ziemian and Milo S. P. Shaffer, *J.Mater.Chem.*, 2012, 22,, 12172
- [142] Kalappa Prashantha, Marie-France Lacrampe and Patricia Krawczak, *J. App. Poly.Sci.*, 2013, 130, 313–321,
- [143] Peng Tao, Ying Li, Richard W. Siegel and Linda S. Schadler, *Journal of Applied Polymer Science*, 2013, 130, 3785–3793,
- [144] Wei Feng, Chunmiao Han and Fuyou Li, *Advanced Materials*, 2013, 25, 5287–5303
- [145] Wei Deng, Dayong Jin, Krystyna Drozdowicz-Tomsia, Jingli Yuan, Jing Wu and Ewa M. Goldys, *Advanced Materials*, 2011, 23, 649–4654
- [146] Zi-Rong Tang, Xia Yin, Yanhui Zhang, and Yi-Jun Xu, *Inorg. Chem.*, 2013, 52 (20), pp 11758–11766
- [147] Hyeyoung Kong, Jooyoung Song and Jyongsik Jang, *Environ. Sci. Technol.*, 2010, 44 (14), pp 5672–5676

6 References

- [148] Paula A. Zapata, Humberto Palza, Katherine Delgado and Franco M. Rabagliati, *Journal of Polymer Science Part A: Polymer Chemistry*, 2012, 50, 4055–4062,
- [149] Indrani Banerjee, Ravindra C. Pangule and Ravi S. Kane, *Advanced Materials*, 2011, 23, 690–718,
- [150] N. Fong, L. A. Poole-Warren and A. Simmons, *J. Biomed. Mat.Res.Part B: Appl.Biomat.*, 2013, 101B, 310–319,
- [151] Nehal Salahuddin, Badr Badr and Rehab Abdeen, *Polym.Intern.*, 2012, 61, 99–110,
- [152] Ming-Chien Wang, Jiang-Jen Lin, Hsiang-Jung Tseng, and Shan-hui Hsu, *ACS Appl. Mater. Interfaces*, 2012, 4 (1), pp 338–350
- [153] Qian Feng Xu, Yang Liu, Fang-Ju Lin, Bikash Mondal, and Alan M. Lyons, *ACS Appl. Mater. Interfaces*, 2013, 5 (18), pp 8915–8924
- [154] Roderick B. Pernites, Ramakrishna R. Ponnampati and Rigoberto C. Advincula, *Advanced Materials*, 2011, 23, 3207–3213,
- [155] Hongdian Lu, Lei Song and Yuan Hu, *Polymers for Advanced Technologies*, 2011, 22, 379–394,
- [156] F. Bauer, V. Sauerland, H.J. Gläsel, H. Ernst, M. Findeisen, E. Hartmann, H. Langguth, B. Marquardt, R. Mehnert, *Macromolecular Materials and Engineering*, 2002, 287, 546–552,
- [157] M. Avella, M. Emanuela Errico, E. Martuscelli, *Nano Lett.*, 2001, 1 (4), pp 213–217
- [158] A. Okada, A. Usuki, *Macromolecular Materials and Engineering*, 2006, 291, 1449–1476,
- [159] Jiangxuan Song, Guangxin Chen, Yun Ding, Jianjun Shi, Ying Liu and Qifang Li, *Polymer International*, 2011, 60, 1594–1599,
- [160] Kamal Mohamed Seeni Meera, Rajavelu Murali Sankar, Sellamuthu N. Jaisankar, and Asit Baran Mandal, *J. Phys. Chem. B*, 2013, 117 (9), pp 2682–2694
- [161] Yucheng Yang, Junwei Wen, Jianhong Wei, Rui Xiong, Jing Shi, and Chunxu Pan, *ACS Appl. Mater. Interfaces*, 2013, 5 (13), pp 6201–6207
- [162] Surawut Chuangchote, Jaturong Jitputti, Takashi Sagawa and Susumu Yoshikawa, *ACS Appl. Mater. Interfaces*, 2009, 1 (5), pp 1140–1143

6 References

- [163] Amanda Alonso, Xavier Muñoz-Berbel, Núria Vigués, Jorge Macanás, Maria Muñoz, Jordi Mas, and Dmitri N. Muraviev ,*Langmuir*, 2012, 28 (1), pp 783–790
- [164] Md. Selim Arif Sher Shah, Manaswita Nag, Thejaswi Kalagara, Shashi Singh and Sunkara V Manorama ,*Chem. Mater.*, 2008, 20 (7), pp 2455–2460
- [165] Ezio Amerio,Paola Fabbri,Giulio Malucelli,Massimo Messori,Marco Sangermano,Rosa Taurino, *Progress in Organic Coatings*, 2008,62, 129–133
- [166] Shadpour Mallakpour, Maryam Madani,*Progress in Organic Coatings*,2012,74,520-525
- [167] Vincent Ojijo, Suprakas Sinha Ray ,*Progress in Polymer Science*,2013,38, 1543-1589
- [168] Jayita Bandyopadhyay, Thomas Malwela, Suprakas Sinha Ray, 2012,*Polymer*, 53, 1747-1759
- [169] Suprakas Sinha Ray, Kazunobu Yamada, Masami Okamoto, Youhei Fujimoto, Akinobu Ogami, Kazue Ueda,2003,*Polymer*,44, 6633-6646
- [170] Suprakas Sinha Ray,2010,*Polymer*,51,3966-3970

7 Ehrenwörtliche Erklärung

Ich versichere, dass ich die von mir vorgelegte Dissertation selbständig angefertigt, die benutzten Quellen und Hilfsmittel vollständig angegeben und die Stellen der Arbeit – einschließlich Tabellen, Karten und Abbildungen, die anderen Werken im Wortlaut oder dem Sinn nach entnommen sind, in jedem Einzelfall als Entlehnung kenntlich gemacht habe; dass diese Dissertation noch keiner anderen Fakultät oder Universität zur Prüfung vorgelegen hat; dass sie – abgesehen von unten angegebenen Teilpublikationen – noch nicht veröffentlicht worden ist sowie, dass ich eine solche Veröffentlichung vor Abschluss des Promotionsverfahrens nicht vornehmen werde.

Die Bestimmungen der geltenden Promotionsordnung sind mir bekannt. Die von mir vorgelegte Dissertation ist von Prof. Dr. Sanjay Mathur betreut worden.

Köln, im November 2013

Osman Arslan

8 Curriculum Vitae

I was born in Manisa, TURKEY on 7th December 1980. My nationality is Turkish.

Education

- 1986–1991 Elementary School in Diyarbakır,
1991-1994 Middle School in Manisa ,
1994-1997 High School in Manisa,
1997-2001 Akdeniz University, Chemistry Department in Antalya,
2002- 2004 M.Sc. Akdeniz University, Chemistry Department (Advisor, Prof.Dr. Ertugrul ARPAC, Thesis Entitled: Use of Ceramic Particles in the Nanocomposite Surface Coatings)
(2004-2006) Akdeniz University-Chemistry, Research Assistant, Prof. Dr. Ertugrul Arpac
(2006-2008) Technology University of Graz (Inorganic Chemistry Institute), Research Assistant, Prof. Dr. Christoph Marschner

Publication

1. How Safe are Nanomaterials for Human Being? L. Xiao, S.Stucky, O.Arslan, D.Hermann, S. Kremer, B.Müller, L.Hermanns, S.Mathur, T.Thurnherr, H.Krug, J.Shi, A.Kunzmann, B.Fadeel, ICACC-11, Daytona Beach, Florida, 2011 (Poster)
2. In vitro mechanistic study towards a better understanding of ZnO nanoparticle toxicity , Buerki-Thurnherr, Tina; Xiao, Lisong; Diener, Liliane; Arslan, Osman; Hirsch, Cordula; Maeder-Althaus, Xenia; Grieder, Kathrin; Wampfler, Bruno; Mathur, Sanjay; Wick, Peter; Krug, Harald F. , Nanotoxicology , Volume 7 (4) – Jun 1, 2013
3. New Approaches towards the Chemical Growth and Modifications of Tin and Zinc Oxide Nanostructures, Lisong Xiao, Osman Arslan, Thomas Lehnen, Hao Shen, Sanjay Mathur, TCM2010, Greece (oral presentation)

4. Magnetic Nanobeads for Biomedical Applications, Laura Wortmann, Lisong Xiao, Osman Arslan, Sanjay Mathur, ICACC-12, Daytona Beach, Florida, 2012 (Poster)
5. In vitro mechanistic study on the toxicity of commercial ZnO nanoparticles, Tina Bürki-Thurnherr, Liliane Diener, Christopher Waldmann, Osman Arslan, Xenia Maeder-Althaus, Peter Wick, Sanjay Mathur, Harald Krug, 50th Annual Society of Toxicology (SOT), Washington DC, March 2011, (Poster)
6. Cysteine-functionalized zwitterionic ZnO quantum dots, Osman Arslan, Aadesh P. Singh, Lhoussaine Belkoura, Sanjay Mathur, Journal of Materials Research / Volume 28 / Issue 14 / 2013, pp 1947-1954
7. A comprehensive evaluation platform to assess nanoparticle toxicity in vitro, Hirsch, C.; Buerki-Thurnherr, T.; Xiao, L.; Arslan, O.; Wampfler, B.; Mathur, S.; Roesslein, M.; Wick, P.; Krug, H. F., Toxicology Letters 06/2012; 211(S), S41-S41:211(S), S41-S41
8. Gene Expression Profiling of Immune-Competent Cells Exposed to Metal Oxide Nanoparticles, Bengt Fadeel, Soile Tuomela, Andrea Kunzmann, Britta Andersson, Tina Bürki-Thurnherr, Peter Wick, Osman Arslan, Sanjay Mathur, Annika Scheynius, Harald Krug, Riitta Lahesmaa, 50th Annual Society of Toxicology (SOT), Washington DC, March 2011, (Poster)
9. Gene expression profiling of immune-competent human cells exposed to engineered zinc oxide or titanium dioxide nanoparticles, Soile Tuomela, Reija Autio, Tina Buerki-Thurnherr, Osman Arslan, Andrea Kunzmann, Britta Andersson-Willman, Peter Wick, Sanjay Mathur, Annika Scheynius, Harald F Krug, Bengt Fadeel, Riitta Lahesmaa, PLoS ONE 01/2013; 8(7):e68415
10. Quantum Dot Based Antibacterial Surfaces, Ania Jurewicz, Osman Arslan, Sanjay Mathur, ICACC-14, Daytona Beach, Florida, USA, 2014 (oral presentation)

Manuscripts in Preparation

11. Swift Synthesis of Ultrastable Oleate@ZnO Quantum Dots as Visible Light Emitters, O.Arslan, L. Belkoura, S.Mathur, Adv. Funct. Mat., submitted,
12. Multibranched, Visible Light Active TiO₂ Nanostructures by Hot Injection Method, O.Arslan, M. Tuncer, L.Belkoura, S. Mathur,
13. Nanoclays as Facile Visible Light Emitting ZnO QD Synthesis Platforms, O.Arslan, Suprakas S. Ray, S.Mathur,
14. Distorted Hexagonal ZnO Nanocrystals and Their Photocatalytic Activity : Zn-carboxylate Thermolysis Revisited , O.Arslan, S.Mathur,
15. Enhanced Photocatalytic Activity and Self Assembly of TiO₂ Nanoparticles by Hot Injection Sensitization, O.Arslan, S.Mathur,
16. Enhanced Antibacterial Activity By Surface Engineered ZnO QD/Hybrid Nanocomposites, O. Arslan, A.Jurewich, S.Mathur,
17. Transparent, UV Protective Hybrid Nanocomposites, O.Arslan, S.Mathur
18. UV Curable, Transparent, Biodegradable ORMOCER Nanocomposites, O.Arslan, S.Mathur

Awards and Honours

- Graduated as Bachelor Top Student at the 2000-2001 term, Akdeniz University- Chemistry Department
- Bachelor Honour Student at the 2000-2001 term
- Poster Prize for How Safe are Nanomaterials for Human Being? (Best Poster Award, 2nd Rank)